EXPERIMENTAL INVESTIGATION OF INTERACTIONS BETWEEN EXPLOSIVE DETONATIONS AND THE RESULTING SNOWPACK RESPONSE

by

Josephine Anne Bones

A thesis submitted in partial fulfillment
of the requirements for the degree

of

Master of Science

in

Civil Engineering

MONTANA STATE UNIVERSITY
Bozeman, Montana

November 2012

APPROVAL

of a thesis submitted by

Josephine Anne Bones

This thesis has been read by each member of the thesis committee and has been found to be satisfactory regarding content, English usage, format, citation, bibliographic style, and consistency and is ready for submission to The Graduate School.

Dr. Daniel A. Miller

Approved for the Department of Civil Engineering

Dr. Jerry Stephens

Approved for The Graduate School

Dr. Ronald W. Larsen

STATEMENT OF PERMISSION TO USE

Josephine Anne Bones

November 2012

ACKNOWLEDGEMENTS

Thank you very much Bridger Bowl Ski Area, Big Sky Resort, and the Yellowstone Club for allowing access and ski patrol support to conduct testing. Thank you to the National Ski Area Association, Forest Service National Avalanche Center, American Avalanche Association, Sigma Xi, and the International Society of Explosive Engineers for contributing to this research.

I would like to thank Dr. Miller for his insight, patience, and guidance as my advisor. Thank you to my committee, Dr. Adams, and Professor Larson, for their time. A special thank you to my family and friends for always encouraging and believing in me throughout this process. Especially, thank you Jono for all of the meals, support, and for continuing the adventure of life with me.

TABLE OF CONTENTS

TABLE OF CONTENTS - CONTINUED

LIST OF TABLES

LIST OF TABLES – CONTINUED

LIST OF FIGURES

LIST OF FIGURES – CONTINUED

Figure Page

LIST OF FIGURES – CONTINUED

LIST OF FIGURES – CONTINUED

ABSTRACT

Avalanches threaten many areas of the world. For many years, risk has been mitigated through artificial avalanche initiation using explosives. Even with extensive use, a lack of experimental determinations of the interactions between explosive detonations and the snowpack response exists. To address this, a multiyear field based research project was conducted at Montana State University, Bozeman, MT. A portable instrument array consisting of pressure and accelerometer sensors was fabricated and utilized to record the overpressure and acceleration of the snowpack resulting from detonation of pentolite cast boosters. Explosives were detonated 0-2 m above the snow surface, at 0.5 m increments. All sensors were placed within a 7 m radius of the explosive in soft slab and hard slab snow conditions. The data was used to characterize relationships between explosive size and location to the resulting overpressure and snow acceleration based on various snow parameters. The snow surface was shown to be able to reflect shockwaves, thus, increasing the shockwave pressure. It was shown that elevating an explosive off the snow surface resulted in greater overpressure and peak snowpack acceleration than surface detonations. Elevating an explosive was found to not influence the vertical or radial attenuation. Therefore raising a charge increased the volume of influence. Overpressure and acceleration were shown to be nonlinearly related to the explosive mass. Doubling the mass resulted in less than double the response. The acceleration of moist snow was determined to be less and the attenuation greater than for dry snow conditions. Hard slab conditions indicated lower acceleration and greater shockwave attenuation than soft slab snow. Snowpack peak acceleration and attenuation were shown to have little dependence on either the total snow water equivalent or snow density. For rock bed surfaces the shockwave was reflected back through the snow while meadow bed surfaces did not. This project verified past theoretical and experimental results, but further research would be beneficial for avalanche mitigation work. A continuation of this work could lead to increased efficiency and safety for the avalanche community.

INTRODUCTION

Avalanche and Mitigation Background

At the simplest level, an avalanche is snow moving down slope. Often avalanches occur in mountainous areas when people are not present without any threat to human life. Other avalanche situations involve people recreating at established ski areas, using transportation corridors, or simply carrying out daily activities in inhabited areas. When avalanches pose a direct threat in these situations, the risk is often mitigated through the use of artificial release methods. Artificial avalanche initiation is a widely used method for reducing the hazard and is primarily done with the use of explosives (LaChapelle, 1977). Initiation methods are very diverse: ranging from hand explosives; military ordinances; solid and gas mixtures; stationary and mobile delivery systems (Atwater, 1968; Gubler, 1977; LaChapelle 1977; McClung and Schaerer, 2006; Perla, 1978). In North America, 0.9 kg pentolite cast boosters are the most commonly used explosive (Perla, 1976). Pentolite cast boosters are manufactured primarily for use in mining operations to initiate non self-igniting explosives such as ANFO (ISEE, 1998). Generally, the explosives used are classified as “fast” based on the detonation velocity. Perla (1976) indicates high-speed explosives are preferred over low speed explosives for many reasons, including handling safety and the untested belief they are more effective at initiation of avalanches. As the detonation velocity increases so does the frequency of the resulting shockwave (Brown, 1980).

While explosive methods for mitigating avalanche hazards are common, a fundamental understanding of the interactions between snow and explosives is lacking. In avalanche mitigation work, practitioners use explosives to overload a weak layer in the snowpack. Often times, the placement of charges is based on experience, with little scientific basis for decision making, due to a lack of research. Explosives are used for avalanche mitigation work because the pressure jump, due to explosive detonations, loads the snowpack (Miller, 2011). To create failure of a weak layer, the pressure resulting from an explosive must be greater than the failure or yield strength of the layer (Johnson, 1994). Explosives are used for avalanche mitigation work due to increasing stress in critically weak zones (Johnson, 1994). The load necessary to initiate failure is not constant due to variability of instability (LaChapell, 1977). To increase the probability of success, it is desired to maximize snow stress and volume impacted by the explosive.

The use of explosives for avalanche mitigation is generally effective and yields the desired result, but occasionally the snowpack responds unexpectedly. Recently, there have been several unintended avalanche releases following explosive mitigation work, at ski areas. In the 2008-2009 winter season there were four fatalities and another 18 people involved in avalanches within US ski area boundaries (Abromeit, 2010). Since 2009, avalanches within resort boundaries have killed an additional five skiers and snowboarders (www.avalanche.org). Most of these incidents have been classified as post-control releases and illustrate the need for continued and expanded research efforts (Ferrari, 2010). The use of “control” in this situation is analogous to risk mitigation work because avalanches cannot be controlled.

Explosives Background

Explosive detonations rapidly transform chemical energy in a limited space accompanied by a sudden increase in pressure, temperature and velocity resulting in the formation of a blast wave. The blast wave is also called an n-wave due to the shape of the pressure-time history of the wave (Gubler, 1977). When the resulting blast wave velocity is greater than the acoustic velocity of the material, a shockwave occurs. Due to geometrical expansion and losses to the surrounding medium, the shockwave eventually attenuates to an elastic or acoustic wave (Kinney and Graham, 1985). The amount of energy transmitted by the blast wave into other mediums depends on the coupling between the explosive and medium. For good mechanical impedance match,

$$(1) \qquad D_V * E_D \approx A_V * M_D$$

Where D_V is the detonation velocity, E_D is the explosive density, A_V is the acoustic velocity of the medium, and M_D is the density of the medium (Mellor, 1973).

To fully describe a blast wave three independent characteristics must be known: initial shock intensity; duration of the blast wave; and impulse. Figure 1 denotes the characteristics on an example blast wave. The initial shock intensity can be described multiple ways, but the simplest to record is the peak overpressure. The overpressure is defined as the difference between the pressure immediately behind a blast wave and the ambient air pressure; such that an overpressure wave is created when the explosive is detonated in the air. Time duration is an indicator of the possible damage a blast wave could cause. A blast wave has a positive pressure phase time duration defined by the time the overpressure is positive. There also is a negative pressure phase duration, but measuring it is more difficult. The negative duration is typically longer than the positive duration. Blast wave impulse also indicates the damage-causing ability of a blast wave, especially for short duration explosions. Impulse is defined as the area under the pressure-time curve and has units of force-time. The blast wave impulse depends on the peak overpressure, time duration, and overpressure rate of decay (Kinney and Graham, 1985).

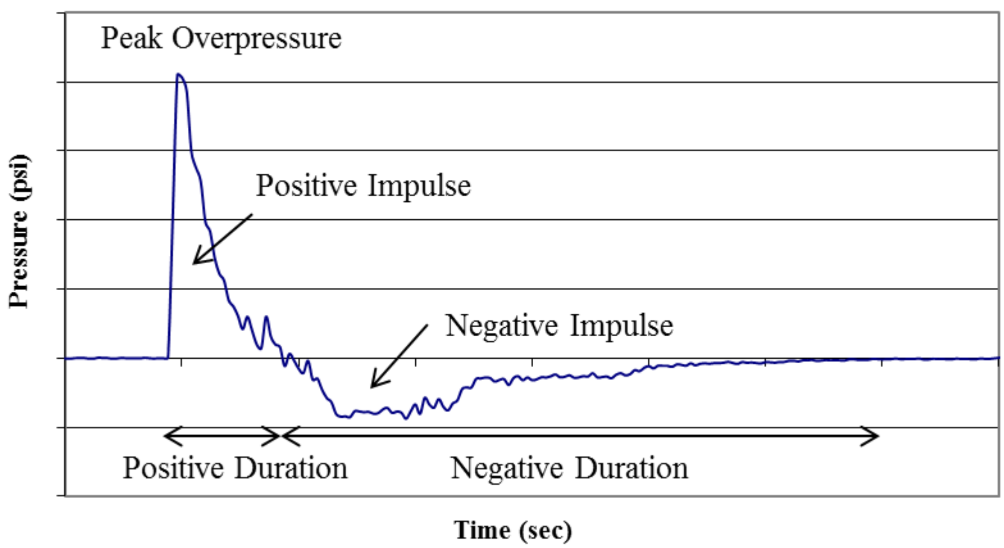

Figure 1 Example blast wave pressure time graph with overpressure, duration, and impulse denoted.

Blast waves can be reflected off solid surfaces. The amount of reflection depends on the material properties. Reflection due to explosives is an oblique reflection due to the near head-on incidence angle of the incoming wave front. Oblique reflection results in the reflective material experiencing two successive shocks. First the direct shock occurs and is followed by the reflected shock (Kinney and Graham, 1985). Shock reflection results in an increase of the pressure wave thus increasing the input the material is subjected to.

Past Research

In the past, there have been limited theoretical and experimental research projects specifically focusing on the dynamic response of snow to explosive detonations. Brief overviews of these projects are presented in the following discussions. While some experimental research has been performed, there has been little modern empirically based experimental analysis work characterizing the interactions of explosives and snow.

Theoretical Investigations

Past theoretical work focused on interactions between explosive detonations and snow cover is limited. By modeling snow as a non-linear viscoplastic material and assuming a rate-sensitive yield stress, Brown (1980) was able to model non-steady plastic shockwaves in snow. Assuming the shockwave is steady does not allow for computational solutions for wave attenuation. Brown was able to show that density change due to surface loading decreases rapidly with depth. By varying the load, the author showed the increased density is significant near the surface, but at deeper depths it became almost negligible. This illustrated the ability of snow to absorb energy. Brown also showed that the peak pressure attenuates quickly, congruent with the findings for density. Brown compared his results to those found experimentally by Wisotski and Snyder (1966). Wisotski and Snyder (summarized in Brown, 1980) buried 0.45 kg pentolite charges and placed piezoelectric transducers 0.25 m to 1 m away at the same depth. Their experiment showed significant attenuation of peak pressure values. Brown also calculated that lower frequency waves have lower attenuation than high frequency waves. This is in agreement with a finding by Lang (1976) for non-plastic waves.

Further work by Brown (1981) showed a fourth order nonlinear partial differential equation could be solved to characterize snow pressure response to rapid compressive deformations. The rapid compressive deformations were the result of explosive detonations. Comparison of the numerical solution, computed using finite differencing methods, to the limited available experimental data, yielded reasonable results. The calculations indicated wave amplitude was reduced by about 90% of the original amplitude within 0.1 m of propagation distance. This method is exceedingly time and computationally intensive and, therefore, is not commonly practiced.

Johnson (1982) applied Biot's theory to snow, treating the snow as a porous medium consisting of an elastic lattice filled with air. Using this theory and applying the necessary parameters, he was able to show an acoustic wave is comprised of three distinct waves. There are two attenuated dilatational waves and an attenuated shear wave. While he was able to calculate theoretical properties of these waves, no experimental data had separated the two dilatational wave types therefore experimental confirmation of the individual wave types was not possible. From the shear wave calculations, Johnson predicted wave propagation velocities decreased as the snow density increased.

Similar to Johnson's (1982) work, Austiguy Jr. and Brown (1993) applied a mixture theory to model stress waves in snow. They focused on stress wave propagation outside of the crater left in the snow due to explosive detonations. The snow densities investigated ranged from 410 kg/m^3 to 600 kg/m^3. The authors looked at two different frequency ranges, 1-100rad/sec and 1000-10x10^8 rad/sec. The two ranges were chosen because they determined shockwaves due to explosive detonations are high frequency and very short time duration events. Waves in the high frequency range were shown to consist of three wave types, similar to Biot's theory (Johnson, 1982) predicted. For low frequencies, only one dilatational wave and the shear wave were detected. Regardless of the frequency range, Austiguy Jr. and Brown showed wave velocity increased with increasing density for all wave types. Similarly, wave attenuation coefficients for all wave types were found to decrease as the snow density increased. Brown (1980) and (1981), Johnson (1982), Austiguy Jr. and Brown (1993) focused on theoretical determination of wave characteristics with little experimental data for comparison purposes.

Laboratory Investigations

Along with theoretical work, laboratory experiments pertaining to snow shockwave interactions to simulate explosive detonation have been conducted. Research conducted in the 1990's was focused on dynamic snow response and fundamental characteristics of snow subjected to high and rapid loading. Johnson et al. (1993) conducted gas gun impact tests and determined the pressure-density relationships for several initial snow densities with stresses up to 40 MPa. The pressure range of interest varied from 2-5 MPa and 20-40 MPa and initial snow densities ranged from 111 kg/m^3 – 520 kg/m^3. Shockwaves were produced by firing flat plates into natural and processed snow samples with stress gauges embedded in the snow. The stress gauges were located directly below and within 5 cm of the impact location (Johnson et al., 1993). Due to the gauge locations, this would be akin to a location directly below an explosive detonation in the field. Johnson used the resulting measurements to determine constitutive pressure-density relationships based on the initial snow density. The data indicate the occurrence of strain hardening as a rapid slope change of the curve. The strain hardening transition occurred at the point of critical density. Prior to reaching critical density, particle deformation has not occurred, but once reached, deformation must occur for the density to increase. Prior to reaching critical density, the snowpack will not accept significant stress. Critical density depends on the snow sample initial density as well as the loading process. Theoretical calculations were in close agreement to the experimental values available.

Furnish and Boslough (1996) explored the interactions between shockwaves and snow by conducting impact tests on snow to experimentally derive Hugoniot states, re-shock characteristics and release properties. The Hugoniot state describes shock relationships pertaining to the state of a material just in front of and just behind a shock wave and is dependent on the material of interest (Cooper, 1996). Furnish and Boslough determined shock Hugoniot states from the transit time of wave within a sample of natural snow and material simulators. They report reliable snow Hugoniot states, with snow density of 500 kg/m^3, at stresses up to ~4 GPa. While these experiments provide critical data and insights on fundamental snow responses, they are difficult to scale up to avalanche control field scenarios.

<u>Field Investigations</u>

Other studies have targeted explosive avalanche control in particular through field measurements. A field experiment conducted by Hansen and Brown (1986) investigated snow microstructure before and after a blast and determined the role of crack formation in energy dissipation. They developed a statistical model with nine parameters; the parameters were measured prior to and following a detonation. From this, it was determined ice fracture does not significantly influence energy dissipation of shockwaves. This finding was applicable for snow densities less than 600 kg/m^3. Hansen and Brown believed interactions between the solid ice and air would have a notable impact on the energy dissipation of a shockwave within snow.

Two field experiments involving sheet explosives were conducted by Johnson et al. (1994) and Solie et al. (1993). Johnson et al. (1994) detonated sheet explosives on the snow surface to produce a plane shock wave. Stress gauges were buried at various depths and were used to determine attenuation of the shockwave pressures with distance. The experiment showed high shockwave attenuation within the snow cover. Power law regression was applied to the data to determine attenuation. The attenuation was determined to be $x^{-1.6}$ for a sheet explosive. Johnson et al. (1994) determined attenuation is related to the explosive geometry and pressure volume deformation during loading and unloading. An examination of explosives detonated on the snow surface indicated a large portion of the energy will be dissipated through snow compaction in the crater zone. Johnson et al. (1994) believed the primary transfer of the pressure wave into the snow was through the air pores. An examination of the snow following charge detonation was done and determined compaction as well as permanent deformation of the snow occurred. The compaction resulted from a combination of particle rearrangement and particle deformation until a critical density was reached. It was noted that beyond the critical density, compaction was a result of deformation. This finding was similar to that described by Johnson et al. (1993). The pressure required to compact snow to a final density value increased with decreasing initial density. An analysis of experimental air blast data from Ingram (1962) and Wisotski and Snyer (1966) (summarized in Mellor (1985)) allowed the authors to present a scaled curve of maximum air pressure as a function of burst height and radius from the blast vertical axis. This curve identifies the scaled burst height for maximum pressure at particular scaled distances. The data supports ~40% increase in overpressure as the detonation height is increased from the surface to the optimal height (for a particular range and net explosive weight). The maximum overpressure was relatively insensitive to scaled detonation heights above ~2 $m/kg^{1/3}$

Solie et al. (1993) also detonated sheet explosives over snow. He detonated the explosives at and above the snow surface in 1 m deep snowpacks. Stress gauges were placed at different depths below the snow surface. The measurements recorded by the stress gauges showed rapid attenuation of shockwaves in snow. To determine the effect of excluding explosive gasses from the snowpack, a thin aluminum membrane was placed at the snow air interface. Tests conducted in this manor resulted in increased pressures within the snowpack as well as reduced wave time of arrival. Both time of arrival and pressure as functions of depth were shown to fit power law decay very well.

The use of power law regression in this study was similar to that employed by Johnson et al. (1994).

Crater Investigations Directionality of explosives and crater sizes resulting from detonations were investigated in multiple studies. Fuchs (1957) conducted a field experiment detonating 40% gelatin and TNT at different depths. Following detonation a visual inspection of the snow was done to characterize the results of the explosion. He found the largest resulting crater for a particular mass of explosive, regardless of type, was for a buried charge. Ram profiles before and after detonations were collected. Ram profiles index the snow hardness through a vertical section of the snowpack (McClung and Schaerer, 2006). Fuchs recorded a decrease in ram hardness in the center of the crater directly after detonation for a buried charge. As time elapsed, the ram number increased at the crater center. While this early study examined changes in the snowpack it was more of a qualitative than quantitative study.

Livingston (1968) conducted explosive studies in Greenland on snow. A combination of seismographs, three types of pressure gauges, and two accelerometer types were used to record responses to explosive detonations. Multiple pressure and accelerometer instruments were necessary for different response ranges based on location from the explosive. Due to detonating charges above, at, and below the snow surface, at multiple depths, Livingston noted the crater size increased to a maximum then decreased as the charge depth increased. While seismic, pressure, and acceleration values were obtained, the study primarily focused on the failure process that occurred in the snow. It was shown implosion as well as scouring and vortex motions occurred in the snow cover as a result of explosive detonations.

Powell (2000) investigated the use of shape charges, to concentrate the energy as desired, for avalanche mitigation work. Shape charges were placed and detonated1.2 m below the snow cover. For the different shape charges studied, all resulted in increased crater volumes when compared to a control crater volume due to a non-shape charge

An experiment conducted in Utah focused on the effectiveness of a charge based on orientation (Binger et al., 2006). Effectiveness was determined by crater characteristics. The charge placement and orientation were varied. Following detonation, the resulting crater was measured and profiled. From the study, the authors concluded the blasting cap orientation did impact layer compression. Downward facing caps resulted in greater compression than caps facing upward. The greater compression was noted both with depth and range. Cap down orientation also resulted in a deeper crater with a larger radius than a cap up did for surface detonations. While Binger et al. showed cast boosters do have directionality due to cap orientation; Sherwood (2000) presented information on the directional characteristics of hand charges and noted that while hand charges do have directionality, this decreases with increasing distance. Therefore, an elevated explosive will have less directionality than a surface or buried charge (Sherwood, 2000). For explosions in air, the resulting waveform is the similar regardless of the explosive shape, but the amount of energy influences the characteristics of the wave (Kinney and Graham, 1985).

A study by Frigo et al. (2010) focused on dynamic snow response to two explosive types. The first explosive was an emulsion and the second was dynamite. The explosives were located below, at and above the snow air interface. Snow profiles, georadar, seismic, vibration, and acoustic measurements were used to compare pre and post detonation situations. Georadar was used to determine density variability and changes in snow depth while the seismic sensors were used to estimate mechanical properties of the snow. A combination of geophones and microphones were used to monitor vibrations due to the detonations, and were located 56-180 m from the blast. The acoustic sensors were used for gathering the overpressure resulting from air blasts. The authors saw a decrease in crater size with elevated shots. The georadar showed changes in the snow layer locations as a result of the detonations. At the time of paper publication, the data was still being analyzed to determine relationships between the different variables. Examination of the crater indicates the amount of energy absorbed by the snow at that location, but does not provide any information on how the shockwave moves through the snow. Even though the crater is larger, the effectiveness of the explosive for avalanche mitigation may not be maximized.

Snow Dynamic Response and Overpressure Investigations To investigate the shockwave snow interactions outside of the resulting crater, a couple of field based research projects were conducted. Gubler (1977) conducted field tests to determine the effect of pressure waves due to explosive detonations in snow beyond the crater zone. Gubler investigated buried, surface and elevated shot locations for different sizes, shapes, and types of explosives. Accelerometers and pressure sensors were placed within the snowpack to record responses to explosive detonations. The measurements were taken 10-60 m, with the majority at 20m or greater, from the detonation. Gubler noted that shots detonated below the snow surface resulted in the smallest response when compared to different charge placements. The low response for explosives placed below the surface indicated coupling between the explosive and snow was low. Gubler noted a peak pressure decrease of 1-2 orders of magnitude for buried detonations when compared to airblasts. Coupling between the air and snow was shown to be better than between the explosive and the snow through greater snowpack response for airblasts. In dry snow conditions, the shockwave coupled to the snow well while in wet snow conditions it did not. Higher attenuation was noted in wet than dry snow. From his work, Gubler determined an elevated charge height of 1-2 m would be the most effective for initiating an avalanche in dry snow.

Ueland (1992) used seismographs to record snow response that resulted from explosive detonations to compare different snowpacks, explosives, and masses along with charge placement. The seismographs allowed for recording acceleration in the vertical direction only and restricted the nearest sensor placement to 20 m from the charge. For an isothermal snowpack, Ueland noted substantial attenuation of the shockwave vertical component. For low density dry snow the attenuation was less than the isothermal snowpack. Ueland believed snow hardness rather than density had a controlling effect on attenuation. It was hypothesized the increased attenuation in an isothermal snowpack was due to three water phases being present. A comparison of 0.9 kg cast boosters to 1.25 kg of ammonia gelatin dynamite was conducted. The two explosives resulted in comparable results. When varying the explosive mass he showed the area of influence increase is not linearly related to the mass increase. Changing the charge elevation confirmed Gubler's finding that airblasts showed greater wave amplitudes than surface or buried charges did.

Machida et al. (2008) focused on wet snow due to common wet conditions found in Japan. They utilized a water gel explosive and inserted the explosive into the snow cover by drilling a hole and backfilling. Buried charges were the standard explosive placement in the region of interest. Air pressure sensors were inserted into the snowpack at different depths. Recordings from these sensors indicate that explosive bury depth along with the explosive mass impact the resulting air pressures recorded in the snow. Explosives also were placed in a pattern attempting to release snow and create a sliding plane. The explosives were placed in two zones for this portion of the project. The first zone was the destruction zone and the second was the sliding plane formation zone. For the two cases explored, the authors were able to show the explosives worked as planned.

The pressure shockwave above the snow surface also was investigated in multiple studies and summarized by Mellor (1985). Using values from Ingram (1962), Joachim (1964), and Mellor and Smith (1967), Mellor determined the overpressure attenuation with radial distance. A plot of the values fit with a power regression indicated an attenuation exponent of -1.6. A summary of overpressure values obtained by Wisotski and Snyder (1966), again summarized by Mellor indicated the overpressure with range was proportional to $1/r^2$ where r is the radial distance from the explosive. A comparison by Mellor of shock reflection showed the reflection to be less over snow than a rigid surface. Values for snow reflection were from work conducted by Ingram (1962). Using data from Wisotski and Snyder (1966), Mellor created plots indicating that regardless of the charge detonation elevation and the radial distance, the overpressure was less for snow than bare ground.

Past Research Impacts

Many avalanche mitigation programs have benefitted from explosive research and consequently adapted their operational techniques. For example, Juergens (1984) discusses implementation of the first and subsequent explosive delivery tramways at Bridger Bowl Ski Area, Montana. A comparison of aerial detonations and hand thrown charges in adjacent slide paths indicated a larger volume of snow was moved due to the suspended charges. Not only has the practice of elevating charges been used, but appears to have increased the effectiveness of avalanche mitigation work. There still needs to be more research into the dynamic snow response due to explosive detonations.

Technological advances would allow for and justify continued research on the snowpack response to explosive detonations. Continued research would allow for confirmation of previously determined relationships and possibly new determinations. Research in this area has the potential to increase the effectiveness of avalanche mitigation work, which in turn could potentially result in increased safety and financial savings for mitigation programs.

To address this need, Miller et al. (2011) started a research project at Montana State University. Using AUTODYN, a commercially available explicit modeling program, the authors modeled surface and air blasts and the resulting snowpack response.

The model allowed for simultaneous non-linear solid and gas interactions to be calculated. This was accomplished by describing the snow as an Eulerian material, the air as a Lagrangian material, and the interface between the materials as interactions between the two material types. The model predicted enhanced surface pressures due to reflection of the shockwave off the snow surface. Compression and shear stress waves were shown to move through the snow vertically as well as radially. Density increases, due to the detonation, were also shown. Comparison of particle velocity at different radial ranges, due to a surface and a 1 m elevated shot was done. Acceleration in close proximity to the blast, ~ 0-.25 m, was greater for a surface detonation than the elevated charge. For distances ~ 0.5-3 m the elevated charge resulted in more than double the acceleration. The model predicted greater air pressures due to a surface charge for radial distances of 0-2.5 m. Beyond 2.5 m the elevated charge resulted in greater pressures (Miller et al., 2011).

Past field research and the recent analytical modeling work by Miller et al. (2011) was a catalyst for the research in this thesis. Multiple projects used crater size as an indicator of explosive effectiveness. Crater size may indicate the destruction due to the explosive at the detonation site, but does not yield any information about the effectiveness of the charge over a large area. Therefore recording the blast wave effect on the snow is necessary.

In past research efforts, the methods used to record interactions between explosives and the snowpack restricted the closest measurements to be at least 10 m from the explosive. Technological advances would allow sensor placement to be closer than in the past resulting in quantification of the snowpack response in close proximity to the detonation. Shockwave attenuation of -1.6 was determined for sheet explosives, but the explosives for avalanche mitigation are spherical. Determination of shockwave attenuation for spherical charges would be applicable to actual field application. A continuation of research to characterize explosive snow interactions would benefit the avalanche mitigation community.

RESEARCH METHODS

Objectives

The main goal for this project was to investigate dynamic snow response in close proximity to explosive detonations by using instruments with greater dynamic range and durability than those used in earlier studies. Modern instrumentation and techniques allow for detailed investigation of effects in close proximity to the blast allowing for greater understanding of explosive use. To do this, a multiyear (2010-2012) field based research project was completed. The experimental goals of this study included:

1) Development of an instrumentation suite that is field portable and capable of capturing snow dynamic response at multiple locations and air blast overpressure values.
2) Determine the relationship of air overpressure values to explosive placement.
3) Characterize the relationship between explosive detonations and the resulting snowpack response.

The first objective was completed prior to conducting field tests, while the remaining objectives involved gathering and analyzing field data. The second and third objectives are multifaceted and are discussed in detail in the Results and Discussion chapter. The overpressure data was examined to establish a relationship between:

- charge locations and overpressure
- overpressure and pressure impulse
- compare overpressure values at the snow surface to an elevated height

Snowpack acceleration was used to characterize snow dynamic response and was analyzed to determine:

- test-to-test repeatability
- response increase due to charge position
- the impact on snow acceleration with depth and range due to different detonation elevations
- charge location effect on shockwave vertical attenuation
- charge location effect on shockwave radial attenuation
- the difference in snowpack response for dry and moist snow conditions
- the response difference between detonating 0.45 kg and 0.9 kg explosives
- the difference in acceleration response for soft and hard slab snow
- acceleration and attenuation dependence on total snow water equivalent
- acceleration and attenuation dependence on snowpack density
- snowpack displacement due to explosive detonations
- bed surface ability to reflect shockwaves

Testing Protocol Overview

During the winter of 2010-2011, the investigation focused on soft slab snow conditions while tests were conducted in hard slab snow conditions during the 2011-2012 season. There were some procedural variations between the two seasons, due to lessons learned in the first season, but the overall experimental methods remained very similar. Detailed methods, per season, are presented in the Test Methods section. On each test day, upon arrival at the test location, a general test layout, comprised of several test sites, was outlined. A snowpit was conducted to characterize the daily snowpack in terms of stratigraphy, density and depth at the test location. Prior to each test, a portable instrumentation array was installed at the selected location. The instrumentation array consisted of accelerometers and over pressure sensors. A general sensor layout is shown in Figure 2, actual sensor locations varied by testing year.

A monitoring station consisting of a computer with a companion data acquisition system and battery for power was established in a safe location. Instrumentation cabling was secured to the sensor array to supply excitation power and monitor analog signals. A data acquisition system and accompanying computer was used to capture analog data in digital formats. The computer program was tested to ensure full system functionality prior to the test. Multiple tests were conducted each day with sensors placed in undisturbed snow. Field data was post processed and analyzed supporting the objectives listed above.

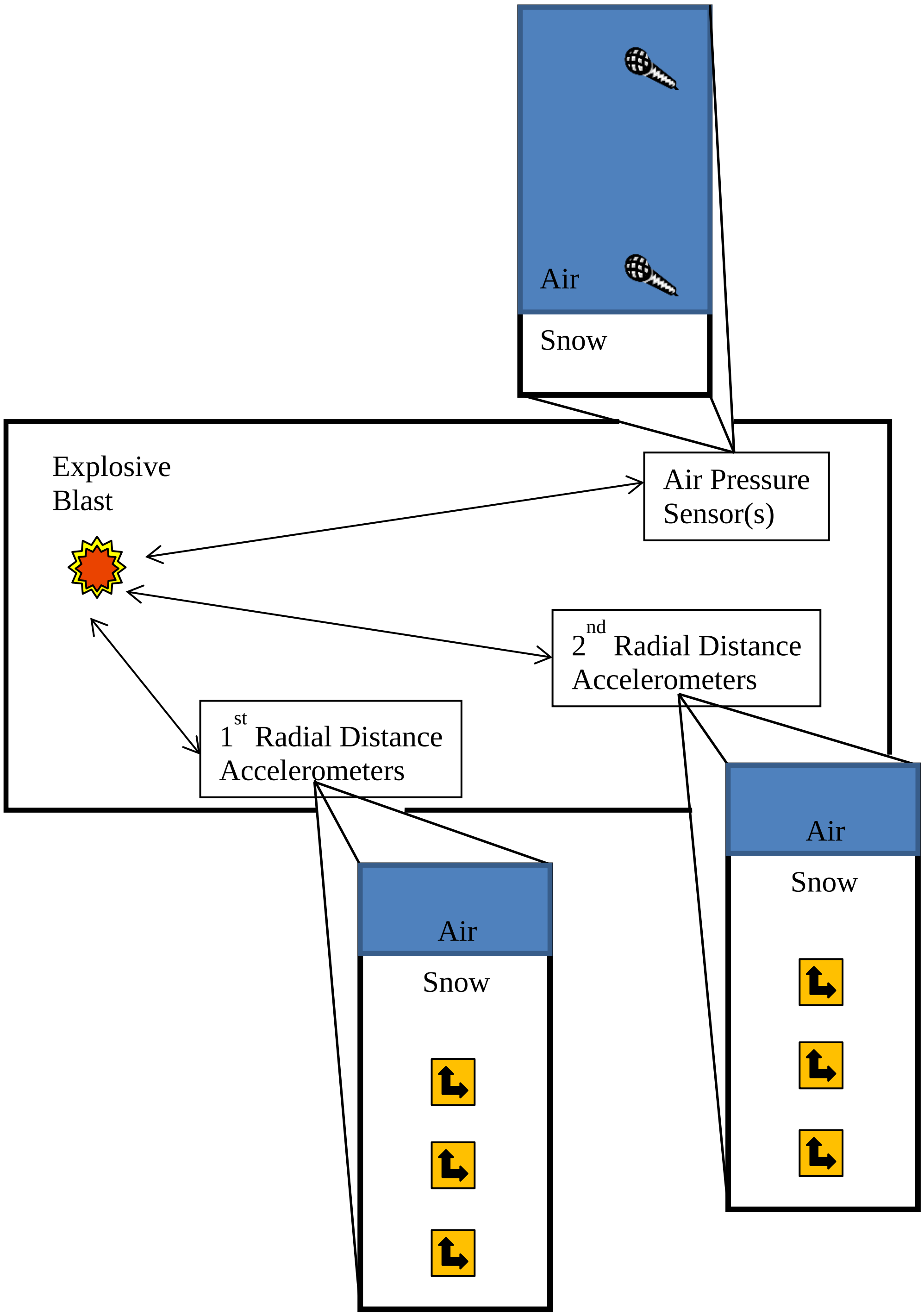

Figure 2 General testing layout plan-view with exploded cross sections. A total of 6 accelerometers were placed within the snowpack at two radial ranges. The accelerometers were placed through the snowpack depth with a sensor in the top, middle, and bottom portions of the snowpack. The overpressure sensors were located at a single radial distance. Sensor placement was determined by the snowpack and varied per day.

Field Locations

Different test sites were necessary to locate naturally occurring soft slab and hard slab snow conditions. Locations were chosen for snow type, site accessibility and ability to safely conduct explosive testing. The sites were not located directly in avalanche terrain, but did provide an excellent opportunity to measure the snow explosive response during multiple tests. Both locations were within operational ski areas and ski patrol personnel performed all explosive handing tasks. All testing locations provided enough area for multiple tests to be conducted per testing day with a minimum of 10 m between blast centers.

Bridger Bowl Ski Area in Southwest Montana was selected for soft slab snow investigations during the 2010-2011 winter season. All tests were conducted in a large low angle, approximately 15-20 degree slope, meadow. Trees bordered the meadow and helped ensure adequate snow depths for testing. The meadow was located beyond the ski area boundary, but within the permitted blasting region, allowing testing to occur during regular operating hours. Figure 3 shows the Bridger Bowl testing site.

Figure 3 Photo taken during sensor placement at Bridger Bowl during the 2010-2011 testing seasons. This site was selected for soft slab testing. The explosive for this test was elevated 2 m above the surface. While research personnel handled instrumentation, snow safety personnel conducted all explosive handling tasks.

Testing for the 2011-2012 season was done at Big Sky Resort in Big Sky, Montana to focus on hard slab snow conditions. Big Sky Resort commonly has hard slab avalanche issues requiring mitigation and therefore was a good hard slab test location. Ski area personnel helped identify areas containing unskied hard slabs. Three locations, within Big Sky, were utilized for testing during this winter season. All three locations were near tree line with talus rock as the primary bed surface. Since the sites were within ski area boundaries, testing occurring after the resort was closed to the public. One of the testing sites is shown in Figure 4.

Figure 4 One of the testing sites at Big Sky resort for hard slab snow conditions conducted 2011-2012. The charge is elevated 1 m (left foreground) and the sensor placement as shown was the season testing standard.

Testing Methods

A general test protocol was previously presented, but detailed methods are included in this section. The 2010-2011 winter season was dedicated to soft slab snow conditions at Bridger Bowl. The snow conditions this season were generally dry, but moist snow was also tested late in the season. Testing that occurred during the 2011-2012 season focused exclusively on hard slab snow conditions at Big Sky Resort. This season was a very low snow year for the area and adequate depth hard slab conditions did not develop until late in the season. As a result, all testing occurred later with moist snow conditions.

Upon arrival at the testing location, regardless of the testing season, individual detonation sites were selected and locations conveyed to the explosives handler. Sites were chosen to ensure a minimum of 0.9 m of snow depth at the charge and sensor locations and 10 m spacing between blast centers. On each testing day, a snow pit was completed. Pit data for each test day is included in Appendix A. The snow pits classified the hand hardness and/or crystal type for individual layers and density values were taken every 10 cm, regardless of the layer locations. Generally, the ski patroller performed a snowpit classification of the snow at the testing site while sensors were being placed. Accelerometers were placed below the snow surface and the air pressure sensors were located above the snow surface, all located within a 7 m radius of the explosive and the computer setup a safe distance away. Placement of sensors is detailed below with the sensor technical details presented in a subsequent section.

Air Pressure Sensor Placement

A prototype Larcor acoustic instrument was used to measure blast overpressure due to the explosive blast, at a single radial distance, illustrated in Figure 2. One sensor was used during the 2010-2011 winter season. The predicted maximum overpressure and the sensor’s range determined the placement distance of 5 m from the explosive. The sensor was located at the snow air interface. Due to acqusition of additional funding, a second sensor was purchased and used in the 2011-2012 winter. With two sensors, one was located at the snow surface and the other was elevated 1.5 m above the snow cover. An elevated sensor allowed for determining if the snow surface reflected the shockwave resulting in higher overpressure values at the surface compared to the elevated location. Originally the sensors were located 5 m radially from the blast center, but were moved to 7 m after exceeding sensor dynamic range and saturating the sensor signal. Regardless of the season, the microphone sensors were aligned facing the blast center for all tests conducted.

Accelerometer Placement

The accelerometers were located at two radial distances referenced to the explosive charge location and at three depths for a total of six locations. Measuring acceleration at multiple depths and ranges allowed for comparisons to be made with range and depth changes. Accelerometer pair placements were placed at general locations near the surface, mid depth and at depth in the snowpack as depicted in Figure 2. The sensor placements on a particular test day were dictated by the snowpack stratigraphy. The accelerometers were oriented to capture vertical and radial snow accelerations, referenced to the explosive. The radial distance of accelerometer placement for the two testing seasons is shown in Table 1. The accelerometer placement depths were determined by the snowpack conditions for each particular test day, but were placed in similar locations for all tests in a testing year. Average depths below the snow surface for the two testing seasons are denoted in Table 1.

Table 1 Accelerometer type utilized and location for both testing season.

Testing Season	2010-2011 Testing		2011-2012 Testing	
Radial Distance	2 m	5 m	3 m	5 m
Accelerometer Utilized	ADXL 193	ADXL 321	ADXL 278*	ADXL 321
Average Top Accelerometer Depth	-0.12 m		-0.22 m	
Average Middle Accelerometer Depth	-0.38 m		-0.53 m	
Average Bottom Accelerometer Depth	-0.62 m		-0.81 m	

The sensors were placed in the snowpack by digging a small pit and inserting the accelerometer cards into the pit face. The pit wall was oriented away from the blast so the sensors could be oriented toward the blast. Each set of accelerometers were placed in separate pits that were offset. Placement in this manner ensured the accelerometers had undisturbed snow between them and the blast center. Care was taken during placement of the accelerometers to allow free movement of the accelerometers and not have the movement restricted by the wires. The pit was completely backfilled following sensor placement.

Instrumentation

Instrumentation for recording the dynamic snow response within close proximity to the explosive detonation included both air over pressure and embedded acceleration sensors. Air blast pressures were measured using high pressure acoustic sensors. The overpressure is of interest because it is a direct measure of shock strength due to an explosive detonation. Snow dynamic responses were measured utilizing a combination of paired single-axis and dual-axis capacitive accelerometers. In pairing single axis accelerometers, care was taken to ensure orthogonality of the two axes. Dual axis accelerometers allowed for capturing the vertical and radial components, referenced to the explosive center, of acceleration for a single location. Acceleration of the snowpack is of interest because it is related to the stress experienced by the snowpack as a result of explosive use in avalanche mitigation work. The signals from the sensors were routed through a signal routing box then to a data acquisition system that was connected to a laptop computer.

Air Overpressure Sensor

Custom made Larcor acoustic instruments were used to measure the explosive shockwave over pressure in the air. These custom sensors were designed and built for this project by Larcor. Operation required a 6-15 VDC excitation voltage, and the output was an analog voltage signal ranging from ±2.5 VDC equating to ±34.4 kPa (± 5 psi). The usable microphone frequency range was between 2 and 1000 Hz. Figure 5 shows the sensors in the field.

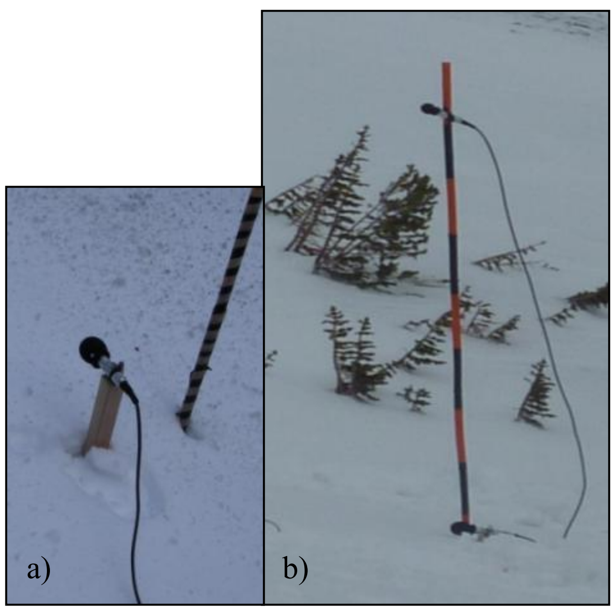

Figure 5 Air over pressure sensors in the field. a) Single sensor for the 2010-2011 season. b) Surface and elevated sensors for the 2011-2012 season.

Accelerometers

Two accelerometer types were utilized to meet expected dynamic responses at different ranges from the blast. When choosing accelerometers the mass and size of the sensors was taken into account. For coupling purposes, it was desired to have the density of the accelerometers be similar to the snow densities expected. The first testing season, 2010-2011, pairs of Analog Devices ADXL193 single-axis accelerometers were utilized; data sheets are located in Appendix B. These accelerometers had a dynamic range of +/-250g. Three sets of these accelerometers were mounted orthogonally on circuit board substrate. The approximate density of these accelerometers and circuit board was 1090 kg/m^3. Analog Devices ADXL321 (see Appendix B for data sheets) dual axis-accelerometers, also mounted on circuit board substrate, were the second accelerometer type used. The range of the ADXL 321 accelerometers was +/-18g and they are dual axis accelerometers. The approximate density calculated for the ADXL 321 accelerometer and circuit board was 1050 kg/m^3. Both accelerometers are shown in Figure 6.

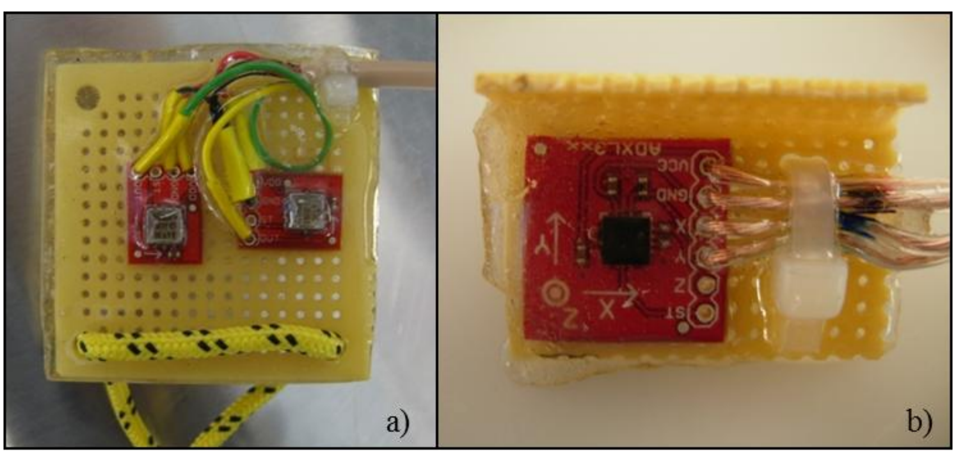

Figure 6 Accelerometers utilized for the 2010-2011 testing season. a) ADXL 193 accelerometers orthogonally paired to be dual axis and b) a dual axis ADXL 321 accelerometer.

For the 2011-2012 testing season, the ADXL 193 accelerometers were replaced due to resizing the accelerometers for a better dynamic range fit based on the previous year's results. This was done for increased precision by utilizing a larger portion of the sensor range. Analog Devices ADXL 278, Appendix B contains data sheets, accelerometers were used instead. These accelerometers had a range of +/-35g in the radial direction and +/-70g in the vertical direction. The larger range was orientated vertically because the largest component of acceleration was in the vertical direction for the locations investigated.

The second set of accelerometers remained the same, Analog Devices ADXL 321 +/-18g. Both types of accelerometers density, including substrate was approximately 850 kg/m^3. The accelerometers used in the 2011-2012 season are shown in Figure 7.

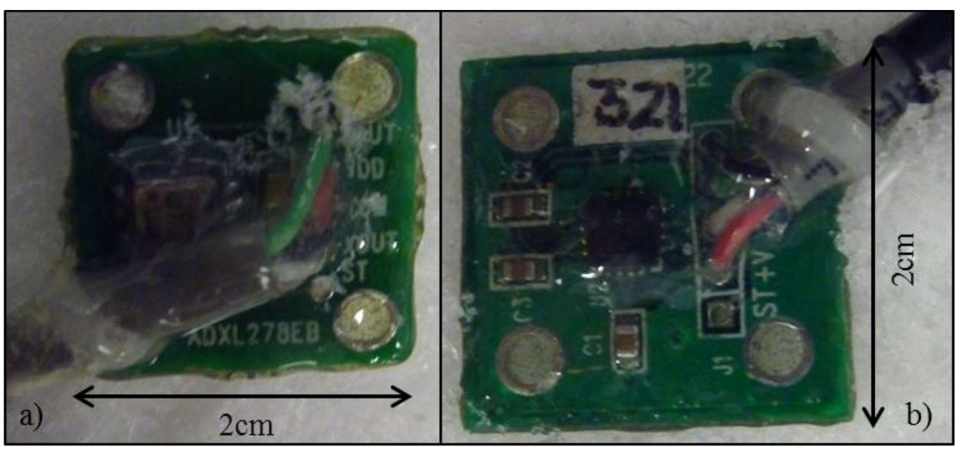

Figure 7 Accelerometers utilized for the 2011-2012 testing season. a) dual axis ADXL 278 accelerometer and b) a dual axis ADXL 321 accelerometer.

Regardless of the accelerometer type, the accelerometers were connected to 5 V power supply, a ground, and signal wires. The wires were attached to the accelerometer boards to strain relieve the wire connections. Following wiring the accelerometers were painted with epoxy for waterproofing purposes. The wires, strain relief, and epoxy coatings can be seen in both Figure 6 and Figure 7.

Data Acquisition System

The data acquisition system (DAQ) had to be field portable, battery operated, support a very high sampling rate and operate at cold temperatures. For each season, these requirements were fulfilled by using a National Instruments DAQ paired with a laptop computer to record transducer signals. For the 2010-2011 testing season, a National Instruments NI-USB-9221 module was utilized. This allowed sampling of 13 sensor channels, 12 accelerometer and 1 overpressure, at frequencies up to 15,000 hertz. Sampling at 15,000 hertz was the maximum the DAQ could perform on all channels. Originally sampling was done at 5,000 hertz, but was increased to the maximum possible of 15,000 hertz to verify capture of the short time duration transient event. Sensor signals were routed through a signal routing box then each channel transmitted to the DAQ that was located with the computer. The DAQ and computer were connected by a USB cable and are shown in Figure 8. The USB communication protocol required the DAQ to be located with the laptop computer and battery as shown by the functionality diagram in Figure 9. Sensor signals were routed through a signal routing box prior to being transmitted to the DAQ. The signal routing box was buried in the snow near the detonation for added protection from the shockwave.

Figure 8 Data acquisition setup for testing season 2010-2011 soft slab snow investigation.

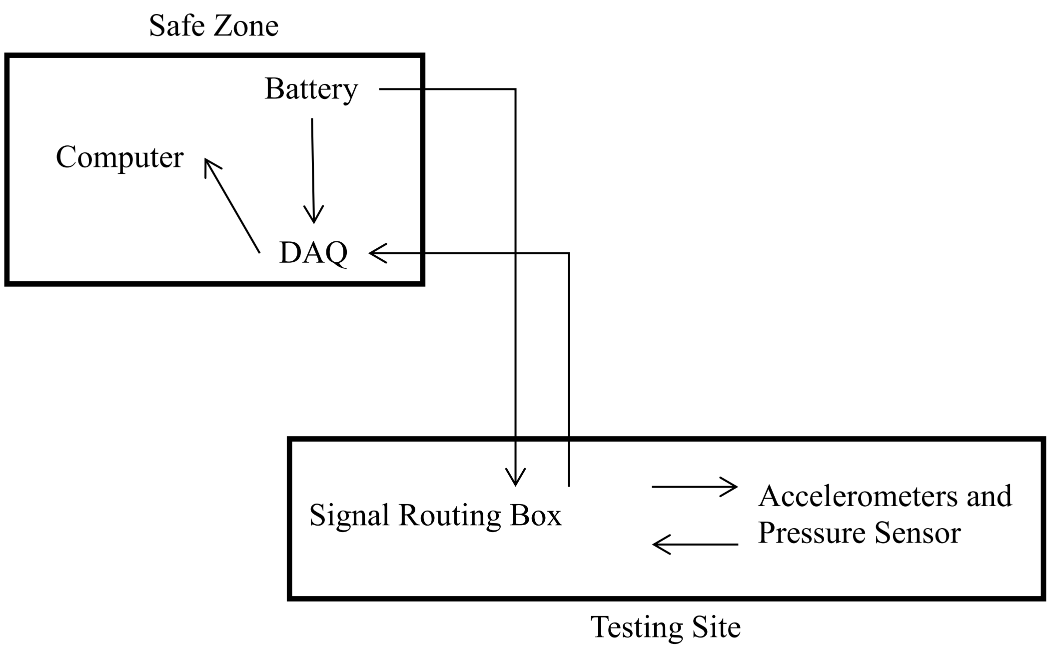

Figure 9 Functionality diagram showing the test setup for the 2010-2011 testing season and the communication between individual components.

During the 2011-2012 testing, the data acquisition system was upgraded to a National Instruments NI cDAQ-9188 chassis. Changing the DAQ and number of sensors utilized, due to lessons learned from the first season of testing, resulted in a complete rebuild of the system. It was desired to minimize cabling and set up time along with use new sensors. The chassis was coupled with three NI 9205 analog input modules. Data sheets for the chassis and modules are in Appendix C. These modules allowed for sampling at 250 KHz split over the number of channels being utilized on each module. This module allowed sampling on a total of 14 channels with the ability to expand the number of channels if necessary. The resulting sampling rate for the experiments was 25,000 Hz on all channels. This DAQ transmitted signals via Ethernet cable rather than USB and could be located farther from the computer. The DAQ is shown in Figure 10. This DAQ configuration allowed for easier movement of the system due to being more portable and integrated than the 2010-2011 design. In the newer design, the battery for power supply, signal routing box and DAQ were encased in a durable waterproof case and buried in the snow near the blast. Figure 10 shows the contents of the waterproof case. The functional layout for the new DAQ is shown in Figure 11.

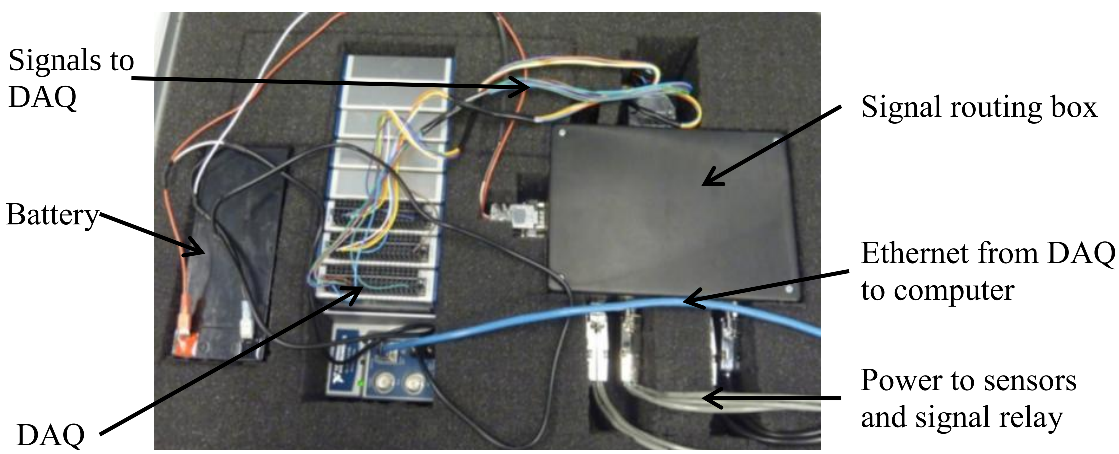

Figure 10 Testing season 2011-2012 data acquisition setup contained in Nanuk case buried below the snow surface.

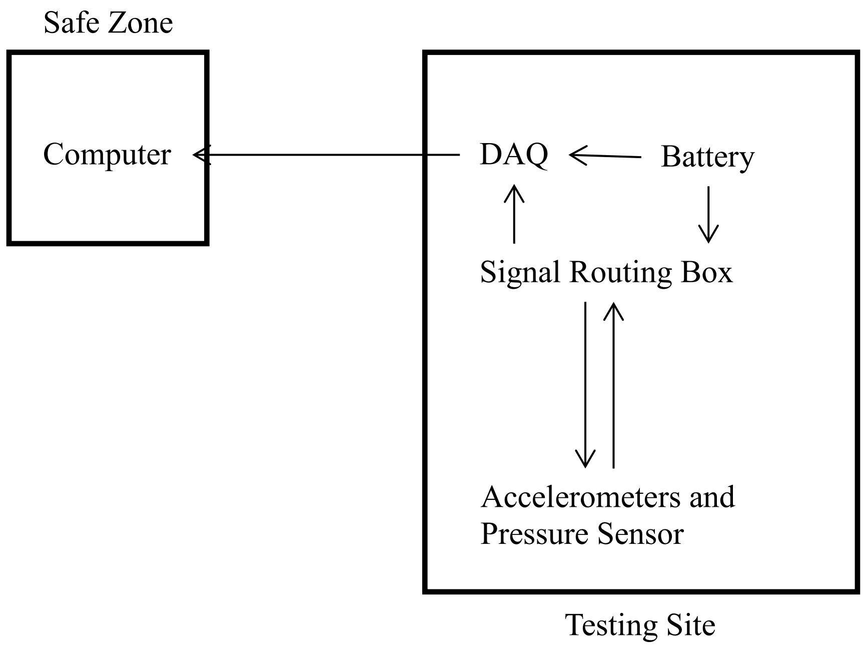

Figure 11 Functionality diagram showing the test setup for the 2011-2012 testing season and the communication between individual components.

Data sampling rates of the sensors were chosen based upon Nyquist theorem sampling considerations. The theorem indicated the sampling rates were more than adequate to capture the transient and relatively high-frequency acceleration signal components, and sufficient to monitor acoustic signals well beyond the range of the microphones.

The signal routing box was necessary to regulate and distribute excitation power to the sensors as well as route analog signals from the sensors to the DAQ. Power was routed through a fuse to protect against damage to the system resulting from a power surge or an accidental short. The power supply to the box was split within the box and through a voltage regulator. This allowed for 5 V to be supplied to the accelerometers and 12 V to the over pressure sensors. This was due to the power requirements for the specific sensors. The accelerometers were connected with 15 pin D-Sub connectors and the pressure sensors were connected with 9 pin connectors. One set of both sensors was connected with a female end and the other was with a male end resulting in a single connection configuration ensuring all instruments were properly connected thereby eliminating the possibility of cross connecting sensors. Wiring diagrams for the signal routing box used in the 2011-2012 testing season are included in Appendix D and a functional wiring diagram is in Figure 12.

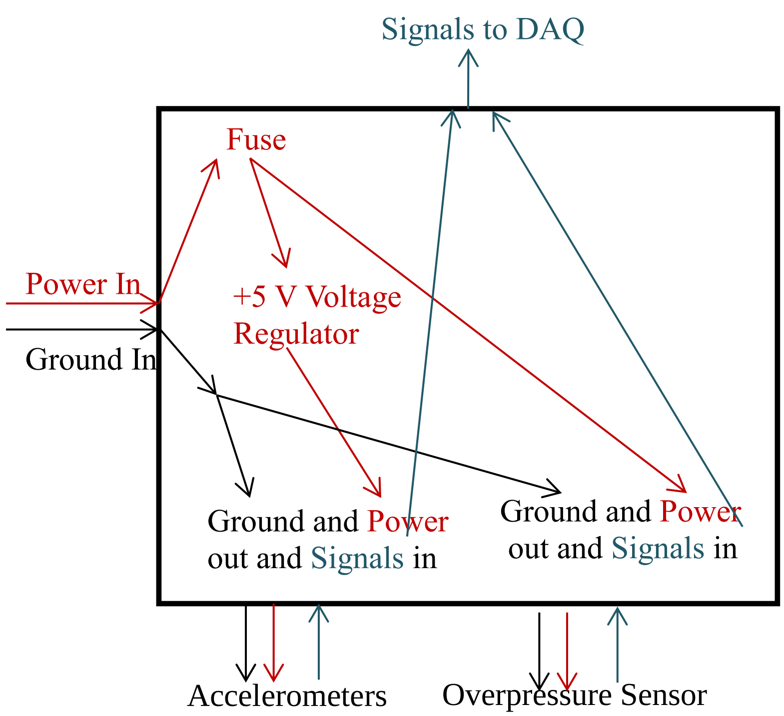

Figure 12 Functional wiring diagram of the signal routing box constructed for the 2011-2012 testing season.

During both seasons, the laptop was running National Instruments Labview v8.6 code using technical data management streaming, a capture format allowing the high sample rates. An example screen shot of a test in Labview is shown in Figure 13. The program was written to show the recorded signals as the event occurred.

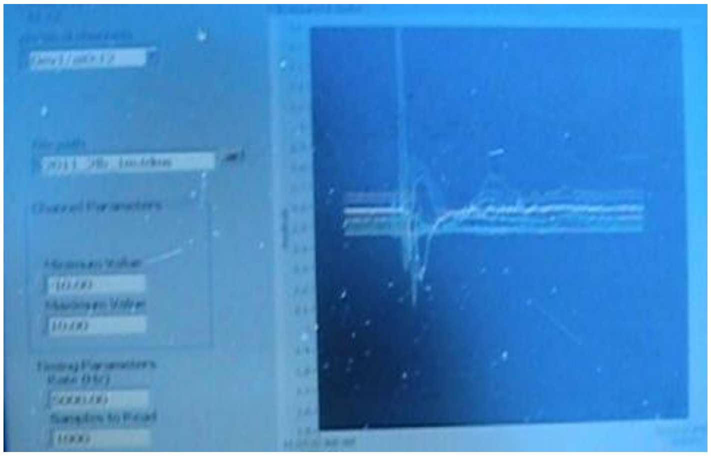

Figure 13 Screenshot of the Labview program following a test detonation from the 2010-2011 testing season. The explosive event is shown as registering on all channels. The entire time duration shown is approximately 0.15 seconds with the actual event occurring in approximately 0.07 seconds.

Sensor Errors

The gathering of field data will inherently have errors associated due to the method of gathering data. Errors associated with the accelerometers were determined for both nonlinearity and the alignment error of the sensors used as presented in Table 2. The error calculations were based on the maximum range of the accelerometers and the typical error values from the data sheets. Therefore, the errors in Table 2 represent the maximum expected. The largest error associated with the accelerometers was due to the nonlinearity, but in comparison to the values of acceleration obtained the errors would not appreciably impact the results.

The data acquisition system (DAQ) accuracy was also determined; see Table 3. Calculations were based on the typical voltage output from the individual accelerometers to the DAQ, resulting in the typical maximum error. The voltage accuracy increased as the accelerometer range increased, but in comparison to the data voltage values were acceptable.

Table 2 Errors associated with the accelerometers used for collection of field data. The alignment error from the manufacture was not available for the single axis 250g accelerometers.

Sensor Range	Alignment Error	Nonlinearity Error
	m/sec^2	m/sec^2
18 g	0.308	0.350
35 g	0.599	0.687
70 g	1.199	1.373
250 g		4.905

Table 3 Accuracy of the DAQ modules per accelerometer type.

Sensor Range	DAQ Accuracy
	Volts
18 g	0.00169
35 g	0.00177
70 g	0.00181
250 g	0.00187

The air overpressure sensors were calibrated by the manufacture and certified to be within 5% of the input value. Calibration was performed with an acoustic calibrator. Response at selected frequencies is shown in Table 4.

Table 4 Percent response of overpressure sensor resulting from calibration.

Calibrated Overpressure for Selected Frequencies				
100 Hz	30 Hz	10 Hz	3 Hz	2 Hz
100%	100%	100%	97%	96%

Explosives and Detonation Practices

Orica Mining pentolite cast boosters were the explosives investigated, technical data sheets are in Appendix F. These explosives are used primarily to boost larger charges in mining applications. They are also very common in avalanche mitigation work in Montana. For the 2010-2011 soft slab snow investigation, Pentex AP Cast Boosters in two masses were used, 0.45 kg and 0.9 kg. These are single cap and fuse explosives. Detonation was achieved using a cap and fuse combination resulting in approximately a 90 second delay between initiation and detonation. *Av*trol Avalanche DUO Cast Boosters were used in hard slab snow investigations during the 2011-2012 testing season. A single mass of 0.9 kg was used. These explosives require double caps and were detonated using shock tubing. Use of shock tubing resulted in a momentary delay between initiation and detonation of the explosive. The shorter delay using shock tubing significantly reduced the extraneous data collected.

Bridger Bowl ski patrol used a single cap and fuse detonation system resulting in using Pentex AP Cast Boosters. Big Sky Resort used *Av*trol Avalanche DUO Cast Boosters because their detonation protocol was to double cap and fuse the charges. Even though the names are different, the chemical components are the same, but with different cap configurations. Both explosives used had a detonation velocity of 7,924 m/s and detonation pressure of 250 kb. The explosives were detonated from the surface up to 2 m elevated in increments of 0.5 m. All elevated shots were placed on bamboo poles, an industry standard.

DATA PROCESSING

After data collection was completed and prior to examination for trends, the accelerometer and air pressure data was processed. The accelerometer and air pressure data was converted to allow for comparisons of engineering terms such as acceleration, velocity, position, and pressure. The data processing also included distance scaling to permit comparison of different charge masses. Wave attenuation in the vertical and radial direction was computed. The field data was used to create surface plots of acceleration with range and depth. These processing methods are described in the following sections.

Overpressure Data

The Larcor pressure sensor data was recorded in voltage. The voltage was converted to units of pressure (psi) using a manufacturer calibration constant by:

$$P = V * 2 \tag{2}$$

Where P is pressure (psi), V is measured voltage (V), and 2 is a conversion constant provided by Larcor (psi/V). Example data from the pressure sensors is shown in Figure 14. Surface and elevated sensor placements are shown together in the figure. Both sensor elevations show an initial rapid positive pressure increase followed by a negative pressure pulse. The negative portion of these figures is due to the outrush of gasses leaving the center of the explosive and is only seen for spherical detonations (Kinney and Graham, 1985). Positive and negative pressure impulses were calculated by integrating the pressure curves in time using the trapezoid method, Equation 4. Determination of the impulse was done to determine the relationship between pressure and impulse.

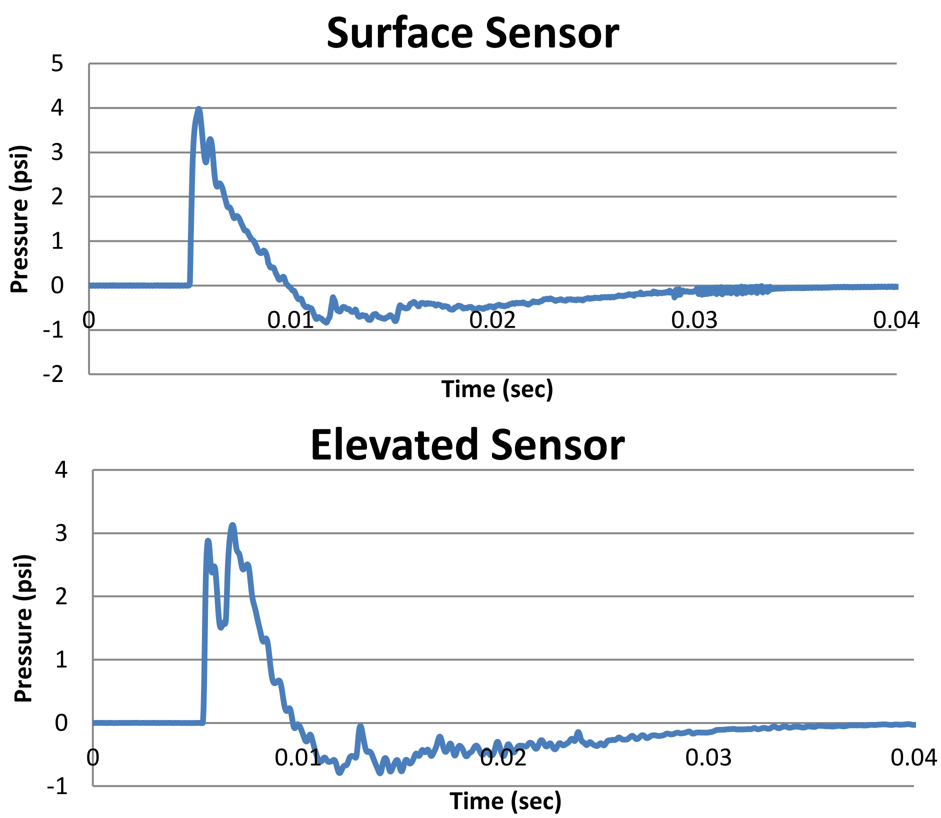

Figure 14 Example pressure sensor data for both surface and 1.5 m elevated heights. The sensors were located a radial distance of 7 m from the explosive detonation. In these examples the positive pressure phase was approximately 0.005 sec, illustrating the short duration of the overpressure wave.

Accelerometer Data

Data obtained via the accelerometers were recorded in voltage by the National Instruments LabView code. The voltages were converted to units of acceleration (m/s^2) with the following conversion:

$$(3) \qquad A = V * \frac{1}{x} * 1000 * 9.81$$

Where *A* is acceleration (m/sec^2), *V* is recorded sensor voltage (V), *x* is a conversion for the specific accelerometer used (g/mV), 1000 (mV/V) and 9.81 (m/sec^2) are unit conversions. Table 5 shows the conversion values, *x*, for the accelerometers used. These values were taken from Analog Device Data Sheets included in Appendix B.

Table 5 Conversion factor used specific to each accelerometers used for converting voltage to acceleration.

	Vertical Direction	Radial Direction
	mV/g	mV/g
ADXL 321	100	100
ADXL 193	8	8
ADXL 278	55	27

Voltage was converted to acceleration for the vertical and radial vector components of acceleration as recorded by the sensors. The accelerometers inherently have some noise and record gravity; by time averaging the acceleration values recorded prior to shockwave arrival and subtracting the value from all subsequent readings to show zero acceleration prior to the event. This also removed the influence of slope angle on the acceleration recorded. Example acceleration data in the vertical direction at 5 m radial distance are shown in Figure 15. The accelerometers were oriented with positive acceleration upward in the snowpack, therefore, the initial acceleration was negative as the pressure pulse moved across the surface. The positive radial direction was orientated away from the blast center resulting in the initial acceleration to be positive. Figure 15 illustrates the initial transient response followed by a damped oscillatory response.

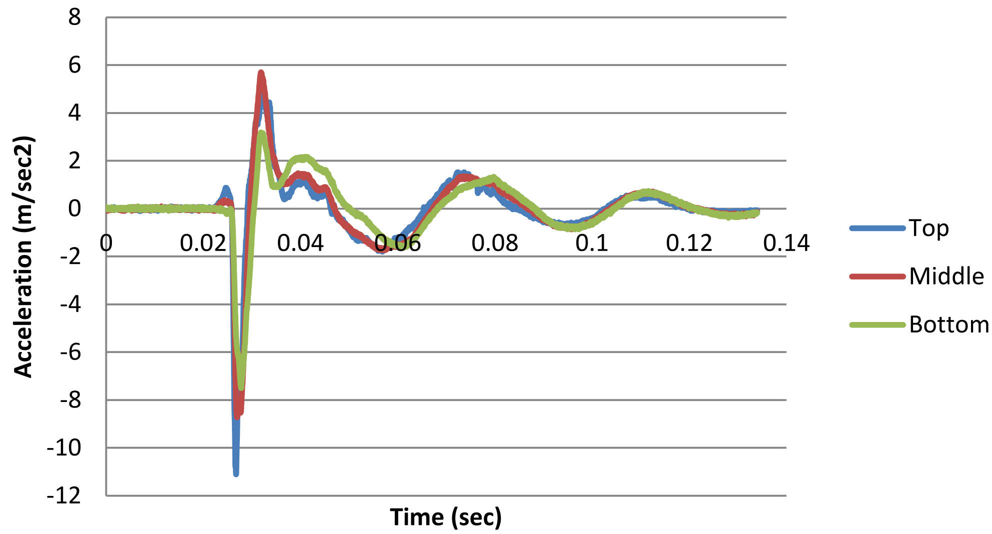

Figure 15 Vertical sensor voltage data converted to acceleration for a test sequence at a radial distance of 5 m. The three sensor depths at this radial distance are shown. The transit time between sensors at different depths is evident by comparing the peak acceleration times. A post-test oscillatory response is evident and frequently observed.

The composite trapezoid method, equation 4, was utilized to numerically integrate the acceleration curves to yield velocity. The same method was then used to integrate velocity to yield position:

$$(4) \qquad I = \sum\left[(t_{i+1} - t_i) * \left(\frac{v_i + v_{i+1}}{2}\right)\right]$$

Where *I* is the numerically evaluated integral, velocity or position, *t* is the time, and *v* is the value of acceleration for velocity calculation or velocity for position calculation (Chapra, 2005). An example of the velocity components at 5 m radial distance, from Figure 15 acceleration, is shown in Figure 16. The initial velocity is negative due to being in the downward direction, the same as the acceleration component in Figure 15. The initial transient velocity has been smoothed when compared to the acceleration figure, a consequence of numerical integration. Position was then found by integrating the velocity values. Figure 17 shows the position of the same test at 5 m radial distance. Similar to the velocity component, the position figure shows further smoothing of the snowpack response. Both the velocity and position do not return to zero due to remaining accelerometer noise or possible sensor movement during testing (orientation relative to gravity).

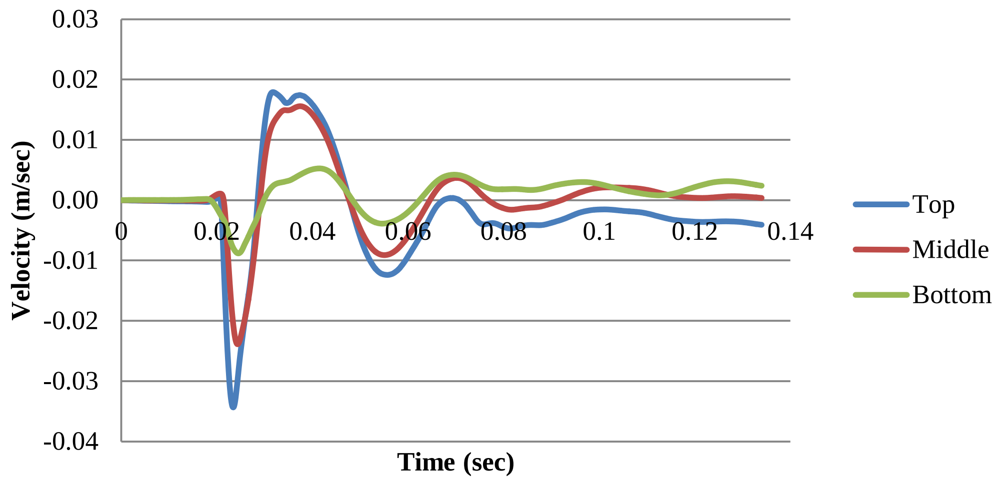

Figure 16 Vertical velocity as integrated from acceleration data shown in Figure 15. The three different depths of accelerometers are shown at 5 m radial distance from the charge.

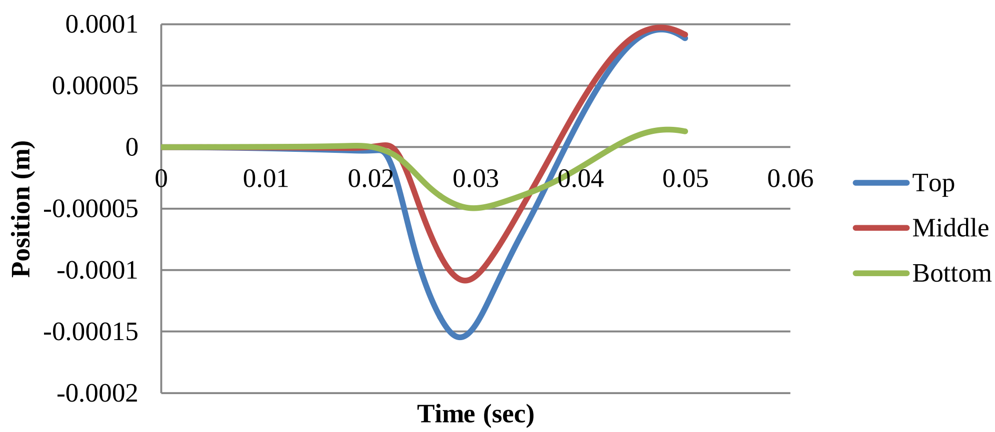

Figure 17 Vertical position components at three different depths, as integrated from the velocity components shown in Figure 16.

Resultant vector magnitudes, based on the vertical and radial components, were computed from the vector components (Beer and Johnston, 1996); this was done for acceleration, velocity, and position, by:

$$M = \sqrt{V_C{}^2 + R_C{}^2} \qquad (5)$$

Where M is acceleration magnitude (m/sec^2), V_c is the vertical component of acceleration (m/sec^2), and R_c the radial acceleration component (m/sec^2). An example of acceleration resultants as recorded by sensors is shown in Figure 18. This example is for a soft slab top layer at radial distances of 2 m and 5 m, and the resultant magnitudes are positive.

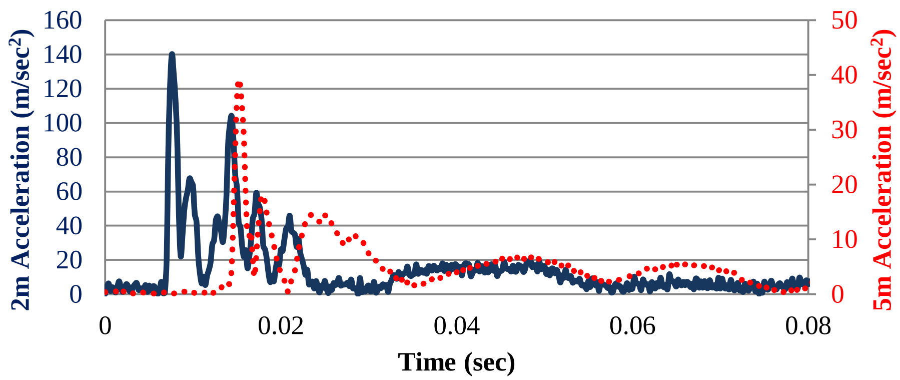

Figure 18 Acceleration resultant magnitudes recorded by top layer accelerometers in a soft snow slab. The blue data series is for the accelerometer located 2 m radial distance and the red series is located 5 m radially, note the different scales.

Distance Scaling

Different explosive masses have different explosive energies associated with them resulting in different shockwave characteristics. Since the test plan called for different sized explosives detonated at differing heights and distances, a method to make comparisons across tests was required. Distances were converted to 1 kg TNT equivalents for comparison purposes. This technique is commonly used for comparisons by converting a specific blast into the equivalent distance, with the same response, for a 1 kg TNT charge. Since pentolite and TNT have different explosive energy per unit mass, pentolite cast booster masses were converted to TNT equivalent masses by:

$$(6) \qquad m_T = m_P * 1.35$$

With m_T being the TNT equivalent mass (kg), m_P the pentolite mass (kg), and 1.35 the conversion factor of pentolite to TNT (kg/kg), as provided by Orica Explosives. Distances were then scaled from the TNT masses, using scaling law theory. The scaled distance relationship employed was (Kinney and Graham, 1985):

$$(7) \qquad L_S = \frac{L_A}{m_T^{\frac{1}{3}}}$$

Where L_S is the scaled distance (m/kg$^{1/3}$), L_A is the actual measured distance (m), and m_T is the TNT mass (kg). This scaling was applied to the distance from the charge center, and the depth of sensors below the snow surface. This technique allowed for direct comparison of different charges and distances through TNT equivalents. Distance scaling yields the distance where a specific effect would be equivalent to a 1 kg TNT charge. For the 2011-2012 testing season, the scaled distances were within 6% of the actual distances because the pentolite charge size used converted to TNT mass was very near 1 kg. Scaled distances during the 2010-2011 winter season showed more variability than the 2011-2012 season due to using two charge masses.

Acceleration Attenuation

Shockwave attenuation is due to a combination of geometric expansion of the shock wave, snow deformation and interactions within the ice pore network (Mellor, 1973). Peak acceleration magnitude as a function of scaled radial distance and scaled depth was determined. Acceleration was plotted as a function of scaled distance and fit with a power regression equation of the form:

$$(8) \qquad A_P = c * L_S * d$$

Where A_p is the peak acceleration magnitude (m/sec^2), L_S is the scaled distance (m/kg$^{1/3}$), c (kg$^{1/3}$/sec^2) is a coefficient and d is the power exponent. Equation 8 has been fit to acceleration with the units presented. Both c and d were found by curve fitting data plots as described in the following descriptions. The exponent d describes the attenuation of the shockwave. Since the shockwave is diminishing with distance due to wave expansion and snow attenuation, the exponent d is negative. The larger the magnitude of d, the faster the shockwave is decaying. Power law fitting of data was shown to be applicable to shockwave attenuation in snow and was applied in other research projects e.g. (Gubler, 1977; Johnson, 1994; Solie, 1993).

Example power law curve fits, showing attenuation d, leading coefficients c and R^2 fit values resulting from all acceleration responses for a particular elevated charge height and snow layer, are shown in Figure 19 and Figure 20. Responses from the top snow layer taken during the 2010-2011 testing season are shown in Figure 19. Responses from the middle snow layer, taken during the 2011-2012 winter season, are shown in

Figure 20. Distance scaling allowed for the two different charge sizes in the 2010-2011 winter season to be graphed together in Figure 19.

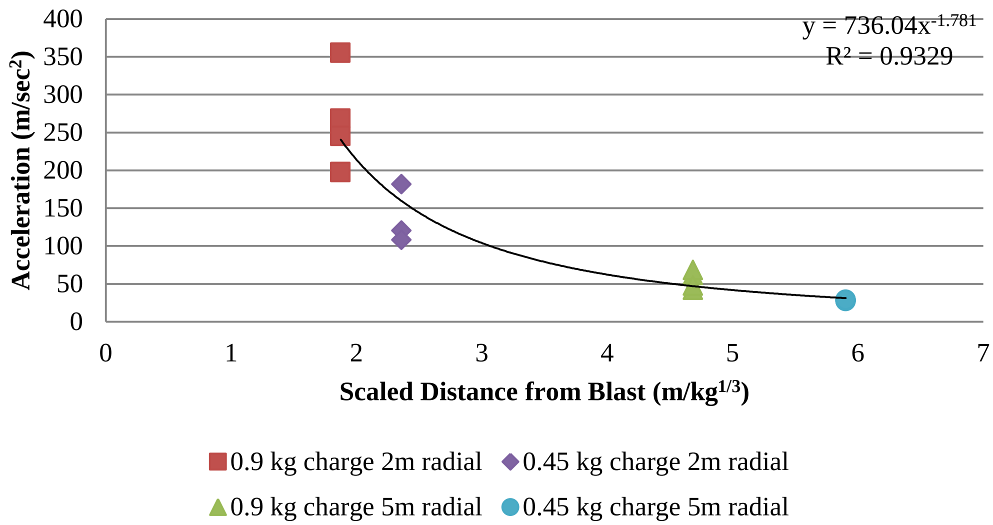

Figure 19 Example acceleration magnitudes recorded by the top accelerometers for multiple charges suspended 1 m above the surface fit with a power law regression for determining radial attenuation for soft slab snow in the 2010-2011 testing season. In this particular case, c=736.04, d=-1.781 and R^2=0.9329.

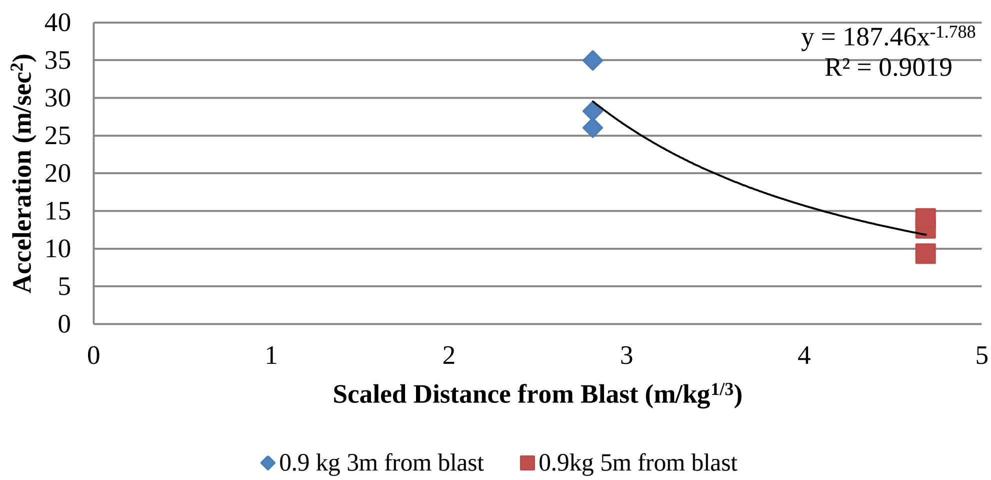

Figure 20 Example acceleration magnitudes recorded by the middle accelerometers for multiple charges placed on the snow surface fit with a power law regression for determining radial attenuation for hard slab snow in the 2011-2012 testing season. In this particular case, c=187.46, d=-1.788 and R^2=0.9019.

Shockwave attenuation in the vertical direction was found by plotting the acceleration resultant magnitude through the snow depth at the individual radial distances for a specific elevated charge height. Examples from the 2010-2011 and 2011-2012 seasons are in Figure 21 and Figure 22. The sensors were not always placed at the same depth and the actual location is reflected by the data points not all being stacked at the same scaled depth below the snow surface.

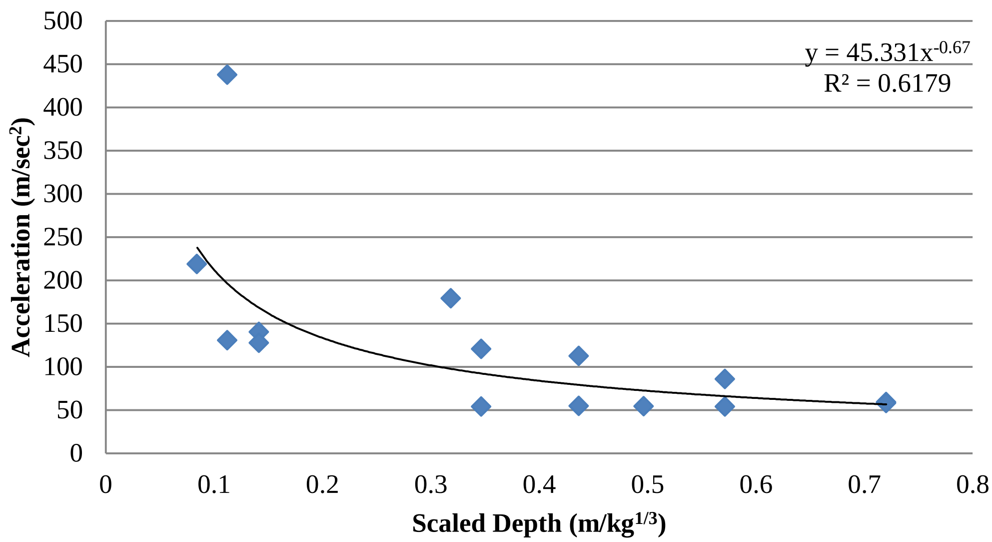

Figure 21 Example acceleration magnitudes recorded through the snow depth at 2 m radial distance from the blast for multiple charges elevated 2 m above the snow surface fit with a power law regression for determining vertical attenuation for soft slab snow in the 2010-2011 testing season. Both 0.45 kg and 0.9 kg charge masses are included in the data set. In this particular case, c=45.331, d=-0.67 and R^2=0.6179.

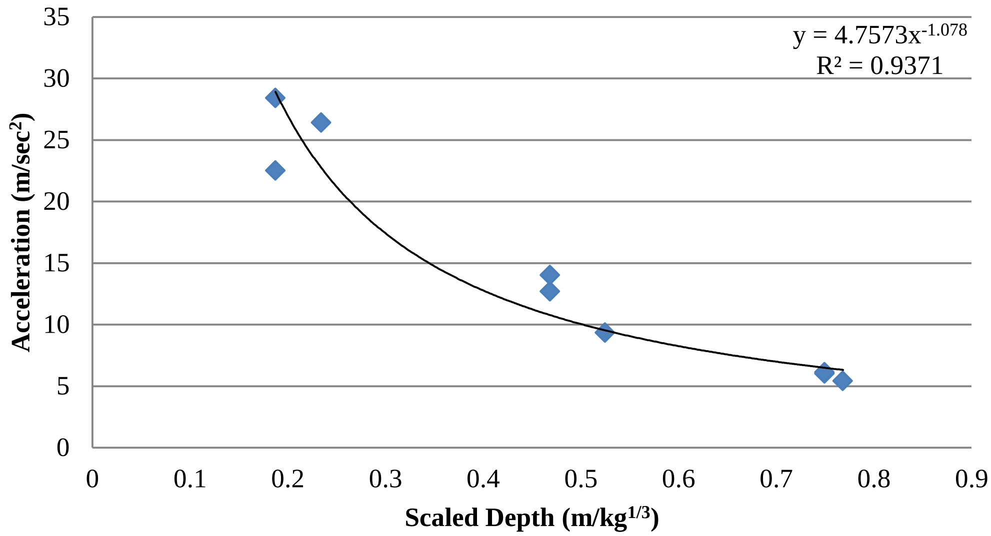

Figure 22 Example acceleration magnitudes recorded through the snow depth at 5 m radial distance from the blast for multiple charges placed on the surface fit with a power law regression for determining vertical attenuation for hard slab snow in the 2011-2012 testing season. Only 0.9 kg charge masses are included in the data set. In this particular case, c=4.7573, d=-1.078 and R^2=0.9371.

<u>Contour and Surface Plot Creation</u>

The acceleration data was used to create contour and surface plots showing acceleration as a function of scaled depth and range simultaneously. Originally, power law regression equations were explored as a means to extrapolate data to cover the same depth and range for each season of testing. This would have allowed for easier comparisons between the hard and soft slab snow conditions. Unfortunately, extrapolation beyond the test ranges resulted in erroneous edge effects. As a result, the contour and surface plots were created directly from field data instead of using the power law equations. The plots allow for comparison of the acceleration in both the vertical and radial direction at the same time. MathCAD software was used to create both contour and surface plots. Each plot resulted from six data points, one for each accelerometer placed in the snowpack. Distances were scaled prior to plotting to allow data from different charge masses to be included in the plots. Contour and surface plots showing the data points used for creation are in Figure 23.

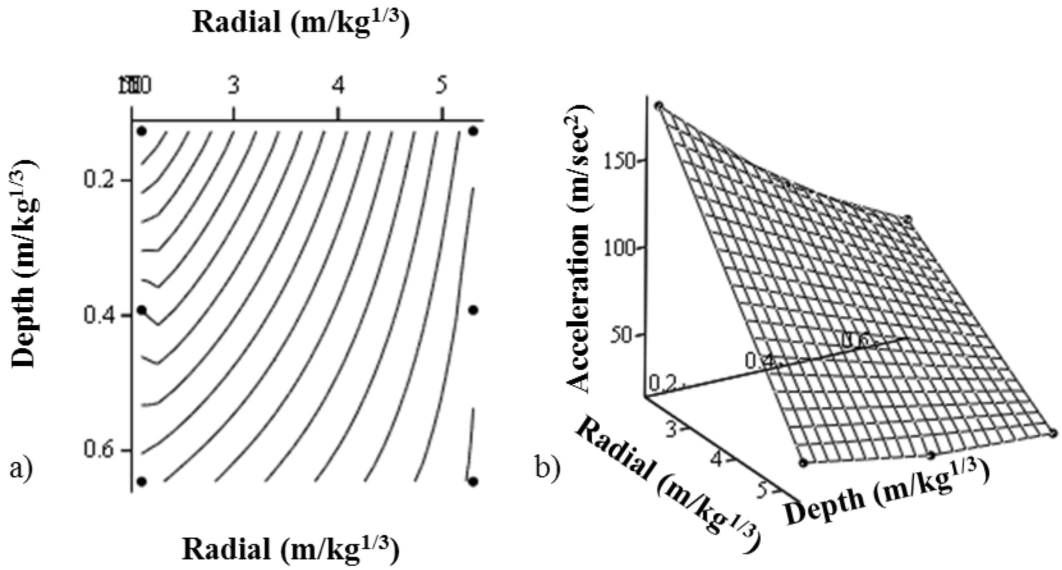

Figure 23 Example contour and surface plots created in MathCAD. a) Contour plot b) Surface plot.

Following data processing of the gathered field data, it was possible to analyze the data to determine trends in snowpack response to explosive detonations. The data examinations are presented and discussed in the following chapter.

RESULTS AND DISCUSSION

Once processed, the data was examined to characterize the overpressure and dynamic snowpack response to pentolite cast boosters. This chapter will report and discuss the testing and the resulting data. Data from the overpressure sensor include the pressure and the impulse of the overpressure wave. These values are investigated to determine correlations between the explosive location and the response. The average acceleration resultant values obtained by the accelerometers were also examined for correlations with the explosives used and the snow characteristics. Acceleration was used as an indicator of the snowpack response because the greater the acceleration the greater the stress and strain experienced. The overpressure values are presented first and followed by the accelerometer data. Each section details the analysis, and discusses the findings particularly those of pertinent interest.

Test Matrix

Each winter season had a different number of total tests conducted. A different number of shots at a particular elevated height and charge sizes also occurred for the two winter seasons.

shows the tests conducted during the 2010-2011 testing season on soft slab snow and includes 0.45 kg and 0.9 kg charge masses. The number of tests conducted in dry and moist snow conditions also are denoted. Hard slab snow test configurations conducting in 2011-2012 are contained in Table 7.

Table 6 Test matrix for the 2010-2011 testing season at Bridger Bowl Ski Area investigating soft slab snow conditions

	0.45 kg Charge		0.9 kg Charge	
Charge Height	Dry Snow	Moist Snow	Dry Snow	Moist Snow
0 m	1		1	
0.5 m	1	1	1	1
1 m	2	1	3	1
1.5 m	1	1	1	1
2 m	1	1	3	1

Table 7 Test matrix for hard slab snow investigations conducted at Big Sky Resort in 2011-2012.

Charge Height	Blast response tests	Repeatability tests
0 m	3	
0.5 m	3	
1 m	3	5
1.5 m	3	
2 m	2	

Overpressure Sensor

Data recorded by the overpressure sensors, along with positive and negative impulse, is presented in Appendix F. In this section, average maximum overpressure and impulse values also are presented for the different charge heights investigated. Impulse rather than duration was examined because even though duration and impulse are linked, in short duration explosive events the impulse generally impacts the damage possible more than the shockwave duration does (Kinney and Graham, 1985). Figure 14 illustrates the rapid increase in pressure as the shockwave reaches the sensor followed by a more gradual decrease in pressure. The positive pressure region is followed by a negative pressure pulse. These wave characteristics were present in all of the data and are indicative of a pressure wave.

Data from the microphone sensors was examined for links between the charge elevation to peak overpressure and the positive and negative impulse based on snow hardness. Peak overpressure and impulse values at the snow surface were compared to values recorded 1.5 m above the snow surface at the same radial distance. Findings from these investigations are presented in the following sections.

Soft Slab Snow Investigations

During the soft slab snow testing, one overpressure sensor was used and was located at the snow surface. Average data for these snow classifications and charge sizes are shown in the following tables. Table 8 is for 0.9 kg charge masses, Table 9 is for 0.45 kg charge sizes.

Table 8 values show that raising the charge was shown to result in increased overpressure at all charge heights when compared to a surface charge. Increased overpressure values at the snow surface directly correlates to a greater input to the snow. In the case of dry snow this increase was at least 1 psi, which was a 50% increase. The moist snow resulted in less of an increase, but still an increase. The overpressure values also indicate the moist snow peak overpressure were greater than the dry snow for all charge heights other than 1 m. The moist snow may create a surface that reflects the shockwave more than the dry snow does. For the 1.5 m and 2 m elevated charge heights in moist, snow the pressure reached the maximum value recordable by the sensor.

Table 8 Average overpressure values, positive and negative impulse values resulting from the pressure shockwave as recorded at the snow surface at a distance of 5 m radially from 0.9 kg blasts. Dry snow conditions are on the left and moist snow are on the right.

	Dry Snow			Moist Snow		
Charge Height	Peak Over-pressure (psi)	Positive Impulse (psi*sec)	Negative Impulse (psi*sec)	Peak Over-pressure (psi)	Positive Impulse (psi*sec)	Negative Impulse (psi*sec)
0 m	3.10	0.00685	-0.00689			
0.5 m	4.08	0.00685	-0.00689	4.54	0.00500	-0.00562
1 m	5.03	0.00809	-0.00837	4.50	0.00925	-0.00932
1.5 m	4.21	0.00719	-0.00696	5.16	0.00958	-0.00938
2 m	4.63	0.00783	-0.00873	5.16	0.00946	-0.01018

The positive and negative pressure wave impulses are very similar for individual charge heights. At some charge heights, the positive impulse is slightly greater than the negative and in others the negative pressure impulse is greater than the positive impulse. This may have to do with the numeric integration calculation of impulse from the pressure wave curve. The breaking point between positive and negative was very clear, but the end of the negative impulse was less apparent as the pressure returned to atmospheric. The integration was stopped when the area in a trapezoid being evaluated was less than $(x)10^{-5}$for the negative pressure impulse. A comparison of positive and negative impulse values for both dry and moist snow conditions is in Figure 24. This figure shows there are similar trends for both snow types as well as between positive and negative impulses. The individual snow types have very similar magnitudes regardless of being positive or negative.

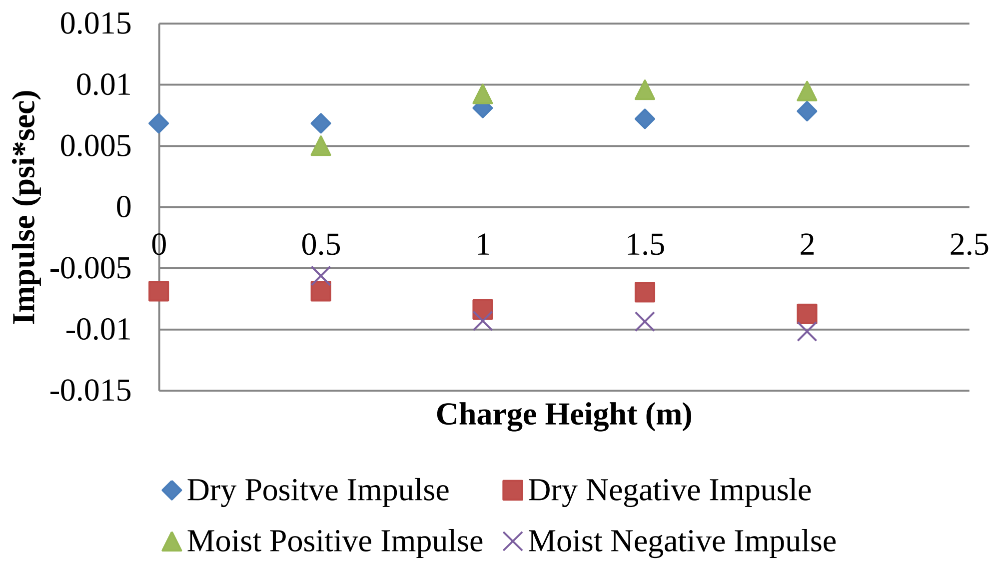

Figure 24 Comparison of positive and negative pressure impulses as a result of 0.9 kg detonations in soft slab snow. Both dry and moist snow conditions are represented. Note the moist snow does not have a surface charge detonation.

Overpressure and pressure impulse are compared in Figure 25 to determine the relationship between the parameters. Comparison of the two parameters was done because together the overpressure and impulse describe the blast wave from the explosive detonation. The left axis shows pressure values while the right axis is for impulse. Only the positive impulse is shown due its similarity of magnitude between positive and negative impulse. Both the overpressure and impulse data series show the same trend; increases due to raising the charge off the snow surface. Fitting Figure 25 with polynomial regression indicated a peak in overpressure and impulse occurs near a charge elevation of 1.5 m. Beyond this charge elevation the response begins to decrease due to the geometric expansion of the wave being greater than the increase due to raising the charge. If the explosive is elevated too high the shockwave will have diminished to a sonic wave by the time it reaches the snow surface (Miller et al., 2011).

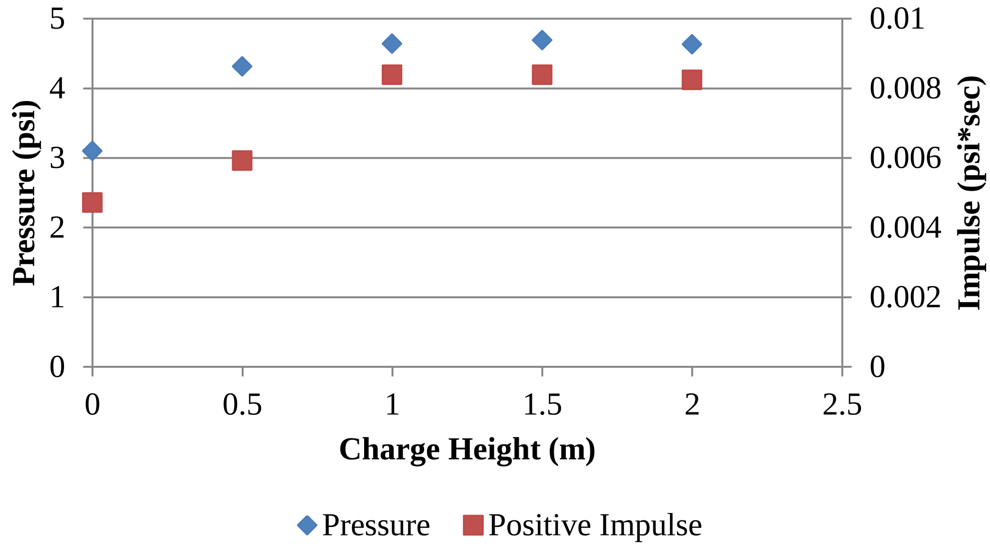

Figure 25 Comparison of pressure and impulse for individual charge heights investigated. Each data series is for 0.9 kg charge masses obtained in soft slab snow conditions and is a combination of dry and moist snow data.

Data for 0.45 kg charges was also examined in the same manner as the 0.9 kg charges. Table 9 shows average peak overpressures, positive and negative impulses recorded 5 m radially from the blast at the snow surface. Raising the charge resulted in increased overpressures for all charge heights investigated. The increase was at least 23% greater. The increase for the 0.45kg charges was less dramatic than for 0.9 kg charges. Similar to the 0.9 kg charges the increase was greater when the snow was dry than when it was moist. The moist snow resulted in greater values of overpressure than the dry snow for all elevated charge heights, other than the 2 m elevated charge height.

Table 9 Average data for soft slab 0.45 kg mass detonations pertaining to peak overpressure, positive and negative impulse experienced at the snow surface 5 m radially from the detonation site.

	Dry Snow			Moist Snow		
Charge Height	Peak Over-pressure (psi)	Positive Impulse (psi*sec)	Negative Impulse (psi*sec)	Peak Over-pressure (psi)	Positive Impulse (psi*sec)	Negative Impulse (psi*sec)
0 m	2.18	0.00318	-0.00394			
0.5 m	2.68	0.00400	-0.00395	2.74	0.00461	-0.00399
1 m	2.85	0.00509	-0.00527	3.62	0.00558	-0.00568
1.5 m	2.99	0.00495	-0.00517	4.32	0.00562	-0.00508
2 m	3.23	0.00586	-0.00594	3.20	0.00534	-0.00534

The positive and negative impulses are shown, for both dry and moist snow resulting from 0.45 kg charges, in Figure 26. Impulse for dry and moist snow are similar as indicated by Figure 26. Regardless of the snow classification, there is an increase in both the positive and negative impulse from an elevated shot. This is a similar trend as seen in the 0.9 kg charge data. At some charge heights the positive impulse was greater and others the negative impulse had a larger magnitude. The moist impulses for 0.9 kg charges showed a greater increase than the 0.45 kg charges did. The magnitude of the impulse was less for the 0.45 kg charges than the 0.9 kg charges. The lower value would be expected because there is less explosive material creating the shockwave.

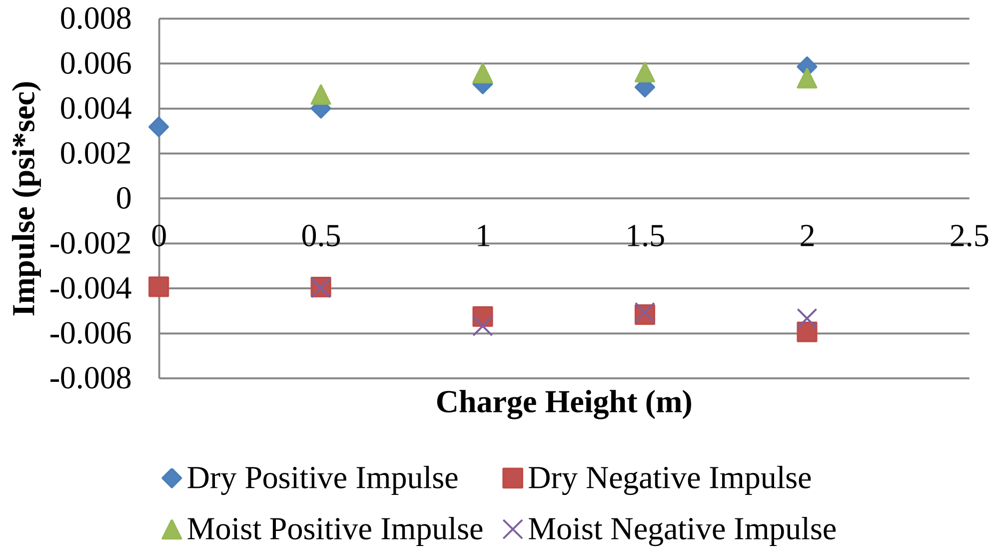

Figure 26 Positive and negative impulse comparison for both dry and moist soft slab snow conditions taken 5 m radially from 0.45 kg charges.

Positive impulse and peak overpressure for 0.45 kg pentolite cast booster detonations in dry and moist snow conditions were compared in Figure 27. Each data series has a unique scale, as shown on the two sides of the figure. Both the peak overpressure and positive impulse show an increase due to raising the charge off the snow surface. Since the impulse is a result of the pressure wave, it would follow that the two would have similar trends. For the 0.45 kg charges the maximum overpressure occurs for a charge height of approximately 1.5 m. This is shown by the decreased peak overpressure at 2 m radial distance. The positive impulse value does not decrease though. It seems it would since the overpressure did. Examination of the pressure-time history shows a longer positive duration in comparison to the other charge heights, resulting in a greater impulse.

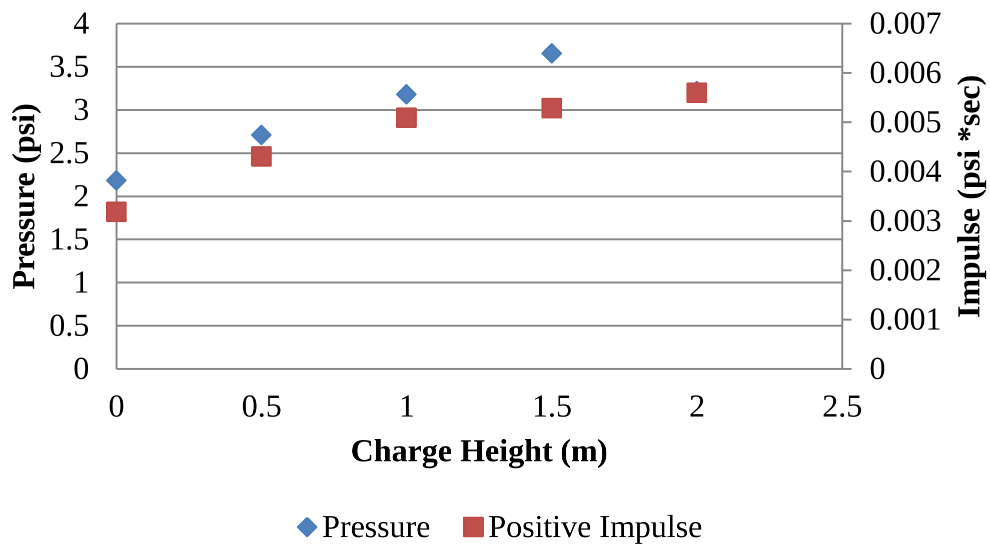

Figure 27 Peak overpressure and positive impulse for 0.45 kg detonations as recorded in soft slab snow. The data series are a combination of dry and moist snow conditions.

The 0.45 kg charges resulted in lower overpressures than the 0.9 kg charges; as expected because the amount of explosive energy is greater for a larger mass. Doubling the mass did not result in double the overpressure, the percent increase in overpressure varied from 40% to 75% increase with an average increase of 50%. The increase in overpressure values is not linearly related to the charge mass increase. The relationship between explosive mass and impulse also was not linear. Twice as much mass resulted in approximately a 60% increase in impulse value.

Johnson et al. (1994) indicated ~40% increase in overpressure when charges were detonated from the optimum height. Assuming the optimum height is 1-2 m, the increase in overpressure from the field data was found to be 49% for 0.9 kg charges and 39% for 0.45 kg charges. These values are very similar to findings by Johnson et al. (1994). Detonations above 2 m were not conducted in this research project due to the practicality of elevating charges above 2 m without a tram. Therefore, it is not possible to determine if the overpressure was insensitive to elevated charge heights greater than 2 m, as was done by Johnson et al. (1994).

Hard Slab Snow Investigations

Due to difficulty with adding a second overpressure sensor, most of the season resulted in a single pressure reading. Additional wire was added to the original sensor for placement farther from the signal conditioning box. The added wire resulted in signal communication errors and unusable data. The reading obtained was for a sensor elevated 1.5 m above the snow surface. Without having a surface pressure for comparison purposes the reading did not yield any appreciable results. The signal issues were fixed with the overpressure sensor so both sensors were operational for repeatability testing. Data obtained during test repeatability investigations is presented in Table 10. The standard deviation values for the overpressure and the impulse were very low. This indicates the data gathering method for overpressure was consistent and appropriate. It also affirms the pressure readings obtained are representative of the test configuration.

The elevated sensor values were more consistent, shown by lower standard deviation values, 0.39 and 0.00057 for peak overpressure and impulse, than the snow air interface sensor. Standard deviation differences indicate the snow surface condition and terrain influenced the pressure. Differences in peak overpressure at the surface and 1.5 m elevated height also were noted. The peak overpressure at the snow surface was 25% greater than at the elevated sensor location. Greater response at the surface supports that the shockwave is interacting with the snow surface resulting in increased pressures.

Table 10 Overpressure at the surface and 1.5 m above the surface at a radial distance of 7 m obtained during repeatability testing with the charge elevated 1 m. Peak overpressure, positive and negative impulse, and the standard deviation of the data are presented.

	Surface Sensor			Elevated		
Charge Height	Peak Over-pressure (psi)	Positive Impulse (psi*sec)	Negative Impulse (psi*sec)	Peak Over-pressure (psi)	Positive Impulse (psi*sec)	Negative Impulse (psi*sec)
1 m	3.98	0.00780	-0.00860	3.13	0.00735	-0.00797
	4.02	0.00764	-0.00868	3.30	0.00796	-0.01210
	4.00	0.00751	-0.01600	3.17	0.00756	-0.01604
	3.45	0.00767	-0.00843	3.32	0.00746	-0.00818
	4.81	0.00952	-0.01016	3.31	0.00791	-0.01114
Average	4.05	0.00803	-0.01037	3.25	0.00765	-0.01109
Std. Dev.	0.48	0.00084	0.00322	0.09	0.00027	0.00331

For some tests, the positive impulse was larger while for other tests the negative impulse was larger. A comparison of the impulse values as recorded at the two elevations show the surface positive impulse being larger by 1% and the elevated negative impulse being larger by 6%, indicated the impulse at the snow surface was comparable to the impulse for the 1.5 m elevated sensor. As previously mentioned the negative impulse values are impacted by the numerical integration stopping criteria while the positive impulse values are not.

The sensor located at the snow surface recorded higher pressures than the elevated sensor, shown in Figure 28. This increase illustrates increased pressures due to shockwave reflection off the snow surface. Increased pressures were expected because the reflected shockwave traveled through air that had already been impacted resulting in increased pressure values (Miller et al., 2011). Testing occurred late in the afternoon on a warm day with a moist snowpack. By the time the fifth shot was detonated the temperature had dropped. A re-evaluation of the snowpack when placing the sensors indicated refreezing of the surface. The higher overpressure seen in the fifth detonation may be due to greater shockwave reflection from a harder frozen snow surface.

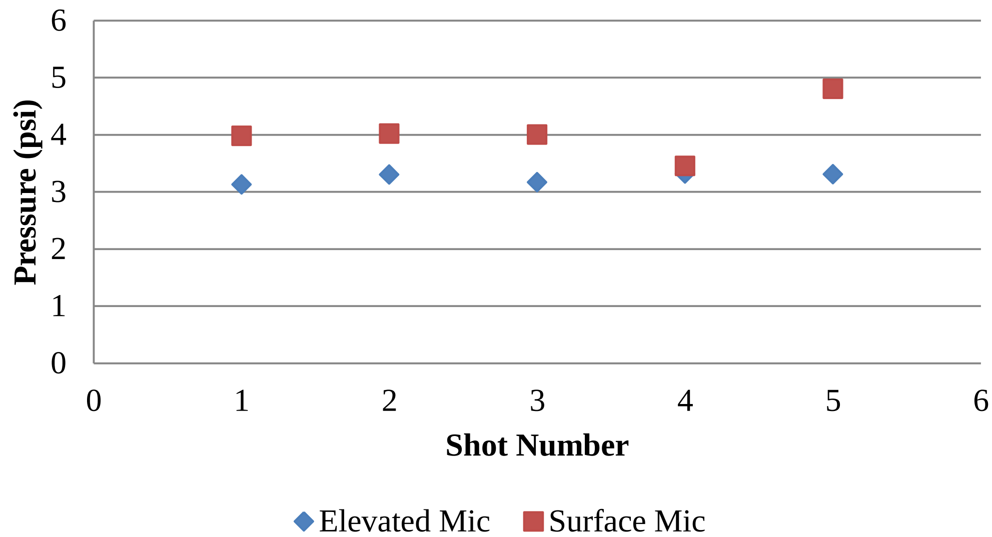

Figure 28 Comparison of 1.5 m elevated and surface pressure measurements for 0.9 kg charge masses detonated 1.5 m above the snow surface. Data was obtained during a repeatability testing sequence.

Regardless of the snow type and charge mass, elevating the charge resulted in increased overpressure as well as impulse. There is a direct relationship between the peak overpressure at the snow surface and the loading input to the snow cover. Therefore, it follows that an increase in overpressure correlates to an increase in snow acceleration. Increasing the overpressure would be more effective in avalanche mitigation work. Overpressure values over moist snow were greater than for dry snow indicating greater reflection of the shockwave. The overpressure values were found to be larger at the surface than for an elevated sensor, indicating refection of the shockwave off the snow surface.

Predicted overpressure for 0.45 kg and 0.9 kg unconfined air blasts were calculated at 5 m and 7 m radial ranges for an air temperature of -7^{o}C. Distance scaling laws and charge size factor relations were utilized in these calculations (Kinney and Graham, 1985). Results of these calculations are in Table 11.

Table 11 Predicted overpressures calculated from explosive scaling law for open air detonations for comparison purposes.

	0.45 kg pentolite	0.9 kg pentolite
Radial Distance (m)	Predicted Overpressure (psi)	Predicted Overpressure (psi)
5	2.7	4.1
7		2.24

Compared to the field experimental data, the open air blast predictions were less. For a 0.45 kg charge mass with the sensor located at the snow surface 5 m from the blast, the observed pressure was 19% greater. A 15% increase was noted for 0.9 kg pentolite charges for the sensor located at 5 m radial range on the snow surface. At 7 m radially, the percent increase was 80% at the snow surface and 45% 1.5 m above the surface. These findings further support the determination that the snow surface reflects the shockwave resulting in increased pressure values. The hard slab snow, 7 m radial range, appears to be a more effective reflective surface than the soft slab, 5 m radial range. Since at two different ranges it is not possible to determine if the snow classification is completely responsible for the increase, the radial range must also be considered.

A comparison of the predicted overpressure for 0.45 kg and 0.9 kg charges indicates doubling the charge mass resulted in a 52% increase in overpressure. This increase is in close agreement to the field data increase, average of 50% increase, due to doubling the charge mass.

Accelerometer Data Investigation

The acceleration responses obtained during the two year research project were investigated to determine:

- The test repeatability of the system and data spread
- The effect of charge elevation on:
    - Snowpack response
    - The ramifications of depth and range from the detonation on the acceleration response
    - The radial attenuation of the acceleration resultant response
    - The shockwave attenuation in the vertical direction
    - Power law leading coefficient value
- The influence of snow moisture content on acceleration response
- The difference in acceleration response due to 0.45 kg and 0.9 kg charge masses
- The significance of slab classification, soft or hard, on dynamic snow response
- The correlation between snowpack response and total snow water equivalent
- The relationship between snowpack response and snowpack density
- Snowpack movement due to explosive detonations

Data investigations and results are detailed in the following sections.

Acceleration Data

Resultant acceleration magnitudes for the six distinct sensor locations are shown in Figure 29. This figure shows acceleration response decreases as the shockwave travels in the radial direction. Irrespective of the sensor depth, the data series at 2 m radial distance is larger than the series at 5 m. The response also decreases with depth in the snowpack, illustrated by the acceleration peak decreasing with depth at the same radial location. The time it takes for the shockwave to travel through the snowpack, radially and vertically is also illustrated by the time delay between the acceleration peaks, both radially and through the depth. This figure is one test, but is representative of all tests days. The acceleration data show an oscillatory damped acceleration response.

Average peak acceleration response magnitudes from the soft slab snow testing, 2010-2011 winter, is presented for both 0.45 kg and 0.9 kg pentolite cast boosters in Table 12. For both charge sizes, dry and moist snow condition data is shown. The hard slab snow conditions, 2011-2012 winter, data for 0.9 kg charges is presented in, Table 13. The snow on each testing day was moist. Test repeatability was explored during the 2011-2012 winter season and the data is included as a subsection in Table 13. The snow for repeatability testing was classified as a moist hard slab and all tests were conducted on the same day.

Peak resultant magnitudes, and sensor scaled distances for both soft and hard slab snow investigations are shown in Appendix G. Acceleration data rather than velocity or position was analyzed for trends. This was done because the acceleration values result from a single conversion from voltage values, rather than a conversion and integration as velocity and position require. Therefore, integration errors are not compounded. The acceleration values investigated are the average peak acceleration response magnitudes.

Peak values of acceleration would correspond to the greatest impact on the snow and would be of the most interest for avalanche mitigation.

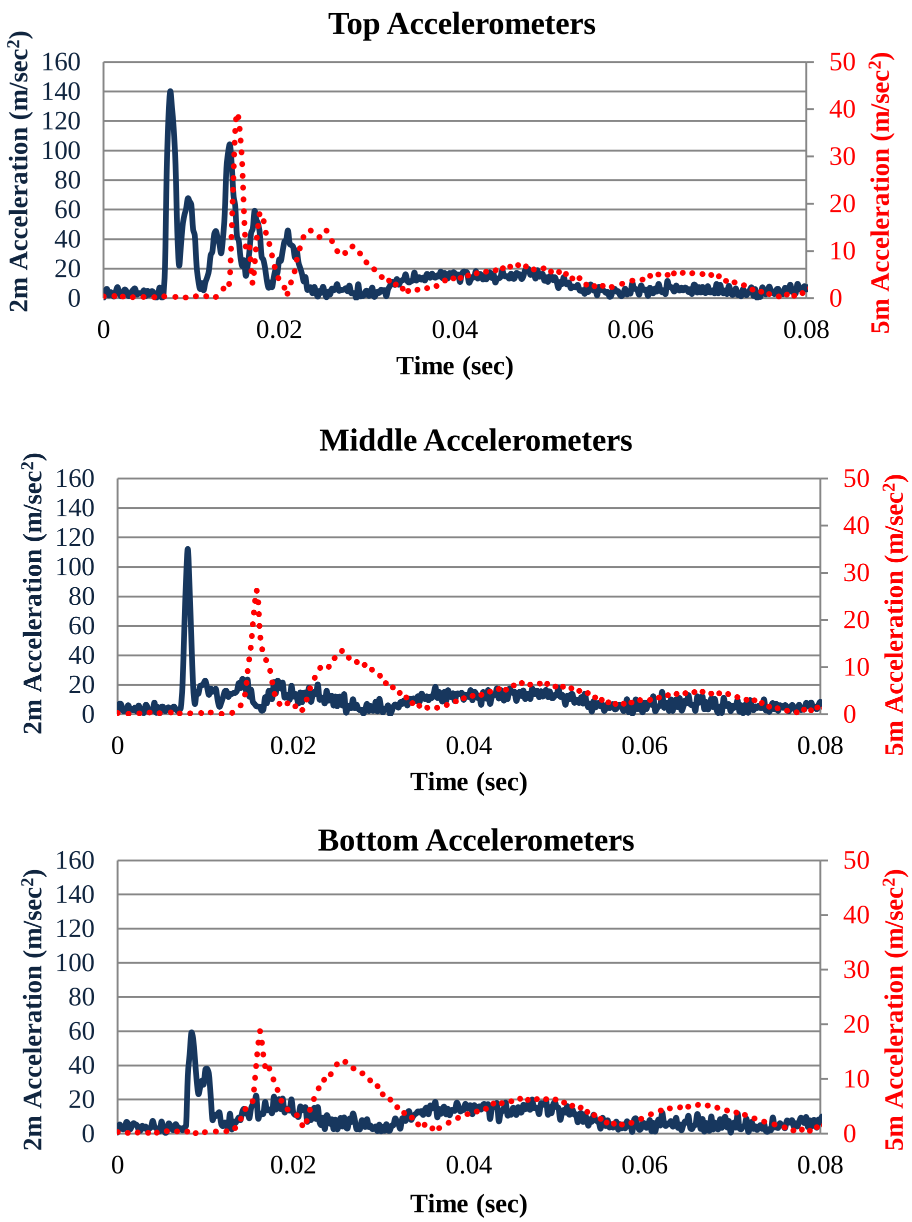

Figure 29 Resultant acceleration values for a 0.45 kg charge detonated during the 2010-2011 testing season illustrating general trends for the acceleration data gathered. There are two data series per section, acceleration at 2 m radial distance, the blue data series, and accelerations at 5 m radial distance shown in red. The two data series are plotted on a separate axis with different scales.

Average peak acceleration response magnitudes from the soft slab snow testing, 2010-2011 winter, is presented for both 0.45 kg and 0.9 kg pentolite cast boosters in Table 12. For both charge sizes, dry and moist snow condition data is shown. The hard slab snow conditions, 2011-2012 winter, data for 0.9 kg charges is presented in, Table 13. The snow on each testing day was moist. Test repeatability was explored during the 2011-2012 winter season and the data is included as a subsection in Table 13. The snow for repeatability testing was classified as a moist hard slab and all tests were conducted on the same day.

Peak resultant magnitudes, and sensor scaled distances for both soft and hard slab snow investigations are shown in Appendix G. Acceleration data rather than velocity or position was analyzed for trends. This was done because the acceleration values result from a single conversion from voltage values, rather than a conversion and integration as velocity and position require. Therefore, integration errors are not compounded. The acceleration values investigated are the average peak acceleration response magnitudes. Peak values of acceleration would correspond to the greatest impact on the snow and would be of the most interest for avalanche mitigation.

Table 12 Average peak acceleration values per charge elevation for both 0.45 kg and 0.9 kg pentolite masses obtained for soft slab snow conditions during winter 2010-2011. Values are given for both radial distances, 2 m and 5 m.

Dry Soft Slab Snow Data for 0.9 kg Pentolite Cast Booster							
Charge Height		2 m Radial Distance			5 m Radial Distance		
		Top	Middle	Bottom	Top	Middle	Bottom
0 m	Average Resultant (m/sec^2)	145.37	115.69	76.00	35.09	25.27	21.44
0.5 m	Average Resultant (m/sec^2)	159.57	96.04	90.03	28.51	22.23	21.51
1 m	Average Resultant (m/sec^2)	273.50	105.18	70.30	57.18	27.82	22.61
1.5 m	Average Resultant (m/sec^2)	173.39	106.66	69.09	34.18	22.92	20.38
2 m	Average Resultant (m/sec^2)	289.69	148.14	103.62	43.08	23.89	19.77
Moist Soft Slab Snow Data for 0.9 kg Pentolite Cast Booster							
0.5 m	Average Resultant (m/sec^2)	153.79	45.19	25.76	33.66	10.95	10.11
1 m	Average Resultant (m/sec^2)	245.21	72.91	46.13	47.75	12.15	12.13
1.5 m	Average Resultant (m/sec^2)	129.22	47.91	33.28	38.46	10.83	7.83
2 m	Average Resultant (m/sec^2)	130.48	53.91	53.91	52.23	12.88	6.88
Dry Soft Slab Snow Data for 0.45 kg Pentolite Cast Booster							
0 m	Average Resultant (m/sec^2)	163.18	107.93	65.99	27.48	15.43	13.77
0.5 m	Average Resultant (m/sec^2)	203.53	143.01	78.57	39.06	21.26	15.87
1 m	Average Resultant (m/sec^2)	150.88	101.80	72.11	27.56	21.49	19.10
1.5 m	Average Resultant (m/sec^2)	174.23	114.86	91.64	34.17	21.87	17.54
2 m	Average Resultant (m/sec^2)	140.12	112.17	59.09	39.26	26.36	18.74
Moist Soft Slab Snow Data for 0.45 kg Pentolite Cast Booster							
0.5 m	Average Resultant (m/sec^2)	99.53	76.83	76.33	19.88	16.97	10.00
1 m	Average Resultant (m/sec^2)	107.89	65.63	68.08	28.79	13.98	10.12
1.5 m	Average Resultant (m/sec^2)	127.23	71.64	34.09	27.05	18.33	13.27
2 m	Average Resultant (m/sec^2)	127.27	54.41	57.63	25.79	16.98	10.80

Table 13 Average peak acceleration values for hard slab snow investigations taken winter of 2011-2012 according to charge elevation. The accelerometers were located 3 m and 5 m radially from the explosive.

Moist Hard Slab Snow Data for 0.9 kg Pentolite Cast Booster							
Charge Height		3 m Radial Distance			5 m Radial Distance		
		Top	Middle	Bottom	Top	Middle	Bottom
0 m	Average Resultant (m/sec^2)	50.30	23.84	15.93	25.78	12.01	5.85
0.5 m	Average Resultant (m/sec^2)	84.60	46.81	20.59	34.84	13.00	9.95
1 m	Average Resultant (m/sec^2)	106.17	49.58	34.63	39.99	13.18	9.23
1.5 m	Average Resultant (m/sec^2)	101.05	74.45	36.31	33.55	14.08	7.61
2 m	Average Resultant (m/sec^2)	109.15	33.65	25.80	47.55	17.80	9.45
Moist Hard Slab Snow Repeatability Data for 0.9 kg Pentolite Cast Booster							
1 m	Average Resultant (m/sec^2)	37.06	21.90	14.48	17.53	12.27	9.34

Repeatability Acceleration Testing

During the 2011-2012 winter testing season, the repeatability of test methods and procedures was explored by doing five repeated tests on the same day. On the testing day, five 0.9 kg pentolite cast boosters were detonated at an elevation of 1 m above the snow surface. Each detonation location was different, but the accelerometers were placed at the same depths and radii from the blast. The complete data from these tests are presented in Appendix G. Table 14 shows the average and standard deviation for individual accelerometer locations.

Table 14 Average acceleration and standard deviation values for repeatability tests conducted in the 2011-2012 winter season.

	3 m Radial			5 m Radial		
	Top	Middle	Bottom	Top	Middle	Bottom
Average	37.1	21.9	14.5	17.5	12.3	9.3
Stdev	12.8	9.1	5.0	5.6	2.5	2.4

The standard deviation values indicate the top accelerometers have the most variability. On this particular day, the snowpack layers 0.2 m below the surface were similar in hardness and density. The top portion of the snow possibly had more variation between individual tests than deeper in the snow. Also, the testing day was warm with moisture in the upper portion of the snowpack. According to McClung and Schaerer (2006) the snow moisture content was classified as less than 3%. When the sun was no longer on the slope, a crust formed on the snow surface as evidenced by visual inspection while placing the sensors, as well as fractured plates on the snow surface following a detonation. The slope experienced sun for tests 1-3 and the slope was shaded for tests 4-5, but the surface did not refreeze until test 5 was conducted. The density of the top portion of the snow was less than deeper in the snowpack. This could have contributed to larger variability of acceleration values at the top accelerometers by greater susceptibility to sensor rotation. From the data it was concluded that the testing method was appropriate for recording snow acceleration values due to explosive detonations.

Impact of Elevating Charges

It was desired to determine what impact raising an explosive off the snow surface would have on the resulting snowpack acceleration. Past research (Gubler (1977), Ueland (1992), and Johnson (1994)) indicated the response would increase, but it was desired to verify and further quantify this. The snow acceleration was expected to be greater for elevated charges because the snow loading is due to the reflected shockwave. A surface charge loses a large portion of the energy by creating a crater. Impacts of raising a charge were examined:

- By calculating peak acceleration resultant percent increase
- For implications on the depth and range of an explosive
- To determine the impact on shockwave attenuation in the vertical direction
- To characterize the ramifications on radial attenuation of the resulting shockwave
- By investigation of the leading coefficient from power law regression

This was done for both soft and hard slab snow conditions and the results are presented in the following sections.

Percent Increase Referenced to Surface Detonations To investigate the implications of raising an explosive above the snow surface on the acceleration of the snow, percent increase in the average peak acceleration response resultant recorded at all accelerometer locations was determined. The surface charge was used as the baseline in calculating percent increase. Detonations on the snow surface resulted in the smallest snow accelerations when compared with other charge heights investigated. Percent increase is shown in Table 15 and Table 16, with the surface charge showing 0% increase since it was used as the baseline value. Data for dry soft slab snow conditions and a combination of 0.45 kg and 0.9 kg charges are shown in Table 15. Inclusion of dry snow only was done to minimize variability of response due to individual testing day snowpack

Table 15 and Table 16 show all accelerometer locations, other than the middle accelerometer at 2 m radial range for charges elevated 1.5 m, indicate elevating a charge increased acceleration. The percent increase varies, but all locations show at least a 5% increase, some are greater than 100%. The percent increase denoted in Table 16 is substantial for all accelerometer locations investigated. The moist hard slab data indicates a greater increase than the dry soft slab data does. This indicates either the water content of the snowpack or a characteristic tied to the snow hardness is influencing the percent increase in acceleration. Unfortunately, during the soft slab snow testing, surface charge data was not obtained for moist snow. Therefore, it is not possible to determine from percent increase if the water content or another snow characteristic difference is responsible for the elevated levels of percent increase seen between the two testing seasons.

Table 15 Percent increase of peak acceleration resultants for elevated charges compared to surface detonations, data is for dry soft slab snow conditions and a combination of 0.45 kg and 0.9 kg charges.

Percent Increase of Acceleration in Soft Slab Snow						
Charge Height	2 m Radially			5 m Radially		
	Top	Middle	Bottom	Top	Middle	Bottom
0 m	0	0	0	0	0	0
0.5 m	18	7	19	8	7	6
1 m	40	6	9	40	45	36
1.5 m	13	-1	13	9	10	8
2 m	71	13	48	54	27	7

Table 16 Percent increase of peak acceleration resultants for elevated charges compared to surface detonations, data is for moist hard slab snow conditions and 0.9 kg charges.

Percent Increase of Acceleration in Hard Slab Snow						
Charge Height	3 m Radially			5 m Radially		
	Top	Middle	Bottom	Top	Middle	Bottom
0 m	0	0	0	0	0	0
0.5 m	68	96	29	35	8	70
1 m	111	108	117	55	10	58
1.5 m	101	212	128	30	17	30
2 m	117	41	62	84	48	61

Gubler (1977) indicated the optimum height for an explosive was 1-2 m above the snowpack. Table 15 and Table 16 indicate the percent increase for this charge elevation range had a low of 6% increase and a high of 212%. The percent increase values determined are in agreement with Gubler's results. Raising a charge too much would eventually result in decreased acceleration resultant response. The decrease would result from geometric expansion and attenuation, resulting in shockwave energy losses while traveling through the air prior to transfer into the snowpack.

Impacts on Acceleration with Depth and Range To further examine the implications of elevating an explosive and to specifically investigate this impact on the snowpack response with depth and range, average peak acceleration response and scaled depth of sensors were computed for each charge elevation. The peak average response for individual accelerometer locations were plotted against the scaled sensor depth. Scaled sensor depths were necessary to allow inclusion of data from both 0.45 kg and 0.9 kg charges. This was done for each charge height as well as both radial accelerometer ranges. Both seasons of data are presented below, soft slab conditions in Figure 30 and Figure 31 and hard slab snow in Figure 32 and Figure 33, respectively.

The figures illustrate similar trends, an increase in snowpack acceleration as a result of elevating charges, regardless of the snow classification and radial distance. The effect is more pronounced closer to the surface, but is also present deeper in the snowpack. The advantage of raising the explosive varies for different snow type, depth of sensor, and radial distance as comparisons of Figure 30 to Figure 33 indicate. The surface charge consistently resulted in the lowest peak acceleration. The increased snow acceleration is larger at 2 m or 3 m radially from the detonation than at 5 m radial distance. The top layer at 2 m radial range showed a maximum increase of 71% while the bottom layer was 48% for soft slab snow. At 5 m radial distance, the maximum increase in the top layer was 54% and the bottom was 36%, respectively. These values support the visual determination from Figure 30 and Figure 31 that the total increased snow acceleration is more significant near the snow surface and at small radial ranges. The values for hard slab snow varied from the soft slab snow, but the trend was the same.

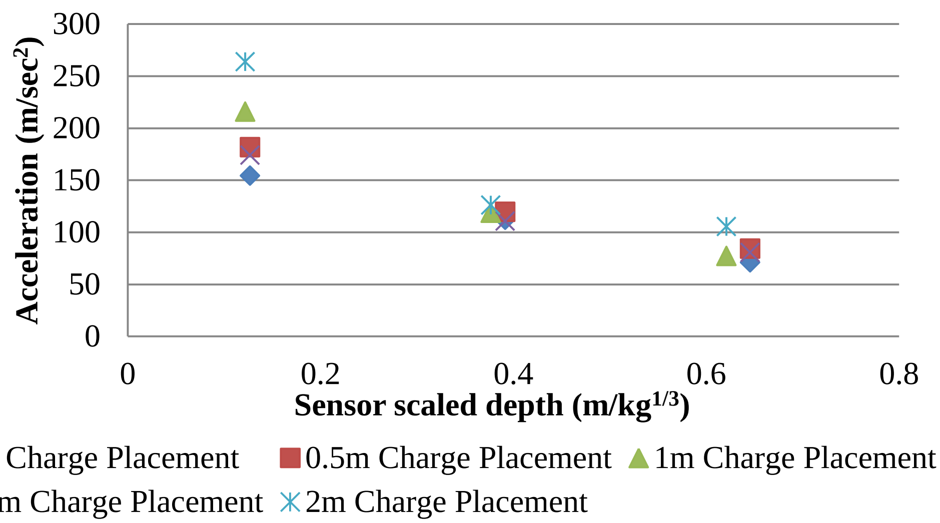

Figure 30 Average peak acceleration resultant response recorded by accelerometers at 2 m radial distance in soft slab snow conditions. Data used for the figure is from dry snow conditions, both 0.45 kg and 0.9 kg charge mass detonations are included.

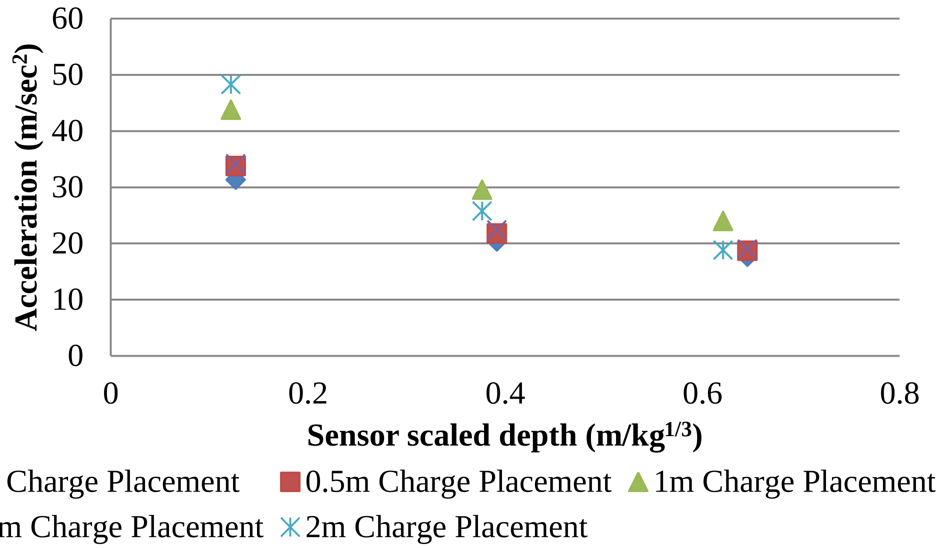

Figure 31 Average peak acceleration resultant response recorded by accelerometers at 5 m radial distance in soft slab snow conditions. Data used for the figure is from dry snow conditions, both 0.45 kg and 0.9 kg charge mass detonations are included.

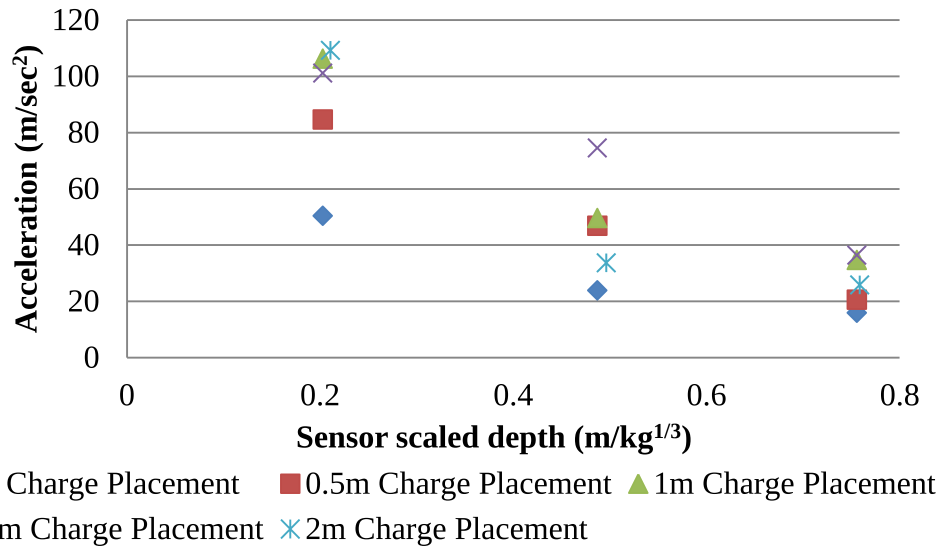

Figure 32 Average peak acceleration resultant response recorded by accelerometers at 3 m radial distance in moist hard slab snow conditions. Data used for the figure is from 0.9 kg charge masses.

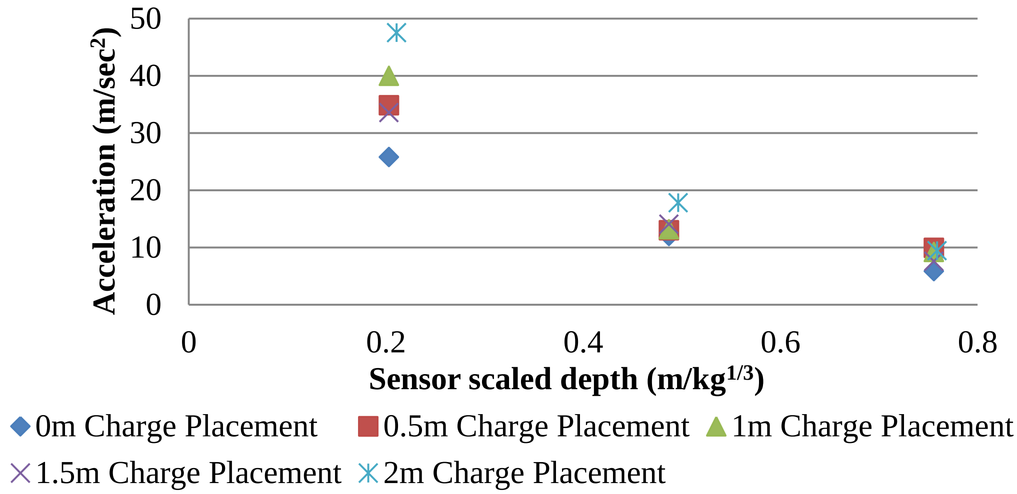

Figure 33 Average peak acceleration resultant response recorded by accelerometers at 3 m radial distance in moist hard slab snow conditions. Data used for the figure is from 0.9 kg charge masses.

Figures similar to those presented in Figure 30 to Figure 33 were created, but with acceleration represented as a function of scaled radial distance rather than scaled depth. Each sensor depth was plotted as an individual figure with multiple data series to represent the different charge locations. These figures further substantiate the acceleration response increase due to elevating an explosive and are included in Appendix H to provide another viewpoint. The data used is the same and trends are not significantly different from those presented above, hence inclusion in the appendix.

From the data gathered it is clear an elevated charge results in greater snow acceleration than a surface charge. Therefore, an elevated charge would be more effective at initiating an avalanche during avalanche mitigation work. Larger acceleration values are associated with greater stress on the snowpack increasing the likelihood of weak layer failure. Larger acceleration at a particular location indicates an increase in the depth and range of effectiveness for the explosive. This would be true if the shockwave attenuation does not increase due to elevating an explosive.

Vertical Attenuation   Attenuation was determined and compared for the different charge heights. Power regression fit functions for determining the vertical attenuation for individual charge heights are shown in Appendix I. The power exponent, *d*, was plotted along with the corresponding charge height to examine the relationship between charge location and vertical attenuation. The resulting attenuation for soft slab snow is shown in Figure 34 and hard slab snow is presented Figure 35.

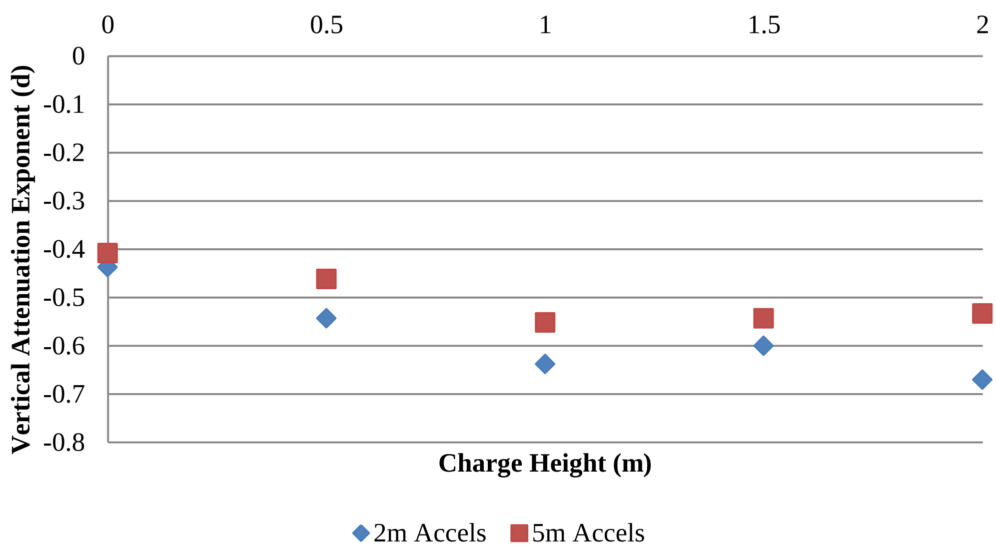

Figure 34 Peak acceleration resultant vertical attenuation for individual charge elevations at both 2 m and 5 m radially for soft slab snow conditions and a combination of 0.45 kg and 0.9 kg charge masses. The average rate at 2 m was found to be -0.61 and at 5 m to be -0.52 respectively.

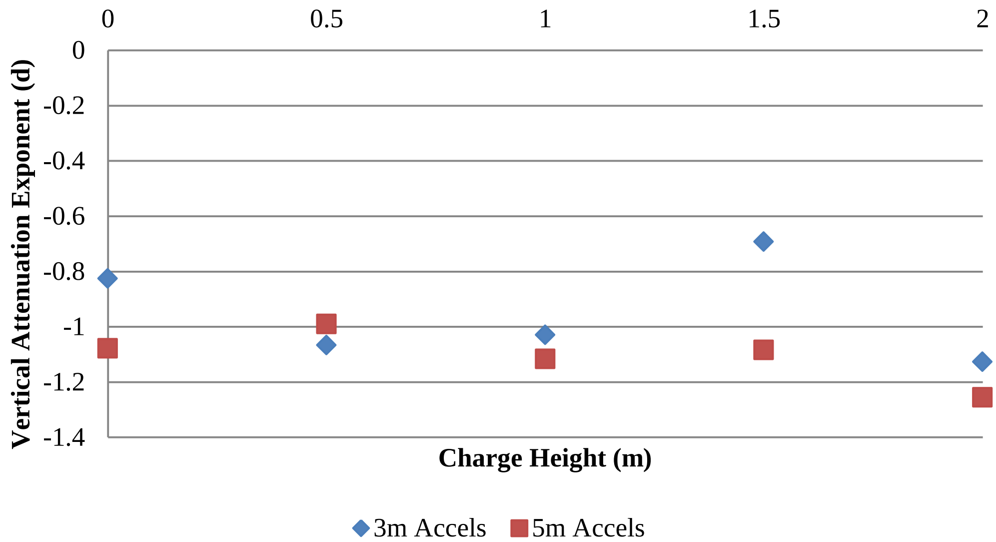

Figure 35 Peak acceleration resultant vertical attenuation for individual charge elevations at both 3 m and 5 m radially for moist hard slab snow conditions and 0.9 kg charge masses. The average decay at 3 m was found to be -0.98 and at 5 m to be -1.11.

Both seasons of data show vertical attenuation independence from the charge height. No clear trend to the data is shown, it is relatively clumped around the average value for a particular radial distance. The two radial distances do show different attenuation, but the averages are 0.09 different for soft slab snow and 0.13 for hard slab snow. The differences in attenuation at the two radial distances are small enough to be insignificant. The vertical attenuation at both radial distances indicate the vertical attenuation is independent of the radial range. In other words, regardless of the radial location the vertical attenuation is essentially the same. The primary cause of vertical shockwave attenuation is believed to be due to snow deformation and interactions of the shockwave within the ice-pore lattice but also includes geometric wave expansion. Due to the close proximity of the sensors through the depth, snow interactions are believed to be a large contributor to attenuation.

The hard slab attenuation exponent was 56% greater than for the soft slab. It was desired to determine why the attenuation was different. The soft slab data is for both dry and moist snow conditions, while the hard slab data is for moist snow only, as such it is not possible to determine from direct comparisons if the vertical attenuation difference is due to the moisture content or hardness of the snow or another snow characteristic difference. To further investigate this, the attenuation for dry and moist soft slab snow classifications were determined from 2010-2011 data. These values are presented in Table 17. At both radial distances, the vertical attenuation for the moist snow was more rapid than for the dry snow. Research by Ueland (1992) and Gubler (1977) indicated moist snow attenuation was greater than dry snow in the vertical direction. This same result was noted in this research project. Moisture in snow is believed to be a contributing factor for different attenuation in dry soft slab snow and moist hard slab snow, but it is not possible to definitely determine the contributing factors. Average vertical attenuation for moist hard slab snow is greater than the moist soft slab snow. Since comparing the attenuation of moist snow with different snow hardness characteristics, the hardness must play a role. The hardness classification of snow involves multiple parameters, therefore, determination of exactly which snow parameter is impacting the attenuation is not possible from this test set up. It can be stated though that for the data examined hard slab snow attenuates faster than soft slab snow does within the depths investigated.

Table 17 Comparison of dry and moist soft slab snow vertical attenuation, *d*, as determined from data obtained in the 2010-2011 testing season from 0.45 kg and 0.9 kg charge masses.

	Dry Soft Slab		Moist Soft Slab	
Charge Height	2 m	5 m	2 m	5 m
0.5 m	-0.421	-0.358	-0.570	-0.567
1 m	-0.608	-0.442	-0.676	-0.775
1.5 m	-0.439	-0.439	-0.762	-1.004
2 m	-0.713	-0.531	-0.541	-0.851
Average	-0.5453	-0.4425	-0.6373	-0.7993

On days the snowpack was classified as moist, the entire snowpack was not isothermal. Moisture was present in the portion of the pack containing the top and middle accelerometers. The bottom accelerometers were located in dry snow. This means the shockwave traveled through moist snow into dry snow; possibly resulting in an impedance mismatch between snow layers. This could explain the greater attenuation indicated in Table 17.

<u>Radial Attenuation</u> Shockwave attenuation not only occurs through the snowpack depth, but also in the radial direction. To investigate the link between charge elevation and radial attenuation, the radial attenuation was plotted similarly to vertical attenuation presented above. Appendix J contains the data used to determine the radial attenuation for the individual charge heights investigated. Average radial attenuation as a function of elevated charge height for soft slab and hard slab snow are in Figure 36 and Figure 37, respectively. Three power exponents were computed in the radial direction: one for the top layer, one for middle of the snowpack, and finally the bottom accelerometer locations.

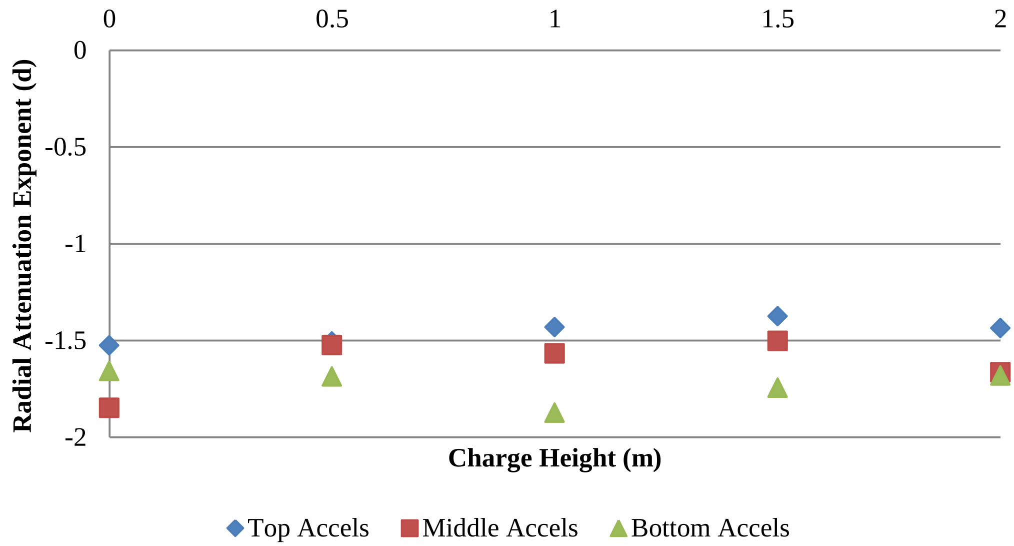

Figure 36 Radial attenuation for individual charge elevations for soft slab snow conditions. Both dry and moist snow conditions are included as well as 0.45 kg and 0.9 kg charge masses. From the top to the bottom of the snowpack the average attenuation was found to be, -1.45, -1.62, and -1.73 respectively.

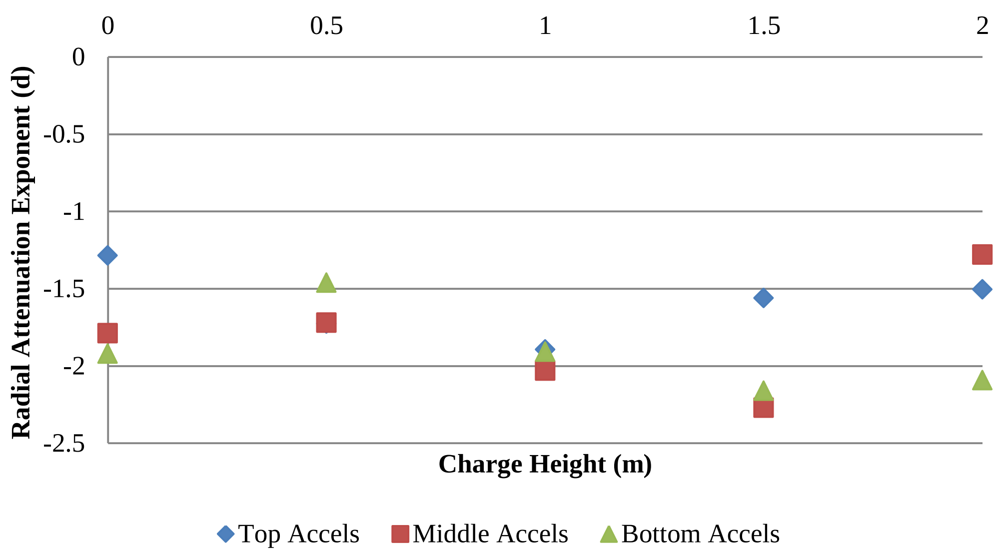

Figure 37 Radial attenuation for individual charge elevations for moist hard slab snow conditions and 0.9 kg charge masses. From the top to the bottom of the snowpack the average attenuation was found to be, -1.67, -1.83, and -1.91.

Similar to the vertical attenuation analysis, the radial attenuation appears to be largely independent of charge elevation. This holds true for all depths and snow types investigated. The average radial attenuation indicates the depth of sensor does not appreciably impact the attenuation. Average attenuation for the three sensor depths was 0.2 different between the soft and hard snow conditions. Figure 36 and Figure 37 indicate the top accelerometers experienced the slowest shockwave decay and the bottom accelerometers the fastest acceleration decay regardless of the snow type, but the difference was less than 0.3, concluding the radial attenuation is relatively independent of depth within the snowpack. The radial attenuation calculated for the soft slab data is less than the hard slab snow by 0.2. A similar trend was also noted for vertical attenuation comparisons in the preceding section.

Theoretically accelerometers at 2 m and 5 m radial distances are located in the same snow layer with the same snow properties. As such there would be little to no snow impedance mismatch between the two locations. Greater shockwave radial attenuation in moist hard slab than combination of moist and dry soft slab snow indicates the snow water content or another snow variable is contributing to increasing the magnitude of *d*. To determine if the moisture content affected the radial attenuation, the soft slab snow power law exponent, *d*, was broken down according to moisture content, Table 18. For the sensor locations investigated the attenuation for dry snow was shown to be greater than for moist snow, a maximum of 0.3 different. This may be due to greater shockwave reflection for moist snow than for dry snow resulting in a greater input at 5 m radial distance. Since moist snow attenuates a shockwave less than dry snow in the radial direction; the greater attenuation seen in moist hard slab snow than dry soft slab snow must not be due to being moist. Another variable between the two snowpacks must be responsible for the attenuation difference, but the current set up does not allow for determination of the particular characteristic.

Table 18 Comparison of dry and moist soft slab snow condition radial attenuation for data obtained in the 2010-2011 winter testing season resulting from 0.45 kg and 0.9 kg charge masses.

	Dry Soft Slab			Moist Soft Slab		
Charge Height	Top	Middle	Bottom	Top	Middle	Bottom
0.5 m	-1.66	-1.71	-1.69	-1.73	-1.34	-1.31
1 m	-1.88	-1.54	-1.35	-1.57	-1.60	-1.85
1.5 m	-1.67	-1.64	-1.53	-1.55	-1.36	-1.22
2 m	-2.08	-1.81	-1.43	-1.38	-1.27	-1.32
Average	-1.82	-1.67	-1.50	-1.56	-1.39	-1.42

Radial attenuation was found to be greater than vertical attenuation regardless of snow type. Shockwave attenuation is due to a combination of spherical shockwave expansion along with snow deformation and interactions between the snow solid and pore space. Radial distances were much greater than vertical, resulting in the geometric shockwave expansion playing a larger role. Since the shockwave is expanding geometrically, there is a different acceleration input at the near and far accelerometer locations in the radial direction. Therefore, the radial attenuation is highly impacted by geometric expansion. While for attenuation in the vertical direction the accelerometers experience the same input to the snow surface resulting in the attenuation being due to snow deformation and interactions within the ice pore lattice. For charges placed 1 m above dry snow with sensors placed >0.8 m below the surface, Gubler (1977) found a vertical power exponent of -1.21 and a radial attenuation of -1.59. Similarly, Mellor (1985) noted a radial attenuation of -1.6. For the field data gathered in this project, radial attenuation for dry snow was -1.59, very close agreement with the previous research. The vertical attenuation determined from the field in dry snow conditions was -0.52. The difference may be due to the sensors, for this research, all being closer to the surface and the charge than the sensors used by Gubler or the snowpack differences. Brown (1981) predicted a 90% loss of response amplitude in 0.1 m of distance. The attenuation determined here were much less than this. Possibly because the parameters used for theoretical modeling by Brown were not the same as the snow properties encountered in the field.

Combining the greater snowpack acceleration due to elevating the explosive and the shockwave attenuation being independent of the charge elevation is a very pertinent finding. This shows the ability to maximize the depth and range of a single explosive. Not only is the area of influence increased, but the volume of influence due to the blast being axisymmetric.

Power Law Leading Coefficient (*c*) Comparison The power law data fit not only determined the power exponent *d*, but also the leading coefficient *c*. It was desired to determine what impact elevating an explosive charge in relation to the snow surface would have on the leading coefficient from the power law fit. Since elevating an explosive off the snow surface resulted in increased accelerations, it would follow that the leading coefficient would indicate the same. Data from the hard slab testing was used for comparison purposes. It was decided to use the hard slab data rather than the soft slab data due to consistent sensor placement for all tests. To compare leading coefficients, the sensor depth needed to be the same, otherwise the comparison would include variables other than charge elevation. Table 19 shows values for shockwave vertical attenuation as a function of charge elevation. Coefficient constants for shockwave radial attenuation are presented in Table 20. The tables show both the leading coefficient and the power exponent. Both values are required to determine which *c* values are comparable. The power exponent dictates the shape of the curve and the leading coefficient determines the location of the curve. For the same *d* value, a larger *c* value indicates the acceleration response to be greater.

Table 19 Leading coefficients (*c*) and power exponent (*d*) as calculated from power law regression of acceleration resultant as a function of depth at both 3 m and 5 m radial distance. The power law fits are for hard slab snow investigations as a result of 0.9 kg charges. Highlighted values were deemed to have similar enough *d* values to allow comparison of the *c* values.

Vertical Power Law Coefficient and Power Comparison				
Charge Height	3 m		5 m	
	c ($kg^{1/3}/sec^2$)	d	c ($kg^{1/3}/sec^2$)	d
0 m	13.89	-0.826	4.76	-1.078
0.5 m	15.28	-1.066	7.07	-0.99
1 m	18.57	-1.029	6.36	-1.116
1.5 m	32.65	-0.692	5.82	-1.084
2 m	17.09	-1.127	6.68	-1.255

Table 20 Leading coefficients (*c*) and power exponent (*d*) as calculated from power law regression of acceleration response resultant as a function of radial distance for the three different accelerometer depths. The power law fits are for hard slab snow responses resulting from 0.9 kg charge mass detonations. Highlighted values were deemed to have similar enough *d* values to allow comparison of the *c* values.

Radial Power Law Coefficient and Power Comparison						
Charge Height	Top		Middle		Bottom	
	c ($kg^{1/3}/sec^2$)	d	c ($kg^{1/3}/sec^2$)	d	c ($kg^{1/3}/sec^2$)	d
0 m	186.93	-1.286	187.46	-1.788	114.52	-1.92
0.5 m	497.95	-1.727	227.86	-1.72	80.303	-1.461
1 m	735.87	-1.895	301.74	-2.031	174.57	-1.909
1.5 m	480.85	-1.561	703.58	-2.271	305.04	-2.162
2 m	476.83	-1.504	126.15	-1.28	223.99	-2.092

For the highlighted values in Table 19 and Table 20, the charge elevation appears to impact the coefficient *c*. In the vertical direction, at both 3 m and 5 m the increase in the constant *c* was approximately 3 times as great. The radial attenuation data indicates that for middle and bottom accelerometer locations, the leading coefficient increased substantially, about 40 $kg^{1/3}/sec^2$ and 110 $kg^{1/3}/sec^2$ for middle and bottom accelerometers, as a result of elevated charge placement. Both of these sensor depths were compared to a surface charge. The top accelerometers are difficult to compare because the surface power law exponent *d* was not similar in any of the tests. There is no base value to be compared to, but if the other sensor locations are any indication, these values would be larger than that for a surface charge.

Comparison of Acceleration in Dry and Moist Snow Conditions

For soft slab snow conditions dry and moist snow conditions were investigated with both 0.45 kg and 0.9 kg charge masses. Acceleration responses due to the two charge sizes were combined and an average response for the individual charge heights in each snow type was determined. It was possible to combine responses from two explosive masses because the sensor locations were scaled as described in the Data Processing Chapter. The average responses at the sensor locations were used to create contour and surface plots using MathCAD Software. This allowed for a comparison of the dry and moist snow responses. Appendix K contains contour and surface plots coupled with the data points used to create them. Data in Appendix K were used to create the figures in this section. The contour and surface plots presented here are used to compare dry and moist snow conditions. Each figure is for a different charge elevation investigated.

Surface charges were only tested in dry snow conditions. Since the response was so much lower than for suspended charges, surface charges were not detonated in moist snow conditions. As such, Figure 38 shows the contour and surface plots for dry snow conditions only. Near the explosive charge, the acceleration is greatest and rapidly deceases with increasing distance. This is true in both the vertical and radial directions.

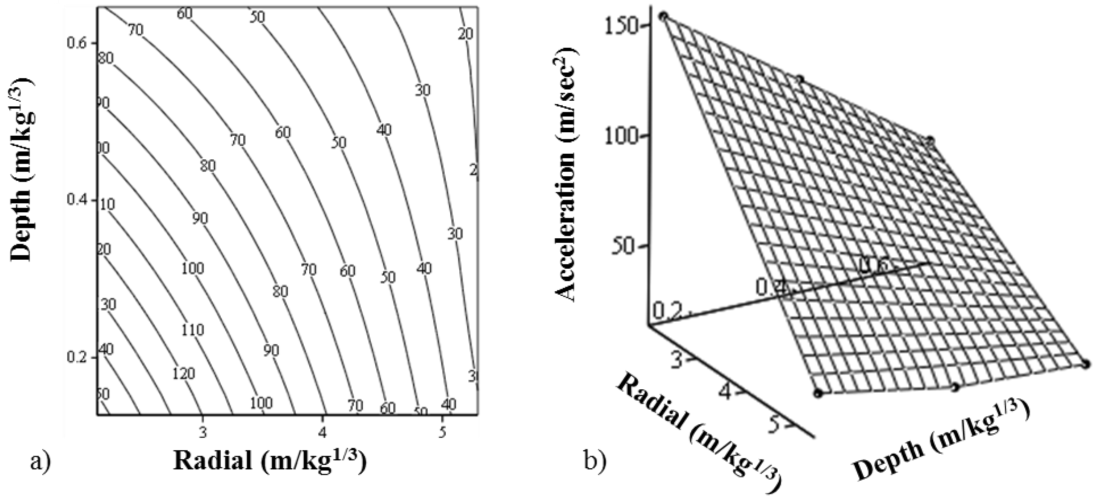

Figure 38 a) Contour and b) surface plots of average acceleration, due to 0.45 kg and 0.9 kg charge masses, as a function of radius and depth for surface charge detonations. The data is from soft slab investigations and is for dry snow conditions, no surface shots were conducted in moist snow conditions.

Elevated charge heights also were examined. The 0.5 m elevated charge comparison of dry and moist snow is shown in Figure 39. The figure indicates that for all sensor locations, dry snow resulted in greater snowpack acceleration than moist snow did. The maximum difference is ~40 m/sec^2 and occurs in close proximity to the charge. For the area of interest, the two surfaces did not intersect. As the radial range increased, the difference between the two responses was less.

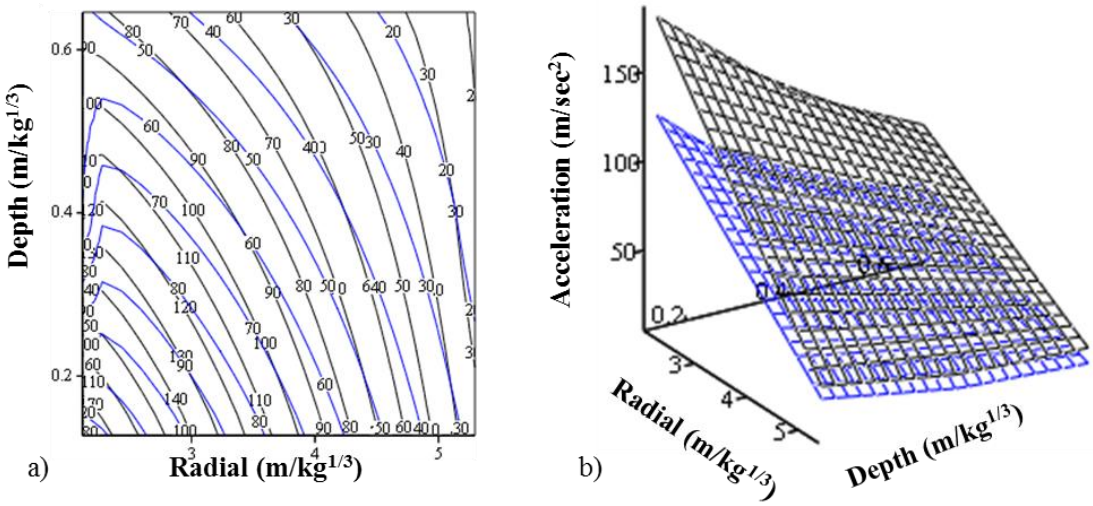

Figure 39 a) Contour and b)surface plots of average acceleration, due to 0.45 kg and 0.9 kg charge masses, as a function of radius and depth for detonations 0.5 m above the snow surface. The data is from soft slab investigations and the dry snow is shown as black and the moist snow is in blue.

For charges elevated 1 m above the snow surface, the dry snow response is greater than moist snow accelerations, as shown in Figure 40. The difference between the two responses is the greatest close to the explosive and diminishes as the distance becomes greater, in both the vertical and radial directions. The dry snow dynamic response ranges from approximately 10 m/sec^2 to 25 m/sec^2 greater than the moist snow response. The response contour shape, as illustrated in Figure 40, is very similar between the two snow types. For the charge elevated 1 m above the snow surface, there was less difference between the dry and moist snow response than seen in a charge elevated 0.5 m. This would support raising an explosive charge results in increased snow accelerations for both snow types.

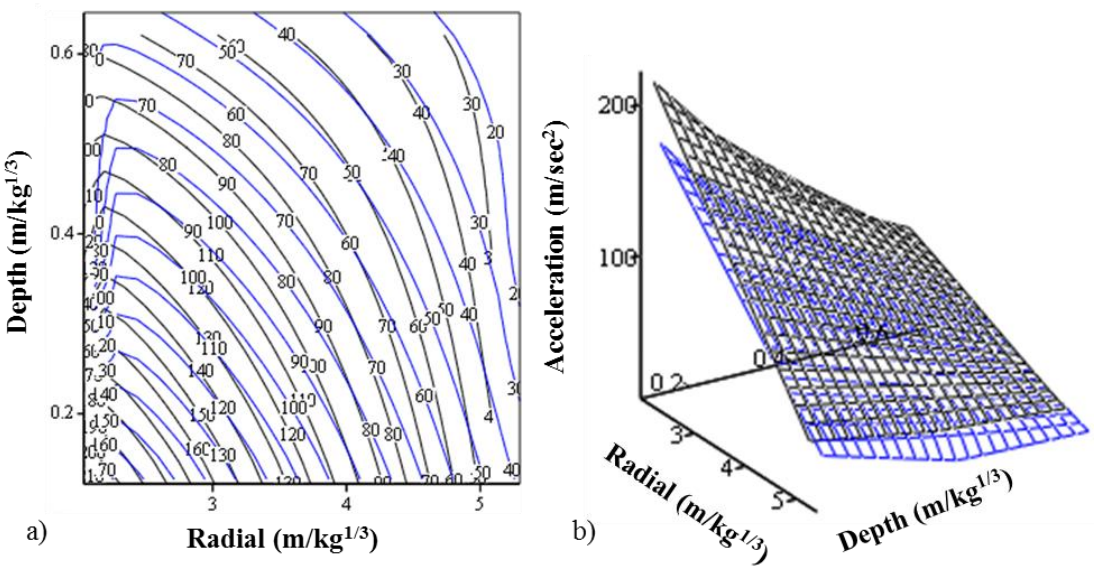

Figure 40 a) Contour and b) surface plots of average acceleration, due to 0.45 kg and 0.9 kg charge masses, as a function of radius and depth for detonations 1 m above the snow surface. The data is from soft slab investigations and the dry snow is shown as black and the moist snow is in blue.

Dry and moist snow comparisons for an elevated charge height of 1.5 m again indicates the dry snow experienced greater acceleration as a result of an explosive detonation than moist snow. Acceleration values in the dry snow varied from 10 m/sec^2 to 25 m/sec^2 greater than the moist values. This variation is comparable to that of the 1 m elevated charge height. Similar to the other charge heights, the greatest difference is near, both vertically and radially, the detonation center. Contour shapes for the dry and moist snow show some variation as indicated in the contour plot of Figure 41.

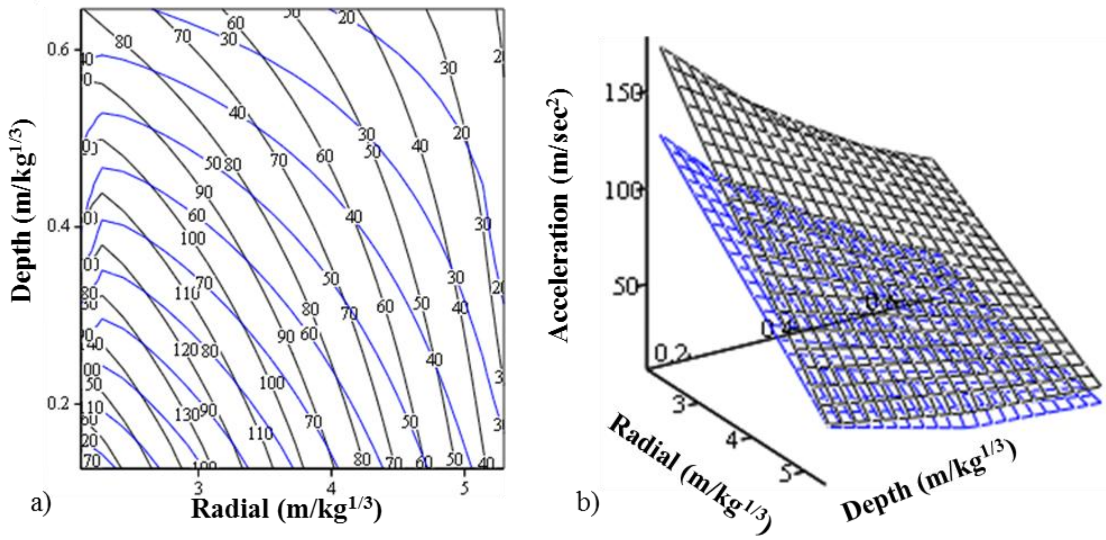

Figure 41 a) Contour and b) surface plots of average acceleration, due to 0.45 kg and 0.9 kg charge masses, as a function of radius and depth for detonations 1.5 m above the snow surface. The data is from soft slab investigations and the dry snow is shown as black and the moist snow is in blue.

In Figure 42, the acceleration for dry snow in response to a 2 m elevated charge detonation is greater than the response for moist snow conditions. The modeled surfaces, based on measured data, show greater acceleration of the dry snow at all locations. This result is the same as seen for charges elevated 0.5 m to 1.5 m above the snow surface. The 2 m elevated charge does indicate a greater spread between the two snow types than the previously examined elevated charge heights. The acceleration difference ranges from approximately 10 m/sec^2 to 50 m/sec^2. The greatest difference between the two snow types occurs in close proximity to the explosive. Dry and moist snow conditions resulted in similar contour shapes. This was also noted for 0.5 m-1 m charge elevations.

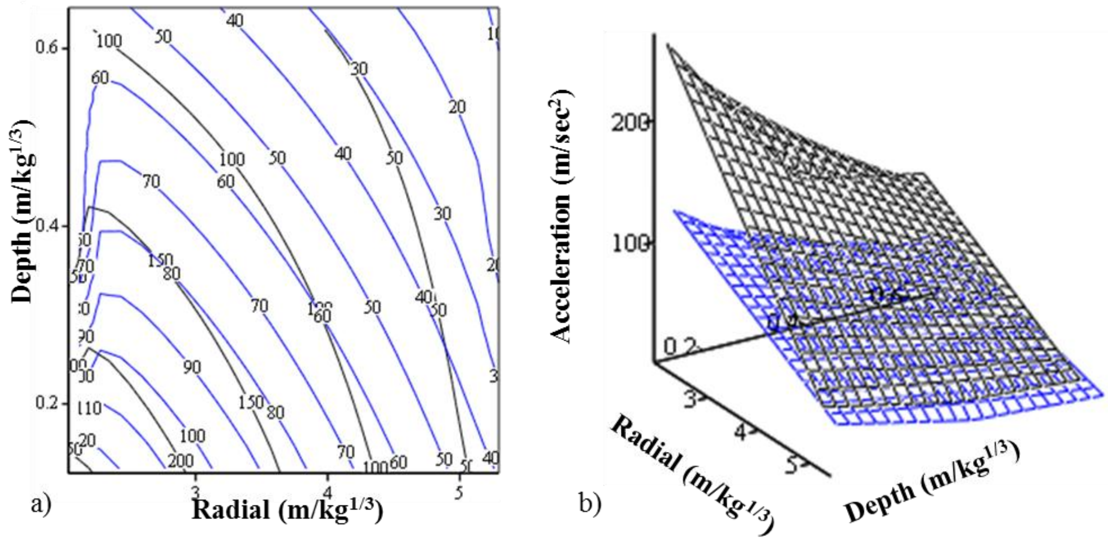

Figure 42 Contour and surface plots of average acceleration, due to 0.45 kg and 0.9 kg charge masses, as a function of radius and depth for detonations 2 m above the snow surface. The data is from soft slab investigations and the dry snow is shown as black and the moist snow is in blue.

Figure 38 to Figure 42 indicate that for the sensor locations investigated, dry snow conditions resulted in greater snow accelerations than moist snow conditions regardless of the charge placement. The trend is accentuated when close to the explosive and diminishes with increasing depth and radial distance. Peak overpressures were higher for moist snow, but the snowpack response was lower when compared to dry snow. Dry and moist snow contours exhibited the same general shape.

Comparison of Acceleration for 0.45 kg and 0.9 kg Charge Masses

During soft slab snow condition investigations, both 0.45 kg and 0.9 kg charge masses were detonated and the resulting dynamic snow responses were recorded. It was desired to determine the influence of explosive size on snow acceleration. Greater acceleration of the snow would presumably increase the effectiveness of avalanche mitigation work. In an effort to minimize the impact on acceleration response due to snow type, 0.45 kg and 0.9 kg charges were compared for the same test days only. This resulted in comparisons being made for 1 m and 2 m elevated charge heights. Data from the tests were used to create contour and surface plots, using MathCAD software, of acceleration response for the two charge masses. Sensor depths and radial distances were scaled to 1 kg TNT equivalents, as described in Data Processing. Due to distance scaling, it was expected to have similar acceleration from 0.45 kg and 0.9 kg charges at particular depths and ranges. To investigate this, contour and surface plots comparing the two charge sizes are shown in Figure 43 and Figure 44. The data points used and the individual surface and contour plots are found in Appendix L. Due to distance scaling, the data for the two charge sizes does not cover the exact same depth or radius. The surface plots show the relative difference between acceleration experienced due to the different charge sizes and the contour plots show the values

Contour and surface plots for the 1 m elevated charges are in Figure 43 and 2 m elevated charges in Figure 44. Two data series were combined for the 1 m elevated charge height, one data series for each charge mass. To solidify the preliminary results here, more data sets are needed. Currently, outlier data has a large impact on the analysis and possibly skew the data. As expected, the 0.9 kg charges resulted in greater acceleration than the 0.45 kg charges in close proximity to the explosive. Near the edge of the surface from the 0.9 kg data, the 0.45 kg charge acceleration is the same. Since this occurs at the edge of the data this may be an effect of the location. For locations where the 0.9 kg response is greater than the 0.45 kg charge, the difference is substantial. The

1 m elevated charge indicates an approximate difference of 10 m/sec^2-110 m/sec^2 while the 2 m charge height shows a 10 m/sec^2-170 m/sec^2 increase. In close proximity, doubling the explosive mass resulted in more than double the acceleration response. The plots indicate the acceleration response decreases with depth and range more rapidly for a 0.9 kg charge than 0.45 kg explosive. The input experienced by dry snow was less than moist snow, but the acceleration resultant was found to be greater. This indicates the shockwave travels from the air into the snow cover better for dry snow conditions than moist snow conditions. For dry and moist snow conditions, the findings from this project are in agreement with those by Gubler (1977). He noted that dry snow coupled well with air shockwaves while wet snow did not. Greater acceleration response is due to better coupling between the snow and air even though the overpressure for moist snow was greater. For a majority of the charge elevations investigated, while the contour

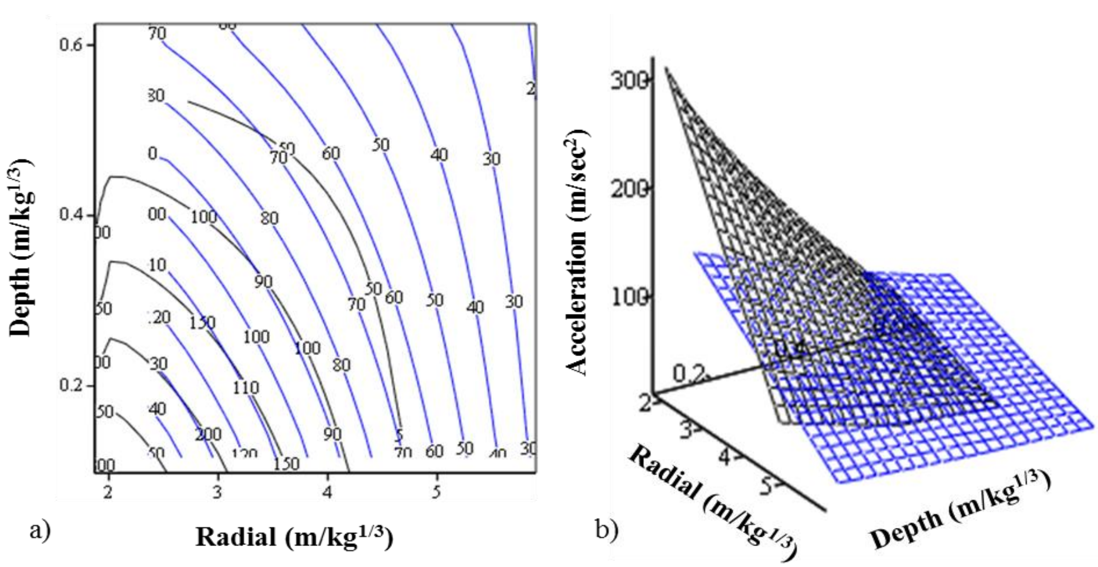

Figure 43 a) Contour plot and b) surface plot, showing comparison of acceleration response due to 0.9 and 0.45 kg charge mass detonations elevated 1 m above the soft slab snow surface. The black data series is for the 0.9 kg charge masses and the blue series is for the 0.45 kg charges.

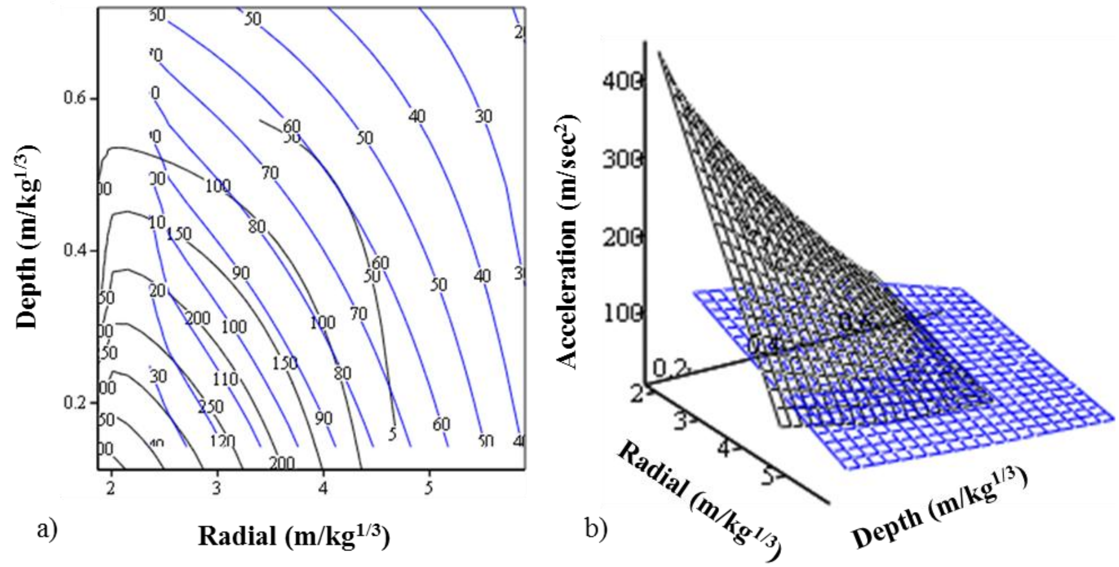

Figure 44 a) Contour plot and b) surface plot, showing comparison of acceleration response due to 0.9 and 0.45 kg charge mass detonations elevated 2 m above the soft slab snow surface. The black data series is for the 0.9 kg charge masses and the blue series is for the 0.45 kg charges.

The larger explosive mass and explosive energy yielding greater snow accelerations would be expected and is supported by the data. Figure 43 and Figure 44 show a 0.9 kg charge mass would be more beneficial than a 0.45 kg charge for avalanche mitigation work because the snow dynamic response was greater even at the same scaled distance. For an elevated charge height of 1 m the 0.9 kg charge acceleration was 20-80% greater than the 0.45 kg charge. At a 2 m elevated detonation the percent increase was found to be 20-130% greater for a 0.9 kg charge when compared to the response due to a 0.45 kg charge. For both charge heights investigated, the increase in acceleration resultant due to doubling the explosive mass was substantial.

Comparison of Acceleration in Soft Slab and Hard Slab Snow Conditions

Hard slab snow conditions typically present different avalanche mitigation hazards than soft slab snow. Therefore, a comparison of soft slab and hard slab test data was done in an attempt to determine the difference in acceleration response for the two snow types. Average peak acceleration data for the investigated charge heights were used in MathCAD to create individual surface and contour plots. The two snow types were combined and overlaid as shown in Figure 45 through Figure 48. The figures are created for moist snow conditions regardless of the snow slab type and scaled distances were used. The two data series do not cover identical ranges due to different sensor placement and different charge masses. For soft slab snow testing, the radial range of data was from 2.1-5.3 m/kg$^{1/3}$ and the vertical depths were from 0.11-0.57 m/kg$^{1/3}$ below the snow surface. For the hard slab snow condition testing season the plots cover from 2.8 m/kg$^{1/3}$ to 4.7 m/kg$^{1/3}$ radially and 0.2-0.76 m/kg$^{1/3}$ below the snow surface.

Surface charge detonations for the two seasons are not compared. In soft slab snow conditions, surface shots were only conducted when the snow was classified as dry. For the hard slab snow testing, the snow conditions always were moist. A comparison of data from the two years would not only be varying the hardness of the snow, but also the moisture content.

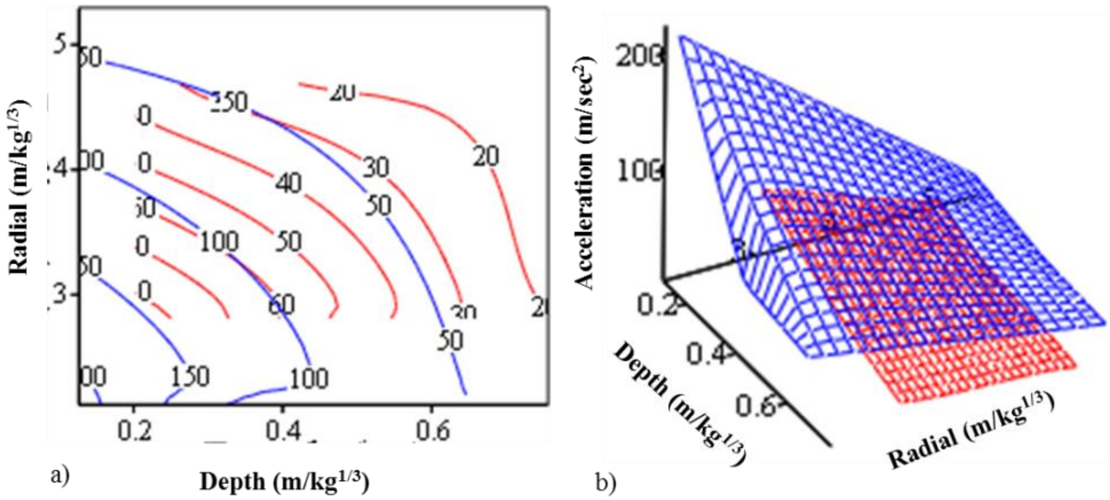

Figure 45 a) Contour and b) surface plot comparison of acceleration response due to an elevated charge height of 0.5 m in soft and hard slab snow conditions. The individual data series are from the two testing seasons, the response in soft slab snow conditions, is shown as the blue data series and the hard slab snow is shown in red.

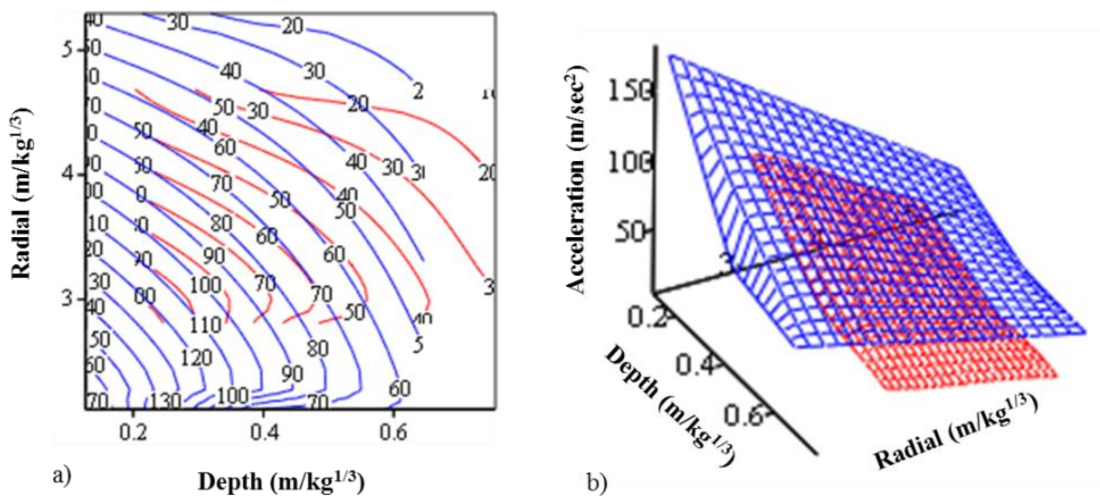

Figure 46 a) Contour and b) surface plot comparison of acceleration response due to an elevated charge height of 1.5 m in soft and hard slab snow conditions. The individual data series are from the two testing seasons, the response in soft slab snow conditions, is shown as the blue data series and the hard slab snow is shown in red.

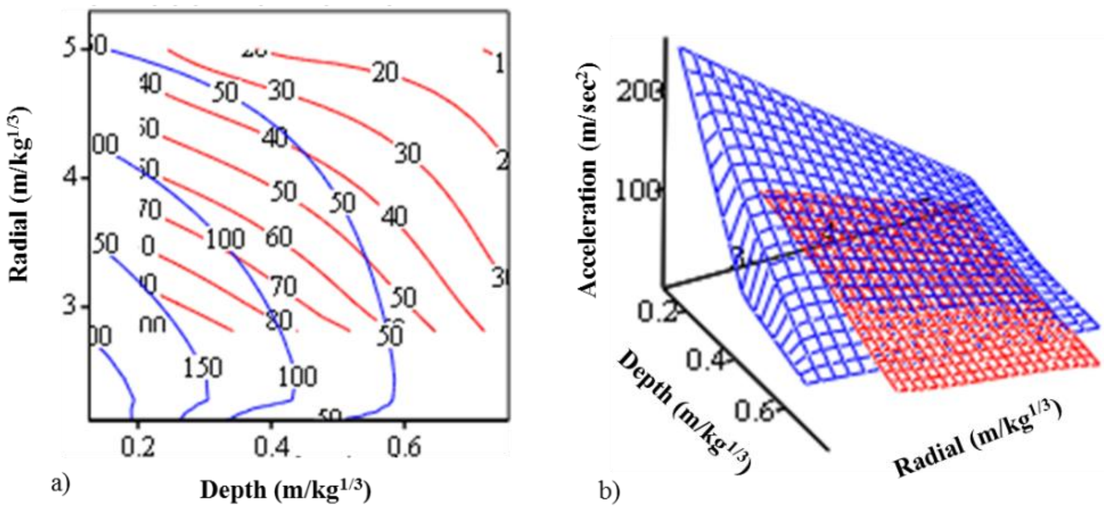

Figure 47 a) Contour and b) surface plot comparison of acceleration response due to an elevated charge height of 1.5 m in soft and hard slab snow conditions. The individual data series are from the two testing seasons, the response in soft slab snow conditions, is shown as the blue data series and the hard slab snow is shown in red.

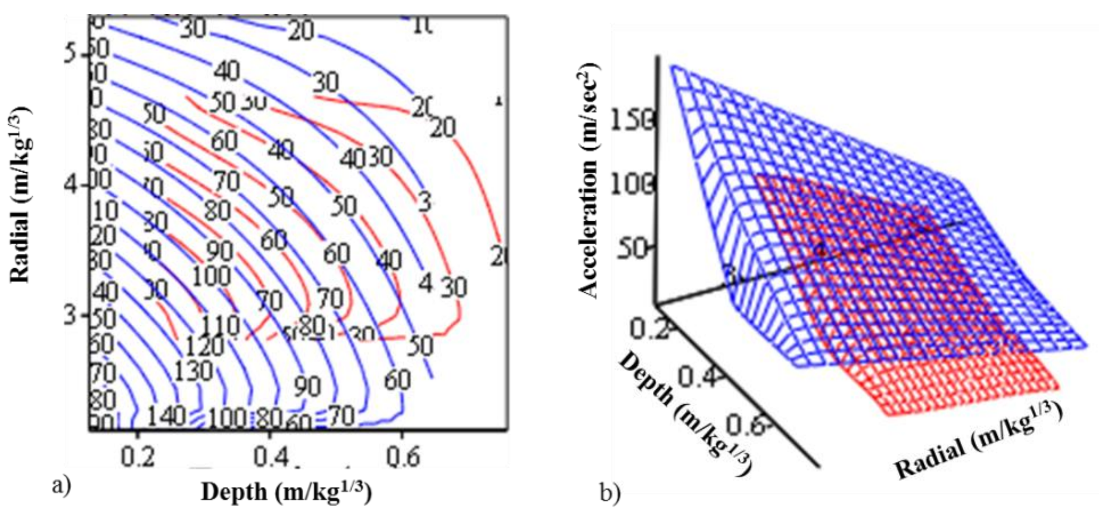

Figure 48 a) Contour and b) surface plot comparison of acceleration response due to an elevated charge height of 0.5 m in soft and hard slab snow conditions. The individual data series are from the two testing seasons, the response in soft slab snow conditions, is shown as the blue data series and the hard slab snow is shown in red.

A comparison of the contour and surface plots reveled the acceleration recorded in soft slabs generally was greater than the snowpack acceleration for hard slabs. Acceleration values indicate the soft slab snow was up to 130% greater than the hard slab snow as a result of a specific charge elevation above the snow surface. Examination of the contour shape for the two snow types indicate similarities between the two. This is to be expected because regardless of the type of snow, the geometric expansion of the shockwave is spherical. The spherical nature of shockwave expansion is indicated by the contours presented.

For a charge elevated 1.5 m, the two surfaces intersect giving the same response at particular locations. The intersection occurred near the bottom edge, with respect to depth, of the soft slab data. This may be a result of the area edge effects or the surfaces may truly intersect. During hard slab snow testing, one of the 1.5 m charge tests showed very high accelerations, an outlier data point and possibly enough to possibly skew the data resulting in the surface intersections.

Examination of the contour plots indicate the acceleration differences varied from ~ 20 m/sec^2 to 60 m/sec^2 for 0.5-2 m elevated charge heights. The greatest difference in acceleration occurred in close vicinity to the explosive detonation center. The 1 m and 2 m elevated charge heights gave the smallest variation in acceleration between the two snow types, 20 m/sec^{2}and 30 m/sec^2, respectively. From the limited quantity of data available, it is indicated that moist soft slab snow acceleration is greater than moist hard slab snow accelerations in response to pentolite cast booster detonations.

Lower acceleration values in hard slab snow indicates it would require a larger input to impact a weak layer located at the same depth or radial range from the explosive. The radial range and depth of influence for the same explosive in hard slab snow conditions would be less than in soft slab conditions. Persistent weak layers may develop and present more of an issue in hard slab snow more often than soft slab snow due to this. Johnson et al. (1994) stated the pressure wave primarily was transferred to into the snow through the air pores. A hard slab would generally be associated with high densities and would theoretically have little pore space and, therefore, transfer of the shockwave from the air into the snow may be limited. This would be in agreement with Johnson et al.'s determination.

Total Snow Water Equivalent Influence

On each testing day and location the snow depth was not consistent. It was desired to determine if the total snow depth at the sensor location impacted the acceleration experienced. The hypothesis was that for sensors at the same location, but a different total snowpack depth, the acceleration due to an explosive detonation would be different. The working assumption was that a deeper snowpack would have a decreased response because it would require more energy to initiate movement of the entire snowpack. To examine the impact of the total snow depth on acceleration response, total snow water equivalents (SWE) were computed for the sensor locations. The repeatability tests conducted on hard slabs from the 2011-2012 testing season were selected for comparison. While it was a similar snowpack for each test, the overall depths did vary. Total SWE was computed by multiplying the density at each layer by the height of that layer. The acceleration at two radial distances were plotted as a function of total SWE. The 3 m radial distance is shown in Figure 49 and the 5 m radial distance is in Figure 50.

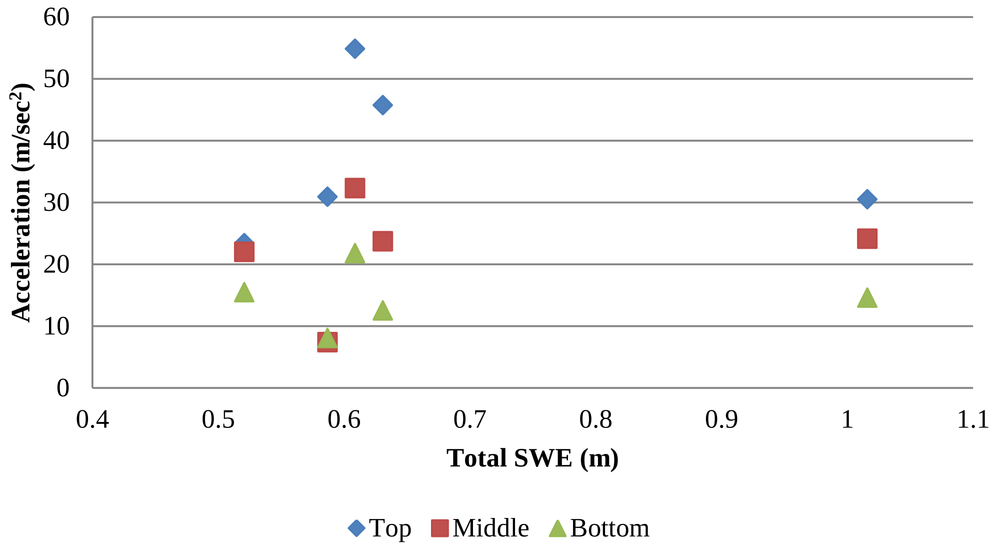

Figure 49 Peak acceleration resultants as a function of total SWE for the tests conducted for test repeatability purposes. Each accelerometer depth at 3 m radial distance is represented as a separate data series. The explosives were 0.9 kg pentolite cast boosters and were detonated 1 m above the snow surface.

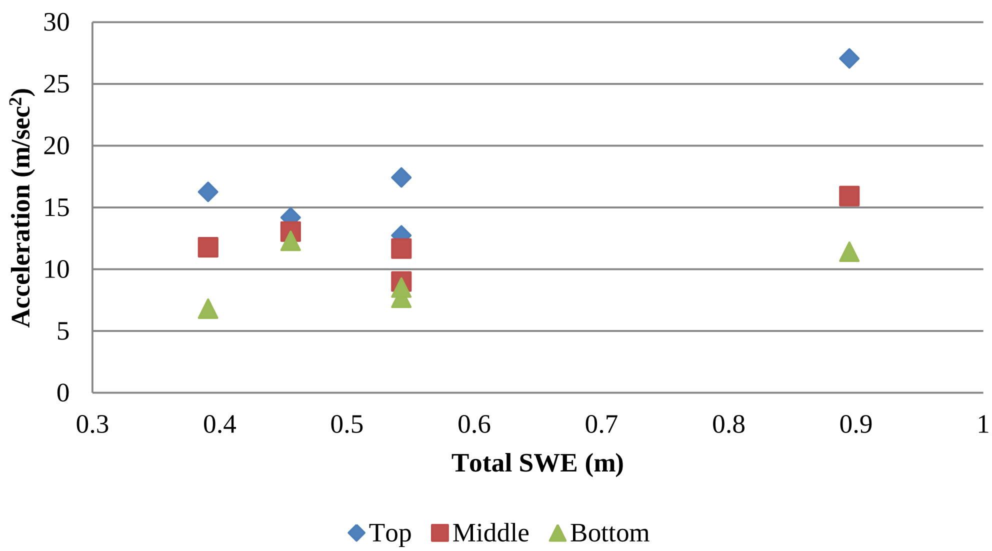

Figure 50 Peak acceleration resultants as a function of total SWE for the tests conducted for test repeatability purposes. Each accelerometer depth at 5 m radial distance is represented as a separate data series. The explosives were 0.9 kg pentolite cast boosters and were detonated 1 m above the snow surface.

Figure 49 and Figure 50 indicate no strong dependence between the total SWE at the sensor location and the peak acceleration resultant response. This finding directly conflicts with what was expected, but was determined from only five tests on a single day. The findings may indicate the explosive creates motion in the top layers independent of the entire of the snowpack when the snowpack is deep.

Since acceleration did not indicate a relationship to the total snow water equivalent at the sensor location, the attenuation was compared to the total SWE. Again, data from the test repeatability day was used to remove as many other snow factors as possible. The vertical attenuation, determined from power law fitting of the data, was used. Figure 51 shows acceleration as a function of sensor depth; therefore, the power exponent *d* is for the attenuation in the vertical dimension. Examination of Figure 51 indicates no definitive relationship between power exponent and total SWE.

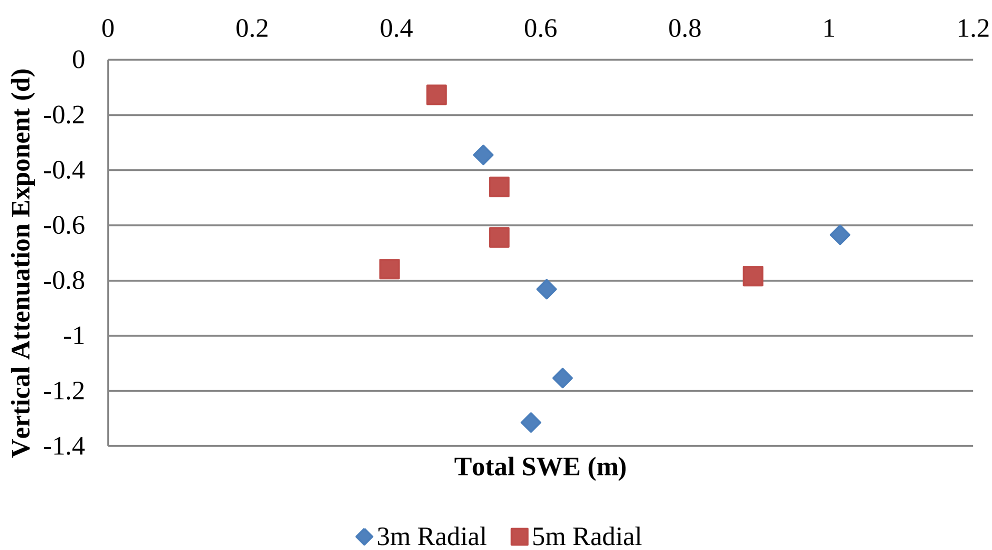

Figure 51 Vertical attenuation, exponent *d*, versus total SWE. Exponents at 3 m radial distance are shown as the blue data series and the red series is for 5 m radial distance. The data used to determine the attenuation and SWE is from test repeatability investigations.

The shockwave radial attenuation for the top accelerometers was compared to the total SWE as well. Since the above investigations did not indicate a correlation to total SWE, this was not expected to yield different results. Figure 52 confirms that there is no correlation between the radial attenuation and total SWE. The total SWE was determined by averaging the total SWE at the 3 m and 5 m radial distances. Only the top layer of accelerometer attenuation is shown since there is no correlation between the attenuation and total SWE.

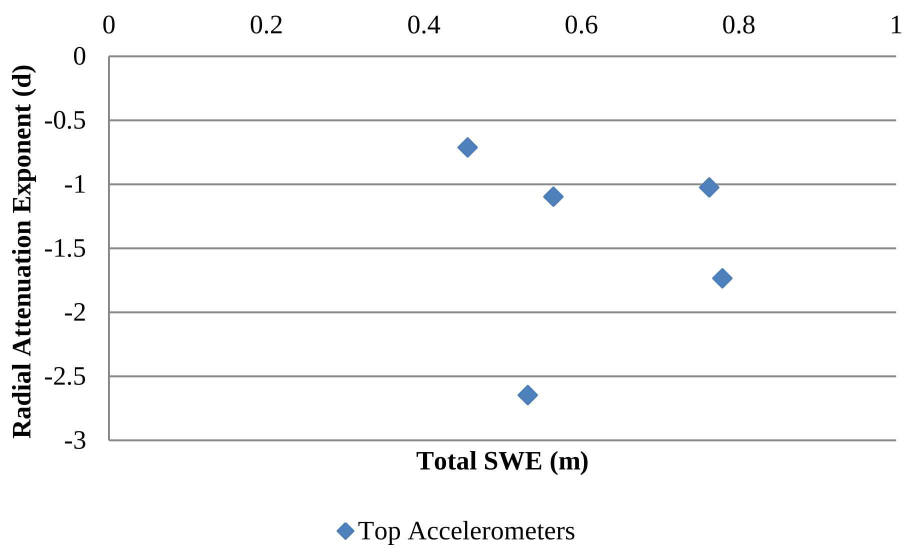

Figure 52 Comparison of radial attenuation at the top accelerometers as a function of total SWE. The attenuation and total SWE are for the test repeatability day conducted in the 2011-2012 testing season.

From examination of acceleration, vertical, and radial attenuation as functions of total SWE there does not appear to be any significant correlation between acceleration or attenuation and the total SWE. It should be noted these determinations are the result of five tests conducted on a single day. To confirm the findings, more test days with one charge configuration should be conducted. A lack of correlation between the quantities investigated was not expected, but did occur. This indicates the total snowpack SWE, may not influence the snowpack acceleration or the attenuation of the shockwave resulting from explosive detonations.

Average Snowpack Density Influence

From the above analysis, the total snowpack water equivalent did not influence the acceleration resultant of the snowpack or the attenuation of the shockwave attenuation. This lead to an examination of the average snowpack density. Average density for the snowpack per day was calculated. The acceleration resultant for each charge elevation was plotted as a function of the test day average snow density. An example is shown in Figure 53 for all explosives detonated 1 m above the snow surface. The 1 m charge elevation was chosen because this elevation had the largest data set. Other charge heights are included in Appendix M.

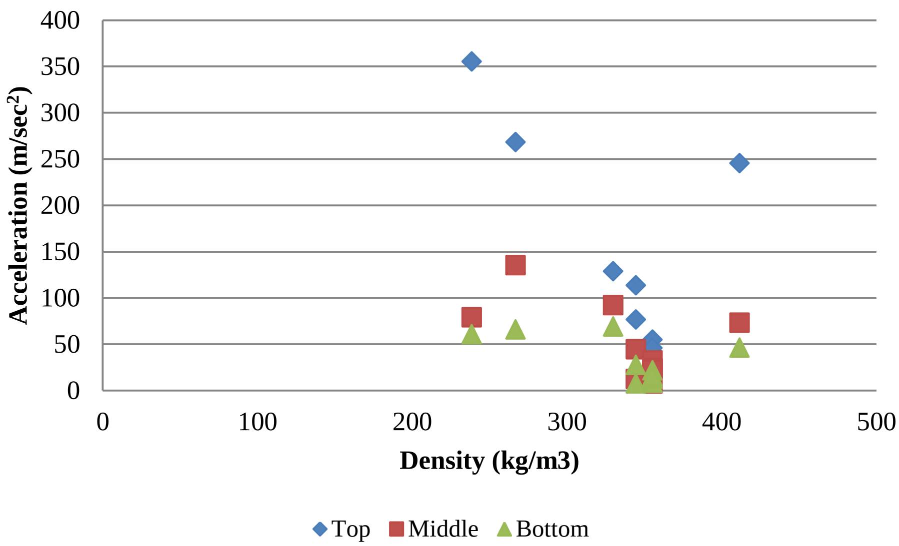

Figure 53 Acceleration resultant as a function of average snow density for all charges detonated 1 m above the snow surface. The acceleration resultant is shown for the top, middle, and bottom accelerometer locations as separate data series.

In Figure 53 there is not a significant correlation between the acceleration and the snow density. This result was not expected. Previously the acceleration and attenuation were shown to vary on different days indicating a snow characteristic is influencing the acceleration response. From this analysis though, the density does not appear to be the characteristic influencing the acceleration.

Due to there being no apparent relationship between acceleration resultant and snow density; the vertical attenuation for 1 m elevated charges as a function of density was determined and shown in Figure 54. From this figure, the vertical attenuation does not have a correlation to the average snow density for the testing day.

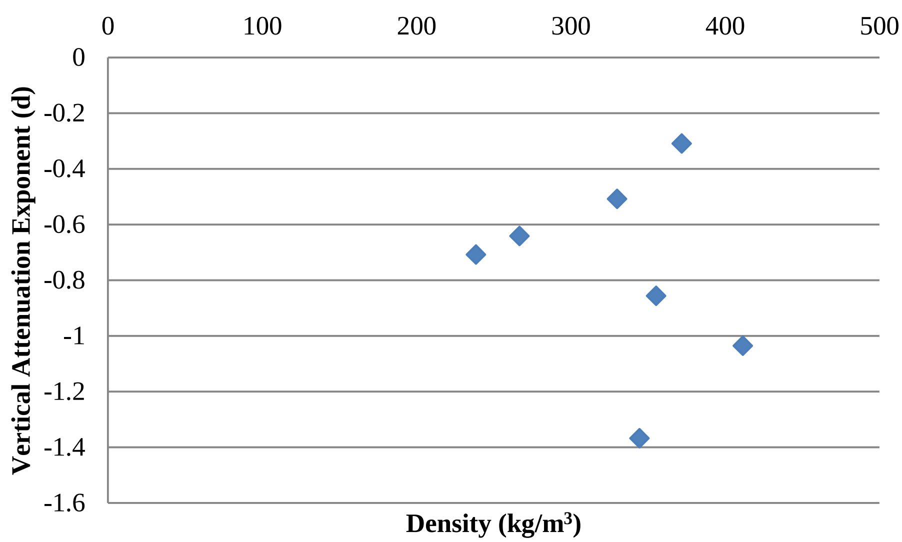

Figure 54 Vertical attenuation as a function of the snow density for individual testing days for explosives detonated 1 m above the snow cover.

There being no dependence of acceleration resultant or vertical attenuation on the snow density was unexpected. There is a snow characteristic influencing the dynamic snow response, but exactly what it is cannot be determined from the data gathered in this project.

Position Change of Snowpack Due to Detonation

Two dimensional position vectors were calculated from the acceleration data via double integration as detailed in the previous Data Processing chapter. Snowpack displacement is important for avalanche mitigation work. Greater relative displacement results in greater strain and therefore stress experienced by the snowpack, possibly resulting in failure of weak layers. The maximum displacements calculated were exceedingly small, on the order of millimeters or less. There were no obvious weak layers present in the snowpacks tested, so small displacement values were expected. The displacement in the vertical direction was greater than in the radial direction. This follows from the vertical component of acceleration being greater than the radial direction, and was expected. Figure 55 and Figure 56 show examples of vertical and radial components of position due to an explosive detonation. The initial radial displacement is positive and the vertical displacement negative due to directional sensor placement.

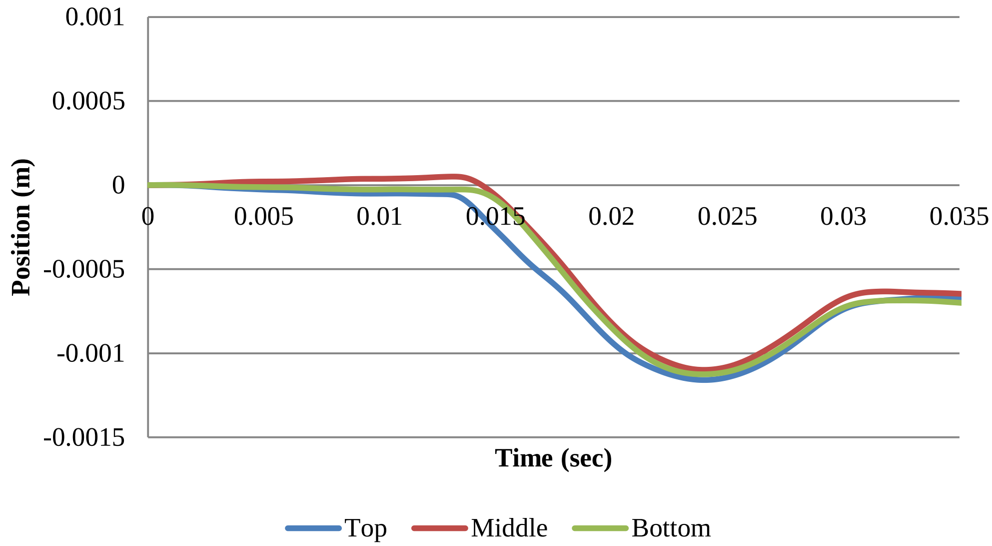

Figure 55 Vertical displacement at 2 m radial distance resulting from a soft slab snow investigation with the charge detonated 0.5 m above the snowpack. From the top to the bottom accelerometer the displacement experienced was 1.19 mm, 1.17 mm, and 1.18 mm.

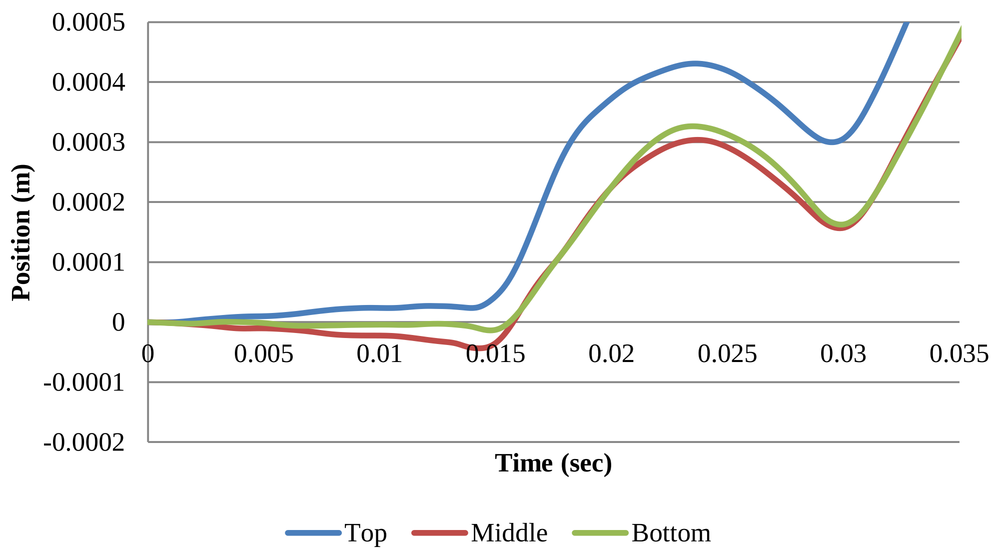

Figure 56 Example of snowpack position in the radial direction as recorded 2 m radially from a 0.5 m elevated charge in soft slab snow conditions. This is for the same test shown in Figure 55. The displacements were: 0.40 mm, 0.30 mm, and 0.31 mm from top to bottom.

From the displacement figures, examples in Figure 55 and Figure 56, the accelerometers experienced permanent displacement, shown by not returning to zero. Not returning to zero displacement could be due to multiple reasons. If the sensors rotated during testing, gravity would be recorded as residual acceleration leading to displacement. The noise associated with the accelerometers would increase due to double integration and contribute to the displacement not returning to zero. The velocity values also did not fully return to zero confirming that integration of noise is included in the position data. From the data available, determining the displacement of the snow independently of extraneous additions to displacement is not possible. Some tests indicated displacement oscillation of the snowpack, as seen in Figure 57.

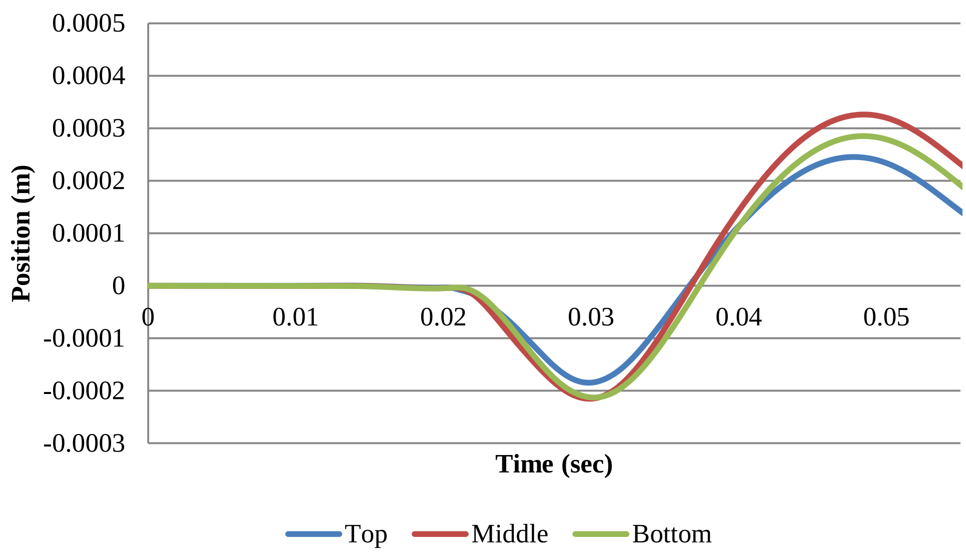

Figure 57 Vertical position as a function of time for a 0.45 kg charge detonated 1 m above the soft snow surface. The sensors are located 5 m radially from the blast and the displacement shows an oscillatory response.

The position of the snowpack is directly related to the acceleration and time duration of the acceleration as illustrated by the above figures. The displacement experienced by the snow was very small. It is important to bear in mind, weak layers were not present within the snowpack that could result in large movements. The displacement recorded was due to the snowpack moving and deformation of the ice crystals as a result of the explosive detonations.

Shock Reflection Off Ground Surface

One of the testing locations utilized during the 2011-2012 testing season consisted of a long rock rib that created a good hard slab drift. The snow depth for a couple of the tests was between .9-1 m deep at the sensor locations. In these tests, the vertical direction of acceleration showed a reflection off the ground surface. This was evidenced by greater positive than negative accelerations in the vertical direction. Not only is the initial positive portion of the acceleration due to reflection of the wave off the bed surface, but also the expected rebound due to unloading and the elastic nature of snow. The bottom accelerometer positive rebound peaked prior to the middle and top accelerometers, also indicating the rebound. Figure 58 shows the acceleration values for one such test. The three different depths of sensors show the reflection phenomenon. The total snow depth for this test at the accelerometer location shown in the figure was 0.98 m deep. Shockwave reflection was not present in all tests, but the tests with shallow depths compared to the sensor placed in greater snowpack depths did.

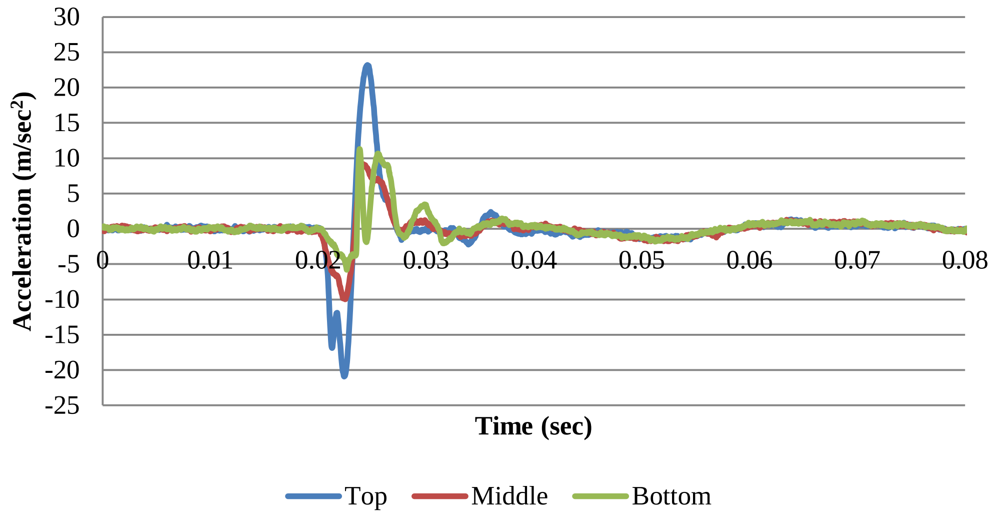

Figure 58 Example of data showing acceleration values in the upward direction greater than the downward due to shockwave reflection off the bed surface. This data was taken 3 m radially from a surface detonation in hard slab snow conditions for a 0.9 kg charge.

SUMMARY

To examine the snowpack's response to explosive detonations, multiple goals were established. The first goal of this research project was to develop a self-contained, field portable system capable of measuring air overpressure and snowpack acceleration due to explosive detonations. This was accomplished by determining the most appropriate componentry and fabricating the system. A combination of overpressure sensors and dual-axis accelerometers in conjunction with a signal routing box, data acquisition system and laptop computer comprised the testing setup.

The second goal was to determine correlations between the explosive detonations to the resulting overpressure and impulse values. Overpressure graphs showed a rapid increase in pressure, when the shockwave reached the sensor, then decreasing pressure as the wave passed and finally a negative backpressure before the pressure returned to ambient. The overpressure values were examined to determine the impact of snow characteristics and charge location on the overpressure and impulse. Regardless of the detonation elevation, moist snow conditions correlated with greater overpressure than dry snow. Examination of the overpressure values obtained at the snow air interface indicated elevated charges resulted in larger overpressures than surface detonations. For charges elevated 1-2 m above the snow surface, the increase was at least 1.1 psi for 0.9 kg charges and 0.7 psi for 0.45 kg charges. Greater overpressure values indicate greater input to the snow. For both 0.45 kg and 0.9 kg charges, the optimum elevated charge height appeared to be around 1.5 m. Pressure impulse (positive and negative) also indicated greater values for moist than dry snow conditions and an increase with elevated

charge height. A comparison of the overpressure values for 0.45 kg and 0.9 kg charges indicated the relationship between charge mass and overpressure or impulse was not linear. Doubling the mass of explosive (0.45 kg to 0.9 kg) resulted in a 20-75% increase in overpressure and 60% increase in impulse were observed.

It also was of interest to determine the difference between the overpressure and impulse at the snow surface and 1.5 m above at the same radial range. For charges detonated 1 m above the snow surface, the pressure at the snow air interface was greater than 1.5 m above the snow for a radial range of 7 m. Surface data indicated a 25% increase over the elevated overpressure values. The pressure difference illustrates the snow surface reflection of the shockwave. Greater variability in the surface pressures than the elevated values indicated the surface characteristics influenced the overpressure recorded at the interface. Irrespective of the snow characteristics, all overpressure values indicated higher pressures than predicted for open air blasts. The percent increase varied from 15-80% based on different radial ranges, snow characteristics, and explosive masses. The gathered data allowed for characterization of relationships between the overpressure, snow attributes, and explosive characteristics.

The final goal of the project was to characterize the snowpack dynamic response due to an explosive blast. Specifically, the test setup was tested for repeatability and the data was analyzed to determine potential correlations between the dynamic snow response, detonation size and location, and snow characteristics. The acceleration data showed a rapid transient response followed by an oscillatory damped response due to the explosive detonations. Test repeatability was evaluated and used to determine that the field testing method was appropriate and repeatable. The impact on the snowpack acceleration as a result of elevating an explosive was analyzed in several ways. Calculating percent increase in acceleration as the charge was raised 0.5-2 m showed at least 5% and up to a 100% increase. Generally, a 1-2 m elevated charge indicated the greatest percent increase. The percent increase was larger in moist hard slab than dry soft slab snow conditions. The acceleration increase was largest both vertically and radially, in close proximity to the explosive. The top accelerometers showed 1.5 times the increase in acceleration due to raising the explosive than the bottom accelerometers. Acceleration at 2 m radial distance increased on average approximately 1.35 times the acceleration increase at 5 m radial distance. These values illustrate that the increase in acceleration was greatest close to the explosive. Raising an explosive resulted in a deeper impact within the snowpack and at larger radial ranges, evidenced by greater acceleration response at the same sensor location.

To verify the increased volume of influence, the relationship between attenuation of the shockwave within the snow cover and charge placement was investigated. The volume of influence only would be greater if there was not an increase in attenuation due to elevating the explosive. The charge location relative to the snow surface was shown, through power law fitting resultant acceleration data, to not influence the attenuation in the vertical or radial directions, regardless of the snow type. The vertical attenuation at 2 or 3 m from the explosive, depending on the testing season and sensor placement, was essentially the same as at 5 m; signifying the vertical attenuation is independent of the radial distance for the radial ranges investigated. The average vertical attenuation in soft slab snow was -0.57 and -1.01 in hard slab snow. The input to the snow at a single radial distance is the same for all locations at that range. Since the accelerometer locations for determining the vertical attenuation are in a vertical plane, the primary reason for the attenuation within the snowpack is due to snow interactions and the geometric wave expansion plays less of a role. The radial attenuation calculated for specific accelerometer depths was similar. Thus, indicating the radial attenuation is independent of depth, for the depths investigated.

The geometric expansion of the shockwave contributed to the radial attenuation being greater than the vertical attenuation. Hard slab snow showed greater vertical (56%) and radial (12%) attenuation than soft slab snow did. Moist snow was shown to increase the vertical attenuation and decrease the radial attenuation, indicated by the comparison of attenuation in moist and dry soft slab snow conditions. Moist snow decreased the radial attenuation because of increased shock reflection as shown by the overpressure data. Not only was the attenuation from power law data regression investigated, but values of the leading coefficient were analyzed. The leading coefficients indicated greater acceleration resultants due to elevating the explosive. Coupling the increased snowpack acceleration as a result of elevating an explosive with attenuation being insensitive to charge height is extremely applicable to avalanche mitigation work. Avalanche mitigation work relies on overloading a weakness within the snowpack. Therefore, influencing the largest volume of snow with a greater load increases the likelihood of impacting a weak layer. The volume of influence for a single charge can be increased by detonation occurring above the snow surface.

The next objective in characterizing the snow response to explosives focused on different snow and explosive characteristics. Results between specific snow classifications were compared to determine the difference in response based on snow type. The dynamic snow response recorded in moist snow was less than that recorded in dry snow conditions, irrespective of the charge height, ranging from 0.5-2 m. The greatest difference in response occurred near the explosive in both the vertical and radial directions. A maximum difference of 50 m/sec^2 or 35% was noted. The air overpressure values indicated a greater input to the snow, but the acceleration response is less. These two findings suggest less of the shockwave is transferred to moist snow than dry snow. A comparison of responses due to 0.45 kg and 0.9 kg charge masses showed the larger mass was associated with greater snow cover acceleration. A larger amount of explosive energy should strengthen the resulting shockwave. The relationship between mass and acceleration was not linear, for charges elevated 1 m, the acceleration increased 20-80% by doubling the mass. An acceleration increase of 20-130% was noted for doubling the explosive mass when the charges were placed 2 m above the snow. Soft and hard slab snow conditions were also compared. The soft slab snow showed greater acceleration than the hard slab snow with an equivalent charge. This finding indicates the shockwave couples with the soft slab snow better than with the hard slab snow.

The total snow water equivalent at the sensor location did not show a correlation to the snowpack acceleration or vertical and radial attenuation. This was shown for both 3 m and 5 m radial distance along with the top layer accelerometers. Snowpack acceleration, vertical and radial attenuation as a function of average snowpack density also did not indicate a correlation regardless of the explosive location. The lack of correlations suggests the total snowpack depth and density does not influence the dynamic snow response or the attenuation of the response. Displacement of the snowpack was small, millimeters or less, but snowpack permanent displacement did occur.

For shallow snowpacks with a rock bed surface, the shockwave was shown to reflect off the bed surface. Similar snowpack depths with an underlying meadow did not significantly demonstrate this response. This phenomenon was indicated by the positive rebound vertical component of acceleration being greater than the initial response as well as the bottom accelerometer rebound peaking prior to the other accelerometers. This may indicate the effectiveness of an explosive detonated above a shallow snowpack is increased from increased snow dynamic response due to the shock reflection from a hard bed surface.

Possible Future Work

This project illustrated a current data collection system capable of recording overpressure and dynamic snow response due to explosive detonations. While the findings of this research project are insightful, more research needs to be conducted to further characterize the interactions that occur between the snowpack and explosive detonations. For example, a larger data set would be beneficial in definitively defining relationships. Having the same number of tests for a particular snow type and charge elevation would reduce data scatter. Additional sensors to gather data at the same radial distances and depths but at another location on the arc to be averaged would also reduce the acceleration response scatter. Using the same radial distance and depths for all tests would result in easier data comparisons. To better determine the amount of shockwave reflection, the overpressure sensors should be located at the same radial distance regardless of the snow type. To diminish the impact of different snow types when comparing various charge masses, the same test matrix should be repeated varying the charge size for a given day. Conducting a detailed daily snowpit for classification of the snow type would allow for further determination of the influence of snow characteristics on the response to explosives.

REFERENCES CITED

Abromeit, D. 2010. Inbounds incidents & fatalities 2008/9. Avalanche Review 28 (3), 26.

Atwater, M. 1968. Avalanche hunters. Macrae Smith Company, Philadelphia.

Austiguy Jr., G. and Brown, R. 1993. Application of a mixture theory to stress waves in snow. Annals of Glaciology 18, 274-80.

Beer, F.P. and Johnston Jr, E.R. 1996. Vector mechanics for engineers. McGraw-Hill, New York, NY.

Binger, C., Nelsen, J. and Olson K.A. 2006. Explosive shock wave compression in snow: effects of explosive orientation and snowpack compression. 2006 International Snow Science Workshop, Telluride, CO.

Brown, R.L. 1981. A method for evaluating shockwave propagation in snow. Cold Regions Science and Technology 5, 151–156.

Brown, R.L.1980. An analysis of non-steady plastic shock waves in snow. Journal of Glaciology 25 (92), 279-287.

Chapra, S. C. 2005. Applied numerical methods with MATLAB. McGraw-Hill, New York, NY.

Cooper, P.W., 1996. Explosives Engineering. Wiley-VCH, New York Chichester Weinheim Brisbane Singapore Toronto.

Ferrari, M. 2010. Post-control avalanches: definition, history, causes and the future. 2010 International Snow Science Workshop, Squaw Valley, CA.

Frigo, B., Chiaia, B., Giraudi, A., Godio, A., and Rege, R. 2010. Experimental analysis of snowpack effects induced by blasts. 2010 International Snow Science Workshop, Squaw Valley, CA.

Fuchs, A. 1957. Effects of explosives on snow. US Army Snow Ice and Permafrost Research Establishment Corps of Engineers Special Report 23.

Furnish, M.D., Boslough, M.B., 1996. Measuring Hugoniot, reshock and release properties of natural snow and stimulants. Sandia National Laboratory Report, SAND92-0985, UC-703.

Gubler, H., 1977. Artificial release of avalanches by explosives. Journal of Glaciology 19 (81), 419–429.

Hansen, A. C., and R. L. Brown. 1987. The role of fracture in the attenuation rate of stress waves in snow. Cold Regions Science and Technology 13, 207-212.

Ingram, L.F., 1962. Air blast in an Arctic Environment. US Army Waterways Experiment Station, Vicksburg ,MS, Technical Report, pp. 2–399.

ISEE. 1998. Blasters' Handbook, 17th ed. International Society of Explosive Engineers, Cleveland.

Joachim, C.E., 1967. Shock transmission through ice and snow. US Army Waterways Experiment Station, Vicksburg, MS, Technical Report, pp. 1–794.

Johnson, J.B. 1982. On the application of biot's theory to acoustic wave propagation in snow. Cold Regions Science and Technology 6, 49-60.

Johnson, J.B., Solie, D.J., 1993. Shock Response of Snow. Journal of Applied Physics 73 (10), 4852–4861.

Johnson, J.B., Solie, D.J., Barrett, S.A., 1994. The response of a seasonal snow cover to explosive loading. Annals of Glaciology 19, 49–54.

Juergens, J. 1984. Practical experience with aerial detonation of explosives for avalanche control. 1984 International Snow Science Workshop, Aspen, CO.

Kinney, G.F., Graham, K.J., 1985. Explosive shocks in air. Springer-Verlag, Berlin Heidelberg New York Tokyo.

LaChapelle, E. 1977. Snow avalanches: a review of current research and applications. Journal of Glaciology 19 (81), 313-24.

Lang, T.E. 1976. Measurements of acoustic properties of hard-pack snow. Journal of Glaciology 17 (76), 269-276.

Livingston, C.W. 1968. Explosions in snow. US Army Material Command Cold Regions Research & Engineering Laboratory Technical Report, 86.

Machida, T., Minjiao, L., Kamiishi, I., Sato, A., Machida, M., and Hayakawa, N. 2008. A basic study on technology of inducing artificial avalanche by explosive detonations inside the snowpack. 2008 International Snow Science Workshop, Whistler, BC.

McClung D. and Schaerer, P. 2006. The avalanche handbook. The Mountaineers Books, Seattle, WA.

Mellor, M. and Smith, N. 1967. Airblast attenuation at low overpressures. US Cold Regions Research and Engineering Laboratory Technical Note.

Mellor, M., 1985. Blasting and blast effects in cold regions Part 1: air blast. US Army Cold Regions Research & Engineering Laboratory Special Report, 85–25.

Mellor,M., 1973. Controlled release of avalanches by explosives. Symposium on Advances in Avalanche Technology, Reno, NV. US Forest Service Technical Report RM-3, pp. 37–49.

Miller, DA, RG Tichota, and EE Adams. 2011. An explicit numerical model for the study of snow's response to explosive air blast. Cold Regions Science and Technology 69, 156-64.

Perla, R. 1976. High explosives and artillery in avalanche control. 1976 Banff Avalanche Workshop, Banff, AB.

Perla, R. 1978. Artificial release of avalanches in north America. Arctic and Alpine Research 10 (2), 235-240.

Powell, K. 2000. Precision blasting techniques for avalanche control. 2000 International Snow Science Workshop, Big Sky, MT.

Sherwood, G. L. 2000. Discussion of the directional characteristics of explosives commonly used in avalanche hazard reduction. 2000 International Snow Science Workshop, Big Sky, MT.

Solie,D.J., Johnson, J.B. and Barrett, S.A. 1993 The response of natural snow to explosive shock waves. American Institute of Physics. 1993. High-Pressure Science and Technology.

Ueland, J., 1992. Effects of explosives on the mountain snowpack. 1992 International Snow Science Workshop, Breckenridge, CO.

Wisotski, J., Snyer, W.H., 1966. A study of the effects of snow cover on high explosive blast parameters. University of Denver, Denver Research Institute, CO: Final Report, 2303.

APPENDICES

APPENDIX A

DAILY TESTING SNOWPIT DATA

1.17.11 Soft Slab Snowpit Data
Total snow depth 0.9 m

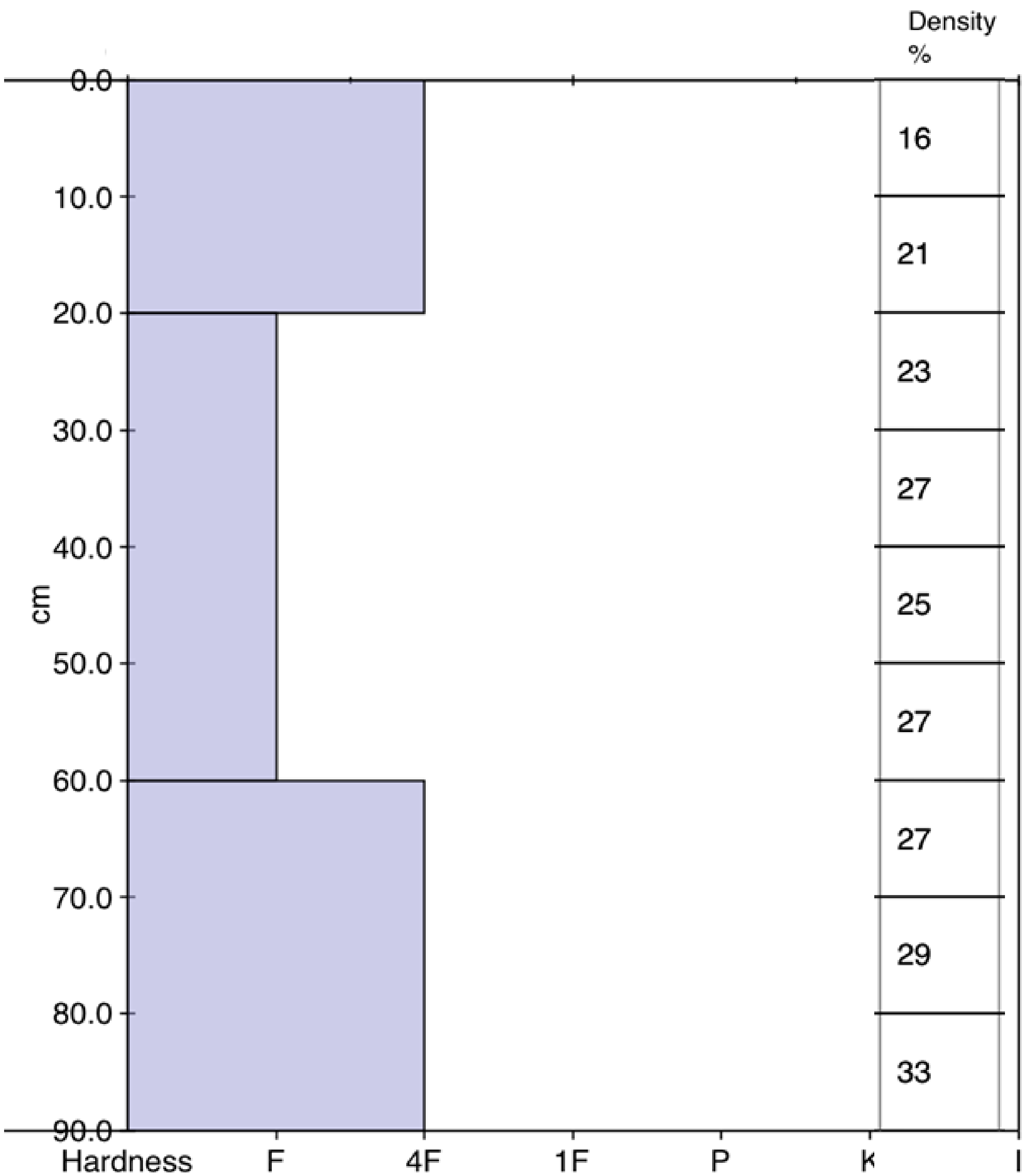

3.3.11 Soft Slab Snowpit Data
Total snow depth 0.86 m

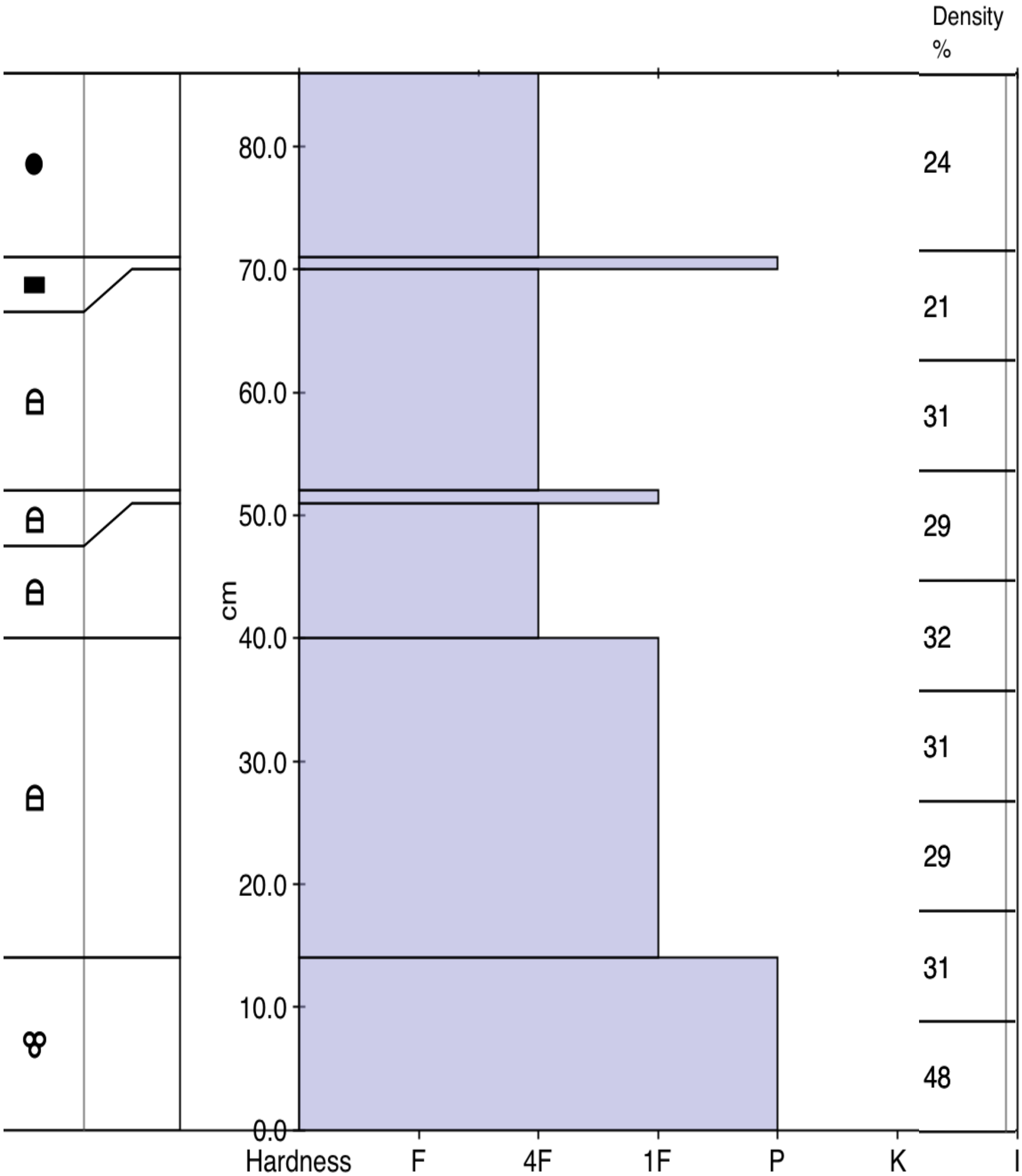

3.3.11 Soft Slab Snowpit Data
Total snow depth 0.86 m

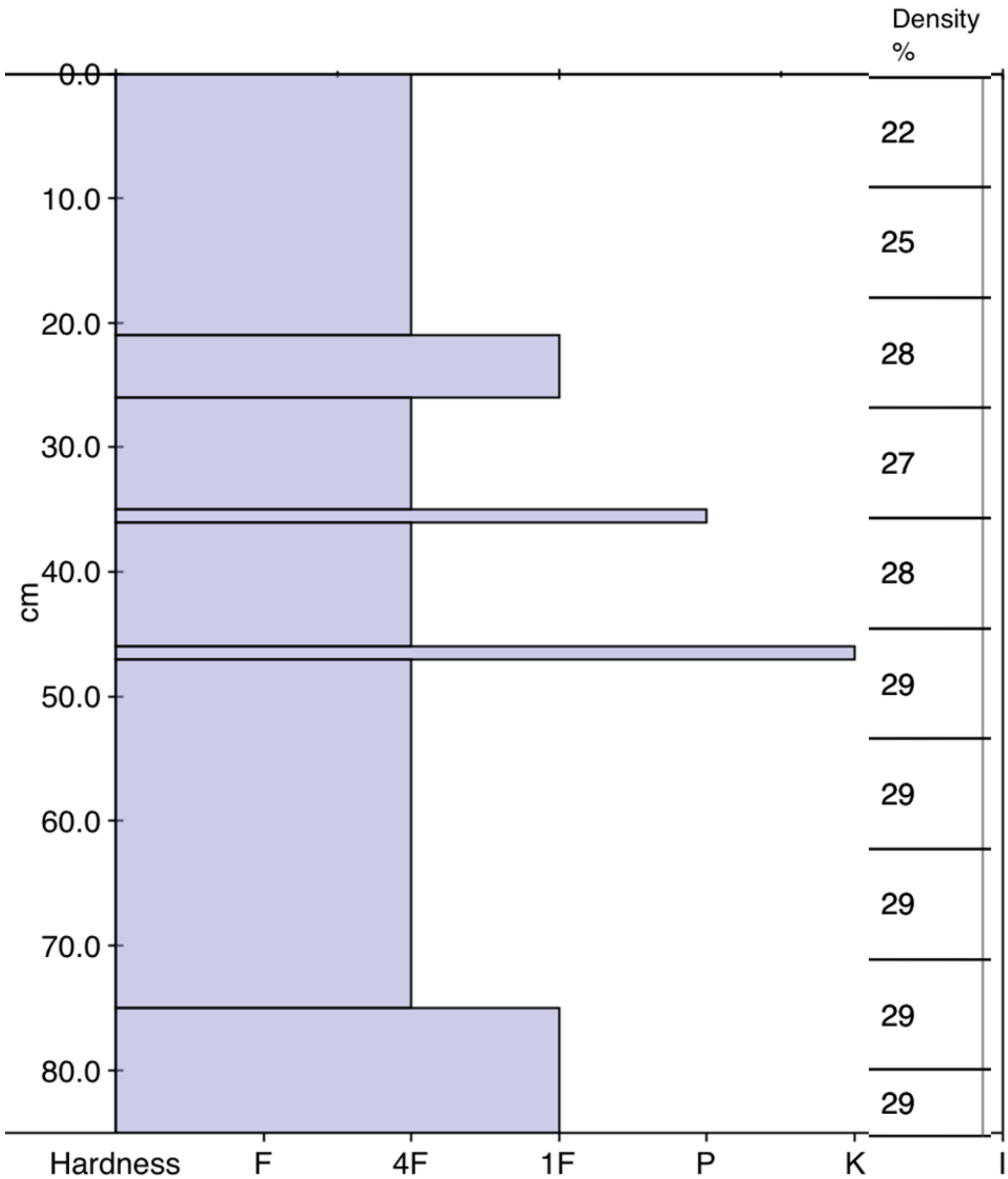

4.12.11 Soft Slab Snowpit Data
Total snow depth 1.47 m

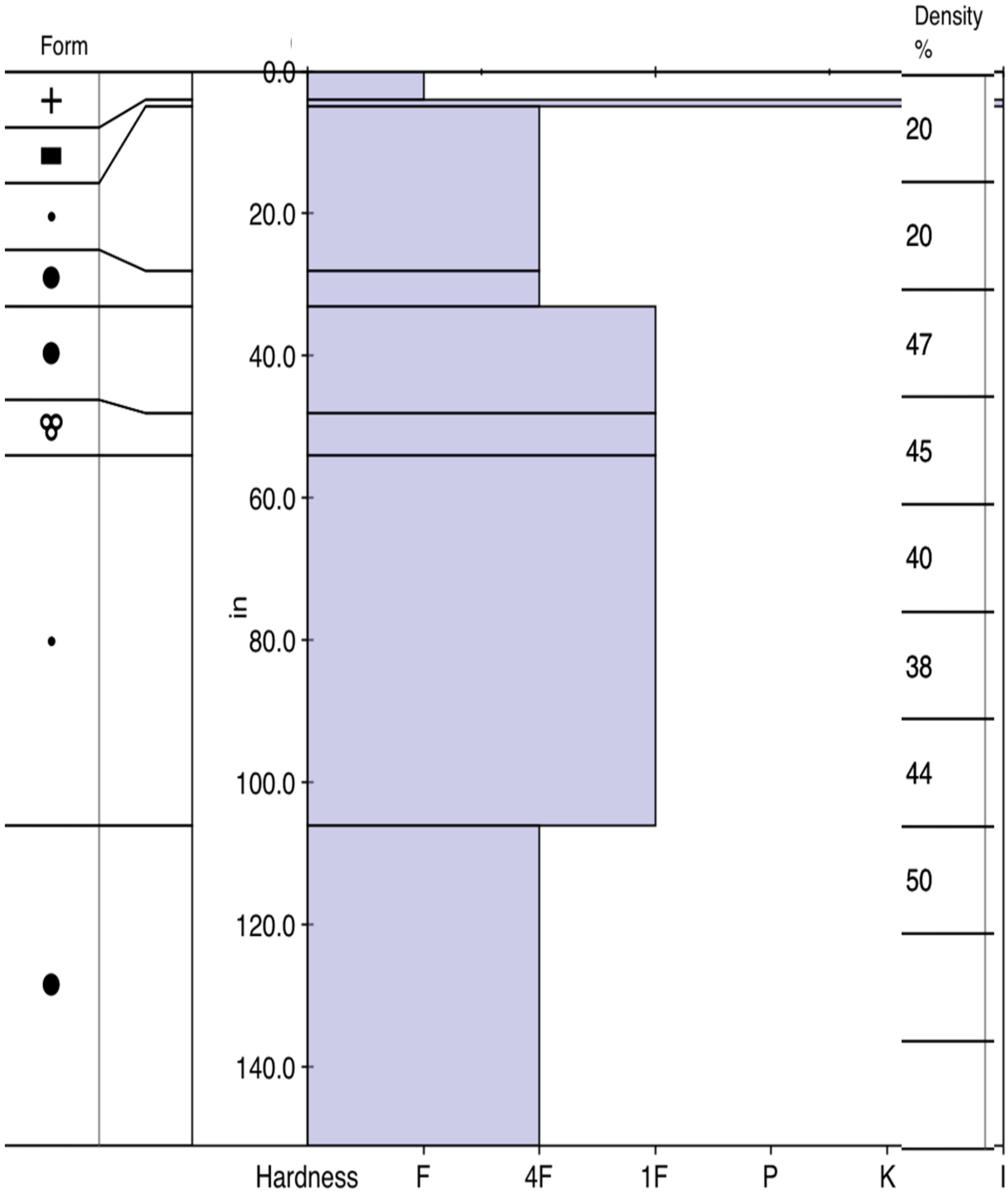

4.28.11 Soft Slab Snowpit Data
Total snow depth 1.75 m

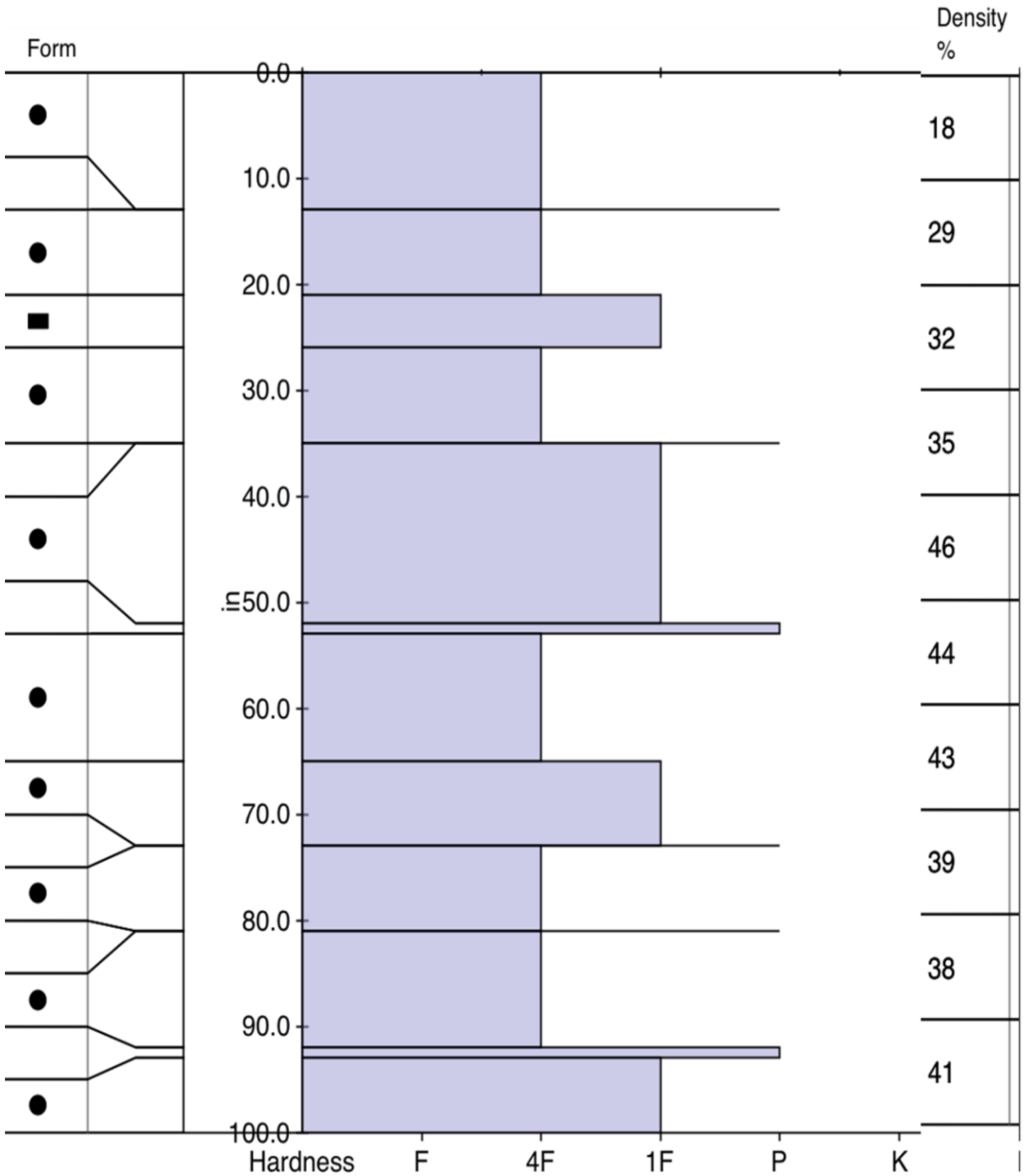

3.16.12 Hard Slab Snowpit Data
Total snow depth > 5 m

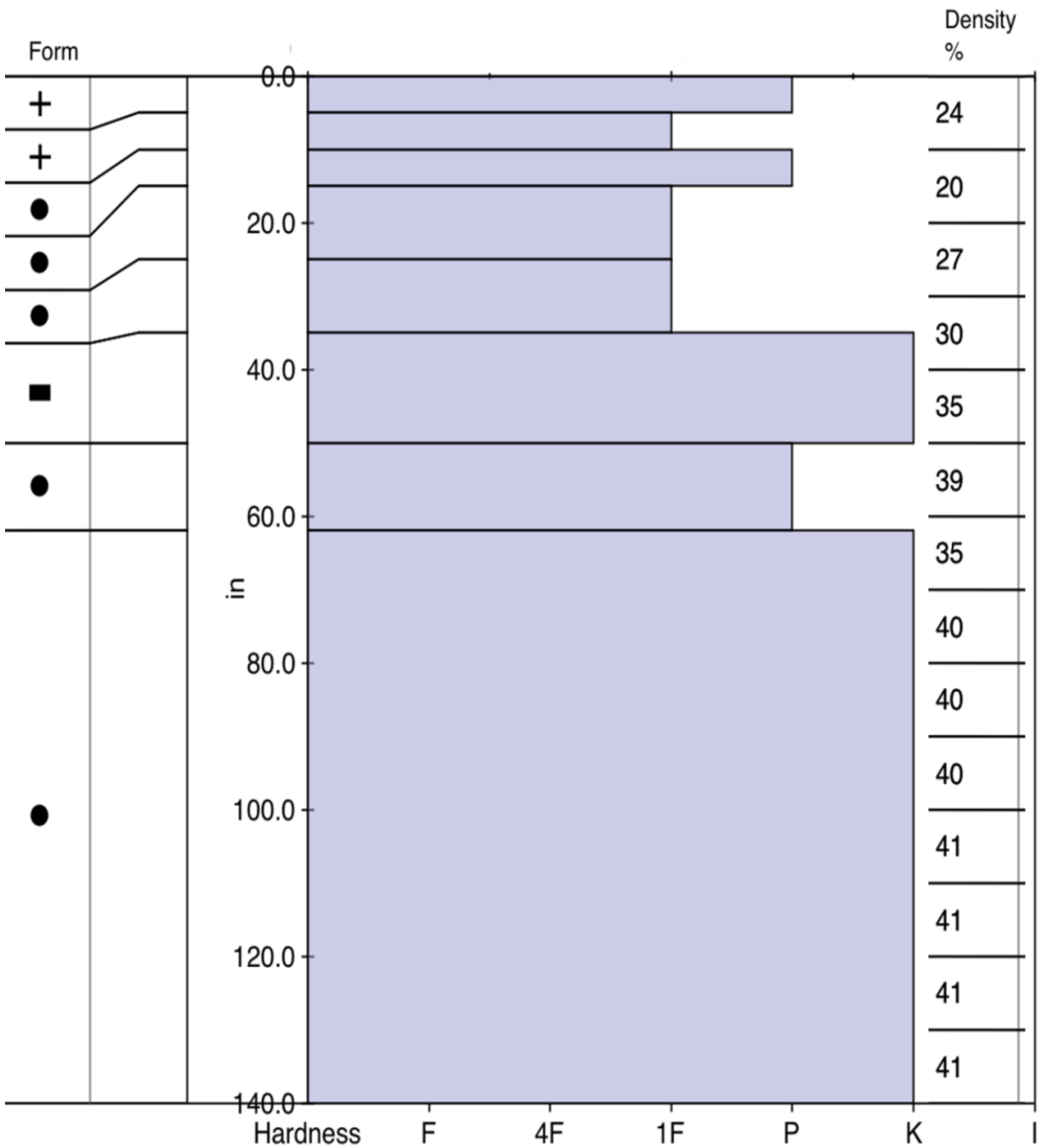

3.27.12 Hard Slab Snowpit Data
Total snowpack depth 3.35 m

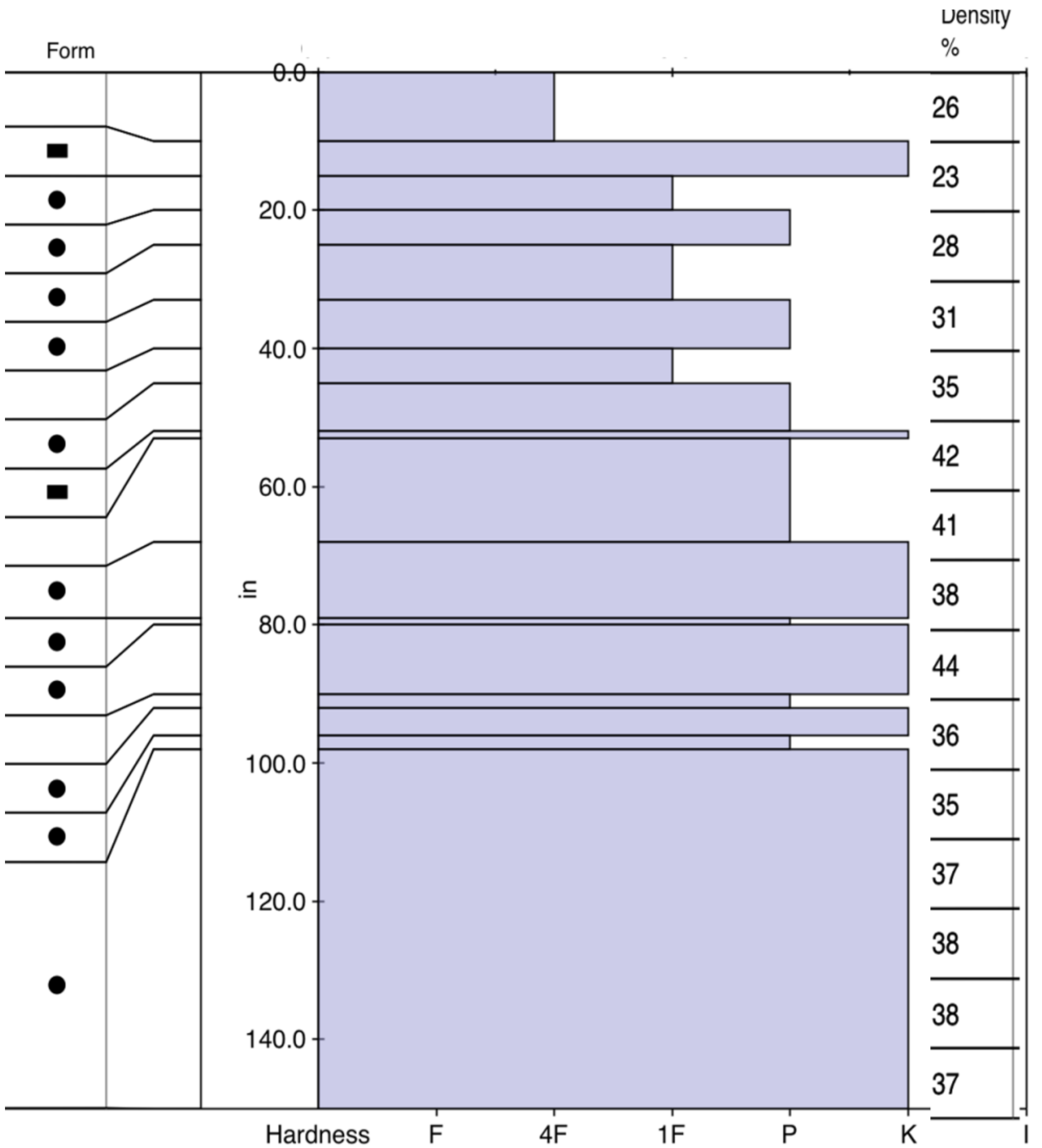

4.8.12 Hard Slab Snowpit Data
Total snow depth 3.55 m

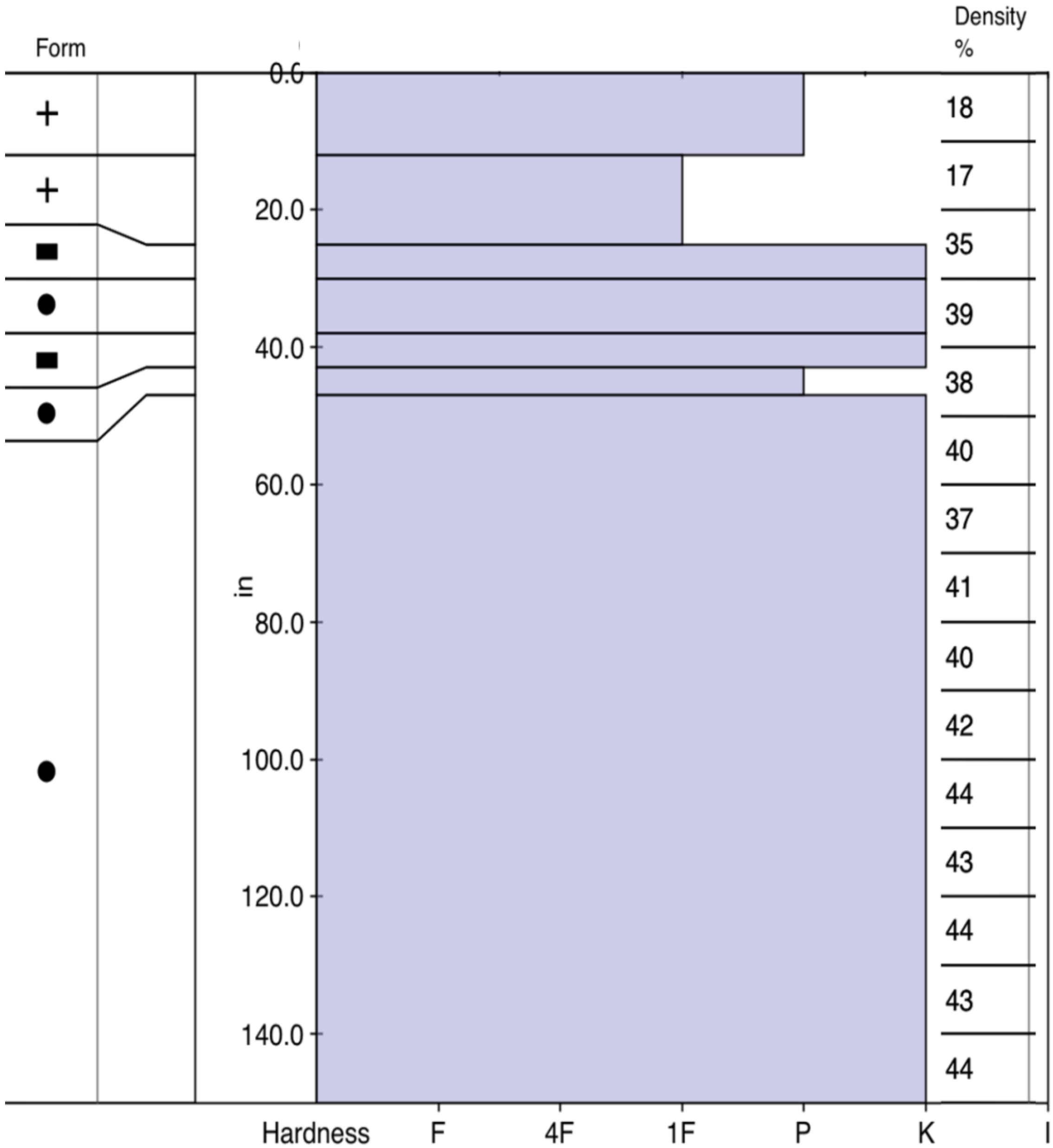

APPENDIX B

ACCELEROMETER DATA SHEETS

ANALOG DEVICES

Small and Thin ±18 *g* Accelerometer

ADXL321

FEATURES

Small and thin
4 mm × 4 mm × 1.45 mm LFCSP package
3 m*g* resolution at 50 Hz
Wide supply voltage range: 2.4 V to 6 V
Low power: 350 μA at V_S = 2.4 V (typ)
Good zero *g* bias stability
Good sensitivity accuracy
X-axis and Y-axis aligned to within 0.1° (typ)
BW adjustment with a single capacitor
Single-supply operation
10,000 *g* shock survival
Compatible with Sn/Pb and Pb-free solder processes

APPLICATIONS

Vibration monitoring and compensation
Abuse event detection
Sports equipment

GENERAL DESCRIPTION

The ADXL321 is a small and thin, low power, complete dual-axis accelerometer with signal conditioned voltage outputs, which is all on a single monolithic IC. The product measures acceleration with a full-scale range of ±18 *g* (typical). It can also measure both dynamic acceleration (vibration) and static acceleration (gravity).

The ADXL321's typical noise floor is 320 μ*g*/√Hz, allowing signals below 3 m*g* to be resolved in tilt-sensing applications using narrow bandwidths (<50 Hz).

The user selects the bandwidth of the accelerometer using capacitors C_X and C_Y at the X_{OUT} and Y_{OUT} pins. Bandwidths of 0.5 Hz to 2.5 kHz may be selected to suit the application.

The ADXL321 is available in a very thin 4 mm × 4 mm × 1.45 mm, 16-lead, plastic LFCSP.

FUNCTIONAL BLOCK DIAGRAM

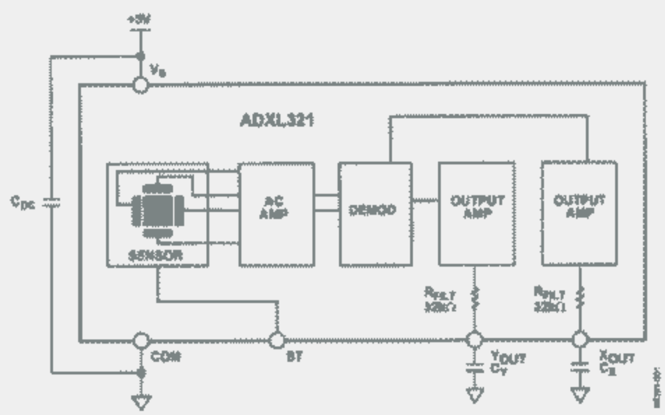

Figure 1.

Rev. 0
Information furnished by Analog Devices is believed to be accurate and reliable. However, no responsibility is assumed by Analog Devices for its use, nor for any infringements of patents or other rights of third parties that may result from its use. Specifications subject to change without notice. No license is granted by implication or otherwise under any patent or patent rights of Analog Devices. Trademarks and registered trademarks are the property of their respective owners.

One Technology Way, P.O. Box 9106, Norwood, MA 02062-9106, U.S.A.
Tel: 781.329.4700 www.analog.com
Fax: 781.326.8703

TABLE OF CONTENTS

REVISION HISTORY

12/04—Revision 0: Initial Version

SPECIFICATIONS[1]

$T_A = 25°C$, $V_S = 3$ V, $C_X = C_Y = 0.1$ μF, Acceleration = 0 *g*, unless otherwise noted.

Table 1.

Parameter	Conditions	Min	Typ	Max	Unit
SENSOR INPUT	Each axis				
Measurement Range			±18		*g*
Nonlinearity	% of full scale		±0.2		%
Package Alignment Error			±1		Degrees
Alignment Error	X sensor to Y sensor		±0.1		Degrees
Cross Axis Sensitivity			±2		%
SENSITIVITY (RATIOMETRIC)[2]	Each axis				
Sensitivity at X_{OUT}, Y_{OUT}	$V_S = 3$ V	51	57	63	mV/*g*
Sensitivity Change due to Temperature[3]	$V_S = 3$ V		0.01		%/°C
ZERO *g* BIAS LEVEL (RATIOMETRIC)	Each axis				
0 *g* Voltage at X_{OUT}, Y_{OUT}	$V_S = 3$ V	1.4	1.5	1.6	V
0 *g* Offset vs. Temperature			±2		m*g*/°C
NOISE PERFORMANCE					
Noise Density	@ 25°C		320		μ*g*/√Hz rms
FREQUENCY RESPONSE[4]					
C_X, C_Y Range[5]		0.002		10	μF
R_{FILT} Tolerance			32 ± 15%		kΩ
Sensor Resonant Frequency			5.5		kHz
SELF-TEST[6]					
Logic Input Low			0.6		V
Logic Input High			2.4		V
ST Input Resistance to Ground			50		kΩ
Output Change at X_{OUT}, Y_{OUT}	Self-test 0 to 1		18		mV
OUTPUT AMPLIFIER					
Output Swing Low	No load		0.3		V
Output Swing High	No load		2.6		V
POWER SUPPLY					
Operating Voltage Range		2.4		6	V
Quiescent Supply Current			0.49		mA
Turn-On Time[7]			20		ms
TEMPERATURE					
Operating Temperature Range		−20		+70	°C

[1] All minimum and maximum specifications are guaranteed. Typical specifications are not guaranteed.
[2] Sensitivity is essentially ratiometric to V_S.
[3] Defined as the change from ambient-to-maximum temperature or ambient-to-minimum temperature.
[4] Actual frequency response controlled by user-supplied external capacitor (C_X, C_Y).
[5] Bandwidth = $1/(2 \times \pi \times 32\ k\Omega \times C)$. For C_X, C_Y = 0.002 μF, bandwidth = 2500 Hz. For C_X, C_Y = 10 μF, bandwidth = 0.5 Hz. Minimum/maximum values are not tested.
[6] Self-test response changes cubically with V_S.
[7] Larger values of C_X, C_Y increase turn-on time. Turn-on time is approximately $160 \times C_X$ or C_Y + 4 ms, where C_X, C_Y are in μF.

ABSOLUTE MAXIMUM RATINGS

Table 2.

Parameter	Rating
Acceleration (Any Axis, Unpowered)	10,000 *g*
Acceleration (Any Axis, Powered)	10,000 *g*
V_S	−0.3 V to +7.0 V
All Other Pins	(COM − 0.3 V) to (V_S + 0.3 V)
Output Short-Circuit Duration (Any Pin to Common)	Indefinite
Operating Temperature Range	−55°C to +125°C
Storage Temperature	−65°C to +150°C

Stresses above those listed under Absolute Maximum Ratings may cause permanent damage to the device. This is a stress rating only; functional operation of the device at these or any other conditions above those indicated in the operational section of this specification is not implied. Exposure to absolute maximum rating conditions for extended periods may affect device reliability.

ESD CAUTION

ESD (electrostatic discharge) sensitive device. Electrostatic charges as high as 4000 V readily accumulate on the human body and test equipment and can discharge without detection. Although this product features proprietary ESD protection circuitry, permanent damage may occur on devices subjected to high energy electrostatic discharges. Therefore, proper ESD precautions are recommended to avoid performance degradation or loss of functionality.

WARNING!

PIN CONFIGURATION AND FUNCTION DESCRIPTIONS

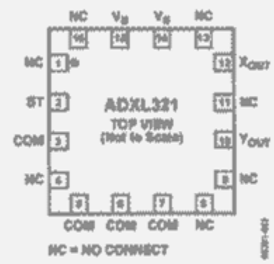

Figure 2. Pin Configuration

Table 3. Pin Function Descriptions

Pin No.	Mnemonic	Description
1, 4, 8, 9, 11, 13, 16	NC	Do Not Connect
2	ST	Self-Test
3, 5 to 7	COM	Common
10	Y_{OUT}	Y Channel Output
12	X_{OUT}	X Channel Output
14, 15	V_S	2.4 V to 6 V

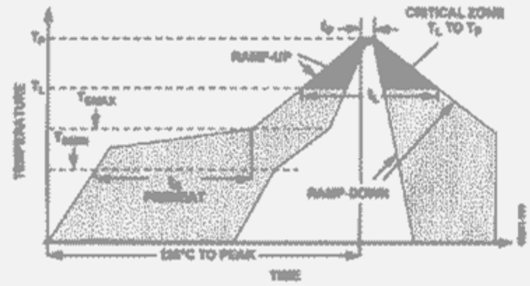

Figure 3. Recommended Soldering Profile

Table 4. Recommended Soldering Profile

Profile Feature	Sn63/Pb37	Pb-Free
Average Ramp Rate (T_L to T_P)	3°C/s max	3°C/s max
Preheat		
Minimum Temperature (T_{SMIN})	100°C	150°C
Minimum Temperature (T_{SMAX})	150°C	200°C
Time (T_{SMIN} to T_{SMAX}), t_S	60 s – 120 s	60 s – 150 s
T_{SMAX} to T_L		
Ramp-Up Rate	3°C/s	3°C/s
Time Maintained Above Liquidous (T_L)		
Liquidous Temperature (T_L)	183°C	217°C
Time (t_L)	60 s – 150 s	60 s – 150 s
Peak Temperature (T_P)	240°C + 0°C/–5°C	260°C + 0°C/–5°C
Time within 5°C of Actual Peak Temperature (t_P)	10 s – 30 s	20 s – 40 s
Ramp-Down Rate	6°C/s max	6°C/s max
Time 25°C to Peak Temperature	6 min max	8 min max

TYPICAL PERFORMANCE CHARACTERISTICS (V_S = 3.0 V)

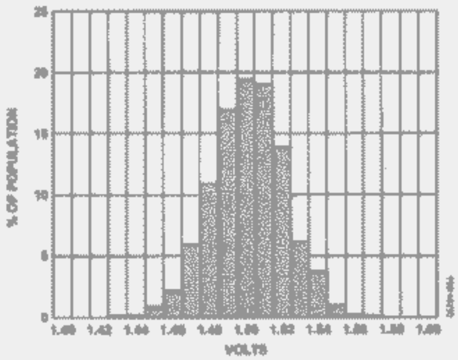

Figure 4. X-Axis Zero g Bias at 25°C

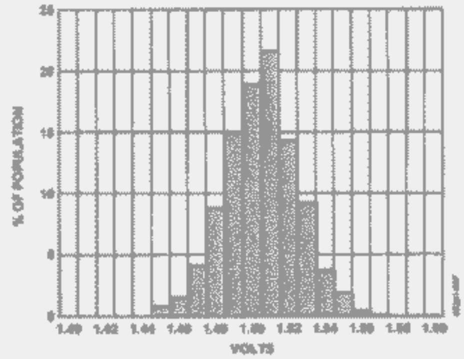

Figure 7. Y-Axis Zero g Bias at 25°C

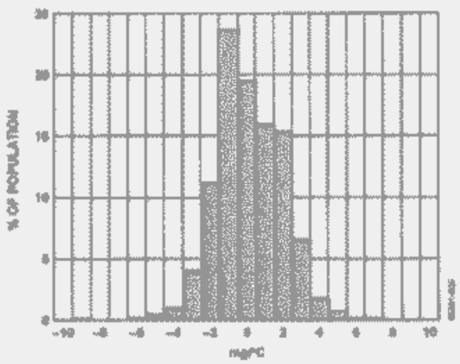

Figure 5. X-Axis Zero g Bias Temperature Coefficient

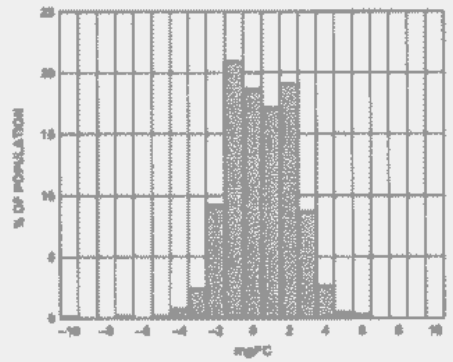

Figure 8. Y-Axis Zero g Bias Temperature Coefficient

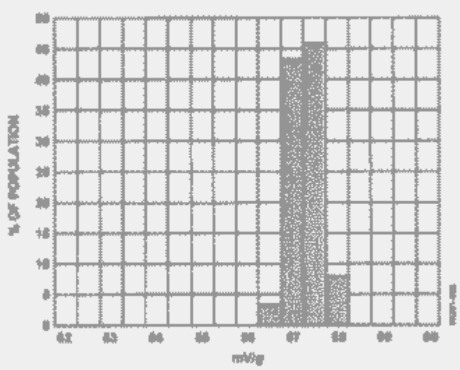

Figure 6. X-Axis Sensitivity at 25°C

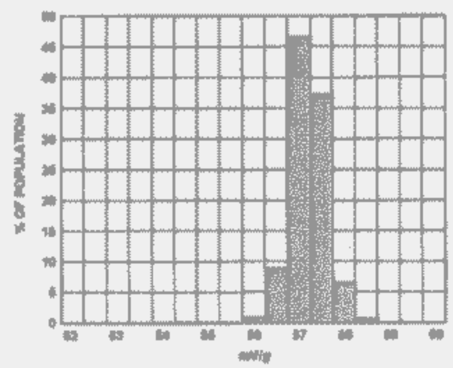

Figure 9. Y-Axis Sensitivity at 25°C

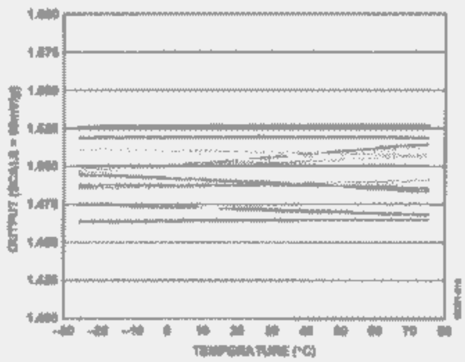

Figure 10. Zero g Bias vs. Temperature—Parts Soldered to PCB

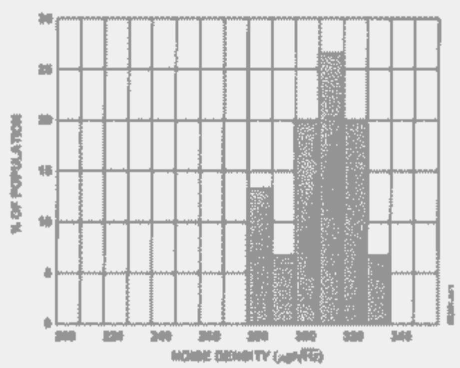

Figure 11. X-Axis Noise Density at 25°C

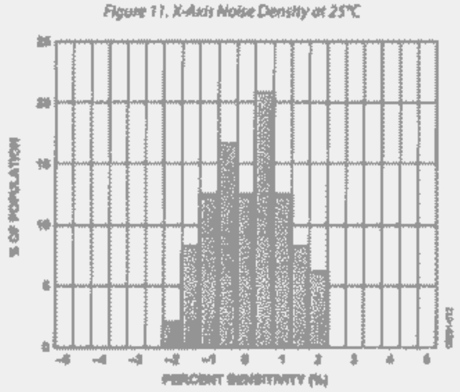

Figure 12. Z vs. X Cross-Axis Sensitivity

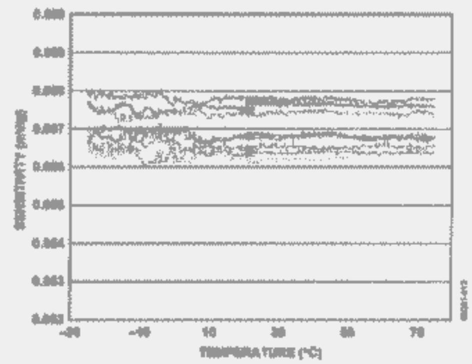

Figure 13. Sensitivity vs. Temperature—Parts Soldered to PCB

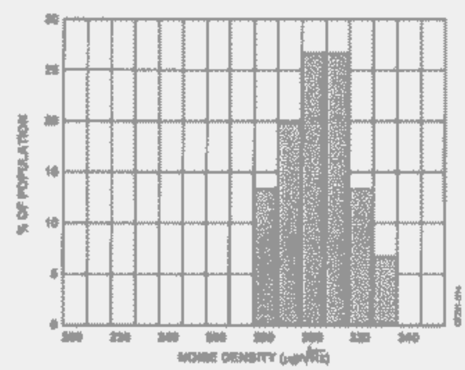

Figure 14. Y-Axis Noise Density at 25°C

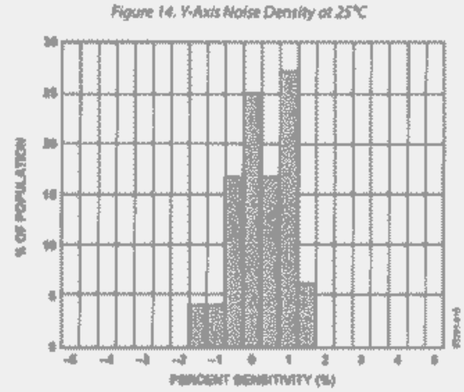

Figure 15. Z vs. Y Cross-Axis Sensitivity

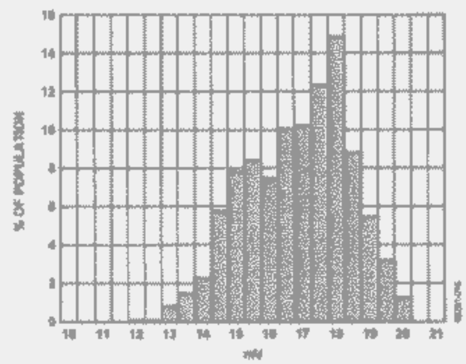

Figure 16. X-Axis Self-Test Response at 25°C

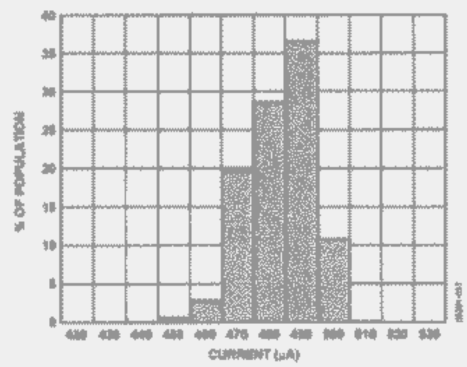

Figure 17. Supply Current at 25°C

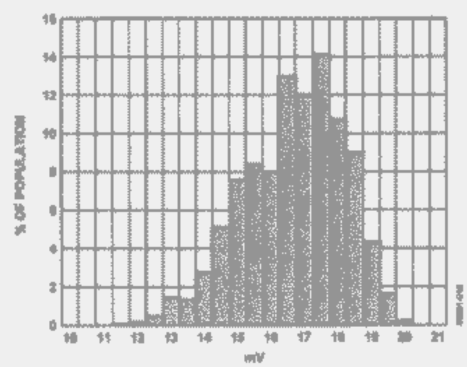

Figure 18. Y-Axis Self-Test Response at 25°C

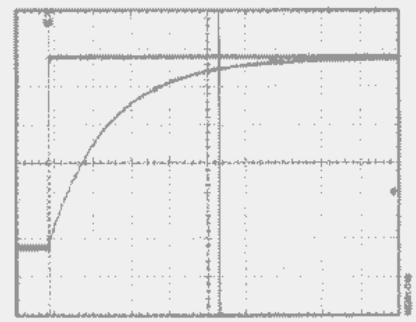

Figure 19. Turn-On Time—C_X, C_Y = 0.1 µF, Time Scale = 2 ms/DIV

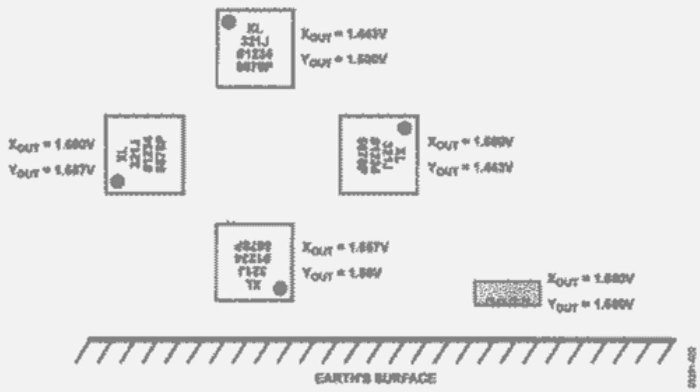

Figure 20. Output Response vs. Orientation (Top View)

THEORY OF OPERATION

The ADXL321 is a complete acceleration measurement system on a single monolithic IC. The ADXL321 has a measurement range of ±18 *g*. It contains a polysilicon surface-micromachined sensor and signal conditioning circuitry to implement an open-loop acceleration measurement architecture. The output signals are analog voltages that are proportional to acceleration. The accelerometer measures static acceleration forces, such as gravity, which allows it to be used as a tilt sensor.

The sensor is a polysilicon surface-micromachined structure built on top of a silicon wafer. Polysilicon springs suspend the structure over the surface of the wafer and provide a resistance against acceleration forces. Deflection of the structure is measured using a differential capacitor that consists of independent fixed plates and plates attached to the moving mass. The fixed plates are driven by 180° out-of-phase square waves. Acceleration deflects the beam and unbalances the differential capacitor, resulting in an output square wave whose amplitude is proportional to acceleration. Phase-sensitive demodulation techniques are then used to rectify the signal and determine the direction of the acceleration.

The demodulator's output is amplified and brought off-chip through a 32 kΩ resistor. The user then sets the signal bandwidth of the device by adding a capacitor. This filtering improves measurement resolution and helps prevent aliasing.

PERFORMANCE

Rather than using additional temperature compensation circuitry, innovative design techniques have been used to ensure high performance is built-in. As a result, there is neither quantization error nor nonmonotonic behavior, and temperature hysteresis is very low (typically less than 10 m*g* over the −20°C to +70°C temperature range).

Figure 10 shows the zero *g* output performance of eight parts (X- and Y-axis) over a −20°C to +70°C temperature range.

Figure 13 demonstrates the typical sensitivity shift over temperature for supply voltages of 3 V. This is typically better than ±1% over the −20°C to +70°C temperature range.

APPLICATIONS

POWER SUPPLY DECOUPLING

For most applications, a single 0.1 µF capacitor, C_{DC}, adequately decouples the accelerometer from noise on the power supply. However, in some cases, particularly where noise is present at the 140 kHz internal clock frequency (or any harmonic thereof), noise on the supply may cause interference on the ADXL321 output. If additional decoupling is needed, a 100 Ω (or smaller) resistor or ferrite bead may be inserted in the supply line. Additionally, a larger bulk bypass capacitor (in the 1 µF to 4.7 µF range) may be added in parallel to C_{DC}.

SETTING THE BANDWIDTH USING C_X AND C_Y

The ADXL321 has provisions for band-limiting the X_{OUT} and Y_{OUT} pins. Capacitors must be added at these pins to implement low-pass filtering for antialiasing and noise reduction. The equation for the 3 dB bandwidth is

$$F_{-3\,dB} = 1/(2\pi(32\ k\Omega) \times C_{(X,\,Y)})$$

or more simply,

$$F_{-3\,dB} = 5\ \mu F/C_{(X,\,Y)}$$

The tolerance of the internal resistor (R_{FILT}) typically varies as much as ±15% of its nominal value (32 kΩ), and the bandwidth varies accordingly. A minimum capacitance of 2000 pF for C_X and C_Y is required in all cases.

Table 5. Filter Capacitor Selection, C_X and C_Y

Bandwidth (Hz)	Capacitor (µF)
1	4.7
10	0.47
50	0.10
100	0.05
200	0.027
500	0.01

SELF-TEST

The ST pin controls the self-test feature. When this pin is set to V_S, an electrostatic force is exerted on the accelerometer beam. The resulting movement of the beam allows the user to test if the accelerometer is functional. The typical change in output is 315 mg (corresponding to 18 mV). This pin may be left open-circuit or connected to common (COM) in normal use.

The ST pin should never be exposed to voltages greater than V_S + 0.3 V. If this cannot be guaranteed due to the system design (for instance, if there are multiple supply voltages), then a low V_F clamping diode between ST and V_S is recommended.

DESIGN TRADE-OFFS FOR SELECTING FILTER CHARACTERISTICS: THE NOISE/BW TRADE-OFF

The accelerometer bandwidth selected ultimately determines the measurement resolution (smallest detectable acceleration). Filtering can be used to lower the noise floor, which improves the resolution of the accelerometer. Resolution is dependent on the analog filter bandwidth at X_{OUT} and Y_{OUT}.

The output of the ADXL321 has a typical bandwidth of 2.5 kHz. The user must filter the signal at this point to limit aliasing errors. The analog bandwidth must be no more than half the A/D sampling frequency to minimize aliasing. The analog bandwidth may be further decreased to reduce noise and improve resolution.

The ADXL321 noise has the characteristics of white Gaussian noise, which contributes equally at all frequencies and is described in terms of µg/√Hz (the noise is proportional to the square root of the accelerometer's bandwidth). The user should limit bandwidth to the lowest frequency needed by the application in order to maximize the resolution and dynamic range of the accelerometer.

With the single-pole, roll-off characteristic, the typical noise of the ADXL321 is determined by

$$rmsNoise = (320\ \mu g/\sqrt{Hz}) \times (\sqrt{BW \times 1.6})$$

At 100 Hz bandwidth the noise will be

$$rmsNoise = (320\ \mu g/\sqrt{Hz}) \times (\sqrt{100 \times 1.6}) = 4\ mg$$

Often, the peak value of the noise is desired. Peak-to-peak noise can only be estimated by statistical methods. A factor of 6 is generally used to convert rms to peak-to-peak. Table 6 is useful for estimating the probabilities of exceeding various peak values, given the rms value.

Table 6. Estimation of Peak-to-Peak Noise

Peak-to-Peak Value	% of Time That Noise Exceeds Nominal Peak-to-Peak Value
2 × rms	32
4 × rms	4.6
6 × rms	0.27
8 × rms	0.006

Peak-to-peak noise values give the best estimate of the uncertainty in a single measurement. Table 7 gives the typical noise output of the ADXL321 for various C_X and C_Y values.

Table 7. Filter Capacitor Selection (C_X, C_Y)

Bandwidth (Hz)	C_X, C_Y (µF)	RMS Noise (mg)	Peak-to-Peak Noise Estimate (mg)
10	0.47	1.3	7.8
50	0.1	2.9	17.4
100	0.047	4	24
500	0.01	9.1	54.6

USE WITH OPERATING VOLTAGES OTHER THAN 3 V

The ADXL321 is tested and specified at V_S = 3 V; however, it can be powered with V_S as low as 2.4 V or as high as 6 V. Note that some performance parameters change as the supply voltage is varied.

The ADXL321 output is ratiometric, so the sensitivity (or scale factor) varies proportionally to supply voltage. At V_S = 5 V, the sensitivity is typically 100 mV/*g*. At V_S = 2.4 V, the sensitivity is typically 45 mV/*g*.

The zero *g* bias output is also ratiometric, so the zero *g* output is nominally equal to $V_S/2$ at all supply voltages.

The output noise is not ratiometric but is absolute in volts; therefore, the noise density decreases as the supply voltage increases. This is because the scale factor (mV/*g*) increases while the noise voltage remains constant. At V_S = 5 V, the noise density is typically 190 µ*g*/√Hz, while at V_S = 2.4 V, the noise density is typically 400 µ*g*/√Hz.

Self-test response in *g* is roughly proportional to the square of the supply voltage. However, when ratiometricity of sensitivity is factored in with supply voltage, the self-test response in volts is roughly proportional to the cube of the supply voltage. For example, at V_S = 5 V, the self-test response for the ADXL321 is approximately 80 mV. At V_S = 2.4 V, the self-test response is approximately 8 mV.

The supply current decreases as the supply voltage decreases. Typical current consumption at V_S = 5 V is 750 µA, and typical current consumption at V_S = 2.4 V is 350 µA.

USE AS A DUAL-AXIS TILT SENSOR

An accelerometer is most sensitive to tilt when its sensitive axis is perpendicular to the force of gravity (that is, when it is parallel to the earth's surface). At this orientation, its sensitivity to changes in tilt is highest. When the accelerometer is oriented on axis to gravity (near its +1 *g* or −1 *g* reading), the change in output acceleration per degree of tilt is negligible. When the accelerometer is perpendicular to gravity, its output changes nearly 17.5 m*g* per degree of tilt. At 45°, its output changes at only 12.2 m*g* per degree of tilt, and resolution declines.

Converting Acceleration to Tilt

When the accelerometer is oriented so both its X-axis and Y-axis are parallel to the earth's surface, it can be used as a 2-axis tilt sensor with both a roll axis and pitch axis. Once the output signal from the accelerometer has been converted to an acceleration that varies between −1 *g* and +1 *g*, the output tilt in degrees is calculated as

$$PITCH = \arcsin(A_X/1\ g)$$

$$ROLL = \arcsin(A_Y/1\ g)$$

Be sure to account for overranges. It is possible for the accelerometers to output a signal greater than ±1 *g* due to vibration, shock, or other accelerations.

OUTLINE DIMENSIONS

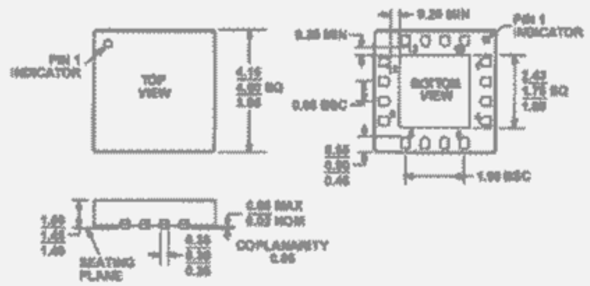

*STACKED DIE WITH GLASS SEAL.

Figure 21. 16-Lead Lead Frame Chip Scale Package (MQ_LFCSP_LQ) 4 mm × 4 mm Body, Thick Quad (CP-16-5a) Dimensions shown in millimeters (Drawing Not to Scale)*

ORDERING GUIDE

Model	Measurement Range	Specified Voltage (V)	Temperature Range	Package Description	Package Option
ADXL321JCP[1]	±18 *g*	3	−20°C to +70°C	16-Lead LFCSP_LQ	CP-16-5a
ADXL321JCP-REEL	±18 *g*	3	−20°C to +70°C	16-Lead LFCSP_LQ	CP-16-5a
ADXL321EB				Evaluation Board	

[1] Lead finish—Matte tin.

ANALOG DEVICES

Dual-Axis, High-g, iMEMS® Accelerometers

ADXL278

FEATURES

- Complete dual-axis acceleration measurement system on a single monolithic IC
- Available in ±35 g/±35 g, ±50 g/±50 g, or ±70 g/±35 g output full-scale ranges
- Full differential sensor and circuitry for high resistance to EMI/RFI
- Environmentally robust packaging
- Complete mechanical and electrical self-test on digital command
- Output ratiometric to supply
- Sensitive axes in the plane of the chip
- High linearity (0.2% of full scale)
- Frequency response down to dc
- Low noise
- Low power consumption
- Tight sensitivity tolerance and 0 g offset capability
- Largest available prefilter clipping headroom
- 400 Hz, 2-pole Bessel filter
- Single-supply operation
- Compatible with Sn/Pb and Pb-free solder processes
- Qualified for automotive applications

APPLICATIONS

- Vibration monitoring and control
- Vehicle collision sensing
- Shock detection

GENERAL DESCRIPTION

The ADXL278 is a low power, complete, dual-axis accelerometer with signal conditioned voltage outputs that are on a single monolithic IC. This product measures acceleration with a full-scale range of (X-axis/Y-axis) ±35 g/±35 g, ±50 g/±50 g, or ±70 g/±35 g (minimum). The ADXL278 can also measure both dynamic acceleration (vibration) and static acceleration (gravity).

The ADXL278 is the fourth-generation surface micromachined iMEMS® accelerometer from ADI with enhanced performance and lower cost. Designed for use in front and side impact airbag applications, this product also provides a complete cost-effective solution useful for a wide variety of other applications.

The ADXL278 is temperature stable and accurate over the automotive temperature range, with a self-test feature that fully exercises all the mechanical and electrical elements of the sensor with a digital signal applied to a single pin.

The ADXL278 is available in a 5 mm × 5 mm × 2 mm, 8-terminal ceramic LCC package.

FUNCTIONAL BLOCK DIAGRAM

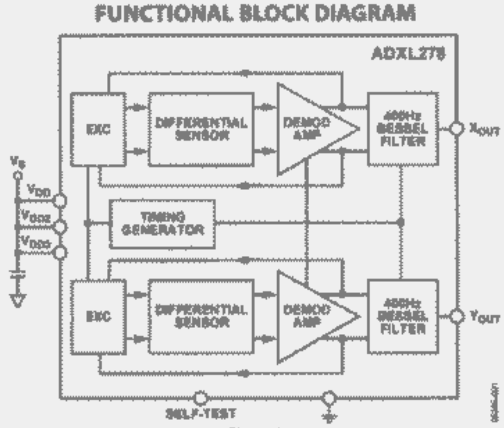

Figure 1.

One Technology Way, P.O. Box 9106, Norwood, MA 02062-9106, U.S.A.
Tel: 781.329.4700 www.analog.com
Fax: 781.461.3113

TABLE OF CONTENTS

REVISION HISTORY

8/10—Rev. A to Rev. B

Updated Format ... Universal
Change to Features Section ... 1
Updated Outline Dimensions ... 9
Changes to Ordering Guide ... 9
Added Automotive Products Section ... 9

7/02—Rev. D to Rev. E

Edits to Features ... 1

5/05—Rev. 0 to Rev. A

SPECIFICATIONS[1]

At T_A = −40°C to +105°C, 5.0 V dc ± 5%, acceleration = 0 g, unless otherwise noted.

Table 1.

Parameter	Conditions	Model No. AD22284 Min	Typ	Max	Model No. AD22285 Min	Typ	Max	Model No. AD22286 Axis	Min	Typ	Max	Unit
SENSOR												
Output Full-Scale Range	I_{OUT} ≤ ±100 µA	37			55			X	70			g
								Y	37			g
Nonlinearity			0.2	2		0.2	2			0.2	2	%
Package Alignment Error			1			1				1		Degree
Sensor-to-Sensor Alignment Error			0.1			0.1				0.1		Degree
Cross-Axis Sensitivity		−5		+5	−5		+5		−5		+5	%
Resonant Frequency			24			24				24		kHz
Sensitivity, Ratiometric (Over Temperature)	V_{DD} = 5 V, 100 Hz	52.25	55	57.75	36.1	38	39.9	X	25.65	27	28.35	mV/g
								Y	52.25	55	57.75	mV/g
OFFSET												
Zero-g Output Voltage (Over Temperature)[2]	V_{OUT} − V_{DD}/2, V_{DD} = 5 V	−150		+150	−150		+150	X	−100		+100	mV
								Y	−150		+150	mV
NOISE												
Noise Density	10 Hz − 400Hz, 5V		1.1	3		1.4	3	X		1.8	3.5	mg/√Hz
								Y		1.1	3	mg/√Hz
Clock Noise			5			5				5		mV p-p
FREQUENCY RESPONSE	2-pole Bessel											
−3 dB Frequency		360	400	440	360	400	440		360	400	440	Hz
−3 dB Frequency Drift	25°C to T_{MIN} or T_{MAX}		2			2				2		Hz
SELF-TEST												
Output Change (Cube vs. V_{DD})[3]	V_{DD} = 5 V	440	550	660	304	380	456	X	216	270	324	mV
								Y	440	550	660	mV
Logic Input High	V_{DD} = 5 V	3.5			3.5				3.5			V
Logic Input Low	V_{DD} = 5 V			1			1				1	V
Input Resistance	Pull-down resistor to GND	30	50		30	50			30	50		kΩ
OUTPUT AMPLIFIER												
Output Voltage Swing	I_{OUT} = ±400 µA	0.25		V_{DD} − 0.25	0.25		V_{DD} − 0.25		0.25		V_{DD} − 0.25	V
Capacitive Load Drive		1000			1000				1000			pF
PREFILTER HEADROOM			280			400				560		g
CFSR @ 400 kHz			6			4.5				3		V/V
										6		V/V
POWER SUPPLY (V_{DD})		4.75		5.25	4.75		5.25		4.75		5.25	V
Functional Range		3.5		6	3.5		6		3.5		6	V
Quiescent Supply Current	V_{DD} = 5 V		2.2	2.9		2.2	2.9			2.2	2.9	mA
TEMPERATURE RANGE		−40		+105	−40		+105		−40		+105	°C

[1] All minimum and maximum specifications are guaranteed. Typical specifications are not guaranteed.
[2] Zero g output is ratiometric.
[3] Self-test output at V_{DD} = (Self-Test Output at 5 V) × $(V_{DD}/5\ V)^3$.

ABSOLUTE MAXIMUM RATINGS

Table 2.

Parameter	Rating
Acceleration (Any Axis, Unpowered)	4,000 *g*
Acceleration (Any Axis, Powered)	4,000 *g*
V_S	−0.3 V to +7.0 V
All Other Pins	(COM − 0.3 V) to (V_S + 0.3 V)
Output Short-Circuit Duration (Any Pin to Common)	Indefinite
Operating Temperature Range	−65°C to +150°C
Storage Temperature	−65°C to +150°C

Stresses above those listed under Absolute Maximum Ratings may cause permanent damage to the device. This is a stress rating only; functional operation of the device at these or any other conditions above those indicated in the operational section of this specification is not implied. Exposure to absolute maximum rating conditions for extended periods may affect device reliability.

ESD CAUTION

ESD (electrostatic discharge) sensitive device. Charged devices and circuit boards can discharge without detection. Although this product features patented or proprietary protection circuitry, damage may occur on devices subjected to high energy ESD. Therefore, proper ESD precautions should be taken to avoid performance degradation or loss of functionality.

PIN CONFIGURATION AND FUNCTION DESCRIPTIONS

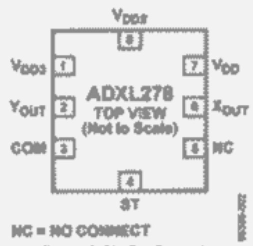

Figure 2. Pin Configuration

Table 3. Pin Function Descriptions

Pin No.	Mnemonic	Description
1	V_{DD3}	3.5 V to 6 V
2	Y_{OUT}	Y Channel Output
3	COM	Common
4	ST	Self-Test
5	NC	Do Not Connect
6	X_{OUT}	X Channel Output
7	V_{DD}	3.5 V to 6 V
8	V_{DD2}	3.5 V to 6 V

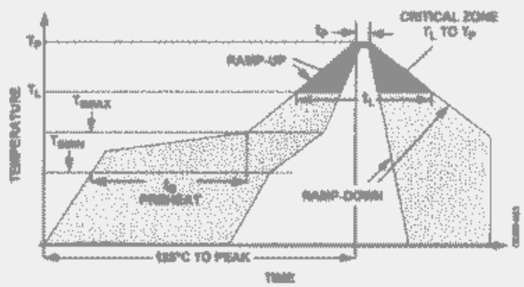

Figure 3. Recommended Soldering Profile

Table 4. Recommended Soldering Profile

Profile Feature	Sn63/Pb37	Pb-Free
AVERAGE RAMP RATE (T_L TO T_P)	3°C/s max	3°C/s max
PREHEAT		
Minimum Temperature (T_{SMIN})	100°C	150°C
Maximum Temperature (T_{SMAX})	150°C	200°C
TIME (T_{SMIN} TO T_{SMAX}), t_S	60 s – 120 s	60 s – 150 s
T_{SMAX} TO T_L		
Ramp-Up Rate	3°C/s	3°C/s
TIME MAINTAINED ABOVE LIQUIDOUS (T_L)		
Liquidous Temperature (T_L)	183°C	217°C
Time (t_L)	60 s – 150 s	60 s – 150 s
PEAK TEMPERATURE (T_P)	240°C + 0°C/–5°C	260°C + 0°C/–5°C
TIME WITHIN 5°C OF ACTUAL PEAK TEMPERATURE (t_P)	10 s – 30 s	20 s – 40 s
RAMP-DOWN RATE	6°C/s max	6°C/s max
TIME 25°C TO PEAK TEMPERATURE	6 min max	8 min max

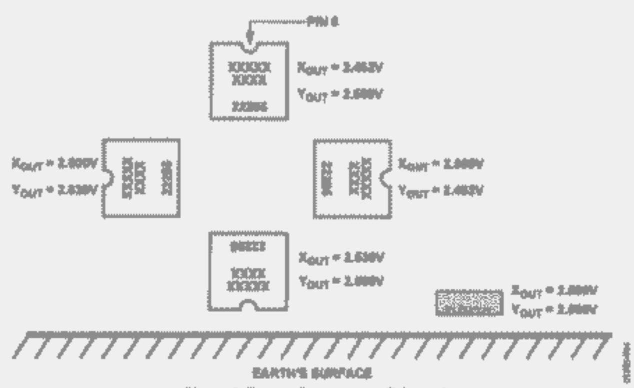

Figure 4. Output Response vs. Orientation

THEORY OF OPERATION

The ADXL278 provides a fully differential sensor structure and circuit path, resulting in the industry's highest resistance to EMI/RFI effects. This latest generation uses electrical feedback with zero-force feedback for improved accuracy and stability. The sensor resonant frequency is significantly higher than the signal bandwidth set by the on-chip filter, avoiding the signal analysis problems caused by resonant peaks near the signal bandwidth.

Figure 5 is a simplified view of one of the differential sensor elements. Each sensor includes several differential capacitor unit cells. Each cell is composed of fixed plates attached to the substrate and movable plates attached to the frame. Displacement of the frame changes the differential capacitance, which is measured by the on-chip circuitry.

Complementary 200 kHz square waves drive the fixed plates. Electrical feedback adjusts the amplitudes of the square waves such that the ac signal on the moving plates is 0. The feedback signal is linearly proportional to the applied acceleration. This unique feedback technique ensures that there is no net electrostatic force applied to the sensor. The differential feedback control signal is also applied to the input of the filter, where it is filtered and converted to a single-ended signal.

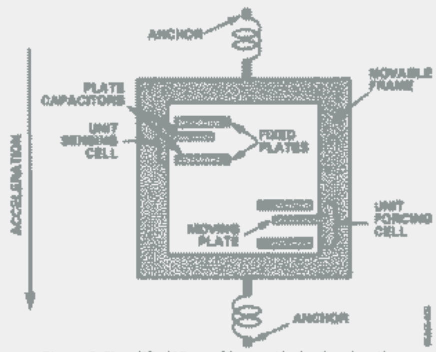

Figure 5. Simplified View of Sensor Under Acceleration

APPLICATIONS

POWER SUPPLY DECOUPLING

For most applications, a single 0.1 µF capacitor, C_{DC}, adequately decouples the accelerometer from noise on the power supply. However, in some cases, particularly where noise is present at the 200 kHz internal clock frequency (or any harmonic thereof), noise on the supply can cause interference on the ADXL278's output. If additional decoupling is needed, a 50 Ω (or smaller) resistor or ferrite bead cany be inserted in the supply line. Additionally, a larger bulk bypass capacitor (in the 1 µF to 4.7 µF range) can be added in parallel to C_{DC}.

SELF-TEST

The fixed fingers in the forcing cells are normally kept at the same potential as that of the movable frame. When the self-test digital input is activated, the voltage on the fixed fingers on one side of the moving plate in the forcing cells is changed. This creates an attractive electrostatic force, which causes the frame to move towards those fixed fingers. The entire signal channel is active; therefore, the sensor displacement causes a change in V_{OUT}. The ADXL278's self-test function is a comprehensive method of verifying the operation of the accelerometer.

Because electrostatic force is independent of the polarity of the voltage across capacitor plates, a positive voltage is applied in half of the forcing cells, and its complement in the other half of the forcing cells. Activating self-test causes a step function force to be applied to the sensor, while the capacitive coupling term is canceled. The ADXL278 has improved self-test functionality, including excellent transient response and high speed switching capabilities. Arbitrary force waveforms can be applied to the sensor by modulating the self-test input, such as test signals to measure the system frequency response or even crash signals to verify algorithms within the limits of the self-test swing.

The ST pin should never be exposed to voltages greater than V_S + 0.3 V. If this cannot be guaranteed due to the system design (for instance, if there are multiple supply voltages), then a low V_F clamping diode between ST and V_S is recommended.

CLOCK FREQUENCY SUPPLY RESPONSE

In any clocked system, power supply noise near the clock frequency may have consequences at other frequencies. An internal clock typically controls the sensor excitation and the signal demodulator for micromachined accelerometers.

If the power supply contains high frequency spikes, they may be demodulated and interpreted as an acceleration signal. A signal appears as the difference between the noise frequency and the demodulator frequency. If the power supply spikes are 100 Hz away from the demodulator clock, there is an output term at 100 Hz. If the power supply clock is at exactly the same frequency as the accelerometer clock, the term appears as an offset.

If the difference frequency is outside of the signal bandwidth, the filter attenuates it. However, both the power supply clock and the accelerometer clock may vary with time or temperature, which can cause the interference signal to appear in the output filter bandwidth.

The ADXL278 addresses this issue in two ways. First, the high clock frequency eases the task of choosing a power supply clock frequency such that the difference between it and the accelerometer clock remains well outside of the filter bandwidth. Second, the ADXL278 is the only micromachined accelerometer to have a fully differential signal path, including differential sensors. The differential sensors eliminate most of the power supply noise before it reaches the demodulator. Good high frequency supply bypassing, such as a ceramic capacitor close to the supply pins, also minimizes the amount of interference.

The clock frequency supply response (CFSR) is the ratio of the response at V_{OUT} to the noise on the power supply near the accelerometer clock frequency. A CFSR of 3 means that the signal at V_{OUT} is 3× the amplitude of an excitation signal at V_{DD} near the accelerometer internal clock frequency. This is analogous to the power supply response, except that the stimulus and the response are at different frequencies. The ADXL278's CFSR is 10× better than a typical single-ended accelerometer system.

SIGNAL DISTORTION

Signals from crashes and other events may contain high amplitude, high frequency components. These components contain very little useful information and are reduced by the 2-pole Bessel filter at the output of the accelerometer. However, if the signal saturates at any point, the accelerometer output does not look like a filtered version of the acceleration signal.

The signal may saturate anywhere before the filter. For example, if the resonant frequency of the sensor is low, the displacement per unit acceleration is high. The sensor may reach the mechanical limit of travel if the applied acceleration is high enough. This can be remedied by locating the accelerometer where it does not see high values of acceleration and by using a higher resonant frequency sensor, such as the ADXL278.

Also, the electronics may saturate in an overload condition between the sensor output and the filter input. Ensuring that internal circuit nodes operate linearly to at least several times the full-scale acceleration value can minimize electrical saturation. The ADXL278 circuit is linear to approximately 8× full scale.

OUTLINE DIMENSIONS

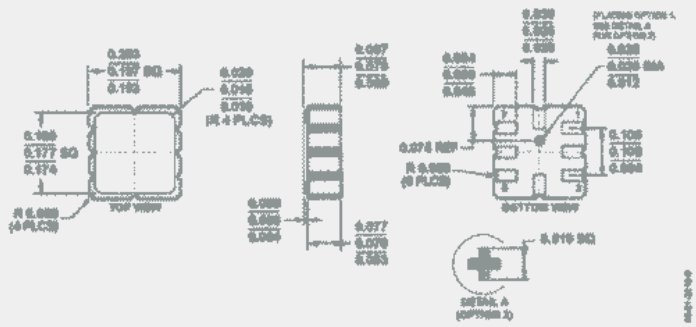

Figure 6. 8-Lead Ceramic Leadless Chip Carrier [LCC] (E-8-1) Dimensions shown in inches

ADXL278 ORDERING GUIDE

Model[1, 2, 3]	Parts per Reel	Measurement Range	Specified Voltage (V)	Temperature Range	Package Description	Package Option
AD22284-A-R2	250	±35 g/±35 g	5	−40°C to +105°C	8-Lead Ceramic Leadless Chip Carrier	E-8-1
AD22284-A	3,000	±35 g/±35 g	5	−40°C to +105°C	8-Lead Ceramic Leadless Chip Carrier	E-8-1
ADW22284ZC	3,000	±35 g/±35 g	5	−40°C to +105°C	8-Lead Ceramic Leadless Chip Carrier	E-8-1
ADW22284ZC-RL7	250	±35 g/±35 g	5	−40°C to +105°C	8-Lead Ceramic Leadless Chip Carrier	E-8-1
AD22285-R2	250	±50 g/±50 g	5	−40°C to +105°C	8-Lead Ceramic Leadless Chip Carrier	E-8-1
AD22285	3,000	±50 g/±50 g	5	−40°C to +105°C	8-Lead Ceramic Leadless Chip Carrier	E-8-1
ADW22285ZC	3,000	±50 g/±50 g	5	−40°C to +105°C	8-Lead Ceramic Leadless Chip Carrier	E-8-1
ADW22285ZC-RL7	250	±50 g/±50 g	5	−40°C to +105°C	8-Lead Ceramic Leadless Chip Carrier	E-8-1
AD22286-R2	250	±70 g/±35 g	5	−40°C to +105°C	8-Lead Ceramic Leadless Chip Carrier	E-8-1
AD22286	3,000	±70 g/±35 g	5	−40°C to +105°C	8-Lead Ceramic Leadless Chip Carrier	E-8-1
ADW22286ZC	3,000	±70 g/±35 g	5	−40°C to +105°C	8-Lead Ceramic Leadless Chip Carrier	E-8-1
ADW22286ZC-RL7	250	±70 g/±35 g	5	−40°C to +105°C	8-Lead Ceramic Leadless Chip Carrier	E-8-1

[1] All models are on tape and reel and are RoHS compliant parts.
[2] Z = RoHS Compliant Part.
[3] W = Qualified for Automotive Applications.

AUTOMOTIVE PRODUCTS

The ADW22284, ADW22285, and ADW22286 models are available with controlled manufacturing to support the quality and reliability requirements of automotive applications. Note that these automotive models may have specifications that differ from the commercial models; therefore, designers should review the Specifications section of this data sheet carefully. Only the automotive grade products shown are available for use in automotive applications. Contact your local Analog Devices account representative for specific product ordering information and to obtain the specific Automotive Reliability reports for these models.

ANALOG DEVICES

Single-Axis, High-*g*, *i*MEMS® Accelerometers

ADXL193

FEATURES

- Complete acceleration measurement system on a single monolithic IC
- Available in ±120 *g* or ±250 *g* output full-scale ranges
- Full differential sensor and circuitry for high resistance to EMI/RFI
- Environmentally robust packaging
- Complete mechanical and electrical self-test on digital command
- Output ratiometric to supply
- Sensitive axes in the plane of the chip
- High linearity (0.2% of full scale)
- Frequency response down to dc
- Low noise
- Low power consumption (1.5 mA)
- Tight sensitivity tolerance and 0 *g* offset capability
- Largest available prefilter clipping headroom
- 400 Hz, 2-pole Bessel filter
- Single-supply operation
- Compatible with Sn/Pb and Pb-free solder processes
- Qualified for automotive applications

APPLICATIONS

- Vibration monitoring and control
- Vehicle collision sensing
- Shock detection

GENERAL DESCRIPTION

The ADXL193 is a low power, complete single-axis accelerometer with signal conditioned voltage outputs that are all on a single monolithic IC. This product measures acceleration with a full-scale range of ±120 *g* or ±250 *g* (minimum). It can also measure both dynamic acceleration (vibration) and static acceleration (gravity).

The ADXL193 is a fourth-generation surface micromachined iMEMS® accelerometer from ADI with enhanced performance and lower cost. Designed for use in front and side impact airbag applications, this product also provides a complete cost-effective solution useful for a wide variety of other applications.

The ADXL193 is temperature stable and accurate over the automotive temperature range, with a self-test feature that fully exercises all the mechanical and electrical elements of the sensor with a digital signal applied to a single pin.

The ADXL193 is available in a 5 mm × 5 mm × 2 mm, 8-terminal ceramic LCC package.

FUNCTIONAL BLOCK DIAGRAM

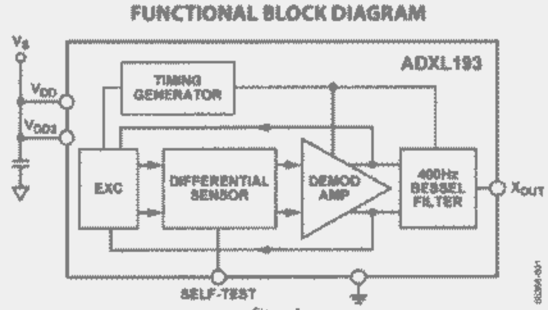

Figure 1.

One Technology Way, P.O. Box 9106, Norwood, MA 02062-9106, U.S.A.
Tel: 781.329.4700 www.analog.com
Fax: 781.461.3113

TABLE OF CONTENTS

REVISION HISTORY

8/10—Rev. A to Rev. B

Updated Format ... Universal
Change to Features Section ... 1
Updated Outline Dimensions ... 9
Changes to Ordering Guide ... 9
Added Automotive Products Section ... 9

5/05—Rev. 0 to Rev. A

SPECIFICATIONS[1]

At $T_A = -40°C$ to $+105°C$, 5.0 V dc ± 5%, acceleration = 0 *g* unless otherwise noted.

Table 1.

Parameter	Conditions	Model No. AD22282			Model No. AD22283			Unit
		Min	Typ	Max	Min	Typ	Max	
SENSOR								
Output Full-Scale Range	$I_{OUT} \le \pm 100$ µA	120			250			*g*
Nonlinearity			0.2	2		0.2	2	%
Package Alignment Error			1			1		Degree
Cross-Axis Sensitivity		−5		+5	−5		+5	%
Resonant Frequency			24			24		kHz
Sensitivity, Ratiometric (Over Temperature)	V_{DD} = 5 V, 100 Hz	17.1	18	18.9	7.6	8	8.4	mV/*g*
OFFSET								
Zero-*g* Output Voltage (Over Temperature)[2]	$V_{OUT} - V_{DD}/2$, V_{DD} = 5 V	−125		+125	−100		+100	mV
NOISE								
Noise Density	10 Hz – 400 Hz, 5 V		3	10		5	15	mg/√Hz
Clock Noise			5			5		mV p-p
FREQUENCY RESPONSE	Two-pole Bessel							
−3 dB Frequency		360	400	440	360	400	440	Hz
−3 dB Frequency Drift	25°C to T_{MIN} or T_{MAX}		2			2		Hz
SELF-TEST								
Output Change (Cube vs. V_{DD})[3]	V_{DD} = 5 V	400	500	600	200	250	300	mV
Logic Input High	V_{DD} = 5 V	3.5			3.5			V
Logic Input Low	V_{DD} = 5 V			1			1	V
Input Resistance	Pull-down resistor to GND	30	50		30	50		kΩ
OUTPUT AMPLIFIER								
Output Voltage Swing	$I_{OUT} = \pm 400$ µA	0.25		V_{DD} − 0.25	0.25		V_{DD} − 0.25	V
Capacitive Load Drive		1000			1000			pF
PREFILTER HEADROOM			800			1400		*g*
CFSR @ 400 kHz			2			1.5		V/V
POWER SUPPLY (V_{DD})		4.75		5.25	4.75		5.25	V
Functional Range		3.5		6	3.5		6	V
Quiescent Supply Current	V_{DD} = 5 V		1.5	2		1.5	2	mA
TEMPERATURE RANGE		−40		+125	−40		+125	°C

[1] All minimum and maximum specifications are guaranteed. Typical specifications are not guaranteed.
[2] Zero *g* output is ratiometric.
[3] Self-test output at V_{DD} = (Self-Test Output at 5 V) × $(V_{DD}/5\ V)^3$.

ABSOLUTE MAXIMUM RATINGS

Table 2.

Parameter	Rating
Acceleration (Any Axis, Unpowered)	4,000 *g*
Acceleration (Any Axis, Powered)	4,000 *g*
V_S	−0.3 V to +7.0 V
All Other Pins	(COM − 0.3 V) to (V_S + 0.3 V)
Output Short-Circuit Duration (Any Pin to Common)	Indefinite
Operating Temperature Range	−65°C to +150°C
Storage Temperature	−65°C to +150°C

Stresses above those listed under Absolute Maximum Ratings may cause permanent damage to the device. This is a stress rating only; functional operation of the device at these or any other conditions above those indicated in the operational section of this specification is not implied. Exposure to absolute maximum rating conditions for extended periods may affect device reliability.

ESD CAUTION

ESD (electrostatic discharge) sensitive device. Charged devices and circuit boards can discharge without detection. Although this product features patented or proprietary protection circuitry, damage may occur on devices subjected to high energy ESD. Therefore, proper ESD precautions should be taken to avoid performance degradation or loss of functionality.

PIN CONFIGURATION AND FUNCTION DESCRIPTIONS

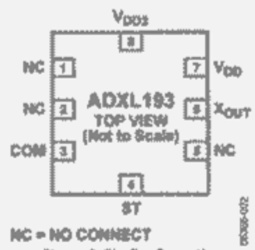

Figure 2. Pin Configuration

Table 3. Pin Function Descriptions

Pin No.	Mnemonic	Description
1	NC	Do Not Connect
2	NC	Do Not Connect
3	COM	Common
4	ST	Self-Test
5	NC	Do Not Connect
6	X_{OUT}	X Channel Output
7	V_{DD}	3.5 V to 6 V
8	V_{DD2}	3.5 V to 6 V

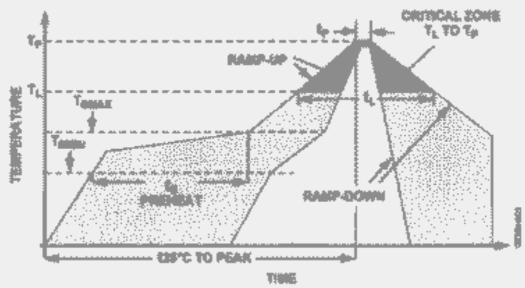

Figure 3. Recommended Soldering Profile

Table 4. Recommended Soldering Profile

Profile Feature	Sn63/Pb37	Pb-Free
AVERAGE RAMP RATE (T_L TO T_P)	3°C/s max	3°C/s max
PREHEAT		
Minimum Temperature (T_{SMIN})	100°C	150°C
Maximum Temperature (T_{SMAX})	150°C	200°C
TIME (T_{SMIN} TO T_{SMAX}), t_S	60 s – 120 s	60 s – 150 s
T_{SMAX} TO T_L		
Ramp-Up Rate	3°C/s	3°C/s
TIME MAINTAINED ABOVE LIQUIDOUS (T_L)		
Liquidous Temperature (T_L)	183°C	217°C
Time (t_L)	60 s – 150 s	60 s – 150 s
PEAK TEMPERATURE (T_P)	240°C + 0°C/–5°C	260°C + 0°C/–5°C
TIME WITHIN 5°C OF ACTUAL PEAK TEMPERATURE (t_P)	10 s – 30 s	20 s – 40 s
RAMP-DOWN RATE	6°C/s max	6°C/s max
TIME 25°C TO PEAK TEMPERATURE	6 min max	8 min max

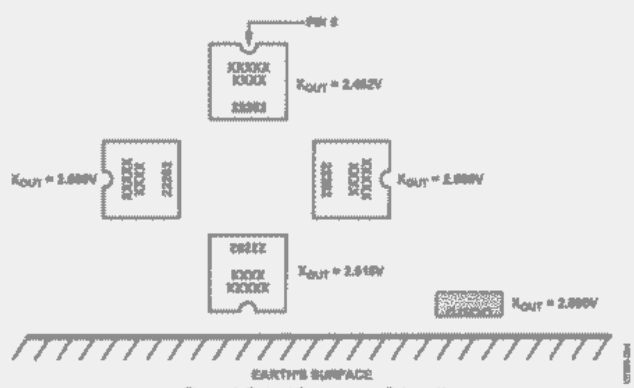

Figure 4. Output Response vs. Orientation

THEORY OF OPERATION

The ADXL193 provides a fully differential sensor structure and circuit path, resulting in the industry's highest resistance to EMI/RFI effects. This latest generation uses electrical feedback with zero-force feedback for improved accuracy and stability. The sensor resonant frequency is significantly higher than the signal bandwidth set by the on-chip filter, avoiding the signal analysis problems caused by resonant peaks near the signal bandwidth.

Figure 5 is a simplified view of one of the differential sensor elements. Each sensor includes several differential capacitor unit cells. Each cell is composed of fixed plates attached to the substrate and movable plates attached to the frame. Displacement of the frame changes the differential capacitance, which is measured by the on-chip circuitry.

Complementary 400 kHz square waves drive the fixed plates. Electrical feedback adjusts the amplitudes of the square waves such that the ac signal on the moving plates is 0. The feedback signal is linearly proportional to the applied acceleration. This unique feedback technique ensures that there is no net electrostatic force applied to the sensor. The differential feedback control signal is also applied to the input of the filter, where it is filtered and converted to a single-ended signal.

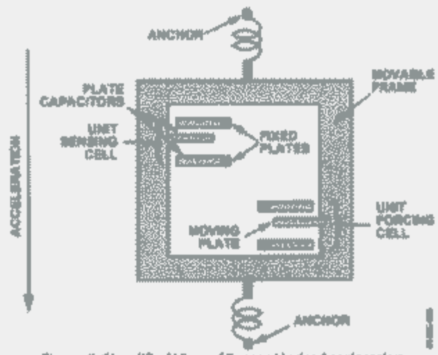

Figure 5. Simplified View of Sensor Under Acceleration

APPLICATIONS

POWER SUPPLY DECOUPLING

For most applications, a single 0.1 μF capacitor, C_{DC}, adequately decouples the accelerometer from noise on the power supply. However, in some cases, particularly where noise is present at the 400 kHz internal clock frequency (or any harmonic thereof), noise on the supply can cause interference on the ADXL193's output. If additional decoupling is needed, a 50 Ω (or smaller) resistor or ferrite bead can be inserted in the supply line. Additionally, a larger bulk bypass capacitor (in the 1 μF to 4.7 μF range) can be added in parallel to C_{DC}.

SELF-TEST

The fixed fingers in the forcing cells are normally kept at the same potential as that of the movable frame. When the self-test digital input is activated, the voltage on the fixed fingers on one side of the moving plate in the forcing cells is changed. This creates an attractive electrostatic force, which causes the frame to move toward those fixed fingers. The entire signal channel is active; therefore, the sensor displacement causes a change in V_{OUT}. The ADXL193's self-test function is a comprehensive method of verifying the operation of the accelerometer.

Because electrostatic force is independent of the polarity of the voltage across capacitor plates, a positive voltage is applied in half of the forcing cells, and its complement in the other half of the forcing cells. Activating self-test causes a step function force to be applied to the sensor, while the capacitive coupling term is canceled. The ADXL193 has improved self-test functionality, including excellent transient response and high speed switching capability. Arbitrary force waveforms can be applied to the sensor by modulating the self-test input, such as test signals to measure the system frequency response, or even crash signals to verify algorithms within the limits of the self-test swing.

The ST pin should never be exposed to voltages greater than V_S + 0.3 V. If this cannot be guaranteed due to the system design (for instance, if there are multiple supply voltages), then a low V_F clamping diode between ST and V_S is recommended.

CLOCK FREQUENCY SUPPLY RESPONSE

In any clocked system, power supply noise near the clock frequency may have consequences at other frequencies. An internal clock typically controls the sensor excitation and the signal demodulator for micromachined accelerometers.

If the power supply contains high frequency spikes, they may be demodulated and interpreted as an acceleration signal. A signal appears as the difference between the noise frequency and the demodulator frequency. If the power supply spikes are 100 Hz away from the demodulator clock, there is an output term at 100 Hz. If the power supply clock is at exactly the same frequency as the accelerometer clock, the term appears as an offset.

If the difference frequency is outside of the signal bandwidth, the filter attenuates it. However, both the power supply clock and the accelerometer clock may vary with time or temperature, which can cause the interference signal to appear in the output filter bandwidth.

The ADXL193 addresses this issue in two ways. First, the high clock frequency eases the task of choosing a power supply clock frequency such that the difference between it and the accelerometer clock remains well outside of the filter bandwidth. Second, the ADXL193 is the only micromachined accelerometer to have a fully differential signal path, including differential sensors. The differential sensors eliminate most of the power supply noise before it reaches the demodulator. Good high frequency supply bypassing, such as a ceramic capacitor close to the supply pins, also minimizes the amount of interference.

The clock frequency supply response (CFSR) is the ratio of the response at V_{OUT} to the noise on the power supply near the accelerometer clock frequency. A CFSR of 3 means that the signal at V_{OUT} is 3× the amplitude of an excitation signal at V_{DD} near the accelerometer internal clock frequency. This is analogous to the power supply response, except that the stimulus and the response are at different frequencies. The ADXL193's CFSR is 10× better than a typical single-ended accelerometer system.

SIGNAL DISTORTION

Signals from crashes and other events may contain high amplitude, high frequency components. These components contain very little useful information and are reduced by the 2-pole Bessel filter at the output of the accelerometer. However, if the signal saturates at any point, the accelerometer output does not look like a filtered version of the acceleration signal.

The signal may saturate anywhere before the filter. For example, if the resonant frequency of the sensor is low, the displacement per unit acceleration is high. The sensor may reach the mechanical limit of travel if the applied acceleration is high enough. This can be remedied by locating the accelerometer where it does not see high values of acceleration and by using a higher resonant frequency sensor, such as the ADXL193.

Also, the electronics may saturate in an overload condition between the sensor output and the filter input. Ensuring that internal circuit nodes operate linearly to at least several times the full-scale acceleration value can minimize electrical saturation. The ADXL193 circuit is linear to approximately 8× full scale.

OUTLINE DIMENSIONS

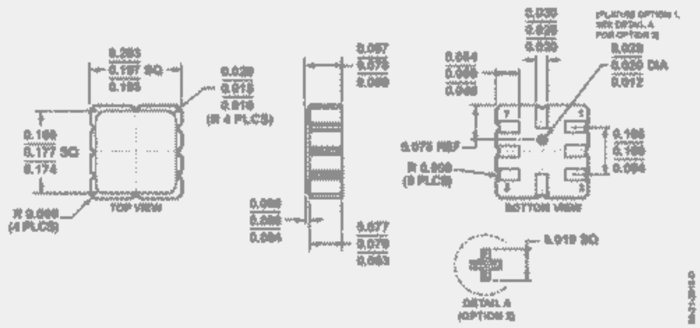

Figure 6. 8-Terminal Ceramic Leadless Chip Carrier [LCC]
(E-8-1)
Dimensions shown in inches

ADXL193 ORDERING GUIDE

Model[1, 2, 3]	Parts per Reel	Measurement Range	Specified Voltage (V)	Temperature Range	Package Description	Package Option
AD22282-A-R2	250	±120 *g*	5	−40°C to +125°C	8-Terminal Ceramic Leadless Chip Carrier	E-8-1
AD22282-A	3,000	±120 *g*	5	−40°C to +125°C	8-Terminal Ceramic Leadless Chip Carrier	E-8-1
ADW22282ZD	3,000	±120 *g*	5	−40°C to +125°C	8-Terminal Ceramic Leadless Chip Carrier	E-8-1
ADW22282ZD-RL7	250	±120 *g*	5	−40°C to +125°C	8-Terminal Ceramic Leadless Chip Carrier	E-8-1
AD22283-B-R2	250	±250 *g*	5	−40°C to +125°C	8-Terminal Ceramic Leadless Chip Carrier	E-8-1
AD22283-B	3,000	±250 *g*	5	−40°C to +125°C	8-Terminal Ceramic Leadless Chip Carrier	E-8-1
ADW22283ZE	3,000	±250 *g*	5	−40°C to +125°C	8-Terminal Ceramic Leadless Chip Carrier	E-8-1
ADW22283ZE-RL7	250	±250 *g*	5	−40°C to +125°C	8-Terminal Ceramic Leadless Chip Carrier	E-8-1

[1] All models are on tape and reel and are RoHS compliant parts.
[2] Z = RoHS Compliant Part.
[3] W = Qualified for Automotive Applications.

AUTOMOTIVE PRODUCTS

The ADW22282 and ADW22283 models are available with controlled manufacturing to support the quality and reliability requirements of automotive applications. Note that these automotive models may have specifications that differ from the commercial models; therefore, designers should review the Specifications section of this data sheet carefully. Only the automotive grade products shown are available for use in automotive applications. Contact your local Analog Devices account representative for specific product ordering information and to obtain the specific Automotive Reliability reports for these models.

APPENDIX C

DATA ACQUISITION DATA SHEETS

Technical Sales
United States
(866) 531-6285
info@ni.com

NI 9205

32-Ch ±200 mV to ±10 V, 16-Bit, 250 kS/s Analog Input Module

- 32 single-ended or 16 differential analog inputs
- 16-bit resolution; 250 kS/s aggregate sampling rate
- ±200 mV, ±1, ±5, and ±10 V programmable input ranges
- Hot-swappable operation; overvoltage protection; isolation; NIST-traceable calibration
- -40 to 70 °C operating range
- Spring terminal or D-Sub connectivity

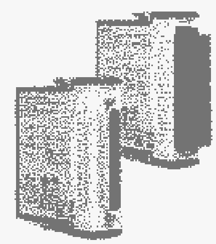

Overview

The National Instruments 9205 is a C Series module, for use with NI CompactDAQ and CompactRIO chassis. The NI 9205 features 32 single-ended or 16 differential analog inputs, 16-bit resolution, and a maximum sampling rate of 250 kS/s. Each channel has programmable input ranges of ±200 mV, ±1, ±5, and ±10 V. To protect against signal transients, the NI 9205 includes up to 60 V of overvoltage protection between input channels and common (COM). In addition, the NI 9205 also includes a channel-to-earth-ground double isolation barrier for safety, noise immunity, and high common-mode voltage range. It is rated for 1,000 Vrms transient overvoltage protection.

There are two connector options for the NI 9205: a 36-position spring terminal connector for direct connectivity or a 37-position D-Sub connector. To add strain relief and high-voltage protection to the 36-position terminal of the NI 9205, NI recommends the NI 9940 strain-relief connector accessory.

The NI 9205 with D-Sub option has an industry-standard 37-position D-Sub connector that provides a low-cost cabling option to a wide variety of accessories available from NI or other vendors. A number of vendors who provide custom D-Sub cable fabrication services, can provide cables with a pin-out that matches your exact application needs. The NI 9933 (or other 37-pin D-Sub connector) is required for use with the NI 9205 with D-Sub. The NI 9933 includes a screw-terminal connector with strain relief as well as a D-Sub solder cup backshell for creating custom cable assemblies.

Specifications

Specifications Documents

- Specifications
- Data Sheet

Specifications Summary

General

Product Name	NI 9205
Product Family	Industrial I/O

Form Factor	CompactDAQ , CompactRIO
Part Number	779519-01
Operating System/Target	Real-Time , Windows
Measurement Type	Voltage
Isolation Type	Ch-Earth Ground Isolation
RoHS Compliant	No
Analog Input	
Channels	32 , 16
Single-Ended Channels	32
Differential Channels	16
Resolution	16 bits
Sample Rate	250 kS/s
Max Voltage	10 V
Maximum Voltage Range	-10 V , 10 V
Maximum Voltage Range Accuracy	6220 µV
Minimum Voltage Range	-0.2 V , 0.2 V
Minimum Voltage Range Accuracy	157 µV
Simultaneous Sampling	No
Analog Output	
Channels	0
Digital I/O	
Bidirectional Channels	0
Input-Only Channels	0
Output-Only Channels	0
Number of Channels	0
Counter/Timers	
Counters	0
Physical Specifications	
Length	9 cm
Width	2.3 cm
I/O Connector	36-position spring terminal , 37-pin D-Sub

Minimum Operating Temperature	-40 °C
Maximum Operating Temperature	70 °C
Minimum Storage Temperature	-40 °C
Maximum Storage Temperature	85 °C
Timing/Triggering/Synchronization	
Triggering	Analog
Triggers cDAQ Chassis	No

Pricing

NI 9205 Packages

To use the NI 9205 , you need all items in the diagram below. Select Option 1 if you already own a C Series System, or Option 2 if you do not already own a chassis, controller, or software.

Roll over the icons below to learn why you need each item in the system

C Series System

NI 9205	Chassis	PC/Controller	Software

- Option 1: **NI 9205 and Accessories Only**
- Option 2: **C Series System**

NI 9205

Spring Terminal Connectivity 779519-01	Qty		$ 823 each
37-Pin D-SUB Front-Mounted Accessories Cabled Accessories 779357-01	Qty	0	$ 723 each
Conformal Coating & D-Sub Connector Front-Mounted Accessories Cabled Accessories 780173-01	Qty	0	$ 874 each

Optional Accessories Hide

Strain relief backshell (qty 1) - 779567-01	Qty	$ 30 each
Extra spring-terminal block (qty 1) - 196740-01	Qty	$ 40 each
Compliant Calibration for NI Distributed I/O - 960460-03	Qty	$ 280 each

Estimated Shipping Days: 5 - 10
Package Price: $ 853

Add to Cart >>

Guarantee your price for 30 days (learn more) Instant Quote

Save for Later

Select a Platform and Configure a System

Create a complete system with the NI 9205 and its accessories. However, the NI 9205 is compatible with multiple C Series Platforms, NI CompactDAQ and CompactRIO. Please review the comparison information below and select a platform to begin configuring your system.

Configure System

Configure System

	NI CompactDAQ	**CompactRIO**
	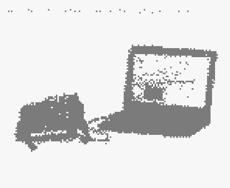	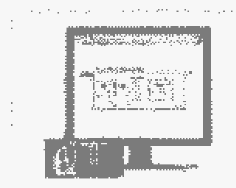
	Mixed-Measurements Customizable with a variety of chassis and module types. Learn more	**Deterministic & Rugged** Time-Critical Control & Monitoring Learn more
Features	NI CompactDAQ	CompactRIO
Bus	USB, Wi-Fi, Ethernet	Ethernet
Operating Temperature	-20 to 50 C	-40 to 70 C
Programming Languages	LabVIEW, C, C++, VB.NET, C#.NET	LabVIEW, LabVIEW RT, LabVIEW FPGA only
System Control	PC Based	Headless Embedded Controller (Standalone or network)
Ruggedness	Laboratory - 30 g shock and 0.3 grms operational vibration	Field Work - 50 g shock (Class I, Div 2 for Hazardous Locations)

The chassis provides rugged, modular housing for your controller (if using CompactRIO) and C Series modules. A high-performance backplane in the chassis contains the system's data, timing, and triggering buses.
The controller runs your application and interfaces with your C Series modules. If you are using the NI CompactDAQ platform, then a Personal Computer (PC) will act as the controller of your system. However, if the CompactRIO platform is used then an embedded real-time controller will be used instead.
You need software to interface with your hardware and to collect, analyze, present, and store your measurements. This device is compatible with a different programming languages depending on the platform used. If you are using the NI CompactDAQ platform then this device is compatible with LabVIEW, C/C++, Visual Basic, and .NET. However, if the CompactRIO platform is used than this device requires the LabVIEW FPGA Module (sold separately), the LabVIEW Real-Time Module (sold separately) and NI-RIO driver

software (included with the hardware).
You have selected **United States** as the country where you will use the product(s) (change).

Services

System Assurance Programs

Reduce your setup time and total cost of ownership, and get a system you can use out of the box with National Instruments system assurance programs. System assurance programs include:

- Installation and integration test of all individual hardware
- Courtesy installation of system driver sets and application development environments
- Extended warranty and calibration coverage for up to five years
- Custom documentation plus a custom restore and startup utility

This service is only available for PXI, NI CompactRIO, and NI Compact FieldPoint systems.

- **Learn More about System Configuration and Deployment Services** [http://www.ni.com/services/configuration.htm]
- **Customize Your CompactRIO System** [http://ohm.ni.com/advisors/crio]
- **Customize Your Compact FieldPoint System** [http://ohm.ni.com/advisors/cfp]
- **Customize Your PXI System** [http://ohm.ni.com/advisors/pxi]
- **Talk to an Expert about Custom System Configurations** [javascript:openCallMeWindowCTA(document.referrer,%20'US')]

Extended Warranties

National Instruments designs and manufactures all products to minimize failures, however unexpected failures can still occur. Extended warranties provide a fixed economical price at the time of system purchase, covering any repair costs for up to three years. In addition, they offer the following benefits:

- Significant cost savings compared to individual repair incidents
- Fault location, diagnostics, and repair by NI any time the system product fails
- All parts and labor costs covered as well as any adjustments needed to restore the hardware to manufacturing specifications

For more information about your warranty options:

- **Learn More about Warranty Services** [http://www.ni.com/services/warranty.htm]
- **Talk to an Expert about Extended Warranties** [javascript:openCallMeWindowCTA(document.referrer,%20'US')]
- **View Warranty Repair Policies** [http://www.ni.com/services/warranty_repair_policies.htm]

Calibration

NI recognizes the need to maintain properly calibrated devices for high-accuracy measurements. NI provides manual calibration procedures, services to recalibrate your products, and automated calibration software to calibrate many NI measurement products.

- **Learn More about Calibration Services** [http://www.ni.com/services/calibration.htm]

Training

NI training is the fastest, most certain route to productivity with NI tools and successful application development.

- **Learn More about NI Training and Certification** [http://www.ni.com/training/]
- **Find a Course Near You and View Schedules** [http://sine.ni.com/apps/utf8/niev.courses]

Repair Services

Return your registered product under warranty at no additional labor and parts cost. NI offers fault location, diagnostics, and repair any time the system fails as well as any adjustments needed to restore the hardware to manufacturing specifications.

- **Learn More about Repair Services** [http://www.ni.com/services/warranty.htm]
- **Contact NI to Obtain a Return Material Authorization (RMA) Form and Shipping Instructions** [http://sine.ni.com/apps/utf8/nieco.call_me]
- **View Your RMA Support Request Status Online** [http://www.ni.com/support/servicereq/]
- **Register Your Product** [http://www.ni.com/register]

Technical Support

ni.com/support [http://www.ni.com/support/]

Resources

Additional Product Information

- Manuals (9)
- Dimensional Drawings
- Product Certifications

Related Information

- Learn More About CompactRIO
- Configure Your Complete CompactRIO System
- Learn More about NI CompactDAQ
- Configure Your Complete CompactDAQ System

Technical Sales
United States
(866) 531-6285
info@ni.com

NI cDAQ-9188

NI CompactDAQ 8-Slot Ethernet Chassis

- Choose from more than 50 hot-swappable I/O modules with integrated signal conditioning
- Measure up to 256 channels of electrical, physical, mechanical, or acoustic signals
- Run up to seven hardware-timed analog I/O, digital I/O, or counter/timer operations simultaneously
- Stream continuous waveform measurements with patented NI Signal Streaming technology
- Simplify setup with zero configuration networking and a built-in Web-based configuration utility
- Measure in minutes with NI-DAQmx software and automatic code generation using the DAQ Assistant

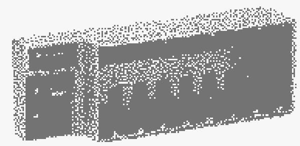

Overview

The NI cDAQ-9188 is an 8-slot NI CompactDAQ Ethernet chassis designed for remote or distributed sensor and electrical measurements. A single NI CompactDAQ chassis can measure up to 256 channels of electrical, physical, mechanical, or acoustic signals. By combining more than 50 sensor-specific NI C Series I/O modules with patented NI Signal Streaming technology, the NI CompactDAQ platform delivers high-speed data and ease of use in a flexible, mixed-measurement system.

Modules are available for a variety of sensor measurements including thermocouples, RTDs, strain gages, load and pressure transducers, torque cells, accelerometers, flow meters, and microphones. NI CompactDAQ systems combine sensor measurements with voltage, current, and digital signals to create custom, mixed-measurement systems with a single Ethernet interface back to a host PC or laptop.

The cDAQ-9188 has four 32-bit general-purpose counter/timers built in. You can access these counters through a hardware-timed digital C Series module such as the NI 9401 for applications that involve quadrature encoders, PWM, event counting, pulse train generation, and period or frequency measurement.

The cDAQ-9188 chassis is shipped with the following:

- AC/DC converter that plugs directly into the chassis

- NI-DAQmx driver DVD

- NI screwdriver (flat and Phillips head)

- NI cDAQ-9188 Quick Start poster

Power cord sold separately.

The NI-DAQmx driver is shipped with every chassis and includes the following:

- LabVIEW SignalExpress LE for simple data-logging applications

- Programming support for NI LabVIEW, ANSI C/C++, C#, and Visual Basic .NET
- DAQ Assistant code generation for LabVIEW, LabWindows™/CVI, and Measurement Studio
- Example programs for all supported languages
- NI Measurement & Automation Explorer (MAX) for system configuration and test

Specifications

Specifications Documents

- Specifications
- Data Sheet

Specifications Summary

General	
Product Name	cDAQ-9188
Form Factor	Ethernet , CompactDAQ
Product Type	Chassis
Part Number	781424-01
Operating System/Target	Windows
LabVIEW RT Support	No
Operating Relative Humidity	10 percent , 90 percent
Chassis	
Number of Slots	8
Total Available Power	15 W
Input Voltage Range	9 V , 30 V
Built-In Trigger	Yes
Counter/Timers	
Counters	4
Resolution	32 bits
Bus Interface	
High-Performance Data Streams	7
Types Available	Analog Input , Digital Output , Counter/Timer Input , Analog Output , Digital Input
Ethernet	
Network Interface	1000BaseT

Shock and Vibration	
Operational Shock	30 g
Random Operating Frequency Range	5 Hz , 500 Hz
Random Vibration	0.3 g
Physical Specifications	
Length	25.4 cm
Width	8.81 cm
Height	5.89 cm
Weight	900 gram
Minimum Operating Temperature	-20 °C
Maximum Operating Temperature	55 °C
Maximum Altitude	5000 m

Pricing

Part Number	Description	Est Ship	US Dollars*	Qty
NI CompactDAQ Chassis and Power Cord (Required)				
781424-01	cDAQ-9188, CompactDAQ chassis (8 Slot ENET)	1 - 3	$ 1,399.00	0
763000-01	Power Cord, AC, U.S., 120 VAC, 2.3 meters	10 - 15	$ 8.00	0
763068-01	Power Cord, 240V, 10A, North American	5 - 10	$ 19.00	0
Connectivity, Mounting, and Other Accessories (Optional)				
782436-01	Moxa AWK-3121 IEEE 802.11g Industrial Wireless Access Point	12 - 20	$ 799.00	0
151733-02	Cable Assembly, CAT-5E Ethernet, Thin Profile, 2M	5 - 10	$ 9.00	0
779558-01	NI 9905 Horizontal Panel Mounting Kit for 8-slot Chassis	5 - 10	$ 30.00	0
779473-01	NI 9901 Desktop Mounting Kit	5 - 10	$ 50.00	0
779102-01	NI 9910 Industrial Sliding Rack Mounting Kit for cRIO/cDAQ	5 - 10	$ 102.00	0
779018-01	NI 9915 DIN Rail Kit for 8-slot Chassis	5 - 10	$ 30.00	0
196917-01	NI 9977 C Series Filler Module for Empty Slot	5 - 10	$ 30.00	0
779697-02	BNC Male (plug) to BNC Male (plug) cables,2m, 4 pack of 183882-02	10 - 15	$ 164.00	0
780702-01	2-Position Screw Terminal Kit for Power Supply Connection, Qty 4	5 - 10	$ 9.00	0

* You have selected the United States as the country where you will use the product(s). Pricing may have changed since you printed this document on 10/28/2012. Please visit *ni.com* to see current pricing.

Place Order or Obtain Quote

Order Online or by Fax

1. Navigate to *ni.com/products* and select "Order by Part Number" found under the "Business Center" section.
2. Once you have added your items to your cart, see the "Your Cart Options" section to place your order, obtain a quote, or print a fax form.

Order by Phone
Call (866) 531-6285 to place your order or obtain a quote.

Services

Extended Warranties

National Instruments designs and manufactures all products to minimize failures, however unexpected failures can still occur. Extended warranties provide a fixed economical price at the time of system purchase, covering any repair costs for up to three years. In addition, they offer the following benefits:

- Significant cost savings compared to individual repair incidents
- Fault location, diagnostics, and repair by NI any time the system product fails
- All parts and labor costs covered as well as any adjustments needed to restore the hardware to manufacturing specifications

For more information about your warranty options:

- Learn More About Warranty Services [http://www.ni.com/services/warranty.htm]
- Talk to an Expert About Extended Warranties [javascript:openCallMeWindowCTA(document.referrer,%20'US')]
- View Warranty Repair Policies [http://www.ni.com/services/warranty_repair_policies.htm]

Calibration

NI recognizes the need to maintain properly calibrated devices for high-accuracy measurements. NI provides manual calibration procedures, services to recalibrate your products, and automated calibration software to calibrate many NI measurement products.

- Learn More About Calibration Services [http://www.ni.com/services/calibration.htm]

Training

NI training is the fastest, most certain route to productivity with NI tools and successful application development.

- Learn More About NI Training and Certification [http://www.ni.com/training/]
- Find a Course Near You and View Schedules [http://sine.ni.com/apps/utf8/niav.ctsted]

Repair Services

Return your registered product under warranty at no additional labor and parts cost. NI offers fault location, diagnostics, and repair any time the system fails as well as any adjustments needed to restore the hardware to manufacturing specifications.

- Learn More About Repair Services [http://www.ni.com/services/warranty.htm]
- Contact NI to obtain a Return Material Authorization (RMA) form and shipping instructions. [http://sine.ni.com/apps/utf8/nicc.call_me]
- View your RMA support request status online. [http://www.ni.com/support/servicereq/]
- Register your product [http://www.ni.com/register/] .

Technical Support

ni.com/support [http://www.ni.com/support/]

Resources

Additional Product Information

- Manuals (7)
- Dimensional Drawings
- Product Certifications

Related Information

- Learn More about NI CompactDAQ Technology
- Read the NI CompactDAQ Ethernet Chassis Overview
- Watch the NI CompactDAQ Ethernet Chassis Out-of-Box Video Demonstration
- Get Started with NI CompactDAQ and LabVIEW Tutorials
- View the NI C Series Module Compatibility Table

APPENDIX D

SIGNAL ROUTING WIRE DIAGRAMS

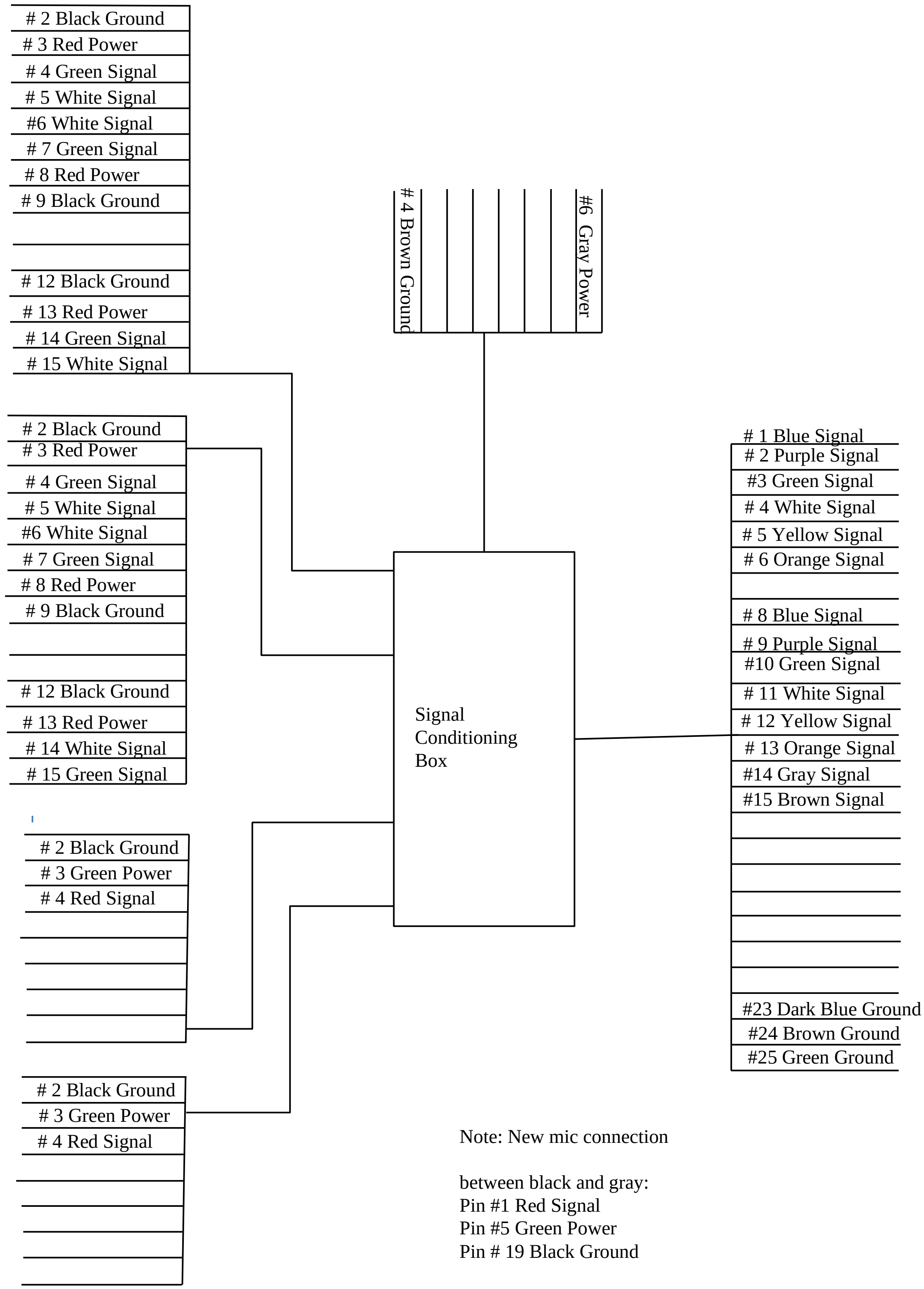

Note: New mic connection

between black and gray:
Pin #1 Red Signal
Pin #5 Green Power
Pin # 19 Black Ground

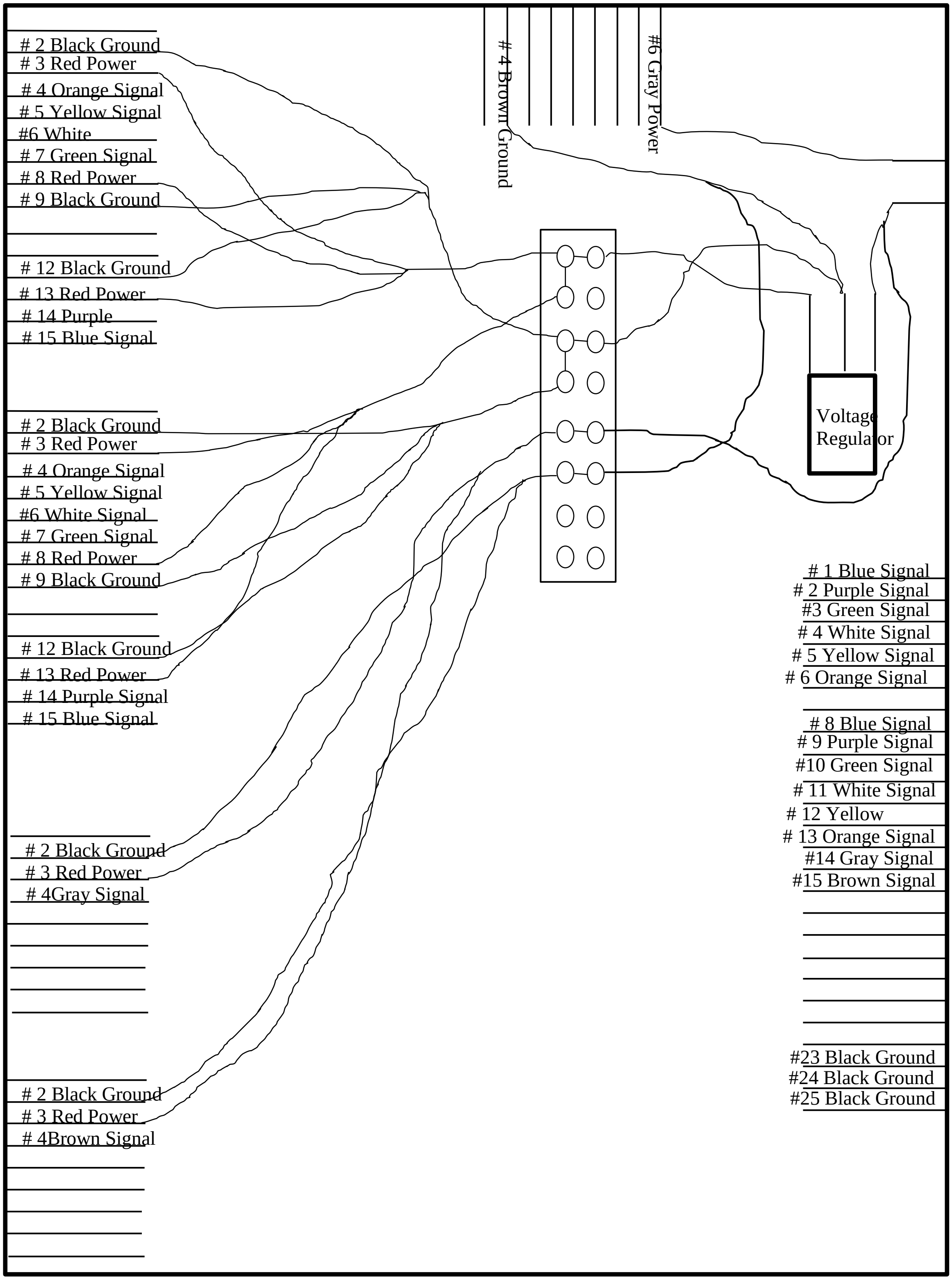
2 Black Ground
3 Red Power
4 Orange Signal
5 Yellow Signal
#6 White
7 Green Signal
8 Red Power
9 Black Ground
12 Black Ground
13 Red Power
14 Purple
15 Blue Signal
4 Brown Ground
#6 Gray Power
2 Black Ground
3 Red Power
4 Orange Signal
5 Yellow Signal
#6 White Signal
7 Green Signal
8 Red Power
9 Black Ground
12 Black Ground
13 Red Power
14 Purple Signal
15 Blue Signal
Voltage Regulator
1 Blue Signal
2 Purple Signal
#3 Green Signal
4 White Signal
5 Yellow Signal
6 Orange Signal
8 Blue Signal
9 Purple Signal
#10 Green Signal
11 White Signal
12 Yellow
13 Orange Signal
#14 Gray Signal
#15 Brown Signal
2 Black Ground
3 Red Power
4Gray Signal
#23 Black Ground
#24 Black Ground
#25 Black Ground
2 Black Ground
3 Red Power
4Brown Signal

APPENDIX E

EXPLOSIVE DATA SHEETS

Technical Data Sheet

The Power of Partnership

Pentex™ AP Cast Boosters

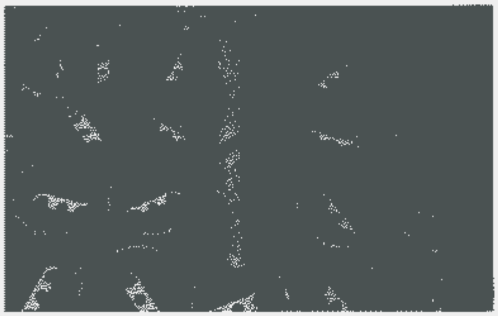

Description

Pentex™ AP Cast Boosters provide high energy initiating power for a wide range of explosive applications. The recessed groove in the base of *Pentex™ AP Cast Boosters* ensures reliable initiation with all types of detonator assemblies. They can be used to provide safe and reliable priming of booster sensitive explosives on most surface and underground blasting operations.

Benefits

- High velocity
- High density
- High detonation pressure
- Unlimited shelf life under proper storage conditions
- Excellent water resistance
- High safety and reliability
- Concentrated detonation energy

Initiation and Handling

Pentex™ AP Cast Boosters can be initiated by standard high strength electric, electronic and non-electric detonators or by 18 grain/ft. (3.6 gram/m) detonating cord threaded into the center through tunnel.

When used with booster-sensitive explosives, ensure that the primer is in intimate contact with, and surrounded by, the explosive.

Properties

Pentex™ AP Cast Boosters	12 * 340 (ounce * gram)	16 * 454 (ounce * gram)	32 * 908 (ounce * gram)
Diameter x Length	53 mm x 120	60 mm x 120	84 mm x 120
	2.106" x 4.724"	2.382" x 4.724"	3.299" x 4.724"
Density	1.6 g/cc		
Velocity of Detonation	7,924 m/s (26,000 ft/s)		
Detonation Pressure	250 kb		
Water	Excellent		
Tunnel Arrangement	One blind detonator well and two through tunnels		

Packaging

Pentex™ AP Cast Boosters are packed in fiberboard cases.

Product	Quantity Per Case	Weight per case (lbs/kg)
Pentex™ AP 12* 340	42	36/16
Pentex™ AP 16* 454	35	39/17.5
Pentex™ AP 32* 908	18	40/18

Storage

Cast boosters are high explosives. For best results, store under moderate temperatures and dry conditions in a well ventilated, approved explosives magazine.

Shelf Life

If stored and handled properly, the **shelf life** of *Pentex™ AP Cast Boosters* is unlimited.

Pentex

V4 April 2008

ORICA

www.oricaminingservices.com

Technical Data Sheet

The Power of Partnership

Pentex™ AP Cast Boosters

Hazardous Materials Shipping Description

Boosters, without detonator
Class and Division 1.1D,
UN 0042, PG II

Distributed to Orica by BST Manufacturing, Inc.
924 Hawaii Avenue, Minden, LA 71055 USA

Trademarks

The word Orica, the Ring device and the Orica mark are trademarks of Orica Group Companies. *Pentex™* is a trademark of Orica Explosives Technology Pty Ltd. ACN 075 659 353, 1 Nicholson Street, East Melbourne, VIC, Australia.

Disclaimer

The information contained herein is based on experience and is believed to be accurate and up to date as at the date of its preparation. However, uses and conditions of use are not within the manufacturer's control and users should determine the suitability of such products and methods of use for their purposes. Neither the manufacturer nor the seller makes any warranty of any kind, express or implied, statutory or otherwise, except that the products described herein shall conform to the manufacturer's or seller's specifications. The manufacturer and the seller expressly disclaim all other warranties, INCLUDING, WITHOUT LIMITATION, WARRANTIES CONCERNING MERCHANTABILITY OR FITNESS FOR A PARTICULAR PURPOSE. Under no circumstances shall the manufacturer or the seller be liable for indirect, special, consequential, or incidental damages without limitation, damages for lost or anticipated profits.

Orica Canada Inc.
301 Hotel De Ville
Brownsburg, QC J8G 3B5
Tel: +1 303 268 5000
Fax: +1 303 268 5250

Orica USA Inc.
33101 East Quincy Ave
Watkins, CO 80137
Tel: +1 303 268 5000
Fax: +1 303 268 5250

Emergency Contact Telephone Numbers

For chemical emergencies (24 hour) involving transportation, spill, leak, release, fire or accidents:
Canada: Orica Canada emergency response **1-877-561-3636**
USA: Chemtrec **1-800- 424-9300**

For lost, stolen or misplaced explosives:
USA: BATFE **1-800-800-3855**. Form ATF F5400.0 must be completed and local authorities (state / municipal police, etc) must be advised.

Technical Data Sheet

The Power of Partnership

avtrol™ Avalanche DUO Cast Boosters

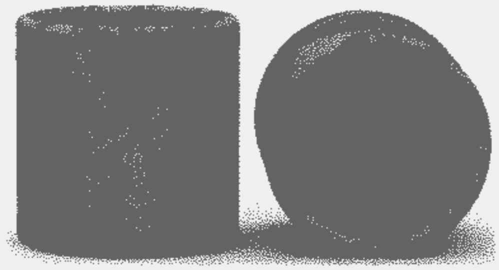

Description

Avalanche DUO Family of Cast Boosters provide high energy power for a wide range of DUO primed avalanche explosive applications. The recessed groove in the base of *Avalanche DUO Cast Booster* ensures reliable initiation with all types of detonator assemblies. They can be used as a hand charge or to provide safe and reliable priming of booster sensitive explosives.

Benefits

- 100% of the booster is detonator sensitive. No PETN balloon or bottle required
- High velocity & High detonation pressure
- Unlimited shelf life under proper storage conditions
- Excellent water resistance
- High safety and reliability in extreme conditions

Initiation and Handling

Avalanche DUO Cast Boosters can be initiated by standard high strength electric, electronic and non-electric detonators.

Note: Detonating cords are not to be used to initiate Avalanche DUO 32 or 80 cast boosters.

Avalanche DUO products are made to be "double capped" with a detonator in each of the 2 blind tunnels.

When used with booster-sensitive explosives, ensure that the primer is in intimate contact with, and surrounded by, the explosive.

Properties

Avalanche DUO Cast Booster	32 * 908 (ounce * gram)	80 * 2,270 (ounce * gram)
Diameter x Length	80 mm x 126 mm	120 mm x 133 mm
	3.15" x 4.95"	4.72" x 5.25"
Density	1.6 g/cc	
Velocity of Detonation	7,924 m/s (26,000 ft/s)	
Detonation Pressure	250 kb	
Water Resistance	Excellent	
Tunnel Arrangement	Two blind detonator wells and one through tunnels	

Packaging

Avalanche Duo Cast Boosters are packed in fiberboard cases.

Product	Quantity Per Case	Weight per case (lbs/kg)
Avalanche DUO 32* 908	18	39/17.7
Avalanche DUO 80 * 2270	6	32/14.5

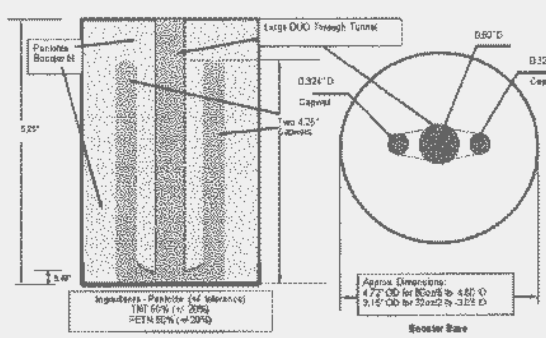

avtrol™

November 2010 v3

1 of 2

ORICA

Technical Data Sheet

The Power of Partnership

avtrol™ Avalanche DUO Cast Boosters

Storage

Cast boosters are high explosives. For best results, store under moderate temperatures and dry conditions in a well ventilated, approved explosives magazine.

Shelf Life

If stored and handled properly, the shelf life of *Avalanche DUO Cast Boosters* is unlimited.

Storage and Handling Product Classification

Authorized Name:	*Avalanche DUO*
Proper Shipping Name:	Boosters, without detonator
Classification:	1.1D
UN No:	UN0042 (boosters w/o detonator)
Packing Group:	II
EX Number:	EX2004120254

All regulations pertaining to the handling and use of such explosives apply.

Distributed to Orica by BST Manufacturing, Inc.
924 Hawaii Avenue, Minden, LA 71055 USA

Trademarks

Disclaimer

The information contained herein is based on experience and is believed to be accurate and up to date as at the date of its preparation. However, uses and conditions of use are not within the manufacturer's control and users should determine the suitability of such products and methods of use for their purposes. Neither the manufacturer nor the seller makes any warranty of any kind, express or implied, statutory or otherwise, except that the products described herein shall conform to the manufacturer's or seller's specifications. The manufacturer and the seller expressly disclaim all other warranties, INCLUDING, WITHOUT LIMITATION, WARRANTIES CONCERNING MERCHANTABILITY OR FITNESS FOR A PARTICULAR PURPOSE. Under no circumstances shall the manufacturer or the seller be liable for indirect, special, consequential, or incidental damages without limitation, damages for lost or anticipated profits.

Orica Canada Inc.	Orica USA Inc.
301 Hotel De Ville	33101 East Quincy Ave
Brownsburg, QC J8G 3B5	Watkins, CO 80137
Tel: +1 303 268 5000	Tel: +1 303 268 5000
Fax: +1 303 268 5250	Fax: +1 303 268 5250
Web address:	www.orica-avtrol.com

Emergency Contact Telephone Numbers

For chemical emergencies (24 hour) involving transportation, spill, leak, release, fire or accidents:
Canada: Orica Canada emergency response **1-877-561-3636**
USA: Chemtrec **1-800- 424-9300**

For lost, stolen or misplaced explosives:
USA: BATFE **1-800-800-3855**. Form ATF F5400.0 must be completed and local authorities (state / municipal police, etc) must be advised.

avtrol

November 2010 v3
2 of 2

ORICA

APPENDIX F

OVERPRESSURE DATA

Peak overpressure values measured at the snow surface 5 m radially from the detonation for soft slab snow investigations taken during the 2010-2011 testing season. The 0.9 kg and 0.45 kg charges are in separate tables organized by charge location relative to the snowcover surface.

2010-2011 Dry and Moist Soft Slab Snow Data for 0.9 kg Pentolite Cast Booster						
	Dry Snow			Moist Snow		
Charge Height	Peak Over-pressure (psi)	Positive Impulse (psi*sec)	Negative Impulse (psi*sec)	Peak Over-pressure (psi)	Positive Impulse (psi*sec)	Negative Impulse (psi*sec)
0 m	3.10	0.00685	-0.00689			
0.5 m	4.08	0.00685	-0.00689	4.54	0.00500	-0.00562
1 m	4.78	0.00762	-0.00759	4.50	0.00925	-0.00932
	5.15	0.00836	-0.00874			
	5.16	0.00830	-0.00879			
Average	5.03	0.00809	-0.00837			
1.5 m	4.21	0.00719	-0.00696	5.16	0.00958	-0.00938
2 m	4.11	0.00706	-0.00730	5.16	0.00946	-0.01018
	4.62	0.00807	-0.00841			
	5.16	0.00836	-0.01050			
Average	4.63	0.00783	-0.00873			

2010-2011 Dry and Moist Soft Slab Snow Data for 0.45 kg Pentolite Cast Booster						
	Dry Snow			Moist Snow		
Charge Height	Peak Over-pressure (psi)	Positive Impulse (psi*sec)	Negative Impulse (psi*sec)	Peak Over-pressure (psi)	Positive Impulse (psi*sec)	Negative Impulse (psi*sec)
0 m	2.18	0.00318	-0.00394			
0.5 m	2.68	0.00400	-0.00395	2.74	0.00461	-0.00399
1 m	2.18	0.00533	-0.00546	3.62	0.00558	-0.00568
	2.74	0.00436	-0.00465			
Average	2.85	0.00509	-0.00527			
1.5 m	2.99	0.00495	-0.00517	4.32	0.00562	-0.00508
2 m	3.23	0.00586	-0.00594	3.20	0.00534	-0.00534

Peak overpressure values resulting from 0.9 kg pentolite cast boosters detonated 1 m above the snow surface. The sensors were located 7 m radially from the charge. One sensor was on the surface and the other 1.5 m elevated above the surface.

2011-2012 Moist Hard Slab Snow Data for 0.9 kg Pentolite Cast Boosters						
	Surface Sensor			1.5 m Elevated Surface		
Charge Height	Peak Over-pressure (psi)	Positive Impulse (psi*sec)	Negative Impulse (psi*sec)	Peak Over-pressure (psi)	Positive Impulse (psi*sec)	Negative Impulse (psi*sec)
1 m	3.98	0.00780	-0.00860	3.13	0.00735	-0.00797
	4.02	0.00764	-0.00868	3.30	0.00796	-0.01210
	4.00	0.00751	-0.01600	3.17	0.00756	-0.01604
	3.45	0.00767	-0.00843	3.32	0.00746	-0.00818
	4.81	0.00952	-0.01016	3.31	0.00791	-0.01114
Average	4.05	0.00803	-0.01037	3.25	0.00765	-0.01109
Std. Dev.	0.48	0.00084	0.00322	0.09	0.00027	0.00331

APPENDIX G

SNOW ACCELERATION DATA

Soft slab snow acceleration data from 2010-2011 testing season for 0.9 kg pentolite cast booster detonations organized by charge detonation location referenced to the snow surface. Dry and moist snow conditions are presented in separate tables.

2010-2011 Dry Soft Slab Snow Data for 0.9 kg Pentolite Cast Booster							
Charge Height		2 m Radial Distance			5 m Radial Distance		
		Top	Middle	Bottom	Top	Middle	Bottom
0 m	Scaled Depth (m/kg$^{1/3}$)	0.11	0.35	0.57	0.11	0.35	0.57
	Resultant (m/sec^2)	145.37	115.69	76.00	35.09	25.27	21.44
0.5 m	Scaled Depth (m/kg$^{1/3}$)	0.11	0.35	0.57	0.11	0.35	0.57
	Resultant (m/sec^2)	159.57	96.04	90.03	28.51	22.23	21.51
1 m	Scaled Depth (m/kg$^{1/3}$)	0.11	0.35	0.57	0.11	0.35	0.57
	Resultant (m/sec^2)	197.21	101.34	84.58	61.54	34.41	31.94
	Scaled Depth (m/kg$^{1/3}$)	0.08	0.32	0.50	0.08	0.32	0.50
	Resultant (m/sec^2)	355.11	78.88	60.63	68.13	18.74	17.30
	Scaled Depth (m/kg$^{1/3}$)	0.11	0.35	0.57	0.11	0.35	0.57
	Resultant (m/sec^2)	268.19	135.31	65.68	41.86	30.31	18.60
Average Resultant (m/sec^2)		273.50	105.18	70.30	57.18	27.82	22.61
Average Depth (m/kg$^{1/3}$)		0.10	0.34	0.55	0.10	0.34	0.55
1.5 m	Scaled Depth (m/kg$^{1/3}$)	0.11	0.35	0.57	0.11	0.35	0.57
	Resultant (m/sec^2)	173.39	106.66	69.09	34.18	22.92	20.38
2 m	Scaled Depth (m/kg$^{1/3}$)	0.11	0.35	0.57	0.11	0.35	0.57
	Resultant (m/sec^2)	213.11	144.88	171.25	50.55	24.54	17.33
	Scaled Depth (m/kg$^{1/3}$)	0.08	0.32	0.50	0.08	0.32	0.50
	Resultant (m/sec^2)	218.55	179.09	54.05	23.77	20.72	21.68
	Scaled Depth (m/kg$^{1/3}$)	0.11	0.35	0.57	0.11	0.35	0.57
	Resultant (m/sec^2)	437.42	120.44	85.55	54.91	26.41	20.30
Average Resultant (m/sec^2)		289.69	148.14	103.62	43.08	23.89	19.77
Average Depth (m/kg$^{1/3}$)		0.10	0.34	0.55	0.10	0.34	0.55

2010-2011 Moist Soft Slab Snow Data for 0.9 kg Pentolite Cast Booster							
Charge Height		2 m Radial Distance			5 m Radial Distance		
		Top	Middle	Bottom	Top	Middle	Bottom
0.5 m	Scaled Depth (m/kg$^{1/3}$)	0.11	0.35	0.57	0.11	0.35	0.57
	Resultant (m/sec^2)	153.79	45.19	25.76	33.66	10.95	10.11
1 m	Scaled Depth (m/kg$^{1/3}$)	0.11	0.35	0.57	0.11	0.35	0.57
	Resultant (m/sec^2)	245.21	72.91	46.13	47.75	12.15	12.13
1.5 m	Scaled Depth (m/kg$^{1/3}$)	0.11	0.35	0.57	0.11	0.35	0.57
	Resultant (m/sec^2)	129.22	47.91	33.28	38.46	10.83	7.83
2 m	Scaled Depth (m/kg$^{1/3}$)	0.11	0.35	0.57	0.11	0.35	0.57
	Resultant (m/sec^2)	130.48	53.91	53.91	52.23	12.88	6.88

Acceleration data for 0.45 kg pentolite detonations obtained during the 2010-2011 testing season for soft slab snow investigations. Dry and moist snow conditions are in separate tables and organized by charge elevation.

2010-2011 Dry Soft Slab Snow Data for 0.45 kg Pentolite Cast Booster							
Charge Height		2 m Radial Distance			5 m Radial Distance		
		Top	Middle	Bottom	Top	Middle	Bottom
0 m	Scaled Depth (m/kg$^{1/3}$)	0.14	0.44	0.72	0.14	0.44	0.72
	Resultant (m/sec^2)	163.18	107.93	65.99	27.48	15.43	13.77
0.5 m	Scaled Depth (m/kg$^{1/3}$)	0.14	0.44	0.72	0.14	0.44	0.72
	Resultant (m/sec^2)	203.53	143.01	78.57	39.06	21.26	15.87
1 m	Scaled Depth (m/kg$^{1/3}$)	0.14	0.44	0.72	0.14	0.44	0.72
	Resultant (m/sec^2)	181.68	119.26	81.22	27.95	23.95	21.38
	Scaled Depth (m/kg$^{1/3}$)	0.09	0.34	0.48	0.11	0.34	0.53
	Resultant (m/sec^2)	120.09	84.34	63.01	27.17	19.02	16.81
Average Resultant (m/sec^2)		150.88	101.80	72.11	27.56	21.49	19.10
Average Depth (m/kg$^{1/3}$)		0.12	0.39	0.60	0.12	0.39	0.63
1.5 m	Scaled Depth (m/kg$^{1/3}$)	0.14	0.44	0.72	0.14	0.44	0.72
	Resultant (m/sec^2)	174.23	114.86	91.64	34.17	21.87	17.54
2 m	Scaled Depth (m/kg$^{1/3}$)	0.14	0.44	0.72	0.14	0.44	0.72
	Resultant (m/sec^2)	140.12	112.17	59.09	39.26	26.36	18.74

2010-2011 Moist Soft Slab Snow Data for 0.45 kg Pentolite Cast Booster							
Charge Height		2 m Radial Distance			5 m Radial Distance		
		Top	Middle	Bottom	Top	Middle	Bottom
0.5 m	Scaled Depth ($m/kg^{1/3}$)	0.14	0.44	0.72	0.14	0.44	0.72
	Resultant (m/sec^2)	99.53	76.83	76.33	19.88	16.97	10.00
1 m	Scaled Depth ($m/kg^{1/3}$)	0.14	0.44	0.72	0.14	0.44	0.72
	Resultant (m/sec^2)	107.89	65.63	68.08	28.79	13.98	10.12
1.5 m	Scaled Depth ($m/kg^{1/3}$)	0.14	0.44	0.72	0.14	0.44	0.72
	Resultant (m/sec^2)	127.23	71.64	34.09	27.05	18.33	13.27
2 m	Scaled Depth ($m/kg^{1/3}$)	0.14	0.44	0.72	0.14	0.44	0.72
	Resultant (m/sec^2)	127.27	54.41	57.63	25.79	16.98	10.80

Hard slab snow acceleration data for the 2011-2012 testing season for 0.9 kg pentolite cast boosters. All data is for moist snow conditions and all tests for a specific charge elevation are presented together with average values as well.

2011-2012 Moist Hard Slab Snow Data for 0.9 kg Pentolite Cast Booster							
Charge Height		3 m Radial Distance			5 m Radial Distance		
		Top	Middle	Bottom	Top	Middle	Bottom
0 m	Scaled Depth ($m/kg^{1/3}$)	0.23	0.52	0.77	0.23	0.52	0.77
	Resultant (m/sec^2)	38.69	34.96	19.27	26.41	9.33	5.42
	Scaled Depth ($m/kg^{1/3}$)	0.19	0.47	0.75	0.19	0.47	0.75
	Resultant (m/sec^2)	52.05	26.03	13.20	22.52	12.68	6.01
	Scaled Depth ($m/kg^{1/3}$)	0.19	0.47	0.75	0.19	0.47	0.75
	Resultant (m/sec^2)	60.16	10.54	15.31	28.40	14.01	6.12
Average Resultant (m/sec^2)		50.30	23.84	15.93	25.78	12.01	5.85
Average Depth ($m/kg^{1/3}$)		0.20	0.49	0.76	0.20	0.49	0.76
0.5 m	Scaled Depth ($m/kg^{1/3}$)	0.23	0.52	0.77	0.23	0.52	0.77
	Resultant (m/sec^2)	92.08	89.44	35.33	40.78		17.64
	Scaled Depth ($m/kg^{1/3}$)	0.19	0.47	0.75	0.19	0.47	0.75
	Resultant (m/sec^2)	66.81	29.12	17.33	32.05	15.97	8.06
	Scaled Depth ($m/kg^{1/3}$)	0.19	0.47	0.75	0.19	0.47	0.75
	Resultant (m/sec^2)	94.91	21.88	9.12	31.69	10.02	4.16
Average Resultant (m/sec^2)		84.60	46.81	20.59	34.84	13.00	9.95
Average Depth ($m/kg^{1/3}$)		0.20	0.49	0.76	0.20	0.49	0.76
1 m	Scaled Depth ($m/kg^{1/3}$)	0.23	0.52	0.77	0.23	0.52	0.77
	Resultant (m/sec^2)	128.55	92.06	68.80	32.07	14.53	10.94
	Scaled Depth ($m/kg^{1/3}$)	0.19	0.47	0.75	0.19	0.47	0.75
	Resultant (m/sec^2)	113.42	12.38	7.54	49.00	13.86	8.15
	Scaled Depth ($m/kg^{1/3}$)	0.19	0.47	0.75	0.19	0.47	0.75
	Resultant (m/sec^2)	76.55	44.29	27.55	38.89	11.14	8.60
Average Resultant (m/sec^2)		106.17	49.58	34.63	39.99	13.18	9.23
Average Depth ($m/kg^{1/3}$)		0.20	0.49	0.76	0.20	0.49	0.76
1.5 m	Scaled Depth ($m/kg^{1/3}$)	0.23	0.52	0.77	0.23	0.52	0.77
	Resultant (m/sec^2)	138.42	111.77	39.81	30.00	17.03	10.77
	Scaled Depth ($m/kg^{1/3}$)	0.19	0.47	0.75	0.19	0.47	0.75
	Resultant (m/sec^2)	103.29	75.53	52.42	24.96	12.99	6.54
	Scaled Depth ($m/kg^{1/3}$)	0.19	0.47	0.75	0.19	0.47	0.75
	Resultant (m/sec^2)	61.45	36.05	16.70	45.69	12.23	5.53
Average Resultant (m/sec^2)		101.05	74.45	36.31	33.55	14.08	7.61

Continued 2011-2012 Moist Hard Slab Snow Data for 0.9 kg Pentolite Cast Booster							
Average Depth (m/kg$^{1/3}$)		0.20	0.49	0.76	0.20	0.49	0.76
2 m	Scaled Depth (m/kg$^{1/3}$)	0.23	0.52	0.77	0.23	0.52	0.77
	Resultant (m/sec^2)	151.12	35.60	26.70	56.30	14.37	6.12
	Scaled Depth (m/kg$^{1/3}$)	0.19	0.47	0.75	0.19	0.47	0.75
	Resultant (m/sec^2)	67.19	31.69	24.89	38.81	21.23	12.78
Average Resultant (m/sec^2)		109.15	33.65	25.80	47.55	17.80	9.45
Average Depth (m/kg$^{1/3}$)		0.21	0.50	0.76	0.21	0.50	0.76

Repeatability testing acceleration data obtained in the 2011-2012 testing season for hard slab snow conditions. All charges were 0.9 kg pentolite and located1 m above the snow surface.

2011-2012 Moist Hard Slab Snow Repeatability Data for 0.9 kg Pentolite Cast Booster							
Charge Height		3 m Radial Distance			5 m Radial Distance		
		Top	Middle	Bottom	Top	Middle	Bottom
1 m	Scaled Depth (m/kg$^{1/3}$)	0.19	0.37	0.56	0.19	0.37	0.56
	Resultant (m/sec^2)	54.83	32.30	21.78	14.17	13.03	12.30
	Scaled Depth (m/kg$^{1/3}$)	0.19	0.37	0.56	0.19	0.37	0.56
	Resultant (m/sec^2)	30.89	7.36	8.04	12.72	9.00	7.69
	Scaled Depth (m/kg$^{1/3}$)	0.19	0.37	0.56	0.19	0.37	0.56
	Resultant (m/sec^2)	30.49	24.11	14.58	17.43	11.67	8.51
	Scaled Depth (m/kg$^{1/3}$)	0.19	0.37	0.56	0.19	0.37	0.56
	Resultant (m/sec^2)	45.70	23.72	12.51	27.06	15.91	11.40
	Scaled Depth (m/kg$^{1/3}$)	0.19	0.37	0.56	0.19	0.37	0.56
	Resultant (m/sec^2)	23.41	21.98	15.48	16.26	11.76	6.79
Average Resultant (m/sec^2)		37.06	21.90	14.48	17.53	12.27	9.34
Average Depth (m/kg$^{1/3}$)		0.19	0.37	0.56	0.19	0.37	0.56

APPENDIX H

ACCELERATION AS A FUNCTION OF SENSOR RADIAL DISTANCE

FOR CHARGE PLACEMENT IMPACT ON ACCELERATION

WITH DEPTH AND RANGE

Acceleration as a function of radial distance for acceleration depths (top, middle, and bottom locations throughout the snowpack) illustrating the advantage due to raising an above the snow surface. The advantage is more pronounced in close proximity to the detonation location in both the vertical and radial direction.

2010-2011 Data

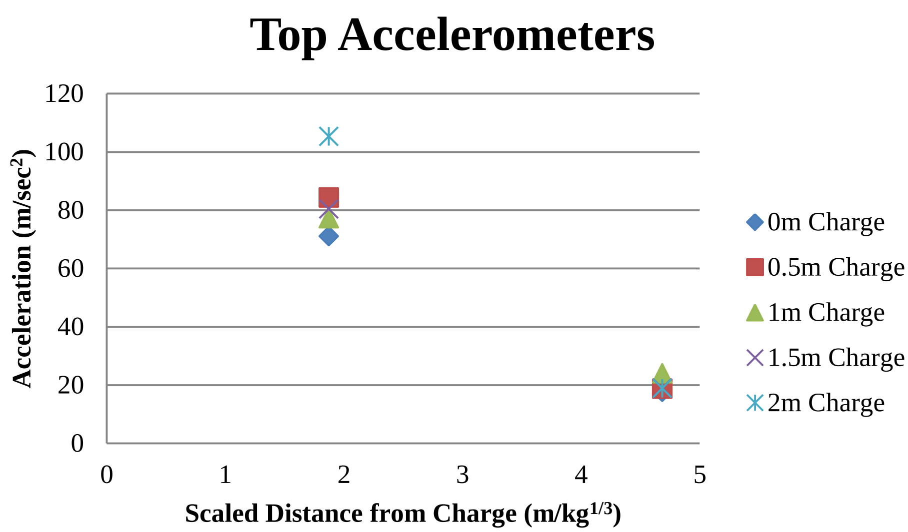

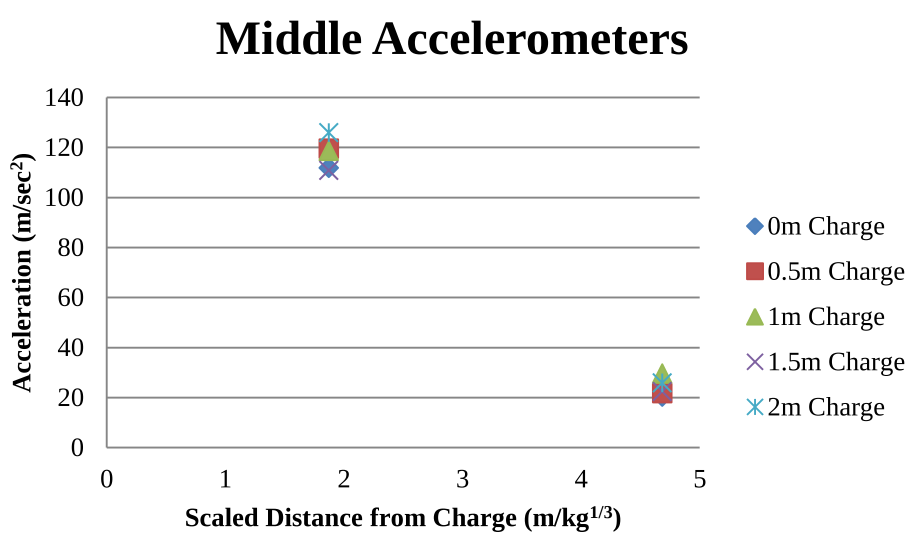

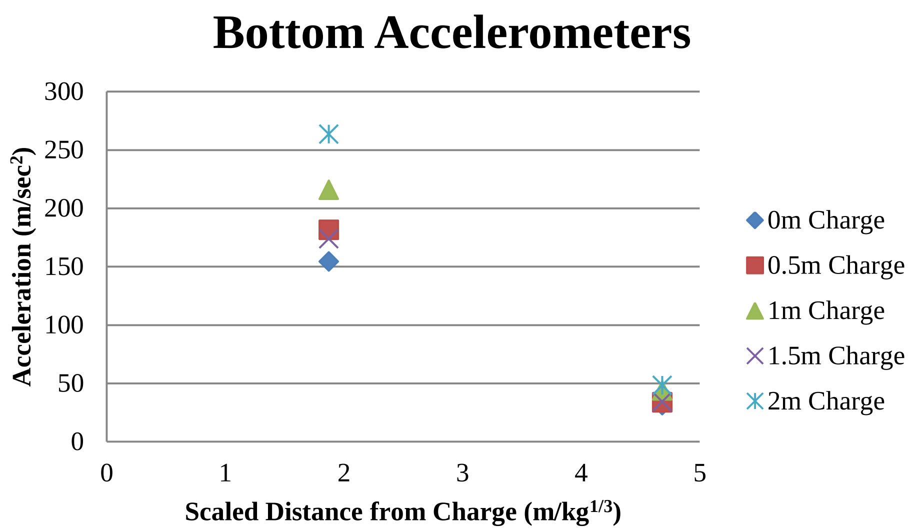

2011-2012 Data

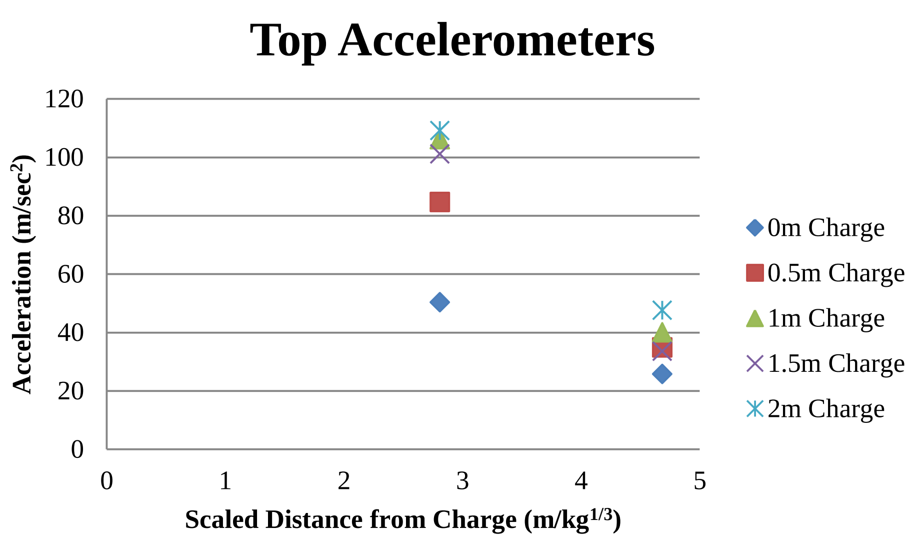

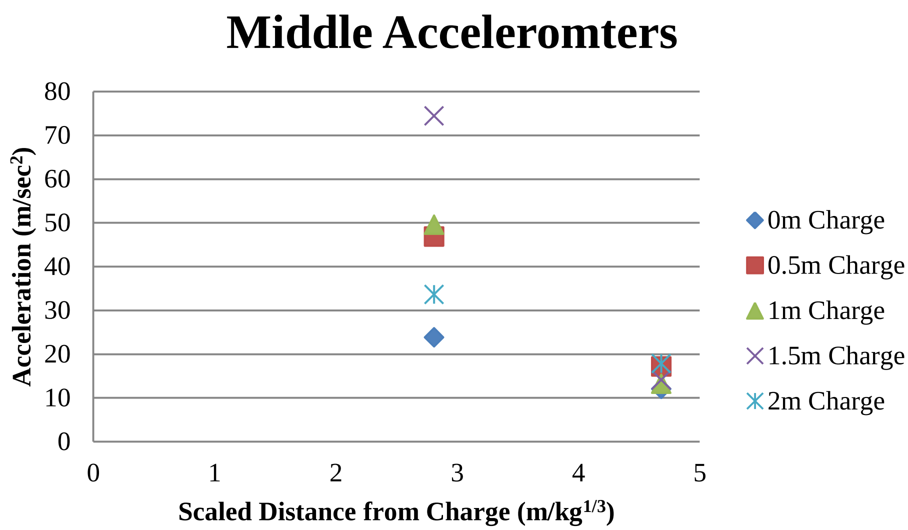
Middle Acceleromters
80
70
60
50
40
30
20
10
0
Acceleration (m/sec2)
0
1
2
3
4
5
Scaled Distance from Charge (m/kg1/3)
0m Charge
0.5m Charge
1m Charge
1.5m Charge
2m Charge

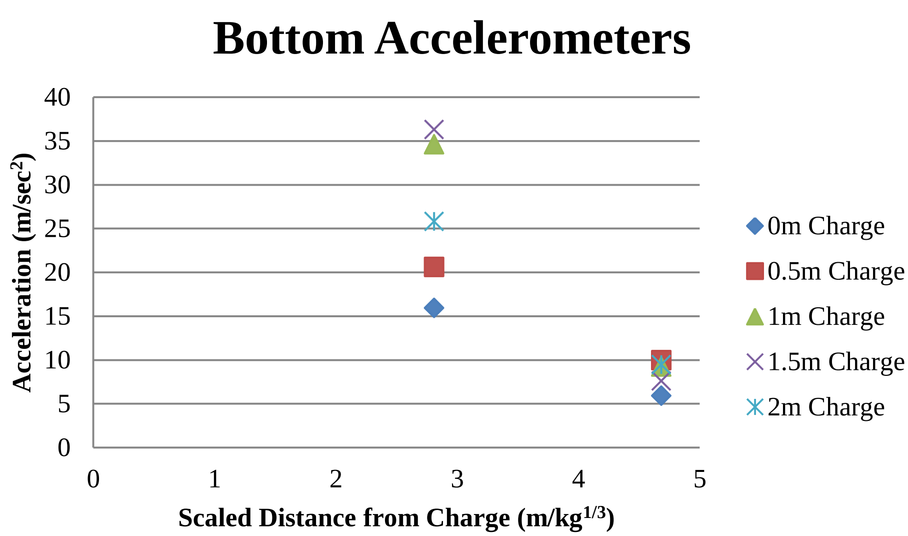
Bottom Accelerometers
40
35
30
25
20
15
10
5
0
Acceleration (m/sec2)
0
1
2
3
4
5
Scaled Distance from Charge (m/kg1/3)
0m Charge
0.5m Charge
1m Charge
1.5m Charge
2m Charge

APPENDIX I

VERTICAL ATTENUATION POWER LAW CURVES

Acceleration plots fit with power law regression to determine vertical attenuation for soft slab snow investigations during the 2010-2011 testing season.

Surface Charge Detonation

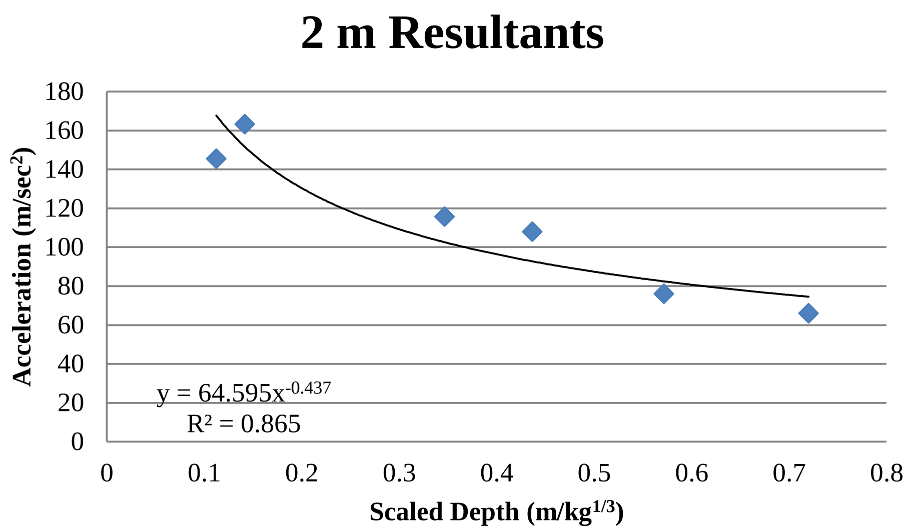

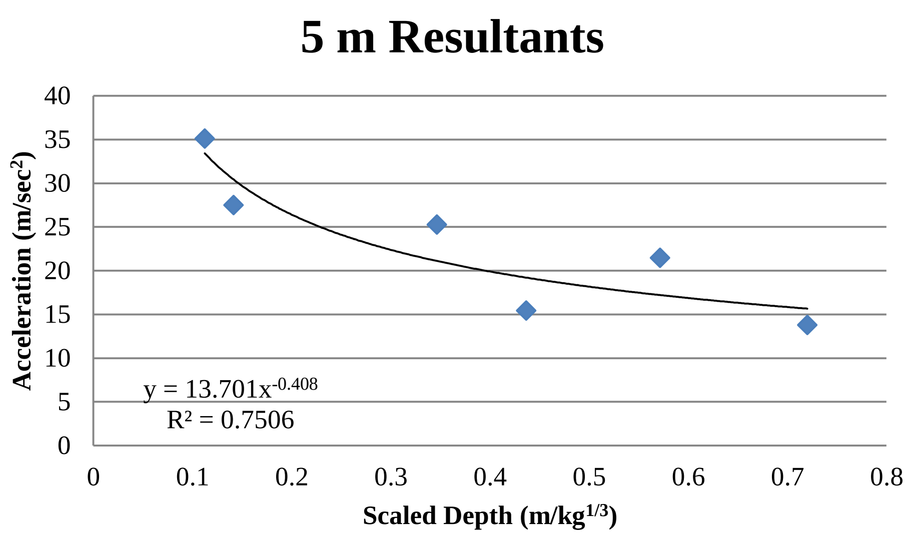

0.5 m Elevated Charge

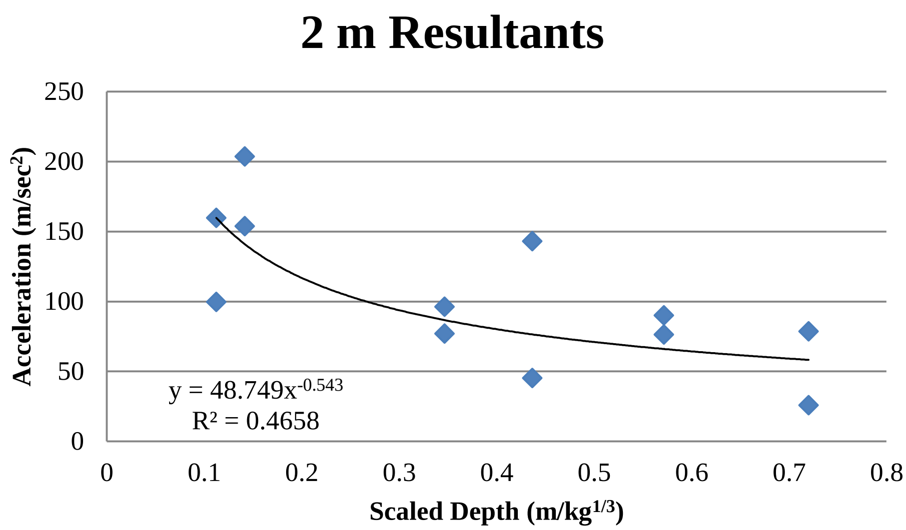

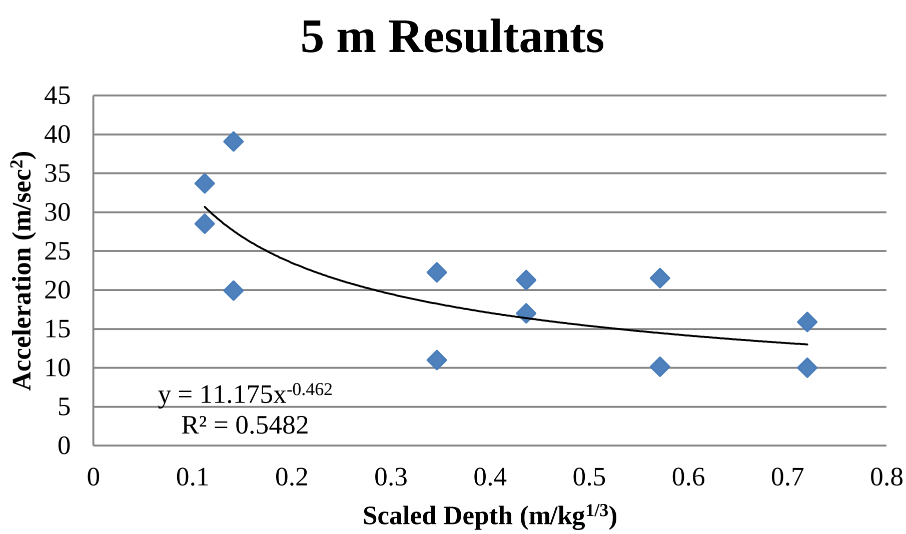

1 m Elevated Charge

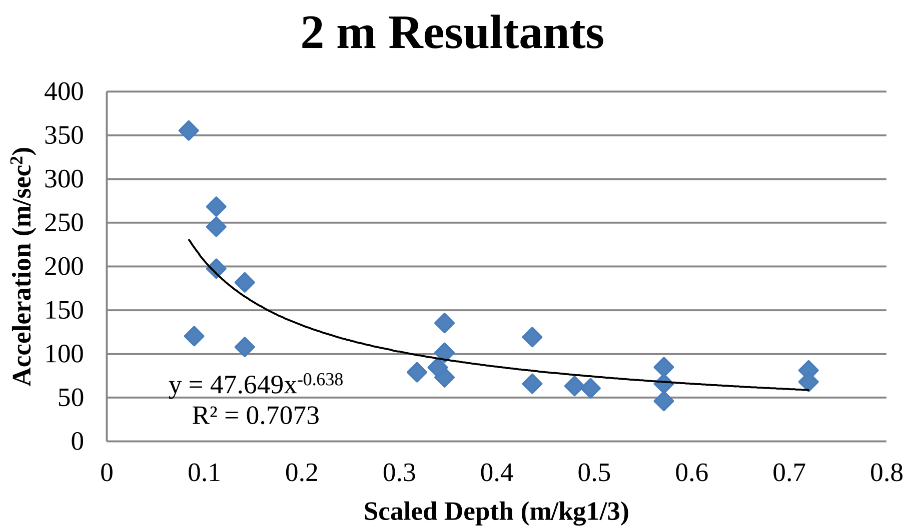

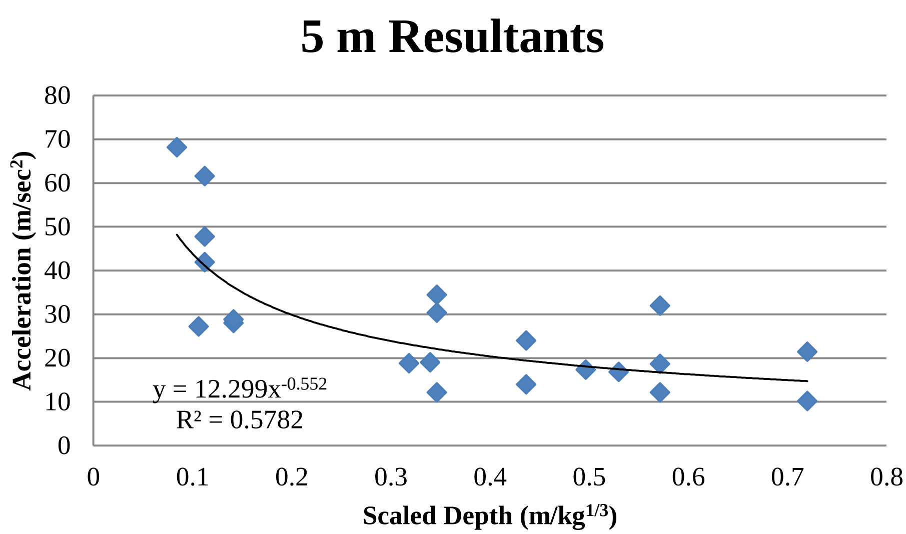

1.5 m Elevated Charge

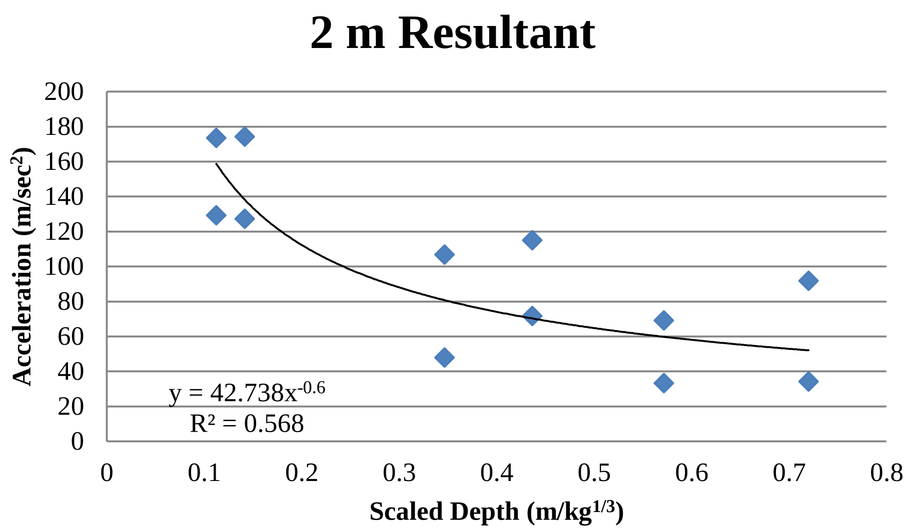

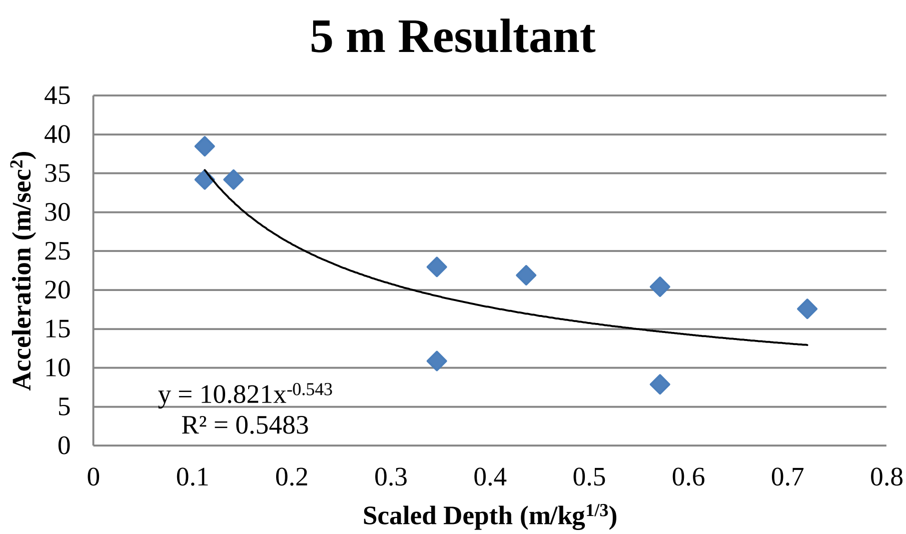

2 m Elevated Charge

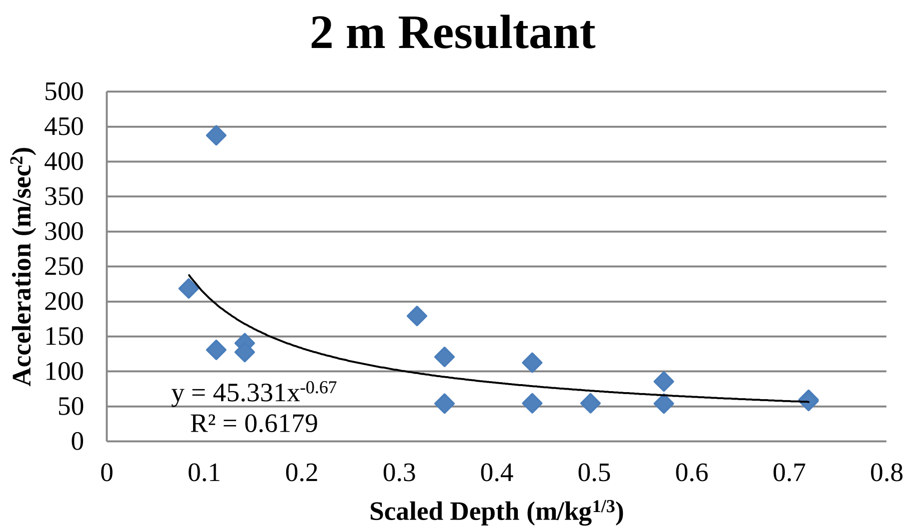

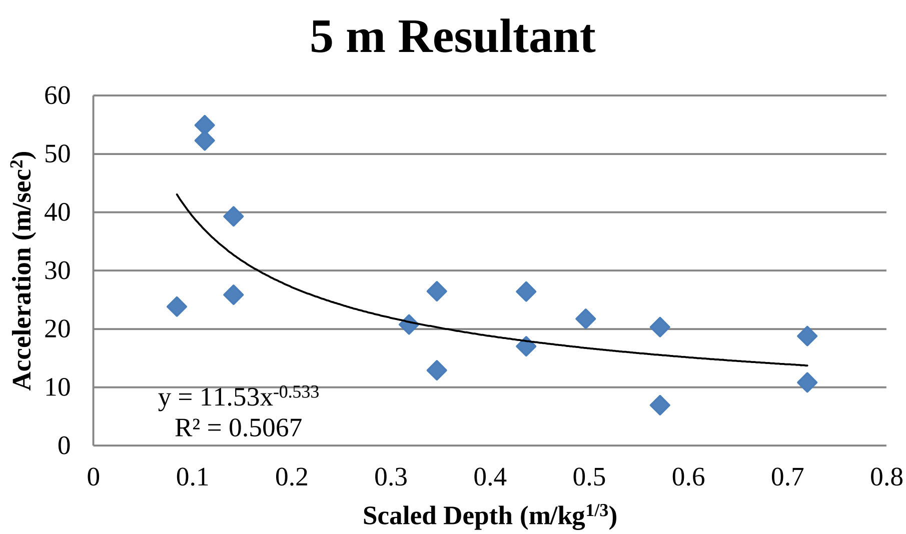

2010-2011 hard slab snow acceleration plots fit with power law regression to determine vertical attenuation.

Surface Detonation

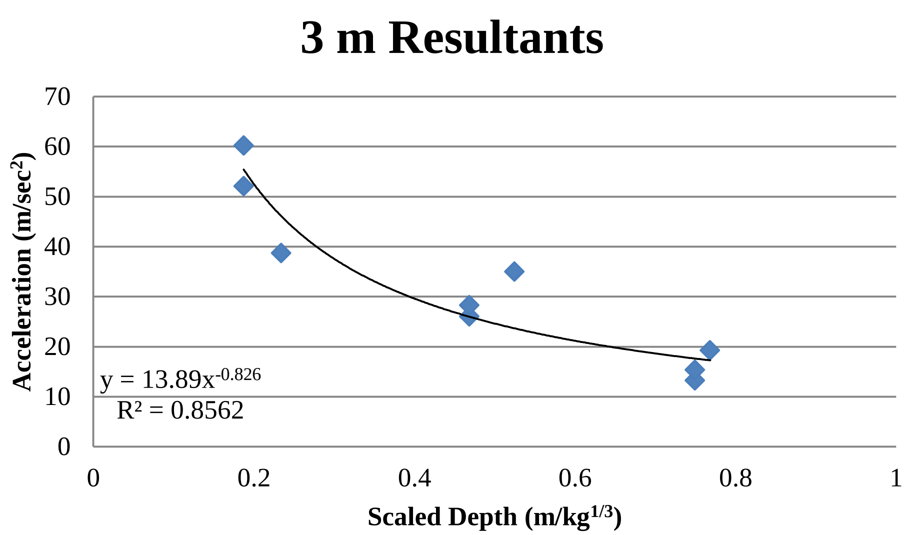

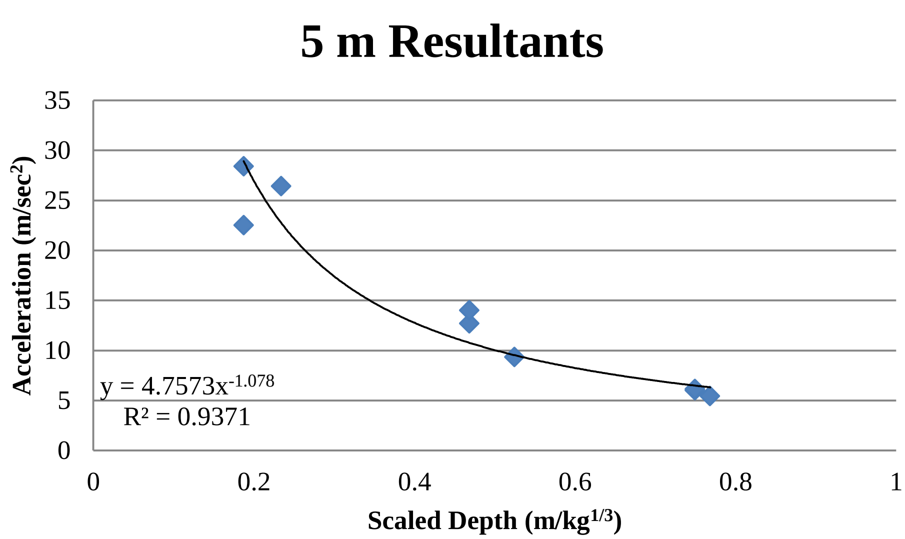

0.5 m Elevated Charge

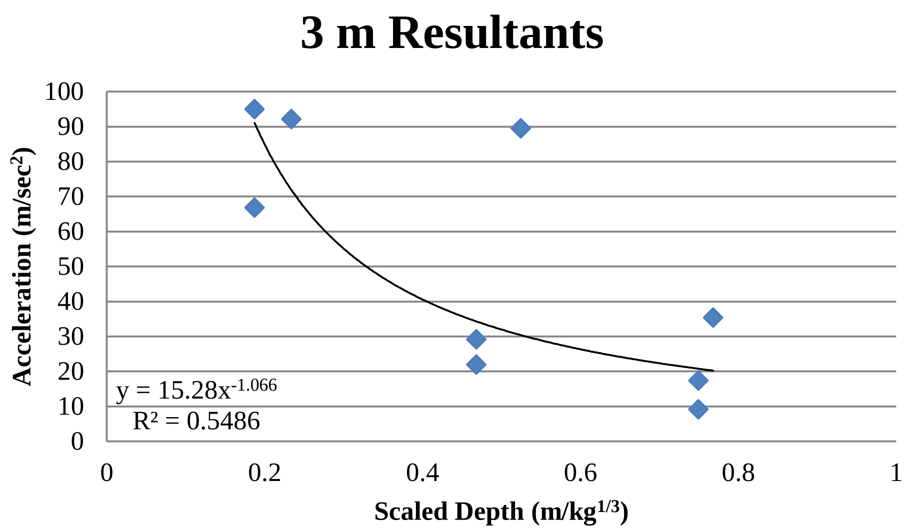

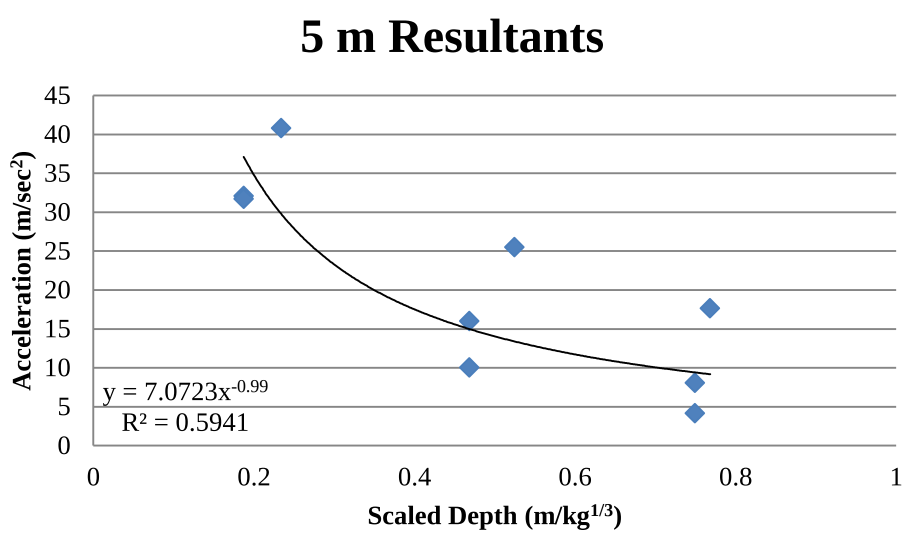

1 m Elevated Charge

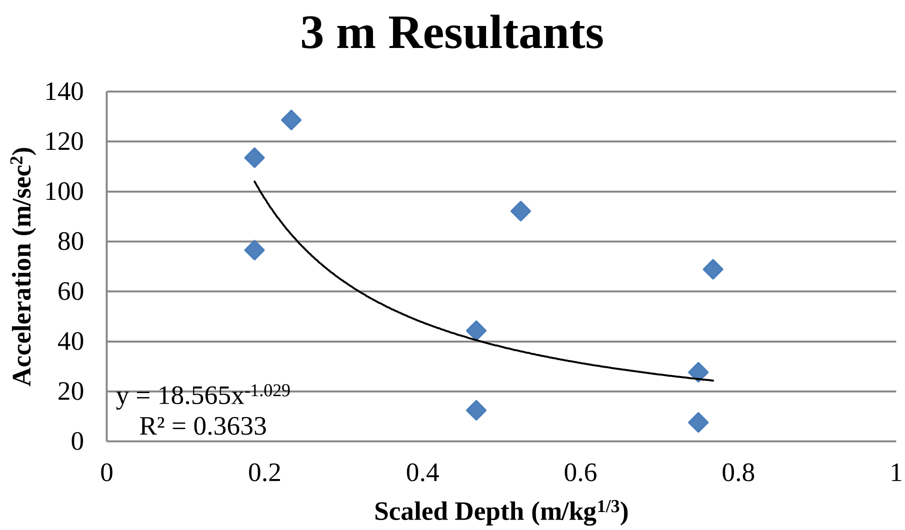

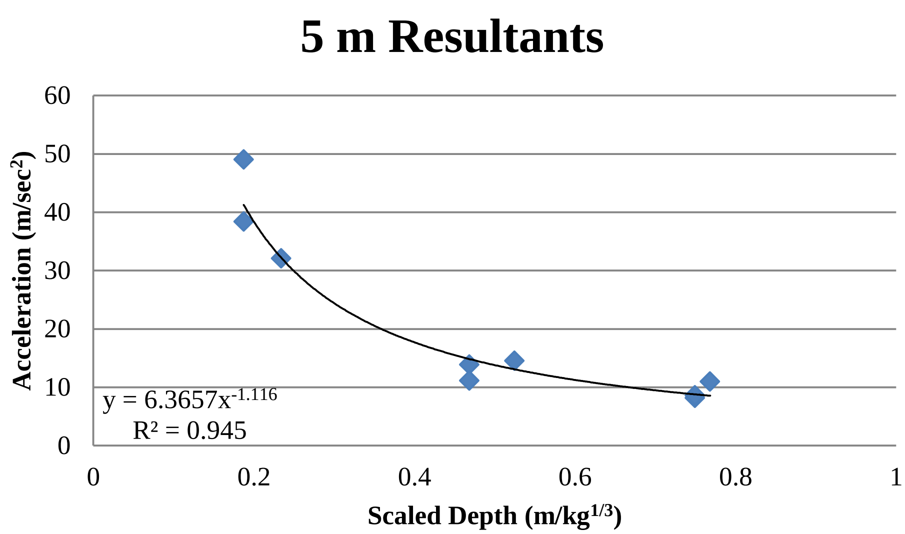

1.5 m Elevated Charge

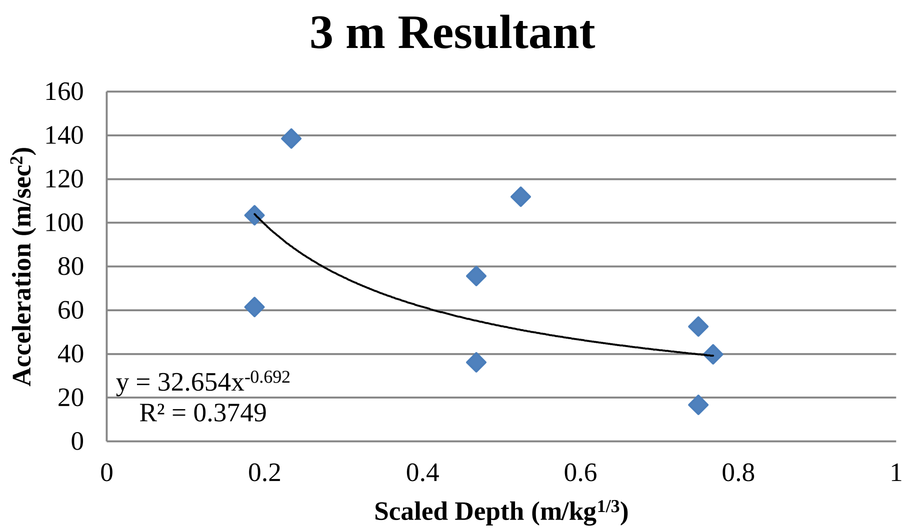

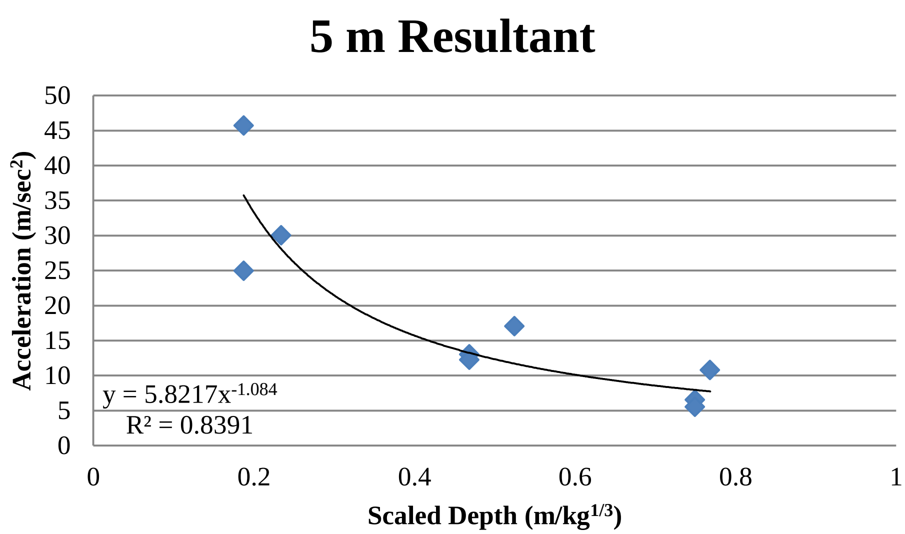

2 m Elevated Charge

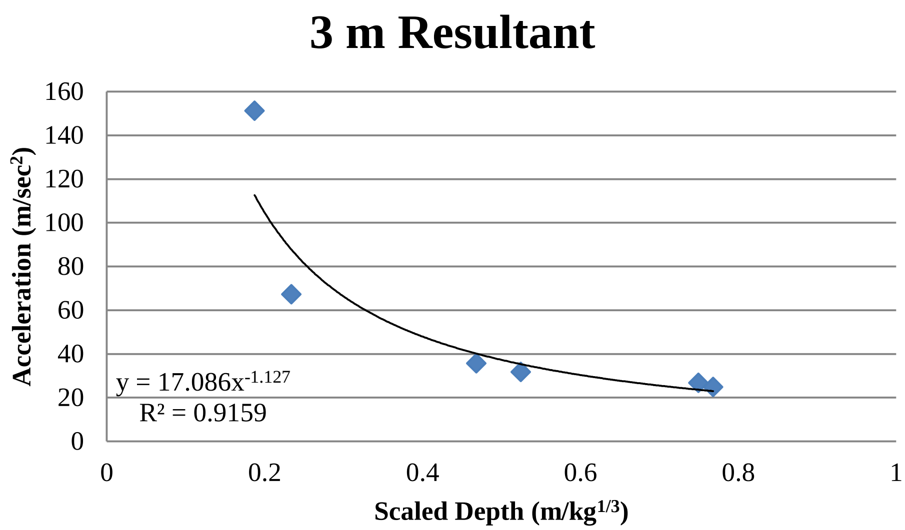

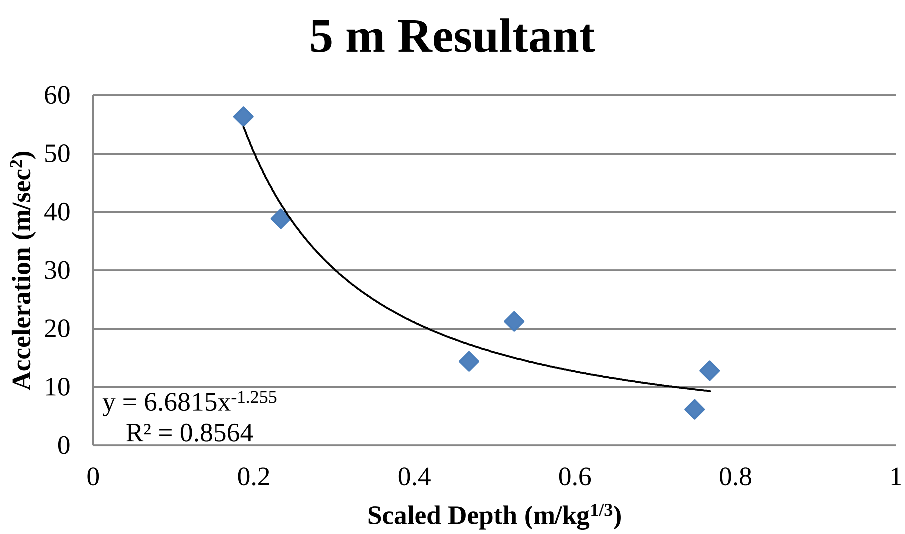

APPENDIX J

RADIAL ATTENUATION POWER LAW CURVES

Radial attenuation determination from power law regression of acceleration plotted as a function of scaled radial distance for soft slab snow investigations during the 2010-2011 winter season of testing. Attenuation was determined and are shown for top, middle, and bottom locations in the snowpack.

Surface Detonation

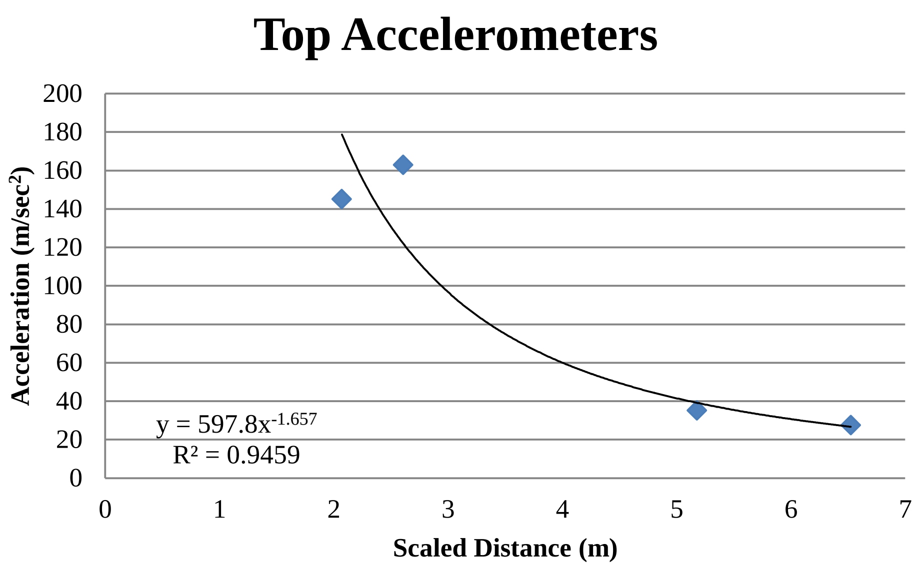

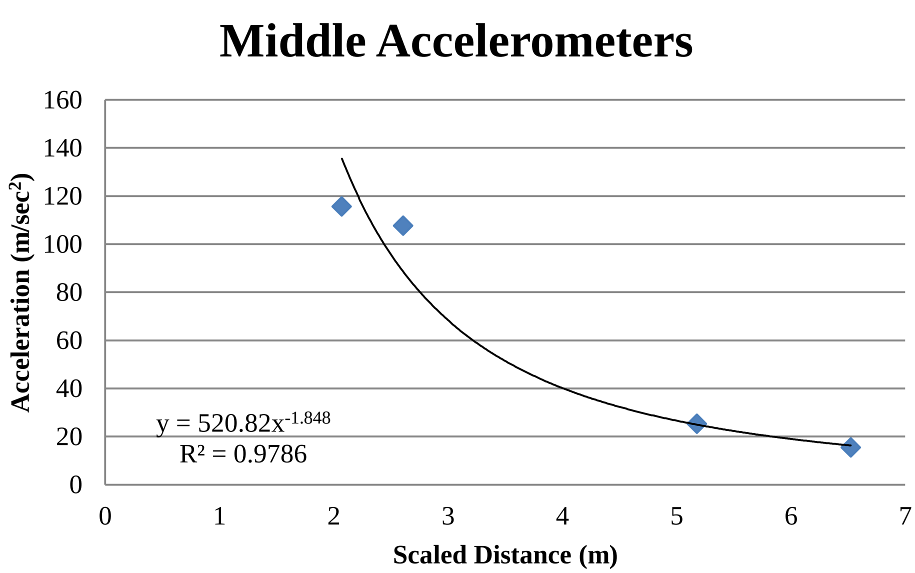

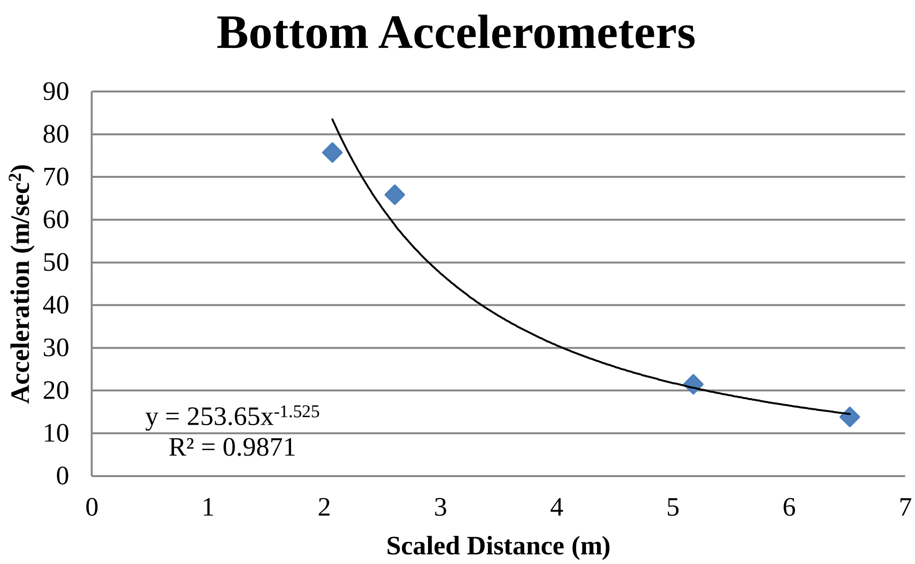

0.5 m Elevated Charge

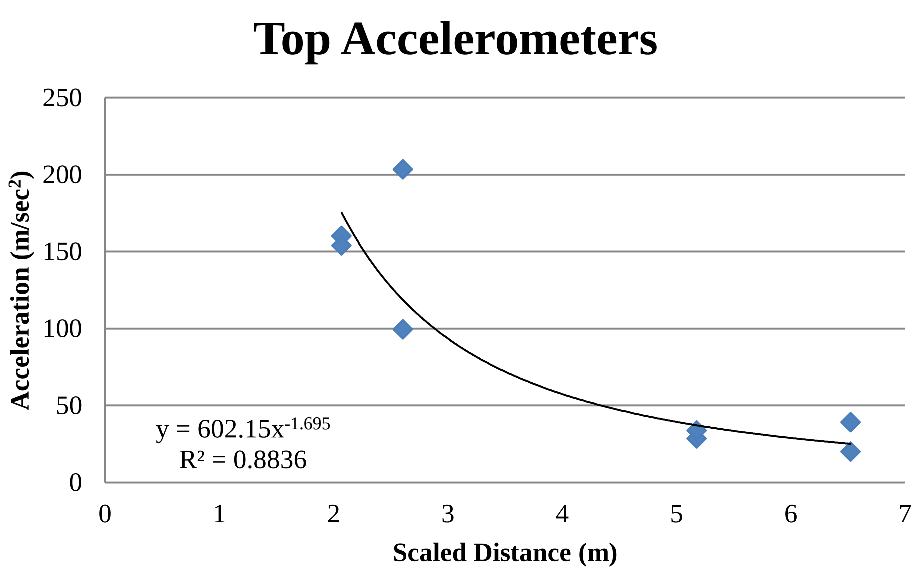

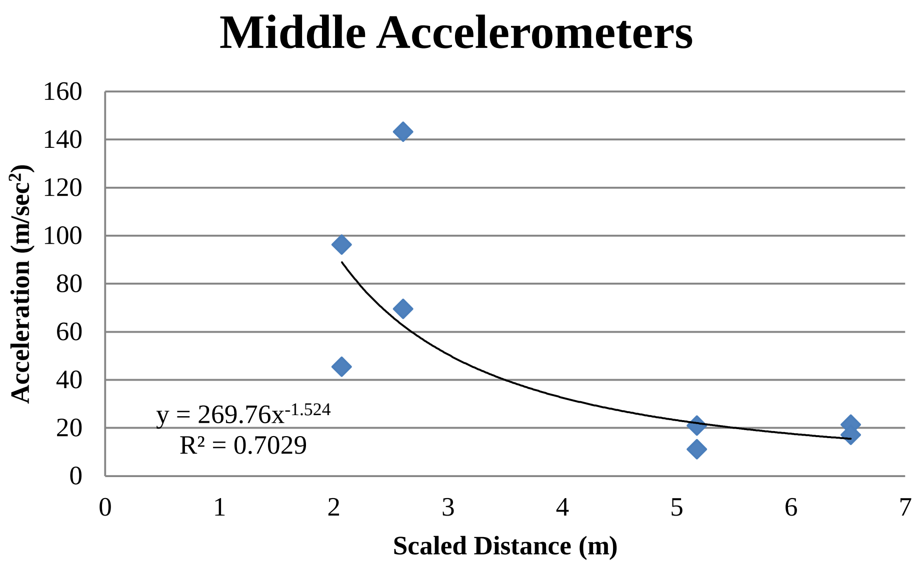
Middle Accelerometers
Acceleration (m/sec2)
160
140
120
100
80
60
40
20
0
y = 269.76x-1.524
R² = 0.7029
0
1
2
3
4
5
6
7
Scaled Distance (m)

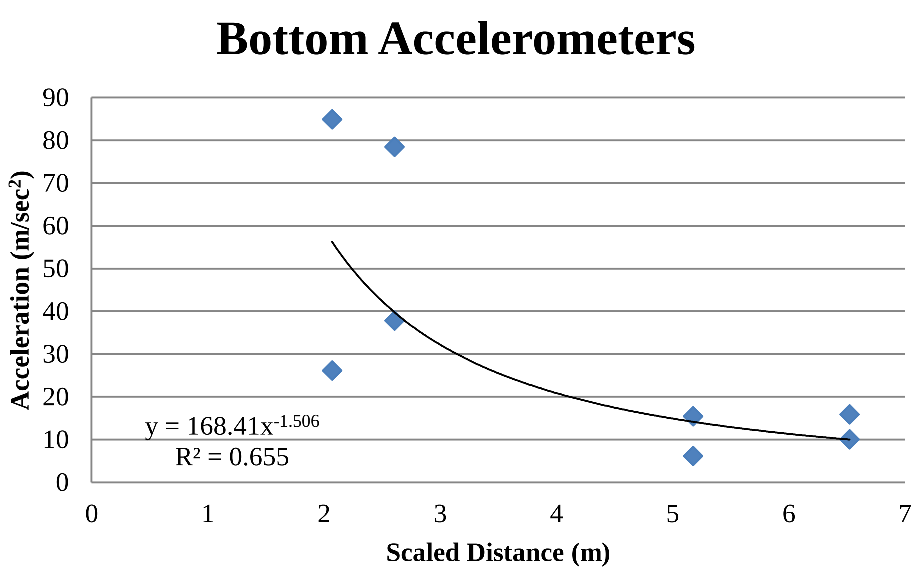
Bottom Accelerometers
Acceleration (m/sec2)
90
80
70
60
50
40
30
20
10
0
y = 168.41x-1.506
R² = 0.655
0
1
2
3
4
5
6
7
Scaled Distance (m)

1 m Elevated Charge

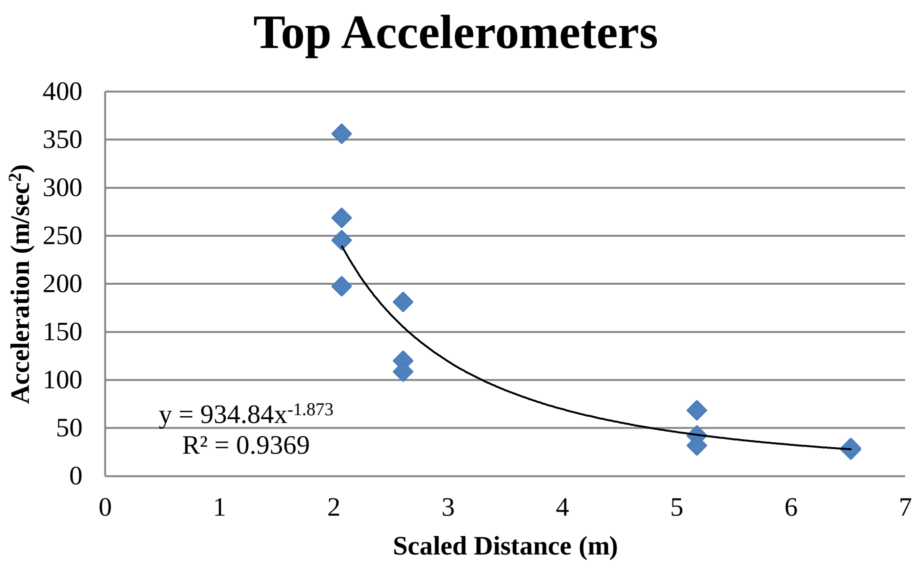

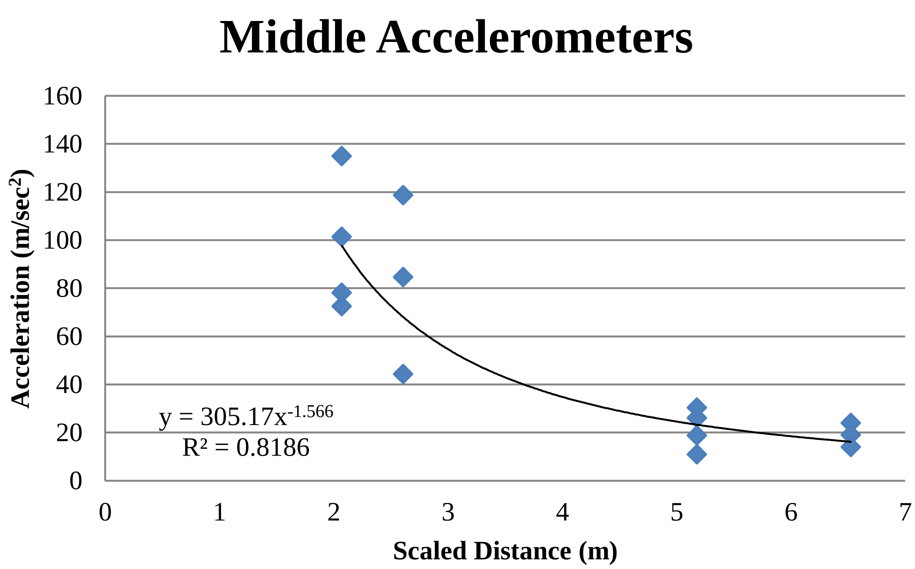

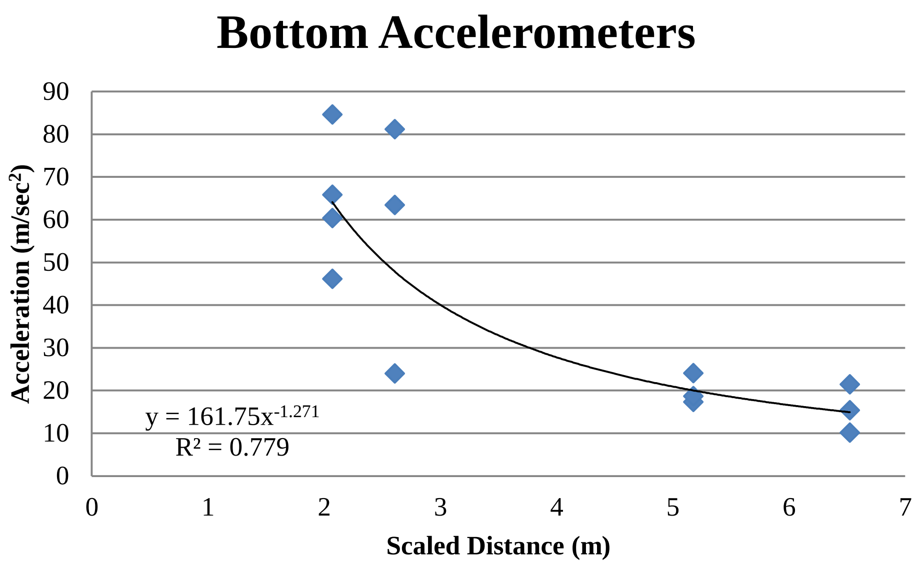

1.5 m Elevated Charge

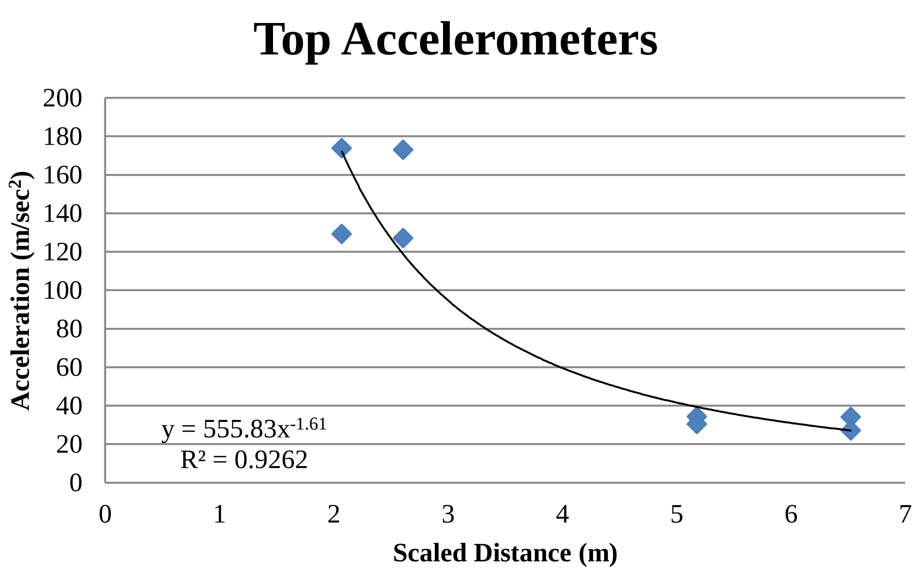

Middle Accelerometers

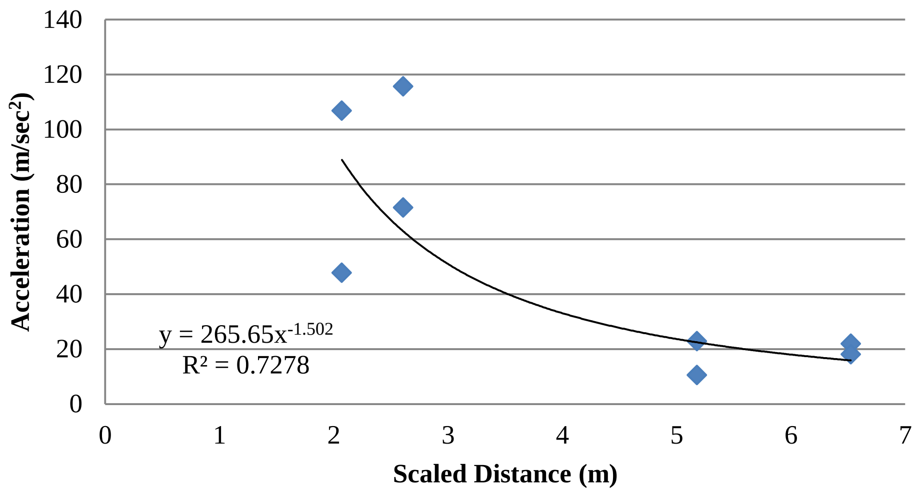

Bottom Accelerometers

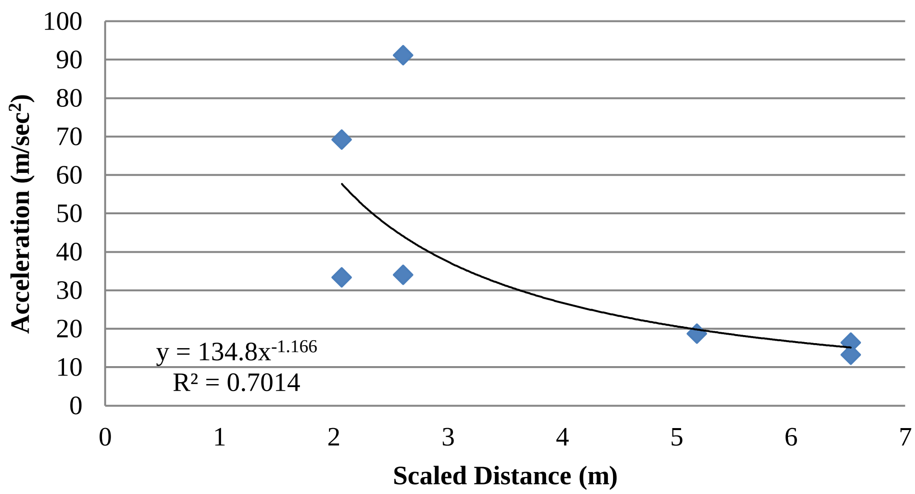

2 m Elevated Charge

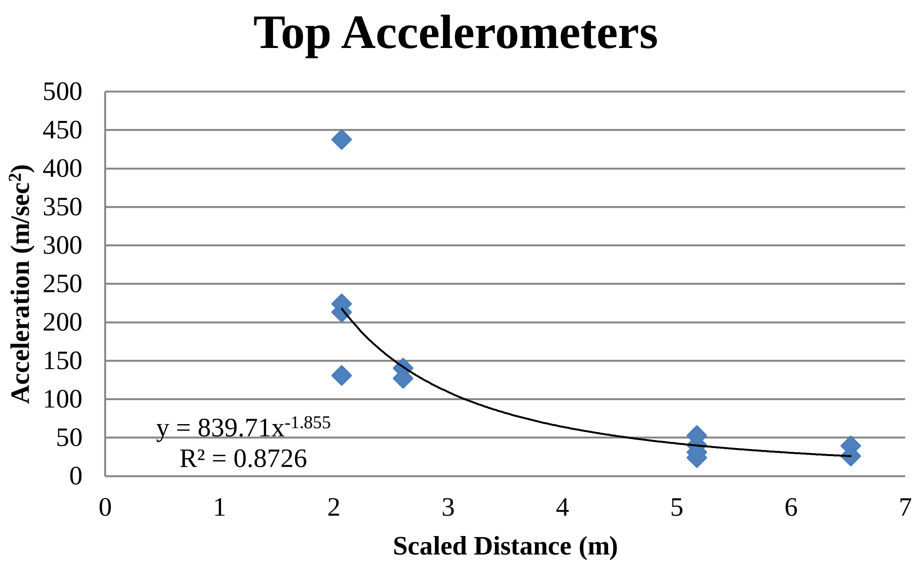

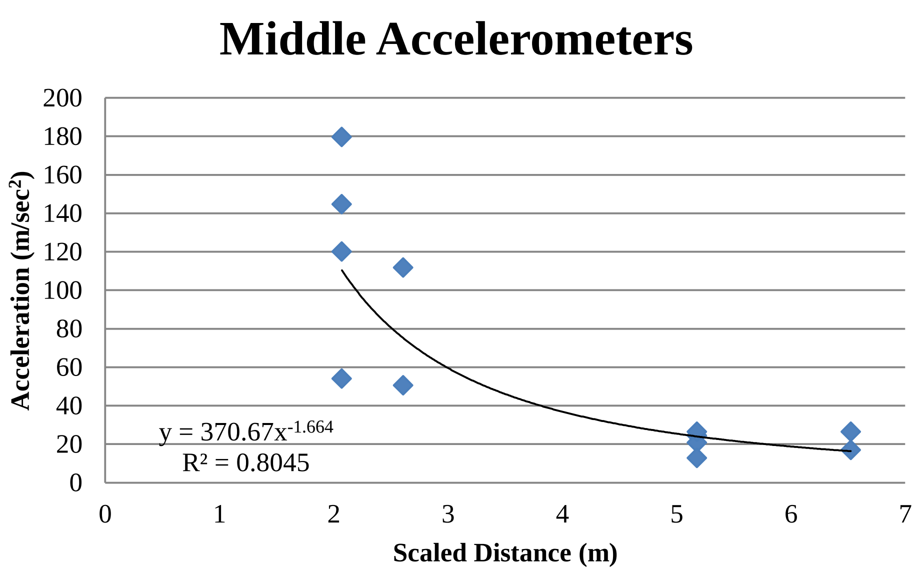

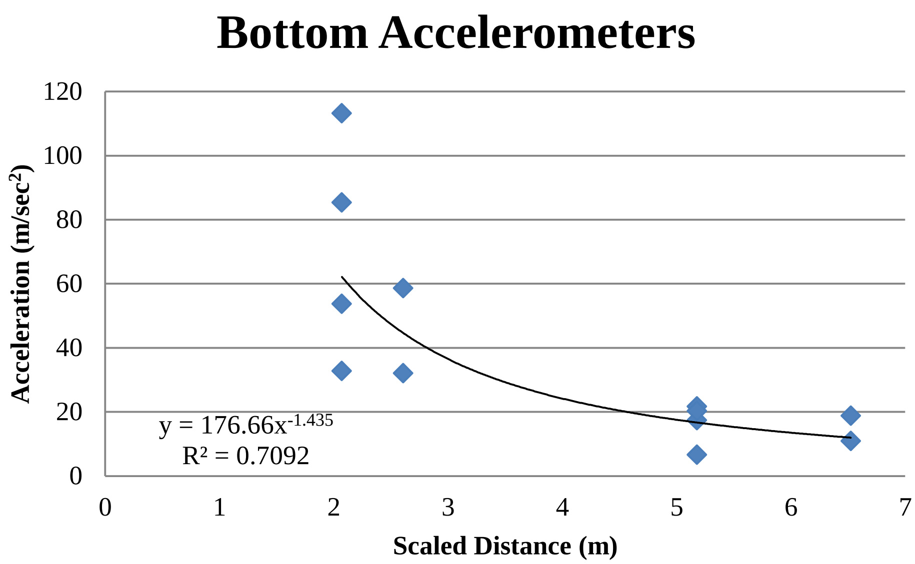

2011-2012 hard slab snow acceleration plots fit with power law regression to determine vertical attenuation.

Surface Detonation

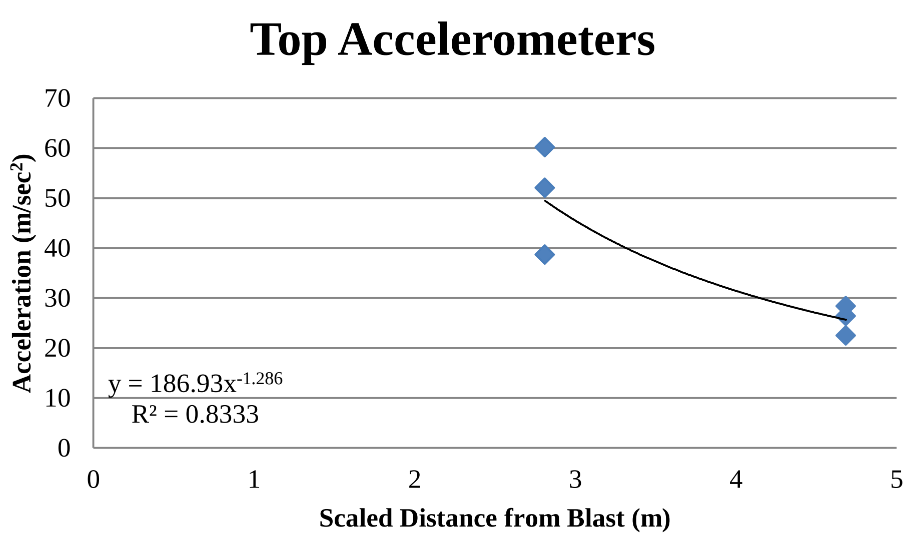

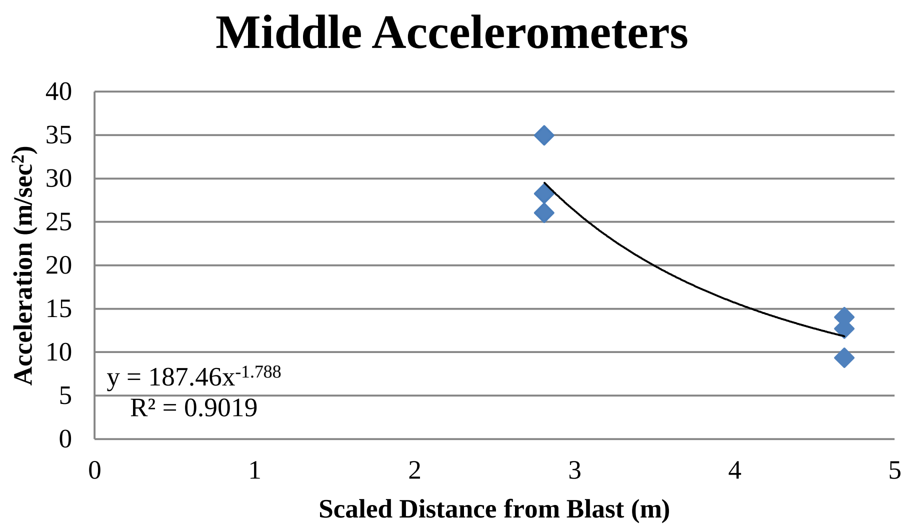
Middle Accelerometers
40
35
30
25
20
15
10
5
0
y = 187.46x-1.788
R² = 0.9019
0
1
2
3
4
5
Acceleration (m/sec2)
Scaled Distance from Blast (m)

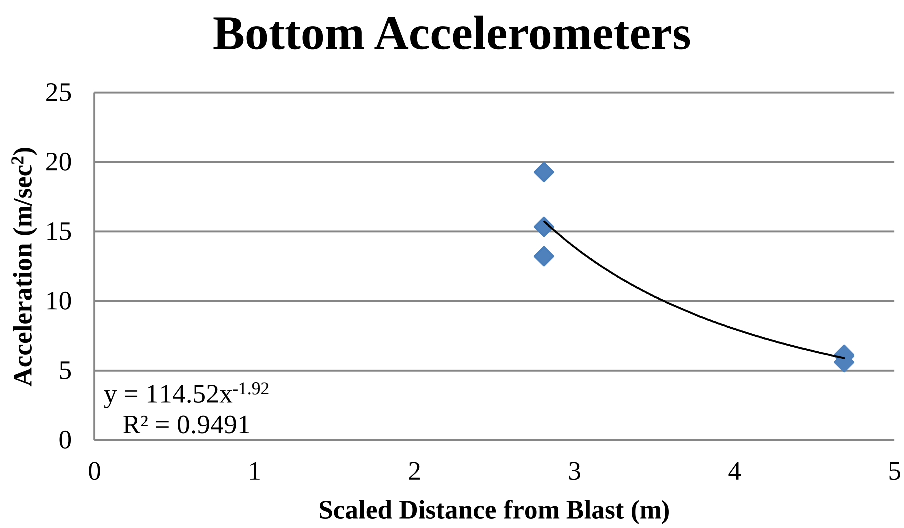
Bottom Accelerometers
25
20
15
10
5
0
y = 114.52x-1.92
R² = 0.9491
0
1
2
3
4
5
Acceleration (m/sec2)
Scaled Distance from Blast (m)

0.5 m Elevated Charge

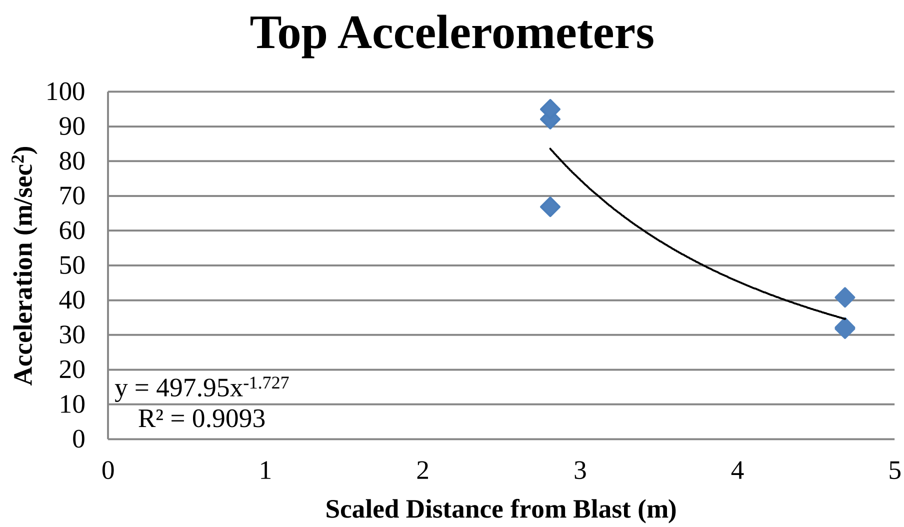

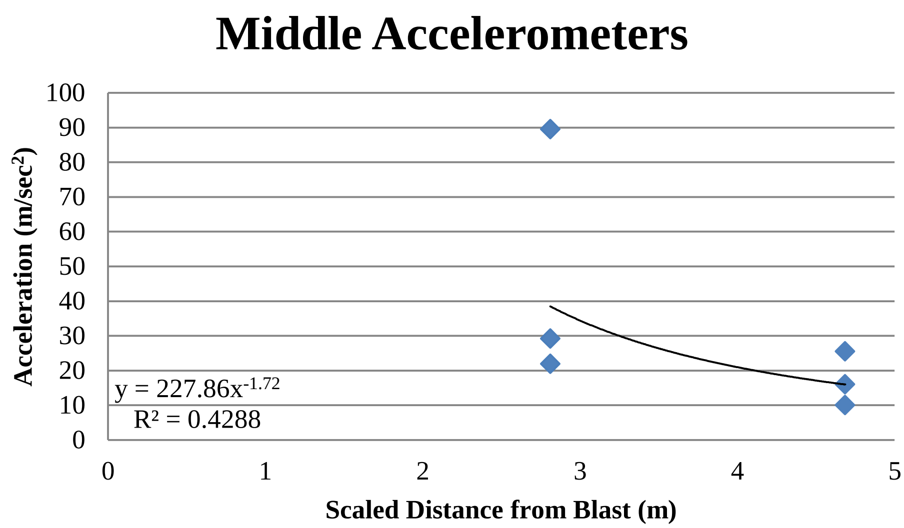

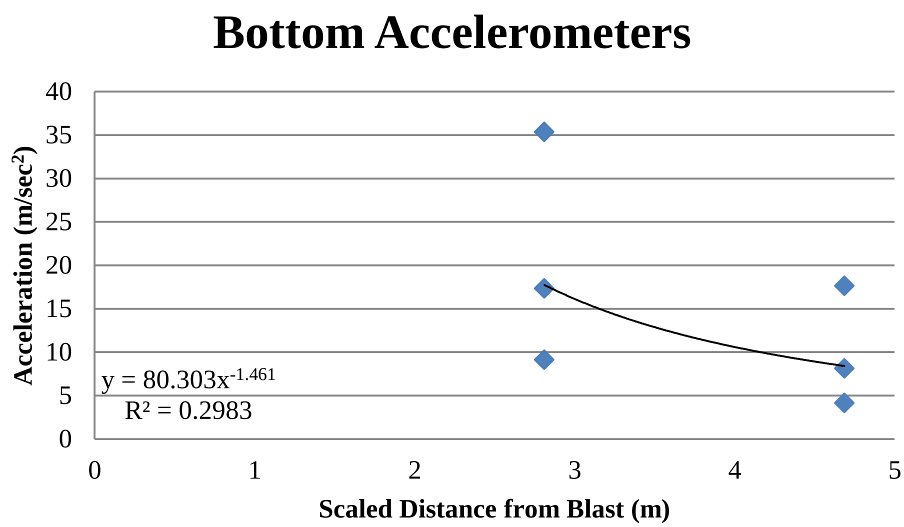

1 m Elevated Charge

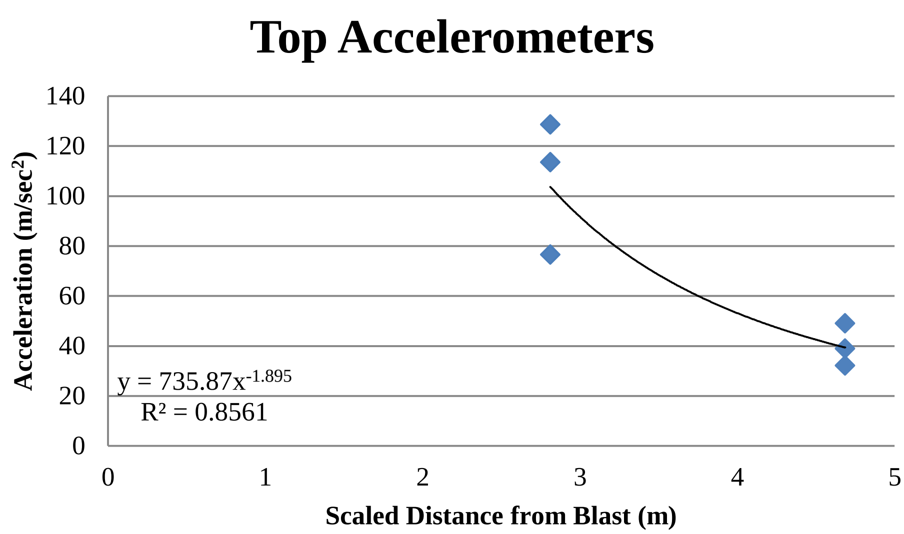

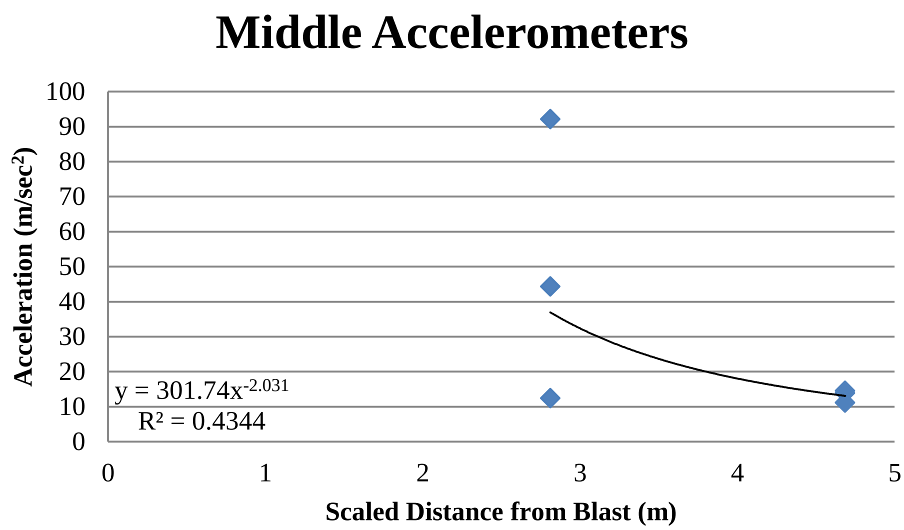

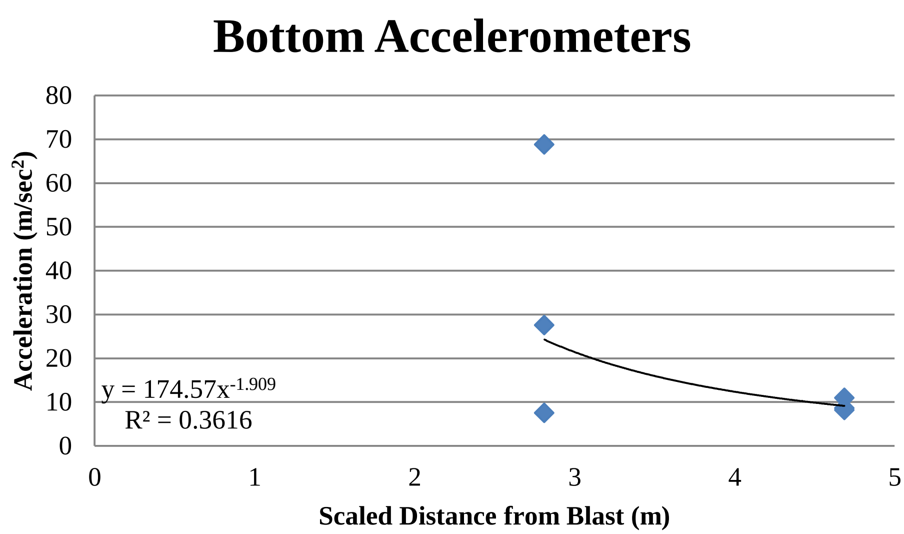

Note: For the one day of data the accelerometers placed in the middle and near the bottom of the snowpack show the acceleration at 5 m to be greater than at 3 m. This is not possible and indicates for this test the accelerometers did not experience the same acceleration due to the detonation as the snowpack did. From the above figures it appears the reading at 5 m is correct and the reading at 3 m is incorrect.

1.5 m Elevated Charge

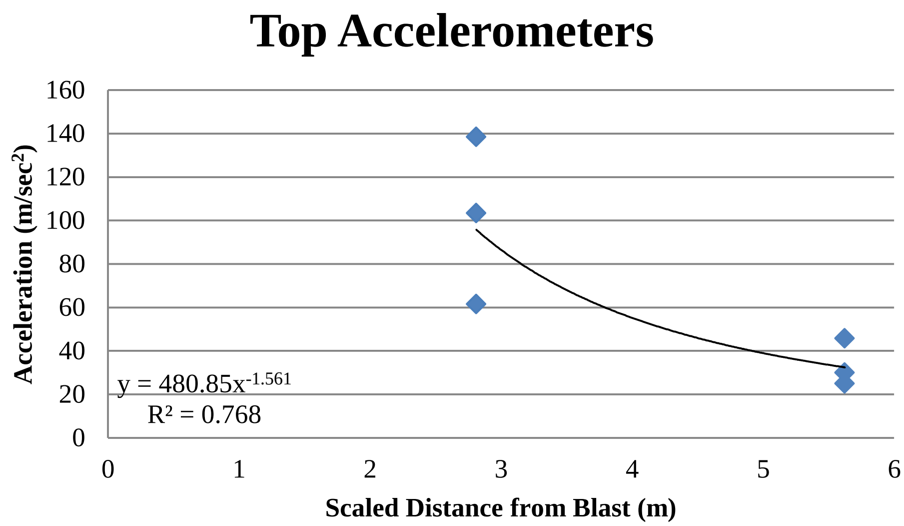

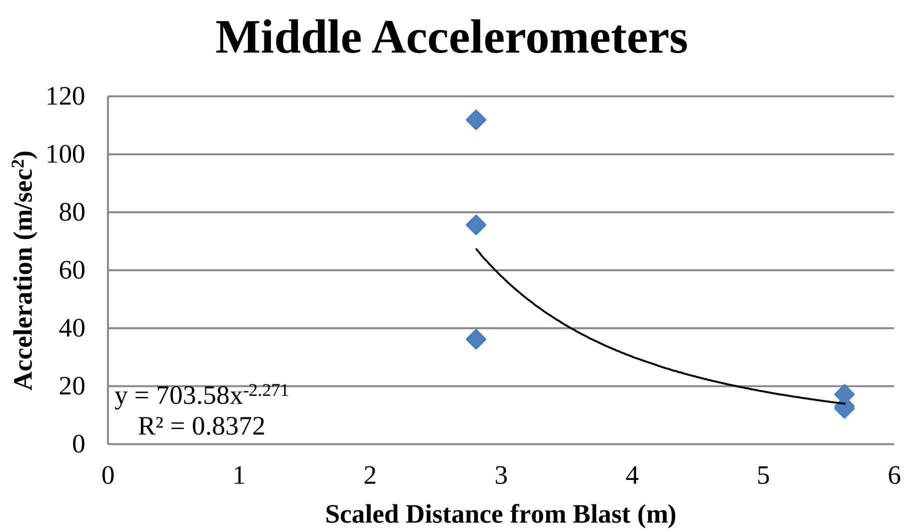

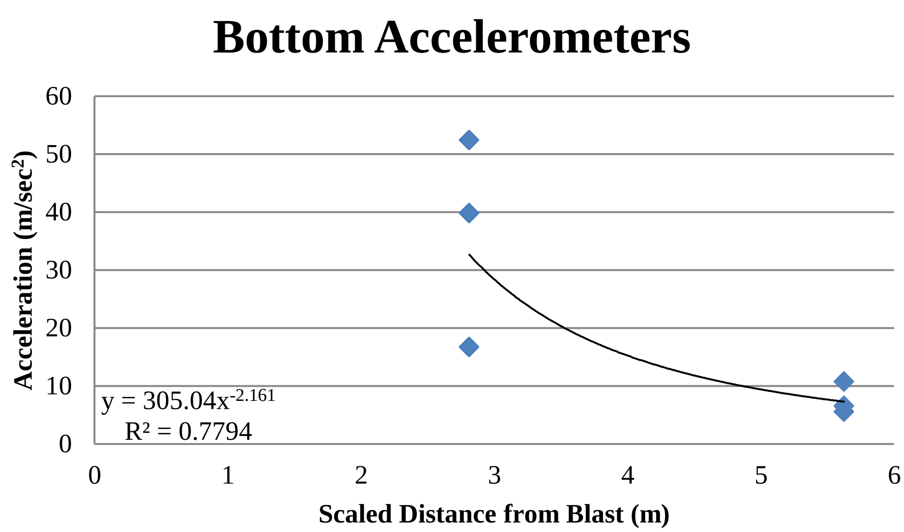

2 m Elevated Charge

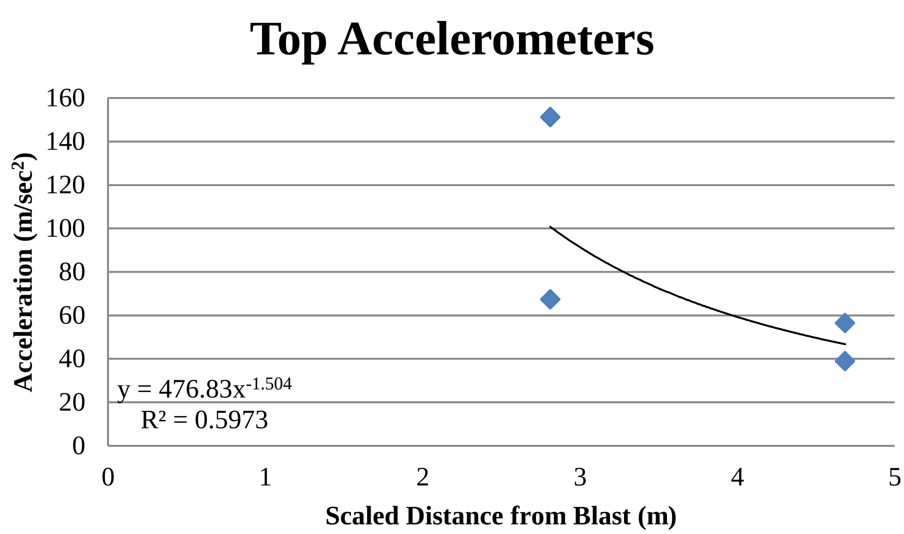

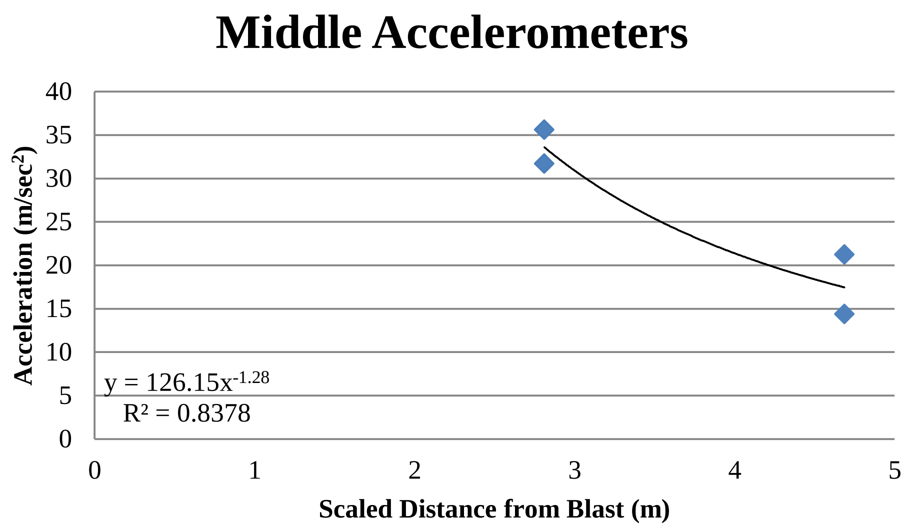
Middle Accelerometers
40
35
30
25
20
15
10
5
0
Acceleration (m/sec²)
y = 126.15x-1.28
R² = 0.8378
0
1
2
3
4
5
Scaled Distance from Blast (m)

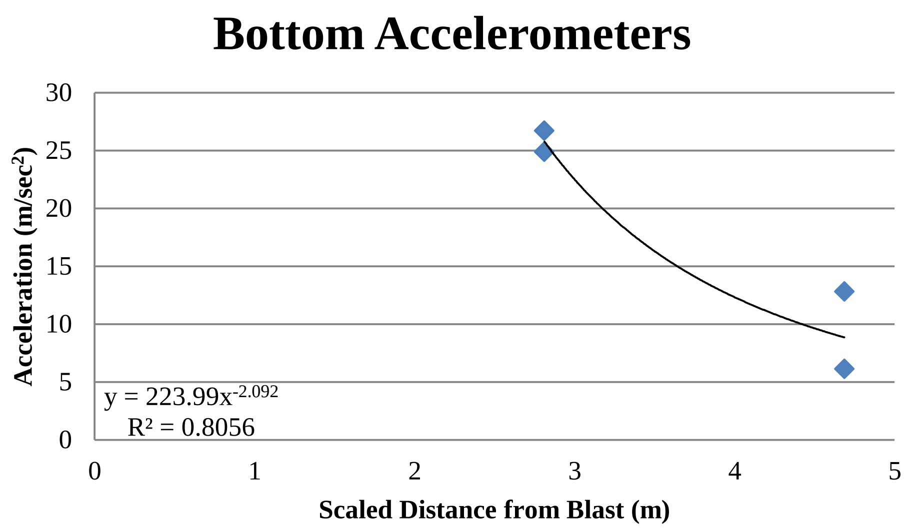
Bottom Accelerometers
30
25
20
15
10
5
0
Acceleration (m/sec²)
y = 223.99x-2.092
R² = 0.8056
0
1
2
3
4
5
Scaled Distance from Blast (m)

APPENDIX K

CONTOUR AND SURFACE PLOT CREATION FOR 2010-2011

DRY AND MOIST SNOW COMPARISONS

Data (acceleration, scaled radial distance, and scaled depth) used to create contour and surface plots for comparison of dry and moist snow conditions during the 2010-2011 soft slab snow investigation. The black figures (corresponding to r, d, a data values) are for dry snow conditions and the blue figures (rw, dw, ra correlating data) are for moist snow conditions.

Surface Detonation

$$r := \begin{pmatrix} 2.118 \\ 2.118 \\ 2.118 \\ 5.295 \\ 5.295 \\ 5.295 \end{pmatrix} \quad d := \begin{pmatrix} 0.127 \\ 0.392 \\ 0.646 \\ 0.127 \\ 0.392 \\ 0.646 \end{pmatrix} \quad a := \begin{pmatrix} 154.273 \\ 111.810 \\ 70.998 \\ 31.288 \\ 20.347 \\ 17.605 \end{pmatrix}$$

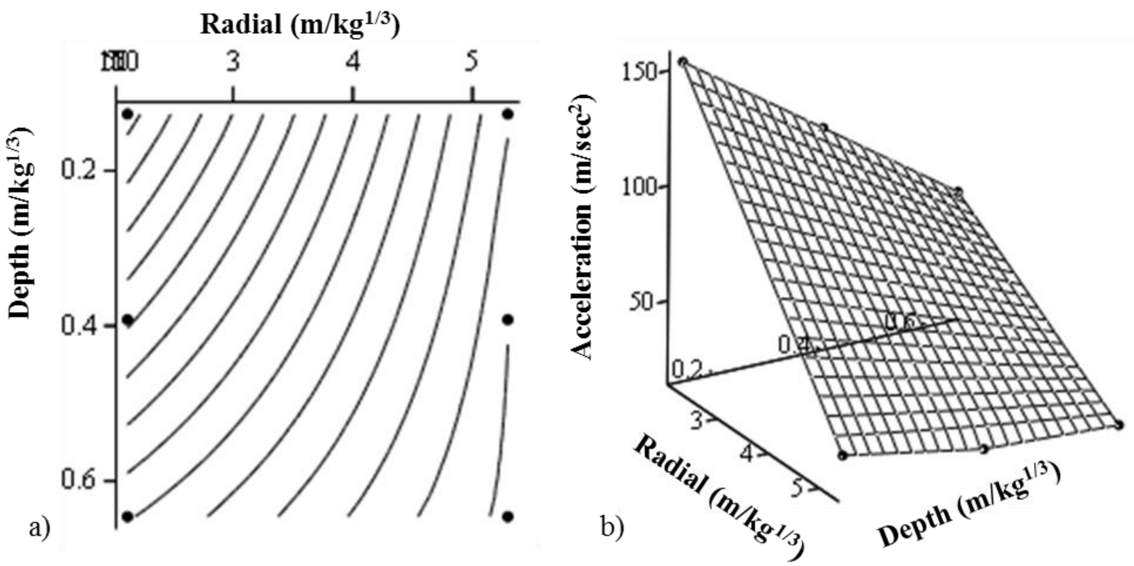

0.5 m Elevated Detonation

$$r := \begin{pmatrix} 2.118 \\ 2.118 \\ 2.118 \\ 5.295 \\ 5.295 \\ 5.295 \end{pmatrix} \quad d := \begin{pmatrix} 0.127 \\ 0.392 \\ 0.646 \\ 0.127 \\ 0.392 \\ 0.646 \end{pmatrix} \quad a := \begin{pmatrix} 181.550 \\ 119.527 \\ 84.296 \\ 33.785 \\ 21.744 \\ 18.692 \end{pmatrix} \qquad rw := \begin{pmatrix} 2.118 \\ 2.118 \\ 2.118 \\ 5.295 \\ 5.295 \\ 5.295 \end{pmatrix} \quad dw := \begin{pmatrix} 0.127 \\ 0.392 \\ 0.646 \\ 0.127 \\ 0.392 \\ 0.646 \end{pmatrix} \quad aw := \begin{pmatrix} 126.660 \\ 61.012 \\ 51.047 \\ 26.770 \\ 13.962 \\ 10.0566 \end{pmatrix}$$

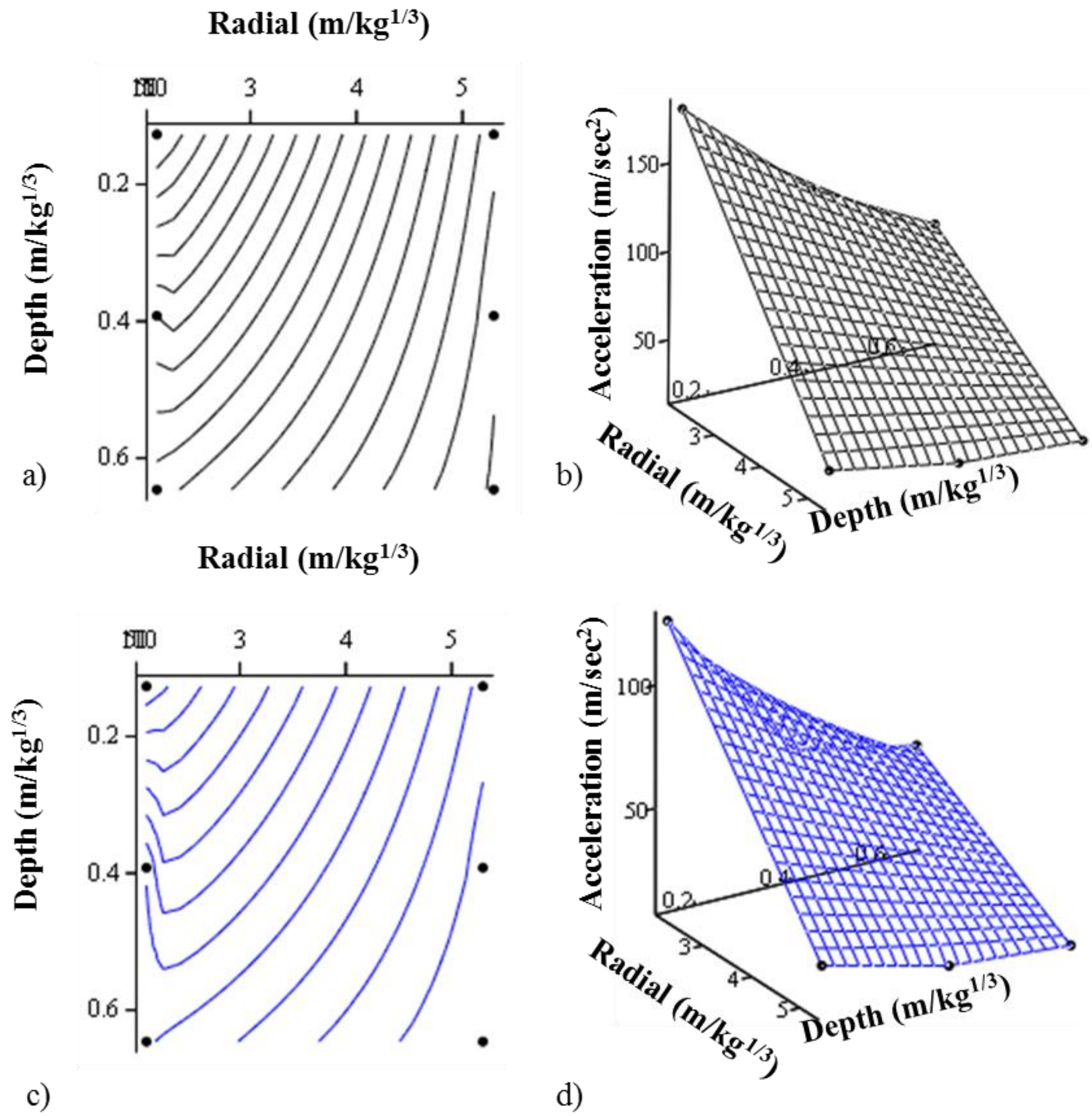

1 m Elevated Detonation

$$r := \begin{pmatrix} 2.037 \\ 2.037 \\ 2.037 \\ 5.092 \\ 5.092 \\ 5.092 \end{pmatrix} \quad d := \begin{pmatrix} 0.122 \\ 0.377 \\ 0.621 \\ 0.122 \\ 0.377 \\ 0.621 \end{pmatrix} \quad a := \begin{pmatrix} 215.693 \\ 118.637 \\ 77.158 \\ 43.784 \\ 29.557 \\ 23.976 \end{pmatrix} \qquad rw := \begin{pmatrix} 2.118 \\ 2.118 \\ 2.118 \\ 5.295 \\ 5.295 \\ 5.295 \end{pmatrix} \quad dw := \begin{pmatrix} 0.127 \\ 0.392 \\ 0.646 \\ 0.127 \\ 0.392 \\ 0.646 \end{pmatrix} \quad aw := \begin{pmatrix} 176.547 \\ 69.269 \\ 57.103 \\ 38.269 \\ 13.064 \\ 11.124 \end{pmatrix}$$

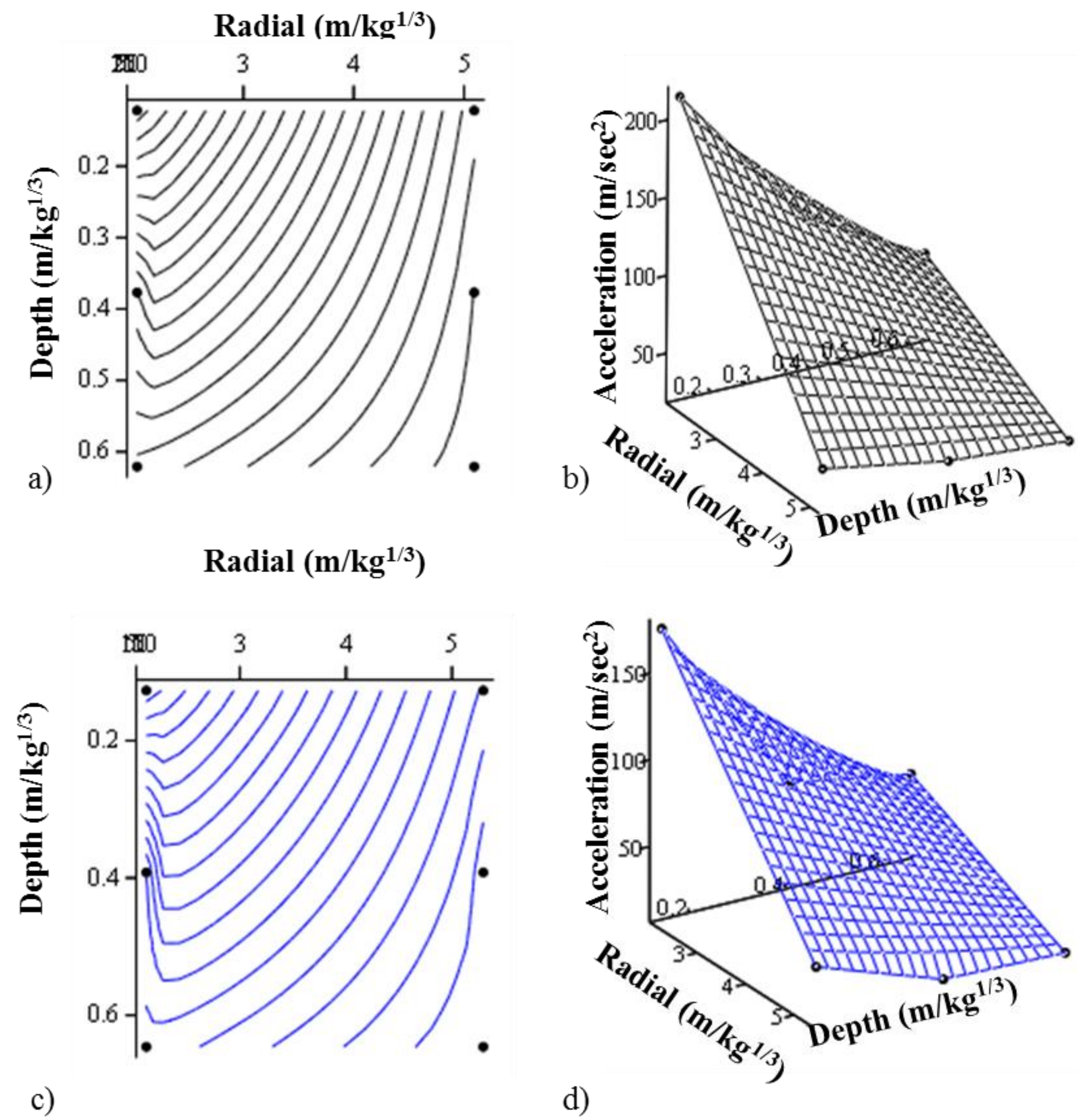

1.5 m Elevated Detonation

$$r := \begin{pmatrix} 2.118 \\ 2.118 \\ 2.118 \\ 5.295 \\ 5.295 \\ 5.295 \end{pmatrix} \quad d := \begin{pmatrix} 0.127 \\ 0.392 \\ 0.646 \\ 0.127 \\ 0.392 \\ 0.646 \end{pmatrix} \quad a := \begin{pmatrix} 173.809 \\ 110.758 \\ 80.361 \\ 34.178 \\ 22.396 \\ 18.957 \end{pmatrix} \qquad rw := \begin{pmatrix} 2.118 \\ 2.118 \\ 2.118 \\ 5.295 \\ 5.295 \\ 5.295 \end{pmatrix} \quad dw := \begin{pmatrix} 0.127 \\ 0.392 \\ 0.646 \\ 0.127 \\ 0.392 \\ 0.646 \end{pmatrix} \quad aw := \begin{pmatrix} 128.230 \\ 59.775 \\ 33.683 \\ 32.756 \\ 14.579 \\ 10.552 \end{pmatrix}$$

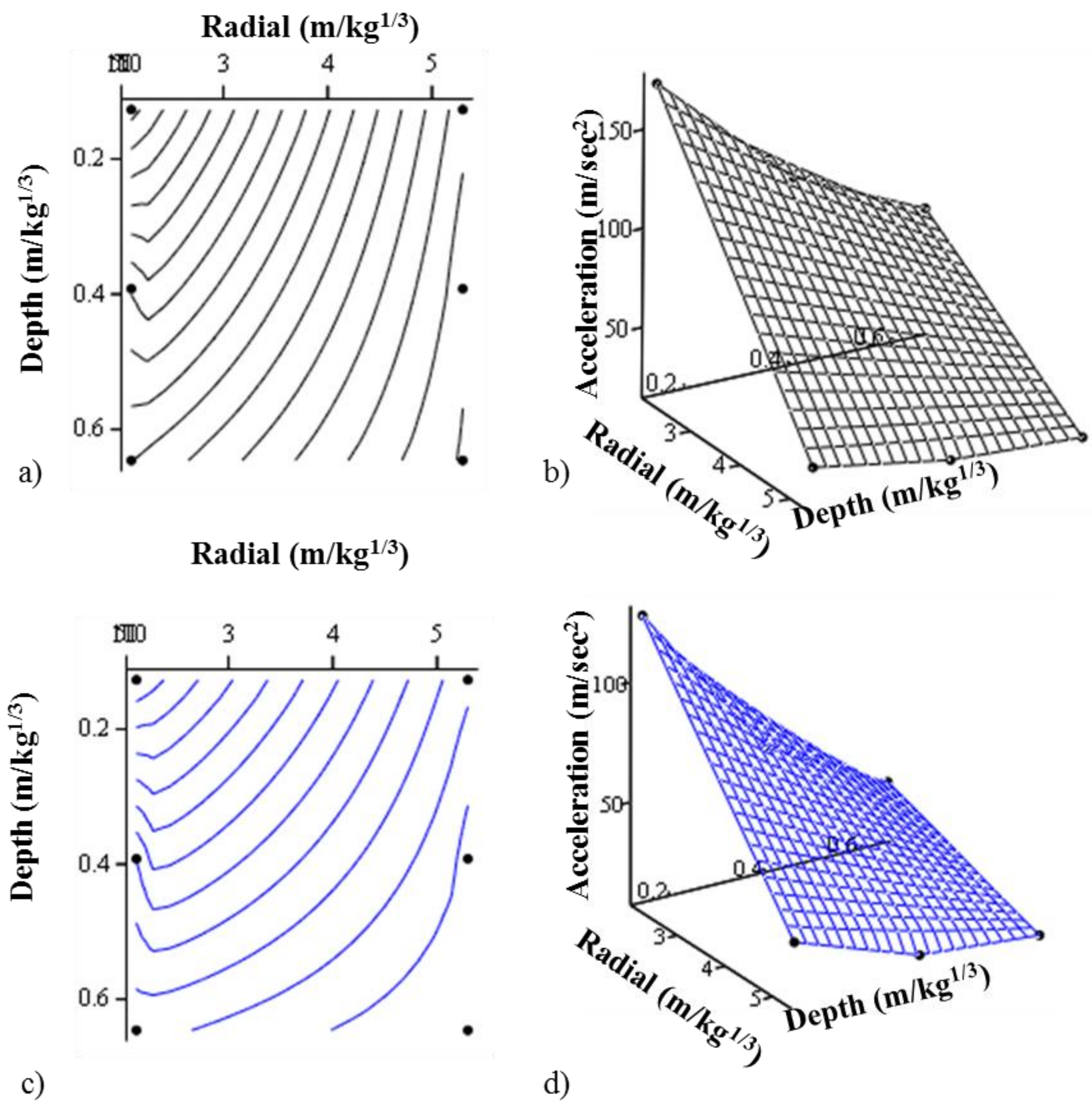

2 m Elevated Detonation

$$r := \begin{pmatrix} 2.037 \\ 2.037 \\ 2.037 \\ 5.092 \\ 5.092 \\ 5.092 \end{pmatrix} \quad d := \begin{pmatrix} 0.122 \\ 0.377 \\ 0.621 \\ 0.122 \\ 0.377 \\ 0.621 \end{pmatrix} \quad a := \begin{pmatrix} 263.550 \\ 125.829 \\ 105.296 \\ 48.238 \\ 25.769 \\ 18.791 \end{pmatrix} \qquad rw := \begin{pmatrix} 2.118 \\ 2.118 \\ 2.118 \\ 5.295 \\ 5.295 \\ 5.295 \end{pmatrix} \quad dw := \begin{pmatrix} 0.127 \\ 0.392 \\ 0.646 \\ 0.127 \\ 0.392 \\ 0.646 \end{pmatrix} \quad aw := \begin{pmatrix} 128.870 \\ 54.159 \\ 55.769 \\ 39.011 \\ 14.934 \\ 8.841 \end{pmatrix}$$

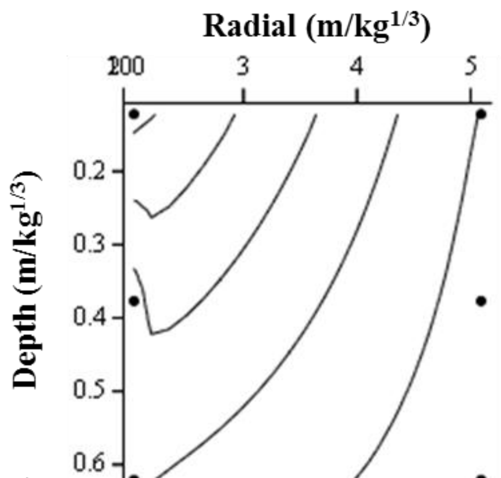

a)

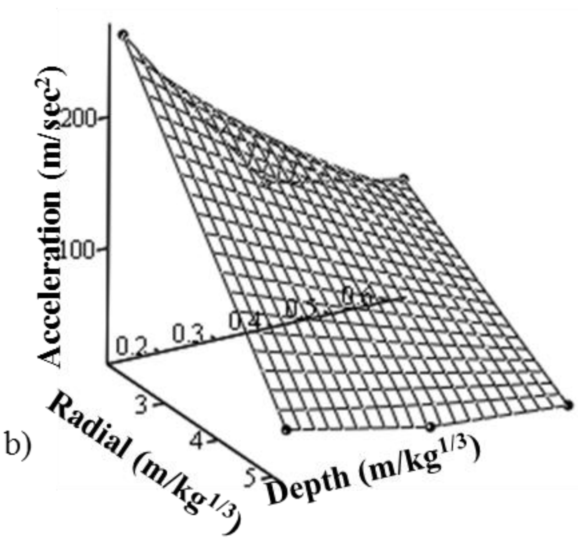

b)

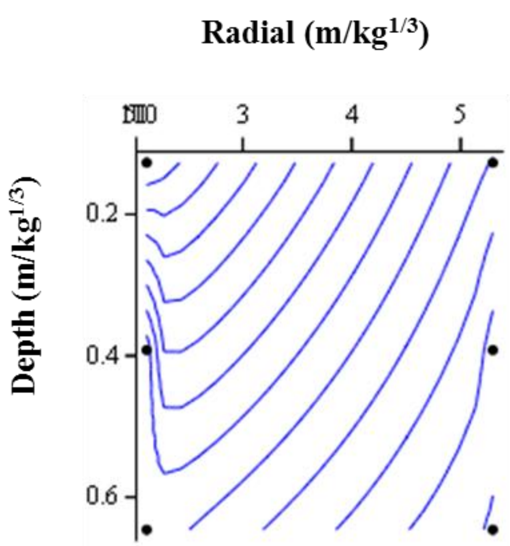

c)

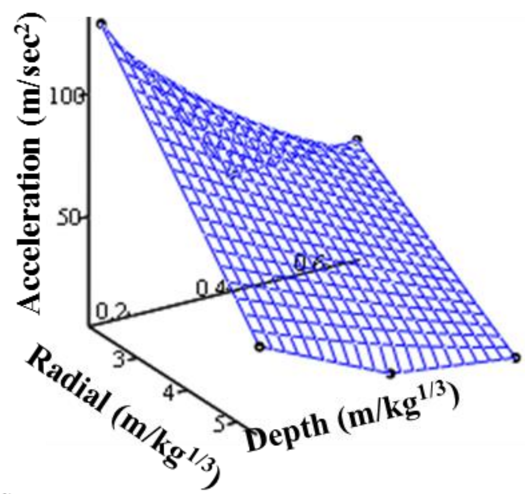

d)

APPENDIX L

CONTOUR AND SURFACE PLOT CREATION FOR 2010-2011

0.45 KG AND 0.9 KG EXPLOSIVE COMPARISONS

Data used to create contour and surface plots for comparison of 0.45 kg and 0.9 kg charges in dry snow conditions during the 2010-2011 soft slab snow investigation. The black figures (corresponding to r, d, a data values) are for 0.9 kg explosive masses and the blue figures (rw, dw, ra correlating data) are for 0.45 kg pentolite masses.

1 m Elevated Detonation

$$r := \begin{pmatrix} 1.87 \\ 1.87 \\ 1.87 \\ 4.69 \\ 4.69 \\ 4.69 \end{pmatrix} \quad d := \begin{pmatrix} 0.534 \\ 0.333 \\ 0.098 \\ 0.534 \\ 0.333 \\ 0.098 \end{pmatrix} \quad a := \begin{pmatrix} 63.153 \\ 107.095 \\ 311.650 \\ 17.950 \\ 24.521 \\ 54.997 \end{pmatrix} \qquad rw := \begin{pmatrix} 2.36 \\ 2.36 \\ 2.36 \\ 5.9 \\ 5.9 \\ 5.9 \end{pmatrix} \quad dw := \begin{pmatrix} 0.600 \\ 0.388 \\ 0.116 \\ 0.625 \\ 0.388 \\ 0.124 \end{pmatrix} \quad aw := \begin{pmatrix} 72.112 \\ 101.804 \\ 150.885 \\ 19.095 \\ 21.487 \\ 27.561 \end{pmatrix}$$

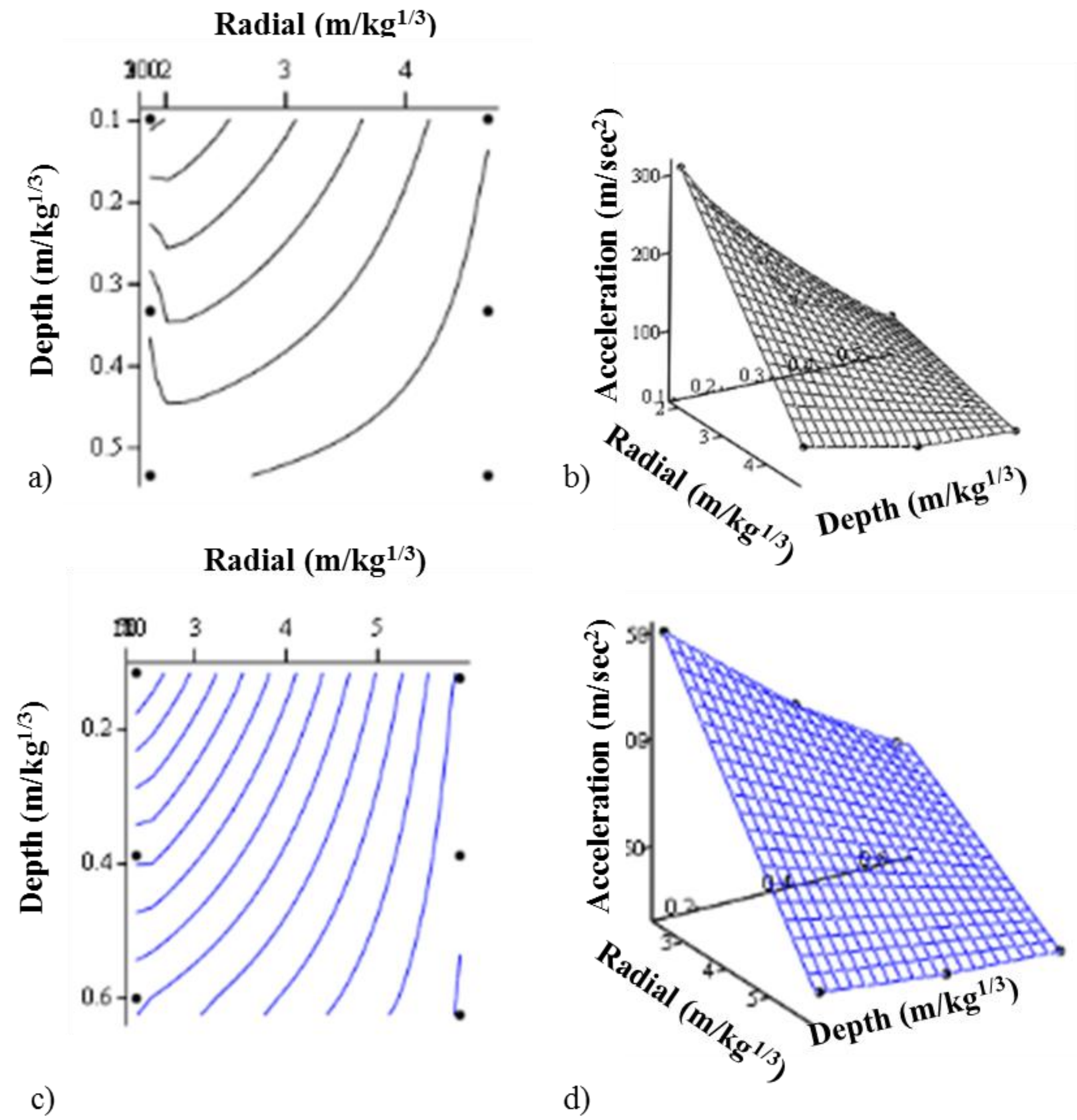

2 m Elevated Detonation

$$r := \begin{pmatrix} 1.87 \\ 1.87 \\ 1.87 \\ 4.69 \\ 4.69 \\ 4.69 \end{pmatrix} \quad d := \begin{pmatrix} 0.572 \\ 0.347 \\ 0.112 \\ 0.572 \\ 0.347 \\ 0.112 \end{pmatrix} \quad a := \begin{pmatrix} 85.549 \\ 120.443 \\ 437.416 \\ 20.298 \\ 26.411 \\ 54.907 \end{pmatrix} \qquad rw := \begin{pmatrix} 2.36 \\ 2.36 \\ 2.36 \\ 5.9 \\ 5.9 \\ 5.9 \end{pmatrix} \quad dw := \begin{pmatrix} 0.720 \\ 0.437 \\ 0.142 \\ 0.720 \\ 0.437 \\ 0.142 \end{pmatrix} \quad aw := \begin{pmatrix} 59.088 \\ 112.166 \\ 140.121 \\ 18.745 \\ 26.359 \\ 39.260 \end{pmatrix}$$

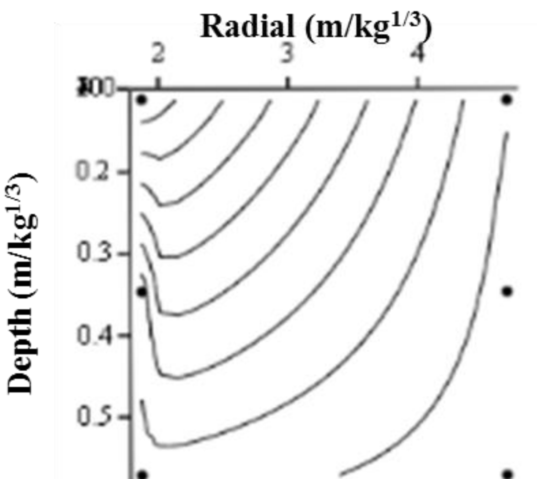

a)

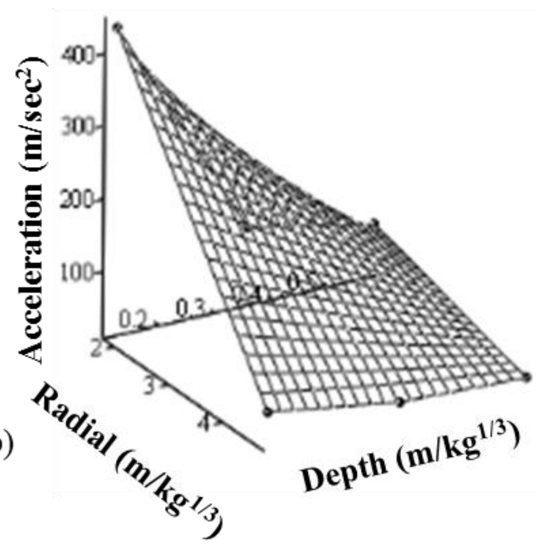

b)

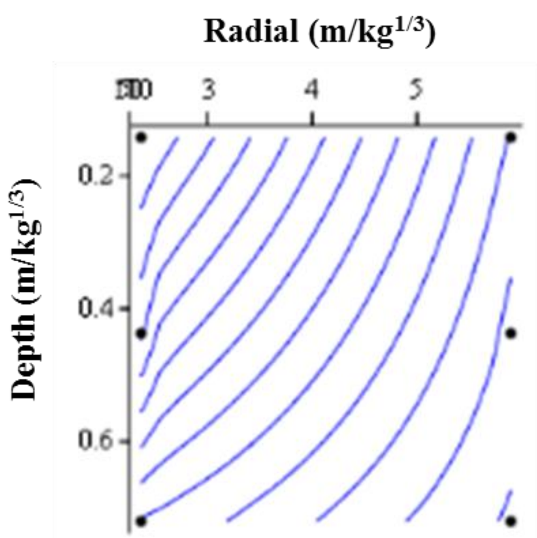

c)

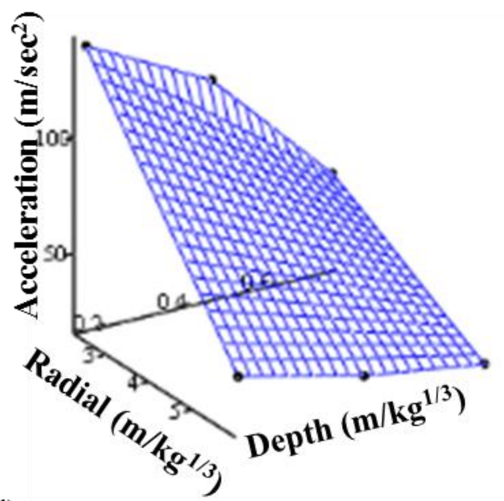

d)

APPENDIX M

ACCELERATION AS A FUNCTION OF DENSITY

Surface Detonation

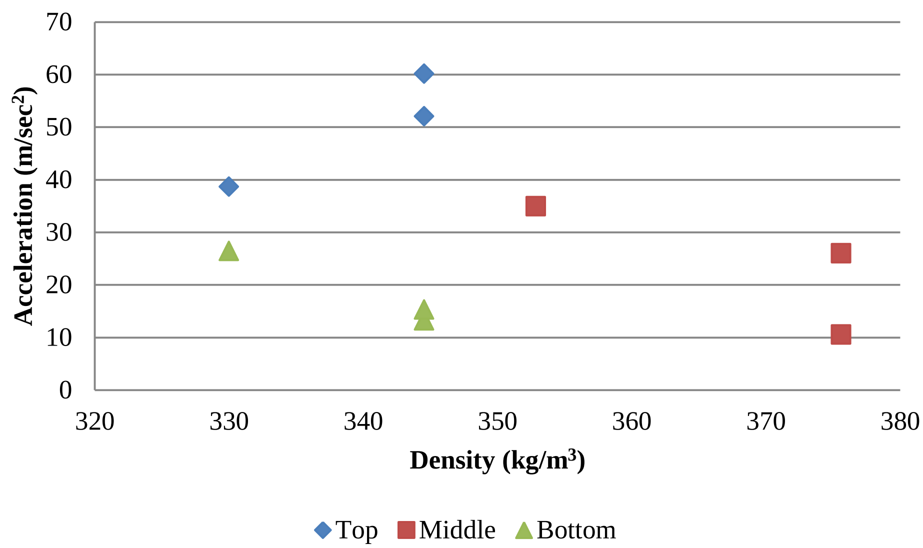

0.5 m Elevated Detonation

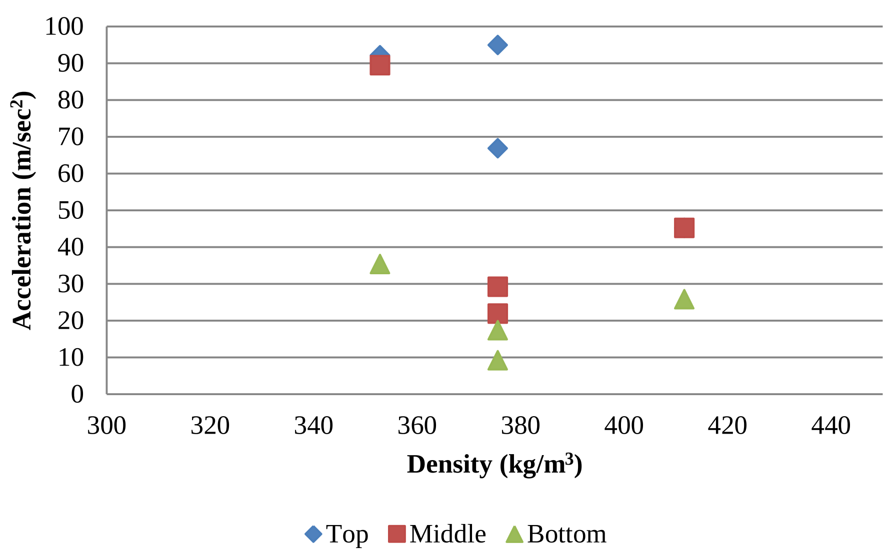

1 m Elevated Detonation

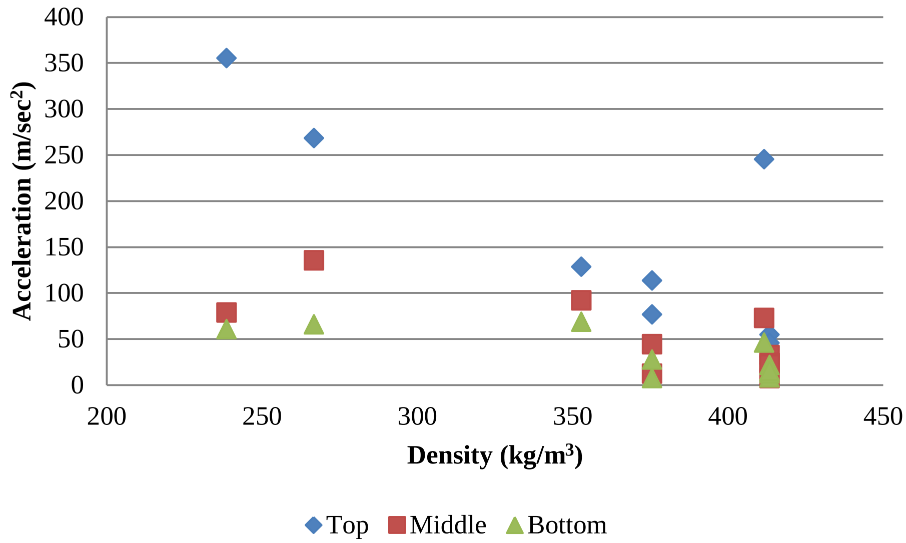

1.5 m Elevated Detonation

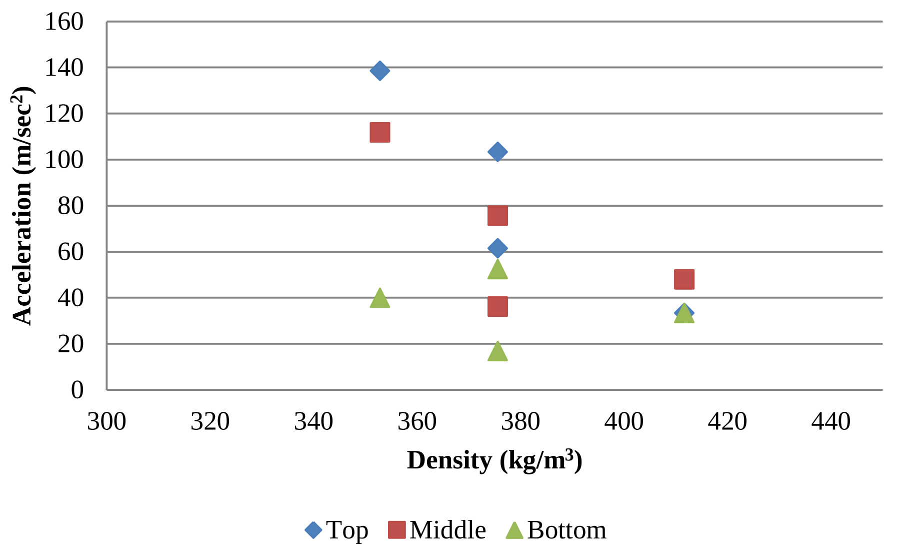

2 m Elevated Detonation